

The Finite-Element Contrast Source Inversion Method for Microwave Imaging Applications

by

Amer Zakaria

A Thesis submitted to the Faculty of Graduate Studies of

The University of Manitoba

in partial fulfilment of the requirements of the degree of

DOCTOR OF PHILOSOPHY

Department of Electrical and Computer Engineering

University of Manitoba

Winnipeg, Manitoba, Canada

Copyright © 2012 by Amer Zakaria

Abstract

This dissertation describes research conducted on the development and improvement of microwave tomography algorithms for imaging the bulk-electrical parameters of unknown objects.

The full derivation of a new inversion algorithm based on the state-of-the-art contrast source inversion (CSI) algorithm coupled to a finite-element method (FEM) discretization of the Helmholtz differential operator formulation for the scattered electromagnetic field is presented. The algorithm is applied to two-dimensional (2D) scalar and vectorial configurations, as well as three-dimensional (3D) full-vectorial problems. The unknown electrical properties of the object are distributed on the elements of arbitrary meshes with varying densities. The use of FEM to represent the Helmholtz operator allows for the flexibility of having an inhomogeneous background medium, as well as the ability to accurately model any boundary shape or type: both conducting and absorbing.

The CSI algorithm is used in conjunction with multiplicative regularization (MR), as it is typical in most implementations of CSI. Due to the use of arbitrary meshes in the present implementation, new techniques are introduced to perform the necessary spatial gradient and divergence operators of MR. The approach is different from other MR-CSI implementations where the unknown variables are located on a uniform grid of rectangular cells and represented using pulse basis functions; with rectangular cells finite-difference operators can be used, but this becomes unwieldy in FEM-CSI. Furthermore, an improvement for MR is proposed that accounts for the imbalance between the real and imaginary parts of the electrical properties of the unknown objects. The proposed method is not restricted to any particular formulation of the contrast source inversion.

The functionality of the new inversion algorithm with the different enhancements is tested using a wide range of synthetic datasets, as well as experimental data collected by the University of Manitoba electromagnetic imaging group and research centers in Spain and France.

Contributions

This dissertation focuses on the development of the finite-element contrast source inversion (FEM-CSI) method for solving inverse scattering problems for microwave imaging applications. While the CSI algorithm is not new, the specific contributions to the field presented in this work are:

- The full derivation of a new inversion algorithm based on the contrast source inversion (CSI) algorithm and a finite-element (FEM) discretization of the Helmholtz differential operator formulation for the scattered electromagnetic field.
- The development of a finite-element solver for microwave imaging applications capable of handling two-dimensional scalar and vectorial problems for different chamber types, as well as three-dimensional full-vectorial configurations for unbounded problems. The solver is integrated as part of the inversion algorithm, as well as used to calculate the fields scattered from known objects.
- The enhancement of the inversion algorithm by incorporating the weighted L_2 -norm total variation multiplicative regularization to FEM-CSI. The novelty herein is the introduction of new techniques to perform necessary spatial gradient and divergence operators on arbitrary meshes.
- The derivation and implementation of an improved multiplicative regularization technique for CSI that accounts for the imbalance between the constituents of an unknown target's electrical properties (this work was performed in conjunction with Dr. Colin Gilmore).
- The inversion of a vast array of synthetic and experimental datasets to test the functionality of the algorithms as well as outline their advantages.

A list of publications directly related to these contributions can be found in Appendix J. All the utilized solvers and algorithms, except for MR-CSI formulated using integral-equations (IE) *, were implemented solely by the author.

*The results using IE-CSI were obtained by Dr. Colin Gilmore.

Acknowledgments

He who does not thank the people, does not thank God Almighty.

–Prophet Muhammad (may peace be upon him)

My first, and most earnest, acknowledgment must go to my advisor Professor Joe LoVetri. Over four years ago, an email conversation with Dr. LoVetri started me on the path that brought me to Canada. Dr. LoVetri has been instrumental in ensuring my academic, professional, financial, and moral well being ever since. In every sense, none of this work would have been possible without him.

I would also like to acknowledge my colleagues Dr. Colin Gilmore, Dr. Ian Jeffrey, Dr. Puyan Mojabi, Dr. Majid Ostasrahimi, Gabriel Faucher and Cameron Kaye for all the support and fruitful discussions we had together for the past years and hopefully will continue to have in the future. Special thanks for Samer Bahaggag and Tyler Seredynski for their help during the summer of 2011.

I would like to express my appreciation for the efforts of my PhD committee: Prof. Greg Bridges, Prof. Stephen Pistorius, Prof. Shaun Lui and Prof. Mohamed Bakr.

I extend my gratitude to the Natural Sciences and Engineering Research Council of Canada, University of Manitoba, Manitoba Ministry of Advanced Education, Western Economic Diversification Canada, MITACS, and CancerCare Manitoba for their financial support. Without their support, this research would simply not be possible.

Finally, to my Parents, family and friends everywhere thanks for all your support and patience.

To my Parents and Family

Table of Contents

List of Figures	xii
List of Tables	xvii
Notations, Symbols and Acronyms	xviii
1 Introduction	1
1.1 Scope	1
1.2 Motivation	2
1.3 Purpose	3
1.4 Outline	6
2 Mathematical Formulation	8
2.1 Maxwell's Equations	9
2.2 Helmholtz Equation	12
2.3 Microwave Imaging System	13
2.3.1 Case 1: 2D Transverse Magnetic	16
2.3.2 Case 2: 2D Transverse Electric	18
2.3.3 Case 3: 3D Full-Vectorial	18
2.4 Integral Equation Formulation	19
2.4.1 Data and Domain Operators	21
2.4.2 Data and Domain Equations	22
2.5 Inverse Scattering Problem	23
2.5.1 Conventional Type Algorithms	24
2.5.2 Modified-Gradient Type Algorithms	25
3 Solving the Forward Problem	27
3.1 The Finite Element Method	28
3.2 Scalar Problems	30
3.2.1 The Boundary-Value Problem	30
3.2.2 The Variational Problem	31
3.2.3 Domain Discretization	32
3.2.4 Elemental Basis Functions	33
3.2.5 Boundary Basis Functions	35

3.2.6	Functional Discretization	36
3.2.7	Dirichlet Boundary Condition	38
3.2.8	Absorbing Boundary Condition	39
3.3	Vector Problems	41
3.3.1	The Boundary-Value Problem	41
3.3.2	Variational Problem	42
3.3.3	Domain Discretization	43
3.3.4	Elemental Basis Functions	43
3.3.4.1	Triangular Edge-based Elements	45
3.3.4.2	Tetrahedral Edge-based Elements	46
3.3.4.3	Vector-basis functions Properties	48
3.3.5	Boundary Basis Functions	48
3.3.5.1	1D Line Elements	48
3.3.5.2	2D Triangle Facets	49
3.3.6	Functional Discretization	50
3.3.7	Dirichlet Boundary Condition	53
3.3.8	Absorbing Boundary Condition	54
3.4	Matrix Operators	56
3.4.1	Measurement Surface Operators	56
3.4.2	Imaging Domain Operators	58
3.4.3	Inverse FEM Matrix Operators	59
3.4.3.1	Scalar Problems	59
3.4.3.2	Vector Problems	61
4	The Inversion Algorithm	65
4.1	The Contrast Source Inversion Method	67
4.2	The FEM-CSI Algorithm	68
4.2.1	Norms and Inner Products	69
4.2.1.1	Nodal Variables, Nodal Unknowns	69
4.2.1.2	Vector Variables, Centroidal Unknowns	70
4.2.2	The Contrast Source Variables Update	71
4.2.2.1	Case 1: 2D TM	73
4.2.2.2	Case 2: 2D TE	73
4.2.2.3	Case 3: 3D Full-Vectorial	74
4.2.3	The Contrast Variables Update	76
4.2.4	Initializing the Algorithm	77
5	Multiplicative Regularization	78
5.1	Multiplicatively Regularized FEM-CSI	80
5.1.1	Updating the Contrast Variables	82
5.2	Spatial Derivatives on Arbitrary Meshes	85
5.2.1	Case 1: 2D TM	85

5.2.2	Case 2: 2D TE	88
5.2.3	Case 3: 3D Full-Vectorial	89
5.2.4	Spatial Derivatives Calculation Summary	91
5.3	Balanced MR-FEMCSI	92
5.3.1	Balancing and the Domain-Error Equation	95
6	Implementation and Evaluation	96
6.1	Implementation	97
6.2	Synthetic Results	99
6.2.1	Inverse Crime	99
6.2.2	Algorithm Evaluation	100
6.2.3	FEM-CSI: 2D TM	101
6.2.3.1	Comparison between FEM-CSI and IE-CSI	102
6.2.3.2	Microwave Tomography in PEC Enclosures of Various Shapes	103
6.2.3.3	Biological Imaging with an Inhomogeneous Background	106
6.2.3.4	Adaptive Meshing	109
6.2.3.5	Section Conclusion	113
6.2.4	MR-FEMCSI: 2D TM	115
6.2.4.1	Low-Contrast Concentric Squares	115
6.2.4.2	Breast Model	117
6.2.4.3	Section Conclusion	123
6.2.5	Balanced MR-FEMCSI: 2D TM	123
6.2.5.1	Human Forearm Model	124
6.2.5.2	E-Phantom	126
6.2.5.3	Section Conclusion	134
6.2.6	Inversion of 2D TE Datasets	135
6.2.6.1	Imaging inside a Conductive Enclosure	135
6.2.6.2	Lossy E-phantom: TM-TE comparison	138
6.2.6.3	Section Conclusion	142
6.2.7	Inversion of 3D Datasets	142
6.2.7.1	A Heterogeneous Lossy Dielectric Cube	143
6.2.7.2	Comparison of Computational Resource using Different Solvers	149
6.3	Experimental Results	154
6.3.1	UofM Microwave Tomography System	154
6.3.1.1	Inversion of UofM Datasets	157
6.3.1.2	E-Phantom	158
6.3.1.3	Wood-Nylon Target	161
6.3.1.4	Human Forearm	161
6.3.2	UPC Barcelona Datasets	166
6.3.2.1	Human Forearm	167

6.3.2.2	Cylindrical Phantom	168
6.3.2.3	Human Arm Phantom	170
6.3.3	Institut Fresnel 2D Datasets	173
6.3.4	Institut Fresnel 3D Datasets	180
6.3.4.1	Two Spheres	183
6.3.4.2	Two Cubes	187
6.3.4.3	Cube of Spheres	189
6.3.4.4	<i>Myster</i>	190
6.3.4.5	Section Conclusion	193
7	Conclusions and Future Work	196
7.1	Future Work	197
	Appendix	200
A	Derivation of FEM Local Matrices	201
A.1	Scalar Problems: Two-Dimensional Case	201
A.2	Vector Problems	204
A.2.1	Two-Dimensional Case	205
A.2.2	Three-Dimensional Case	206
B	Assembly of FEM Global Matrices	210
C	Required Gradients for FEM-CSI	213
C.1	Data-Error Equation Gradient	213
C.1.1	Case 1: 2D TM	214
C.1.2	Case 2: 2D TE	215
C.1.3	Case 3: 3D Full-Vectorial	217
C.2	Domain-Error Equation Gradient	218
C.2.1	Case 1: 2D TM	219
C.2.2	Case 2: 2D TE	220
C.2.3	Case 3: 3D Full-Vectorial	221
C.3	Summary	222
D	The Contrast Variables Update - Analytic	223
E	The Initial Guess for FEM-CSI	225
F	Required Gradients for MR-FEMCSI	227
F.1	Domain-Error Gradient with respect to the Contrast	227
F.2	MR term Gradient with respect to Contrast	229
G	Multiplicative Regularization Step-size	231

H	Approximating Spatial Derivatives	233
I	Incident Field in Conductive Enclosures	234
J	Selected Publications	236
J.1	Published Journal Papers	236
J.2	Submitted Journal Papers	236
J.3	Referred Conference Papers	237
	References	238

List of Figures

2.1	(a) Two-dimensional (2D) and (b) three-dimensional (3D) geometrical models for the imaging problem: Ω is the problem domain, \mathcal{D} is the imaging domain where the object-of-interest is located, Γ is the boundary enclosing the problem, and \mathcal{S} is the measurement surface where the transmitters and receivers are positioned.	13
3.1	Example mesh created using GMSH	32
3.2	(a) First-order triangular element and (b) first-order line element	34
3.3	Transformation of line segment to an isoparametric element.	36
3.4	(a) A cross-section of a 3D mesh created using GMSH (b) First-order tetrahedral element.	44
3.5	Transformation of a triangle element to an isoparametric element.	51
5.1	Region surrounding node i to approximate the spatial derivatives. The “●” in the diagram represents the centroid of a triangle.	87
6.1	(a)-(b) \ddot{U} exact profile and reconstructions at $f = 2$ GHz using (c)-(d) FEM-CSI and (e)-(f) IE-CSI.	104
6.2	Exact profile of circular targets with lossy background at a frequency of $f = 1$ GHz.	105
6.3	PEC enclosure configurations and FEM-CSI reconstructions at $f = 1$ GHz for (a)-(c) a circular domain, (d)-(f) a square domain and (g)-(i) a triangular domain.	107
6.4	(a)-(b) Brain exact profile and (c)-(d) given prior information at $f = 1$ GHz.	108
6.5	FEM-CSI reconstructions at $f = 1$ GHz (a)-(b) when no prior information is given, (c)-(d) when prior information is utilized as initial guess, and (e)-(f) when prior information is used as background.	110
6.6	Exact relative permittivity of OI (a) Real and (b) Imaginary	111
6.7	The reconstructions at $f = 2$ GHz with (a)-(c) a coarse mesh, (d)-(f) an adapted mesh and (g)-(i) a fine mesh.	112
6.8	The FEM-CSI cost functional versus the iteration number for (a) \ddot{U} -profile, (b) MWT in PEC enclosures, (c) BMI of brain model and (d) adaptive meshing dataset reconstructions.	114

6.9	(a)-(b) Low-contrast concentric squares exact profile, (c)-(d) FEM-CSI reconstruction and (e)-(f) MR-FEMCSI reconstruction at frequency $f = 1$ GHz.	118
6.10	A cross-section at $y = 0$ for the exact profile (solid blue), FEM-CSI reconstruction (dash-dot black) and MR-FEMCSI (dash red).	119
6.11	Low-contrast concentric squares reconstructions using IE-MRCSI.	120
6.12	(a)-(b) Breast Model exact profile and (c)-(d) given prior information at frequency $f = 1.6$ GHz.	121
6.13	Reconstructions at $f = 1.6$ GHz using (a)-(b) FEM-CSI and (c)-(d) MR-FEMCSI.	122
6.14	The cost functional versus the iteration number for (a) low-contrast concentric squares and (b) breast model synthetic datasets reconstruction.	123
6.15	Synthetic arm exact profile at a frequency $f = 1$ GHz.	125
6.16	Human forearm model reconstructions using (a)-(b) MR-FEMCSI and (c)-(d) BMR-FEMCSI for $Q = 5$ and (e)-(f) for $Q = 20$	127
6.17	The “e-phantom” with circular inclusion exact profile at a frequency $f = 2$ GHz.	128
6.18	The “e-phantom” with circular inclusion reconstructions using (a)-(b) MR-FEMCSI and (c)-(d) BMR-FEMCSI for $Q = 10$ and (e)-(f) for $Q = 30$	129
6.19	Statistical analysis of the $-\text{Im}(\epsilon_r)$ reconstructions using different Q -factors.	132
6.20	(a) Map of balancing factor Q inside the imaging domain and (b) the imaginary part reconstruction using BMR-FEMCSI at $f = 2$ GHz.	133
6.21	The cost functional versus the iteration number for (a) human forearm model and (b) “e-phantom” synthetic datasets reconstruction.	134
6.22	The MR-FEMCSI reconstructions at a frequency $f = 1$ GHz for (a)-(b) an unbounded domain problem and for (c)-(d) a domain enclosed by triangular conductive boundary.	136
6.23	The exact profile of “e-phantom” at a frequency $f = 0.9$ GHz.	139
6.24	MR-FEMCSI reconstructions at $f = 0.9$ GHz for (a)-(b) the TE case and (c)-(d) the TM case.	140
6.25	BMR-FEMCSI reconstructions for $Q = 20$ at $f = 0.9$ GHz for (a)-(b) the TE case and (c)-(d) the TM case.	141
6.26	The cost functional versus the iteration number for (a) imaging inside a conductive enclosure and (b) lossy E-phantom synthetic datasets reconstruction.	142
6.27	(a) The coordinates configuration and the OI depiction. (b) The cost functional progress for the inversion of 3D synthetic dataset.	143

6.28	The real component $\text{Re}(\epsilon_r)$ of the (a)-(c) the actual OI, the reconstructions using (d)-(f) FEM-CSI and (g)-(i) MR-FEMCSI at planes $x = 0.015\text{m}$, $y = 0.015\text{m}$ and $z = 0.015\text{m}$	146
6.29	The imaginary component $-\text{Im}(\epsilon_r)$ of the (a)-(c) the actual OI, the reconstructions using (d)-(f) FEM-CSI and (g)-(i) MR-FEMCSI at planes $x = 0.015\text{m}$, $y = 0.015\text{m}$ and $z = 0.015\text{m}$	147
6.30	A 1-D cross-section across the plane $y = 0.015\text{ m}$ for the exact profile (solid blue), FEM-CSI reconstruction (dash red) and MR-FEMCSI (dash-dot black).	149
6.31	The MR-FEMCSI reconstruction at plane $z = 0.015\text{ m}$ interpolated to a cubic grid (a), (c) without spatial filtering and (b), (d) with spatial filtering.	150
6.32	(a) The MWT system with the Plexiglas casing. (b) A Vivaldi antenna.	155
6.33	(a) The metallic enclosure. (b) A dipole antenna with quarter wavelength balun.	156
6.34	The cost functional versus the iteration number for (a) the E-Phantom, (b) wood-nylon and (c) volunteer one forearm experimental datasets reconstruction.	158
6.35	The “e-phantom” (a) inside the imaging setup, (b) its exact profile at $f = 5\text{ GHz}$	159
6.36	The “e-phantom” reconstruction results using (a) FEM-CSI and (b) MR-FEMCSI.	160
6.37	The OI consisting of a wooden block and a nylon cylinder.	160
6.38	The reconstructions at a frequency $f = 3\text{ GHz}$ using (a)-(b) MR-FEMCSI and (c)-(d) BMR-FEMCSI for $Q = 20$	162
6.39	A volunteer’s forearm in the microwave imaging system.	163
6.40	The complex relative permittivity of the matching fluid used for microwave imaging.	164
6.41	(a) The MRI of a volunteer’s arm and the MWI reconstructions at frequencies (b), (e) $f = 0.8\text{ GHz}$, (c), (f) $f = 1.0\text{ GHz}$ and (d), (g) $f = 1.2\text{ GHz}$	165
6.42	The cost functional versus the iteration number for (a) BRAGREG, (b) FANCENT and (c) PHANARM experimental datasets inversion.	167
6.43	(a) FANCENT and (b) PHANARM target configurations.	168
6.44	Inversion of BRAGREG dataset using (a)-(b) FEM-CSI, (c)-(d) MR-FEMCSI and BMR-FEMCSI for (e)-(f) $Q = 5$ and (g)-(h) $Q = 10$	169
6.45	Inversion of FANCENT dataset using (a)-(b) FEM-CSI, (c)-(d) MR-FEMCSI and BMR-FEMCSI for (e)-(f) $Q = 5$ and (g)-(h) $Q = 10$	171
6.46	Inversion of PHANARM dataset using (a)-(b) FEM-CSI, (c)-(d) MR-FEMCSI and BMR-FEMCSI for (e)-(f) $Q = 5$ and (g)-(h) $Q = 10$	172
6.47	The targets of the 2D Fresnel dataset (a) <i>FoamDielInt</i> (b) <i>FoamDielExt</i> (c) <i>FoamTwinDiel</i> (d) <i>FoamMetExt</i>	173

6.48	The cost functional progress for (a) <i>FoamDielInt</i> , (b) <i>FoamDielExt</i> , (c) <i>FoamTwinDiel</i> and (d) <i>FoamMetExt</i> TM and TE experimental datasets inversions.	174
6.49	The reconstruction of the <i>FoamDielInt</i> target at $f = 2$ GHz using simultaneous-frequency MR-FEMCSI for (a)-(b) the TM case and (c)-(d) the TE case.	175
6.50	The reconstruction of the <i>FoamDielExt</i> target at $f = 2$ GHz using simultaneous-frequency MR-FEMCSI for (a)-(b) the TM case and (c)-(d) the TE case.	176
6.51	The reconstruction of the <i>FoamTwinDiel</i> target at $f = 2$ GHz using simultaneous-frequency MR-FEMCSI for (a)-(b) the TM case and (c)-(d) the TE case.	177
6.52	The reconstruction of the <i>FoamMetExt</i> target at $f = 2$ GHz using simultaneous-frequency MR-FEMCSI for (a)-(b) the TM case and (c)-(d) the TE case.	178
6.53	The reconstruction of the <i>FoamMetExt</i> target at $f = 2$ GHz with $\max \text{Im}(\epsilon_r) < 6$ using simultaneous-frequency MR-FEMCSI for (a)-(b) the TM case and (c)-(d) the TE case.	179
6.54	The coordinates configuration of the Institut Fresnel 3D setup.	181
6.55	(a) The two spheres target configuration and (b) the cost functional convergence.	184
6.56	The reconstructions at $f = 5$ GHz for the two spheres target using frequency-hopping FEM-CSI . (a) The isosurface plot (level = 2.0), (b) the 3D slice plot, and the 2D cross-section plots at planes (c) $x = 0$, (d) $y = 0$ and (e) $z = 0$	185
6.57	The reconstructions at $f = 5$ GHz for the two spheres target using frequency-hopping MR-FEMCSI. (a) The isosurface plot (level = 2.0), (b) the 3D slice plot, and the 2D cross-section plots at planes (c) $x = 0$, (d) $y = 0$ and (e) $z = 0$	186
6.58	(a) The two-cubes target configuration and (b) the cost functional conversion.	187
6.59	(a)-(b) The isosurface plot (level = 1.5) at $f = 8$ GHz of the two cubes target and the 2D slice plots of the reconstruction at planes (c)-(d) $x = [-14, 14]$ mm, (e)-(f) $y = [-14, 14]$ mm and (f)-(g) $z = [30, 64]$ mm. The figures on the left are the FEM-CSI reconstructions while those on the right are the MR-FEMCSI results. The results are obtained using a frequency-hopping approach.	188
6.60	(a) The cube of spheres target configuration and (b) the cost functional convergence.	189

6.61	(a)-(b) The isosurface plot (level = 1.9) at $f = 8$ GHz of the cube of spheres target and the 2D slice plots of the reconstruction at planes (c)-(d) $z = 12.5$ mm, (e)-(f) $y = 0$ mm and (f)-(g) $x = 0$ mm. The figures on the left are the FEM-CSI reconstructions while those on the right are the MR-FEMCSI results. The results are obtained using a frequency-hopping approach.	191
6.62	(a) <i>Myster</i> target configuration and (b) an icosahedron. The red circles at the vertices of the icosahedron are the sphere centers of the <i>Myster</i> target.	192
6.63	The cost functional convergence for the <i>Myster</i> dataset inversion. . .	193
6.64	(a)-(b) The isosurface plot (level = 1.5) at $f = 8$ GHz of the <i>Myster</i> target and the 2D slice plots of the reconstruction at planes (c)-(d) $x = [-11.12, -6.87]$ mm and (e)-(f) $y = [-4.10, 19.25]$ mm. The figures on the left are the FEM-CSI reconstructions while those on the right are the MR-FEMCSI results. The results are obtained using a frequency-hopping approach.	194
6.65	The <i>Myster</i> dataset frequency-hopping FEM-CSI reconstructions at different z -planes for $f = 8$ GHz.	195
6.66	The <i>Myster</i> dataset frequency-hopping MR-FEMCSI reconstructions at different z -planes for $f = 8$ GHz.	195

List of Tables

0.1	Common Symbols and Notations	xix
0.2	Common Acronyms	xx
3.1	Edge Numbering for a Triangular Element	45
3.2	Edge Numbering for a Tetrahedral Element	46
3.3	Local Indices to calculate Nodal Basis Functions	47
6.1	Relative Dielectric Permittivities of Brain Model at $f = 1$ GHz	106
6.2	Summary of 2D TM Inversion Examples	113
6.3	Errors for 2D TM Inversion Examples	116
6.4	Relative Dielectric Permittivities of Breast Model at $f = 1.6$ GHz . .	120
6.5	Statistical Analysis of results	131
6.6	Summary of 2D and 3D Vectorial Inversion Examples	137
6.7	Errors for 2D and 3D Vectorial Inversion Examples	138
6.8	Computational Resources Required for Different Solvers	152
6.9	Summary of 2D Experimental Datasets	154
6.10	Summary of 3D Experimental Datasets	183

Notations, Symbols and Acronyms

It is of interest to note that while some dolphins are reported to have learned English—up to fifty words used in correct context—no human being has been reported to have learned dolphinese.

—Carl Sagan [1]

Herein some general remarks about the notations used throughout the thesis as well as a list of commonly used symbols and acronyms are provided.

- **Spatial-vectors:** continuous functions or data-vectors and matrices with entries that have more than one component in the Cartesian coordinates are denoted with an overhead arrow such as \vec{v} , \vec{p} , $\vec{\mathcal{M}}$.
- **Data column-vectors:** data column-vectors are denoted by underlined letters. For example, $\underline{\chi}$ represents the discrete form of $\chi(\vec{r})$ and $\underline{\vec{E}}_t^{\text{sct}}$ denotes the discrete form of the spatial vector \vec{E}_t^{sct} .
- **Matrices:** matrices are denoted by uppercase bold calligraphic letters such as $\mathcal{T}_{\mathcal{D}}$ and $\vec{\mathcal{L}}$.
- **Dyads:** dyads are denoted with uppercase letters with two overhead lines such as $\bar{\bar{I}}$ and $\bar{\bar{\mathcal{G}}}_S$.
- **Spatial derivative operators:** Spatial gradient and divergence matrix operators are given as (∇) and $(\nabla \cdot)$.
- **Integration Differentials:** The differential boundary element is denoted by ds ; for two-dimensional (2D) problems the boundary elements are lines, while for three-dimensional (3D) problems the elements are surface patches. The differential volumetric (domain) element, in 2D and 3D, is denoted by dv .

Table 0.1: Common Symbols and Notations

Symbol	Description
$\hat{x}, \hat{y}, \hat{z}$	Unit vectors in the x , y and z directions.
\hat{n}	Normal unit vector to the boundary.
\vec{r}, \vec{r}'	Position vectors in the Cartesian coordinates.
\mathbb{R}	Set of real numbers.
\mathbb{C}	Set of complex numbers.
Ω	Problem Domain.
\mathcal{D}	Imaging Domain.
\mathcal{S}	Measurement Surface.
Γ, Γ_1 and Γ_2	Problem boundary, Dirichlet boundary and Robin boundary.
ϵ_0	Permittivity of free-space.
ϵ_r	Relative complex permittivity of the OI.
ϵ_b	Relative complex permittivity of the background medium.
ϵ'_r	Real relative permittivity of the OI.
σ	Conductivity of the OI.
χ	Contrast variable.
μ_0	Permeability of free-space.
μ_r	Relative permeability of the OI.
k_0	Wavenumber of free-space.
k	Wavenumber.
k_b	Wavenumber of the background medium.
ω	Radial frequency.
f	Frequency of operation.
t	Active transmitter index.
\vec{w}_t	Contrast source variable for an active transmitter t .
\vec{E}_t^{inc}	Incident vector-field for an active transmitter t .
\vec{E}_t^{sct}	Scattered vector-field for an active transmitter t .
\vec{E}_t	Total vector-field for an active transmitter t .

$\bar{\bar{G}}_b$	Dyadic Green's function.
$\mathcal{G}_S, \mathcal{G}_D$	Data and domain operators.
$\vec{\mathcal{H}}_b$	Helmholtz operator.
$\vec{\mathcal{M}}_S, \vec{\mathcal{M}}_D$	Data and domain transformation operators.
Re	Real part operator.
Im	Imaginary part operator.
∇	Gradient operator.
$\nabla \cdot$	Divergence operator.
$\nabla \times$	Curl operator.
∇^2	The Laplacian.
$(\cdot)^{-1}$	Inverse Operator.
$(\cdot)^T$	Transpose Operator.
$(\cdot)^*$	Complex-conjugate Operator.
$(\cdot)^H$	Hermitian (transpose complex-conjugate) Operator.
$\ \cdot\ $	L_2 - norm or Euclidean norm.
$\langle \cdot, \cdot \rangle_S$	Inner product defined on \mathcal{S} .
$\langle \cdot, \cdot \rangle_D$	Inner product defined on \mathcal{D} .

Table 0.2: Common Acronyms

Acronym	Description
1D	One-dimensional.
2D	Two-dimensional.
3D	Three-dimensional.
ABC	Absorbing boundary condition.
BC	Boundary condition.
BMR	Balanced multiplicative regularization.
BVP	Boundary value problem.
CG	Conjugate gradient.
CSI	Contrast source inversion.
DBIM	Distorted Born iteration method.

DG	Discontinuous Galerkin.
EM	Electromagnetic.
FD	Finite-difference.
FDTD	Finite-difference time domain.
FEM	Finite-element method.
FFT	Fast Fourier transform.
FMM	Fast multipole method.
FVTD	Finite-volume time domain.
GNI	Gauss-Newton inversion.
IE	Integral equation.
MGM	Modified-gradient method.
MoM	Method-of-Moments.
MoWR	Method of weighted residuals.
MR	Multiplicative regularization.
MRI	Magnetic resonance imaging.
MWI	Microwave imaging.
MWT	Microwave tomography.
OI	Object-of-interest.
PDE	Partial differential equation.
PEC	Perfect electric conductor.
PMR	Pre-scaled multiplicative regularization.
TE	Transverse electric.
TM	Transverse magnetic.

Introduction

Everyone wants something without having any idea how to obtain it and the really intriguing aspect of the situation is that nobody quite knows how to achieve what he desires. But because I know what I want and what the others are capable of I am completely prepared.

–Prince Klemens von Metternich

1.1 Scope

This thesis presents research work in the area of microwave imaging (MWI) algorithms in the framework of the electromagnetic inverse scattering problem. Microwave imaging is of interest for various applications such as medical imaging [2–4], geophysical surveying [5, 6], through-wall imaging [7], industrial non-destructive testing [8] and security scanners [9]. In the form of MWI considered herein, one attempts to quantitatively reconstruct the unknown electrical properties (i.e. permittivity and/or conductivity) of an object-of-interest (OI) which is immersed in a background medium of known electrical properties within a chamber. The OI is successively illuminated by various sources of electromagnetic radiation at either a single-frequency or consecutive discrete frequencies. The introduction of the OI into the chamber results in a different field from that in the empty chamber. The difference between the two fields

is referred to as the scattered field. In the absence of the OI, the field produced by the same sources located in the background medium is referred to as the incident field. Both fields are measured at several locations within accessible regions surrounding the OI.

The inverse scattering problem associated with MWI can be cast as an optimization problem over variables representing the unknown electrical properties which are to be reconstructed. This inverse problem is nonlinear and ill-posed. The nonlinearity arises due the existence of two unknowns: the field within the OI and the object-of-interest electrical properties. Furthermore, the problem is ill-posed in the sense of Hadamard [10] hence: (*i*) the solution for the inverse problem is not guaranteed to be unique; (*ii*) the solution is unstable, *i.e.* small changes in the measured fields can cause large changes in the reconstructed unknowns; and (*iii*) a solution might not exist. The nonlinearity and ill-posedness are treated by utilizing various specialized optimization and regularization techniques [11–13].

Another approach to solving inverse problems is linearizing them by making assumptions regarding the electromagnetic wave propagation within the scatterer [14–19]. While the linearization techniques provide some useful qualitative images, they cannot quantitatively reconstruct the bulk-electric parameters (permittivity and/or conductivity). As methods to solve the inverse problem linearly are beyond the scope of the thesis they will not be discussed further.

1.2 Motivation

For the past several years, the electromagnetic imaging laboratory (EMIL) at the University of Manitoba (UofM) has embarked on research related to the field of microwave imaging for biomedical applications. The research involves the implemen-

tation of microwave imaging systems [20–26] along with the development of inversion algorithms to solve the inverse scattering problem associated with MWI [27–29]. The importance of accurate modeling of the MWI systems necessitates the realization of innovative methods to bring the mathematical model representing the MWI system closer to the actual physical model. Contributing to this group effort is the driving force behind the work in this thesis.

1.3 Purpose

When the inverse scattering problem formulation makes use of an integral equation (IE) for the electromagnetic field a Green’s function corresponding to the background medium and the problem’s boundaries is required [19]. If the background medium is inhomogeneous or if the problem’s boundary is complicated (*e.g.* arbitrary and/or conducting) deriving and calculating the Green’s function can be a complex, computationally expensive process. With knowledge of the Green’s function, the IE is typically solved using the Method-of-Moments (MoM), which produces a dense system of equations that can be a computational burden [20, 28, 30].

Partial differential equation (PDE) formulations of the scattering problem can be discretized directly using numerical techniques such as finite-difference (FD) or finite-element (FE) methods [31–33]. Using PDE operators, there is no need to determine the problem’s Green function and, thus, the presence of an inhomogeneous background or a complicated boundary can be easily taken into account without affecting the computational complexity of the numerical solution. In addition, unlike IE formulations, PDE formulations readily produce sparse systems of equations which can be solved efficiently.

The objective of the thesis is to develop inversion algorithms that will be efficient,

as well as offer flexibility in terms of:

1. Solving two-dimensional (2D) and three-dimensional (3D) electromagnetic (EM) problems whether they are scalar or vectorial.
2. Modeling chamber boundaries of different shapes and types.
3. Having the inversion unknowns distributed on an arbitrary mesh of varying densities.

A computational technique that can offer these capabilities for the forward EM problem is the finite-element method (FEM). A state-of-the-art efficient inversion algorithm that has had success in solving the inverse scattering problem is the contrast-source inversion method.

Prior to the research undertaken for this thesis, the electromagnetic imaging laboratory had expertise with the IE formulation of CSI for 2D scalar problems with the transverse magnetic (TM) assumption of the fields [20, 27, 34]. The work herein formulates the CSI algorithm using FEM to satisfy the objectives above. The algorithm will be referred to often in the text as the FEM-CSI method. Further, the work includes enhancing the outcome of the algorithm via two forms of multiplicative regularization (MR). The inclusion of MR into FEM-CSI is complicated because the unknowns are located on an arbitrary mesh. This requires the development of novel techniques to perform spatial differentiation operations on arbitrary meshes.

Due to an abundant availability of datasets assuming the 2D TM polarization of the fields, the algorithms studied in this research were formulated initially for scalar two-dimensional problems. Next, the FEM-CSI algorithm was developed for vectorial 2D transverse electric problems. Based on numerical investigation, it has been shown that using the transverse electric (TE) polarization in the near-field can result in more

accurate reconstructions than interrogating the OI with the TM polarization [35]. There are two standard approaches to solve the TE electromagnetic problem. The first is to formulate the TE problem as a scalar problem using a single magnetic field component. As concluded in [36], such a formulation results in a less stable algorithm with degraded performance as compared to the second approach which formulates the problem in terms of the two electric field components in the transverse plane. Further, as discussed in [37], the numerical modeling of dielectric discontinuities is more difficult for TE problems formulated in terms of the longitudinal magnetic field component due to the difficulty of modeling polarization charges. Thus, the second standard approach which uses the vector electric field in the transverse plane has been chosen and is described in this work. Further, the next natural extension beyond 2D TE is the 3D full-vectorial, which is also presented in this thesis. The algorithm expansion to handle vectorial problems was encouraged by the availability of vectorial experimental datasets from the Institut Fresnel of Marseilles, France [38, 39].

Inversion algorithms based on the finite element method (FEM) have been introduced in the past. In [31], Rekanos *et al.* uses FEM for the field solution but the unknown electrical properties for the problem are located on a uniform grid of square cells. Each cell in the grid is discretized into several triangles for the field solution. Such a dual-grid technique does not take advantage of the full flexibility of using an FEM discretization: the inversion is not actually performed on an arbitrary mesh. Furthermore, the method in [31] is only applied to 2D TM synthetic datasets for unbounded-region problems. In [33, 40], a hybrid method that combines FEM and a boundary-element method (BEM) is utilized. A dual mesh scheme is also used in their work, where the contrast variables are located on nodes of a coarse triangular mesh and the electric fields are calculated on a finer triangular mesh. For

3D problems, an accelerated finite-difference time-domain vectorial code is used to calculate the fields [40]. At each iteration, the contrast variables are updated using a Gauss-Newton method and then the updates are utilized to calculate the scattered fields. This method has been applied successfully to experimental data [2, 40]. A disadvantage of both of these FEM-based inversion algorithms is that the system of FEM equations have to be re-assembled at every iteration in order to solve for the scattered field. This disadvantage is not applicable to the present method wherein FEM is coupled with CSI.

1.4 Outline

In Chapter 2, the mathematical formulation associated with the inverse scattering problem for microwave imaging applications is presented. The formulation is presented for two- and three- dimensional problems. For 2D problems, the scalar and vectorial cases are considered, whereas for 3D the full-vectorial problem is examined. The partial-differential equation as well as the integral-equation form of the problem are shown. A brief explanation of the inversion algorithms is provided.

In Chapter 3, the PDEs associated with the electromagnetic model of the microwave imaging problem are solved using the finite-element method. The details for solving the 2D and 3D MWI problems, whether scalar or vectorial, using FEM are outlined. Further, the matrix operators required to describe and implement the inversion algorithms effectively in following chapters are explained. The operators result from the FEM discretization of the MWI problem. Appendices A and B serve as companions for this chapter to provide further explanation.

In Chapter 4, the contrast source inversion (CSI) technique is formulated using FEM. First a general overview of the CSI algorithm is outlined. Next, a full descrip-

tion for the FEM-CSI algorithm is given for the three MWI problem configurations: 2D TM, 2D TE and 3D full-vectorial. The detailed derivation of the algorithm update procedures are given in Appendices C, D and E.

In Chapter 5, a weighted L_2 -norm total variation multiplicative regularization term is incorporated to the FEM-CSI algorithm. As the algorithm unknowns are located at either mesh nodes or element centroids, novel techniques to perform the spatial gradient and divergence operators are introduced. Additionally, in this chapter an enhancement for the multiplicative regularization term is proposed. The improvement accounts for the imbalance between the real and imaginary components of the OI's electrical properties. The full details of the algorithm are contained in Appendices F, G and H.

Chapter 6 focuses on the development and evaluation of the FEM-CSI algorithm and its variants. The implemented algorithms are tested using a vast number of synthetic as well as experimental datasets. The purpose of the synthetic datasets is to provide an understanding of the advantages offered by the FEM-CSI algorithm and its multiplicatively regularized forms. Furthermore, the experimental datasets are intended to test the functionality of the code using data collected by the University of Manitoba imaging group, as well as other electromagnetic research groups in Spain and France.

The thesis is concluded in Chapter 7, followed by prospects for future work.

2

Mathematical Formulation

From a long view of the history of mankind seen from, say, ten thousand years from now there can be little doubt that the most significant event of the 19th century will be judged as Maxwell's discovery of the laws of electrodynamics. The American Civil War will pale into provincial insignificance in comparison with this important scientific event of the same decade.

–Richard Feynman [41]

In this chapter, the mathematical formulation associated with microwave imaging (MWI) is presented in the frequency-domain. The formulation is shown for two-dimensional (2D) as well as three-dimensional (3D) configurations. For 2D field problems two polarizations are considered, transverse magnetic (TM) and transverse electric (TE); whereas in the 3D case the full-vectorial formulation is studied. The wave equation associated with each case is derived from Maxwell's equations, outlining any necessary assumptions as required.

In the second part of the chapter, the integral equation (IE) based formulation of the electromagnetic field is presented pointing out any required new terms. The IE form is utilized to more easily define several operators along with a set of equations required to describe the inverse scattering problem. Further, the inverse problem is briefly explained, as well as the two types of optimization algorithms commonly used to treat problem nonlinearities.

2.1 Maxwell's Equations

In 1873 James Clerk Maxwell completed the formulation of his renowned equations which are considered as one of the greatest contributions in the 19th century. The importance of “Maxwell's Equations” is due to their predictive power of the electromagnetic phenomena at a macroscopic scale, which aided in the development of a vast number of modern technologies. In differential form, Maxwell's equations are

$$\nabla \times \vec{\mathcal{E}}(\vec{r}, t) = -\frac{\partial \vec{\mathcal{B}}(\vec{r}, t)}{\partial t}, \quad (2.1)$$

$$\nabla \times \vec{\mathcal{H}}(\vec{r}, t) = \frac{\partial \vec{\mathcal{D}}(\vec{r}, t)}{\partial t} + \vec{\mathcal{J}}(\vec{r}, t), \quad (2.2)$$

$$\nabla \cdot \vec{\mathcal{D}}(\vec{r}, t) = \rho_v(\vec{r}, t), \quad (2.3)$$

$$\nabla \cdot \vec{\mathcal{B}}(\vec{r}, t) = 0, \quad (2.4)$$

where the spatial vector quantities $\vec{\mathcal{E}}$, $\vec{\mathcal{D}}$, $\vec{\mathcal{H}}$, $\vec{\mathcal{B}}$, and $\vec{\mathcal{J}}$ are, respectively, the electric field intensity in [volts/meter], the electric flux density in [coulombs/meter²], the magnetic field intensity in [amperes/meter], the magnetic flux density in [webers/meter²] and the electric current density in [amperes/meter²], while the scalar quantity ρ_v is the electric charge density in [coulombs/meter³]. Each quantity is a function of time t and the three-dimensional position vector $\vec{r} = (x, y, z)$. Each spatial vector quantity has three components, in the \hat{x} -direction, \hat{y} -direction and \hat{z} -direction. The mathematical operators, $\nabla \times$ and $\nabla \cdot$, implement the curl and divergence operations respectively.

The electric current density $\vec{\mathcal{J}}$ in (2.2) can be expressed as the sum of two components: the conduction current density, $\vec{\mathcal{J}}_c$, and the impressed current density, $\vec{\mathcal{J}}_i$, thus

$$\vec{\mathcal{J}}(\vec{r}, t) = \vec{\mathcal{J}}_c(\vec{r}, t) + \vec{\mathcal{J}}_i(\vec{r}, t). \quad (2.5)$$

The distinction between the two components is useful as $\vec{\mathcal{J}}_c$ is related to the medium's ability to conduct electric current, while $\vec{\mathcal{J}}_i$ is due to given impressed current sources, *e.g.* at antenna ports.

In addition to (2.1)-(2.5), three more equations are needed to specify the relationships between the field quantities. These constitutive relationships are dependent on the medium where the fields exist, and they are

$$\vec{\mathcal{D}}(\vec{r}, t) = \epsilon_0 \epsilon'_r(\vec{r}) \vec{\mathcal{E}}(\vec{r}, t), \quad (2.6)$$

$$\vec{\mathcal{B}}(\vec{r}, t) = \mu_0 \mu_r(\vec{r}) \vec{\mathcal{H}}(\vec{r}, t), \quad (2.7)$$

$$\vec{\mathcal{J}}_c(\vec{r}, t) = \sigma(\vec{r}) \vec{\mathcal{E}}(\vec{r}, t). \quad (2.8)$$

Here ϵ_0 is the permittivity of free space in [Farads/meter]. ϵ'_r is the real relative permittivity (unit-less), μ_0 is the permeability of free space in [Henrys/meter], μ_r is the relative permeability (unit-less), and σ is the conductivity in [Siemens/meter]. The medium considered here is isotropic and linear, thus ϵ'_r , μ_r and σ are scalar quantities that are independent of the field intensity strength.

In this work, Maxwell's equations are assumed to have a time-harmonic dependency of $\exp(j\omega t)$ where $j^2 = -1$ and $\omega = 2\pi f$ is the angular frequency in [radians/second] for a frequency f in [hertz]. Under this assumption, Maxwell's equations

become

$$\nabla \times \vec{E}(\vec{r}) = -j\omega\vec{B}(\vec{r}) \quad (2.9)$$

$$\nabla \times \vec{H}(\vec{r}) = j\omega\vec{D}(\vec{r}) + \vec{J}(\vec{r}) \quad (2.10)$$

$$\nabla \cdot \vec{D}(\vec{r}) = \rho_v(\vec{r}) \quad (2.11)$$

$$\nabla \cdot \vec{B}(\vec{r}) = 0 \quad (2.12)$$

$$\vec{J}(\vec{r}) = \vec{J}_c(\vec{r}) + \vec{J}_i(\vec{r}) \quad (2.13)$$

where the vector fields are time-harmonic forms of their time-domain counterparts and are related to them, *e.g.*, by [42]

$$\vec{\mathcal{E}}(\vec{r}, t) = \sqrt{2}\text{Re}\{\vec{E}(\vec{r}) \exp(j\omega t)\}. \quad (2.14)$$

Here, the real component is multiplied by the $\sqrt{2}$ factor because the magnitude of the complex quantity is assumed to be the effective (root-mean-square) value of the instantaneous quantity. If the magnitude is the peak of the complex variable, the $\sqrt{2}$ can be omitted [42].

The time-harmonic assumption also applies to the constitutive relationships (2.6)-(2.8) by substituting the time-domain field quantities by their time-harmonic representations. Furthermore, the constitutive parameters can now be complex variables dependent on the operating frequency f .

In this work, we consider an electromagnetic problem where the electric field has an $\exp(j\omega t)$ time dependency*.

*Note that with this assumption a time variable is no longer needed and that the index 't' will be used later to indicate the number corresponding to the active transmitter.

2.2 Helmholtz Equation

For the MWI problem being solved, the interest is to derive a governing partial differential equation (PDE) that involves only the electric field vector \vec{E} . In this derivation, the assumptions are: (i) the problem domain is free of charge, *i.e.* $\rho_v = 0$, and (ii) the materials in the problem are non-magnetic, *i.e.* $\mu_r = 1$. Under these assumptions, \vec{H} is eliminated from (2.9) and (2.10) with the aid of the constitutive relationships (2.6)-(2.8) and (2.13), which results in

$$\nabla \times \nabla \times \vec{E}(\vec{r}) - \omega^2 \mu_0 \epsilon_0 \epsilon_r(\vec{r}) \vec{E}(\vec{r}) = -j\omega \mu_0 \vec{J}_i(\vec{r}). \quad (2.15)$$

This equation is called the inhomogeneous vector Helmholtz equation or simply the inhomogeneous vector wave equation. Here ϵ_r is the complex relative permittivity and is given by

$$\begin{aligned} \epsilon_r(\vec{r}) &= \epsilon_r'(\vec{r}) - j\epsilon_r''(\vec{r}) \\ &= \epsilon_r'(\vec{r}) - j \frac{\sigma(\vec{r})}{\omega \epsilon_0}. \end{aligned} \quad (2.16)$$

Note here that since the problem is now formulated in terms of the electric field, the later will be referred to as just *field* when there is no ambiguity.

Applying the vector relationship $\nabla \times \nabla \times \vec{U} = \nabla(\nabla \cdot \vec{U}) - \nabla^2 \vec{U}$, the expression (2.15) can be simplified to [43]

$$\nabla^2 \vec{E}(\vec{r}) + k^2(\vec{r}) \vec{E}(\vec{r}) + \nabla(\vec{E}(\vec{r}) \cdot \nabla \ln \epsilon(\vec{r})) = j\omega \mu_0 \vec{J}_i(\vec{r}) \quad (2.17)$$

where $k^2(\vec{r}) = \omega^2 \mu_0 \epsilon_0 \epsilon_r(\vec{r})$ is the wavenumber squared, ∇^2 is the Laplacian and $\nabla \ln \epsilon(\vec{r})$ is the gradient of the natural logarithm of the complex permittivity $\epsilon(\vec{r}) =$

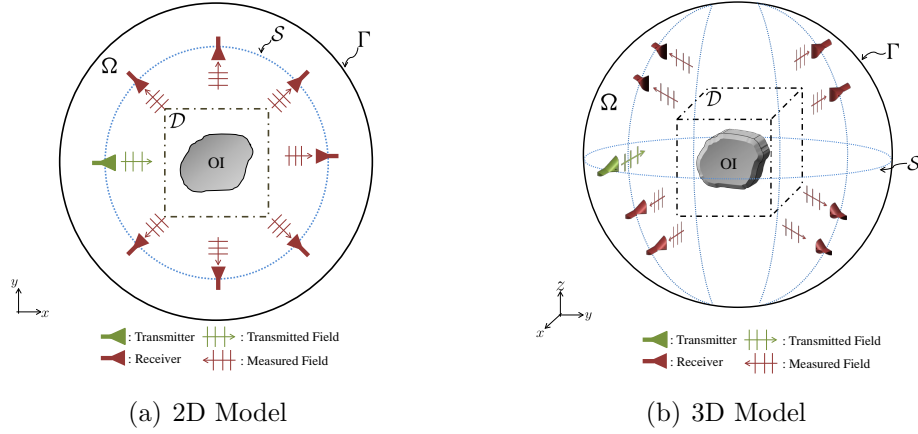


Figure 2.1: (a) Two-dimensional (2D) and (b) three-dimensional (3D) geometrical models for the imaging problem: Ω is the problem domain, \mathcal{D} is the imaging domain where the object-of-interest is located, Γ is the boundary enclosing the problem, and \mathcal{S} is the measurement surface where the transmitters and receivers are positioned.

$\epsilon_0 \epsilon_r(\vec{r})$. The simplified wave equation obtained in (2.17) will be used to derive the Helmholtz wave equation that governs scalar problems.

2.3 Microwave Imaging System

In a microwave imaging (MWI) system, an object-of-interest (OI) is located within a bounded chamber, as depicted in Figure 2.1. The OI and the imaging domain, \mathcal{D} , are contained within a problem domain, Ω , and are immersed in a background medium whose electrical properties are known but can be inhomogeneous. The domain Ω is surrounded by a boundary Γ that can be of any shape, size or type depending on the imaging setup being modeled. The complex relative permittivity of the OI is $\epsilon_r(\vec{r})$. The corresponding electric contrast is defined as

$$\chi(\vec{r}) \triangleq \frac{\epsilon_r(\vec{r}) - \epsilon_b(\vec{r})}{\epsilon_b(\vec{r})} \quad (2.18)$$

where $\epsilon_b(\vec{r})$ is the relative complex permittivity of the background medium (outside \mathcal{D} , the contrast $\chi(\vec{r}) = 0$). Note that the terms *contrast* and *electrical properties* will be used interchangeably to refer to the variable χ unless otherwise mentioned.

The chamber is successively illuminated by one of T transmitters, while the resultant field from the OI is measured at R receiver locations per transmitter. The transmitters and receivers are positioned on a measurement surface \mathcal{S} . In the absence of the OI, a transmitter t produces an incident field \vec{E}_t^{inc} , which is governed by the vector wave equation

$$\nabla \times \nabla \times \vec{E}_t^{\text{inc}}(\vec{r}) - k_b^2(\vec{r})\vec{E}_t^{\text{inc}}(\vec{r}) = -j\omega\mu_0\vec{J}_t(\vec{r}), \quad (2.19)$$

where $k_b^2(\vec{r}) = \omega^2\mu_0\epsilon_0\epsilon_b(\vec{r})$ is the square of the background medium wavenumber which is allowed to be inhomogeneous, and \vec{J}_t is used to model the transmitter.

With the presence of the OI in the imaging domain, the total field, \vec{E}_t , satisfies the wave equation

$$\nabla \times \nabla \times \vec{E}_t(\vec{r}) - k^2(\vec{r})\vec{E}_t(\vec{r}) = -j\omega\mu_0\vec{J}_t(\vec{r}). \quad (2.20)$$

The scattered field due to the presence of the OI is defined as

$$\vec{E}_t^{\text{sct}}(\vec{r}) \triangleq \vec{E}_t(\vec{r}) - \vec{E}_t^{\text{inc}}(\vec{r}). \quad (2.21)$$

By substituting (2.21) in the total field wave equation (2.20) and using the relationship in (2.19), the vector wave equation that governs the scattered field can be written as

$$\nabla \times \nabla \times \vec{E}_t^{\text{sct}}(\vec{r}) - k^2(\vec{r})\vec{E}_t^{\text{sct}}(\vec{r}) = (k^2(\vec{r}) - k_b^2(\vec{r}))\vec{E}_t^{\text{inc}}(\vec{r}). \quad (2.22)$$

This can be written in terms of the contrast, $\chi(\vec{r})$, as

$$\nabla \times \nabla \times \vec{E}_t^{\text{sct}}(\vec{r}) - k_b^2(\vec{r}) (\chi(\vec{r}) + 1) \vec{E}_t^{\text{sct}}(\vec{r}) = k_b^2(\vec{r}) \chi(\vec{r}) \vec{E}_t^{\text{inc}}(\vec{r}). \quad (2.23)$$

Rearranging (2.23) so that the contrast variable is on the right-hand side of the equation yields

$$\nabla \times \nabla \times \vec{E}_t^{\text{sct}}(\vec{r}) - k_b^2(\vec{r}) \vec{E}_t^{\text{sct}}(\vec{r}) = k_b^2(\vec{r}) \vec{w}_t(\vec{r}) \quad (2.24)$$

where \vec{w}_t is the contrast source variable defined as

$$\vec{w}_t(\vec{r}) \triangleq \chi(\vec{r}) \vec{E}_t(\vec{r}). \quad (2.25)$$

The right-hand side term of (2.24) effectively represents a source located within the scatterer that produces the scattered field \vec{E}_t^{sct} in a background medium k_b ; hence the namesake *contrast source*.

For further analysis, the vector wave equation can be written in operator notation as

$$\vec{\mathcal{H}}_b \left\{ \vec{E}_t^{\text{sct}} \right\} = k_b^2(\vec{r}) \vec{w}_t(\vec{r}). \quad (2.26)$$

The inverse of this operator evaluates the scattered field values in the problem domain Ω given the contrast source variables \vec{w}_t , along with the background medium wavenumber k_b . As will be described later, for inverse scattering problems the field values are required on the measurement surface \mathcal{S} and inside the imaging domain \mathcal{D} , thus two more operators are introduced. The surface operator $\vec{\mathcal{M}}_{\mathcal{S}}$ takes the field \vec{E}_t^{sct} in Ω to the receiver locations on the measurement surface \mathcal{S} . The imaging domain operator $\vec{\mathcal{M}}_{\mathcal{D}}$ returns the field values in \mathcal{D} given the field \vec{E}_t^{sct} .

Solving for the incident field \vec{E}_t^{inc} and the scattered field \vec{E}_t^{sct} requires that the

boundary conditions (BCs) on Γ be defined. For a conductive-enclosure system, perfect electrical conductor (PEC) boundary conditions are used (as explained in Appendix I) resulting in homogeneous Dirichlet BCs:

$$\hat{n} \times \vec{E}_t^{\text{inc}}(\vec{r} \in \Gamma) = 0 \quad \text{and} \quad \hat{n} \times \vec{E}_t^{\text{sct}}(\vec{r} \in \Gamma) = 0. \quad (2.27)$$

For some MWI systems, the background medium can be assumed to extend to infinity in two cases: (i) the reflections from the boundaries of the enclosure are negligible and can be ignored, and/or (ii) sufficient loss is incorporated in the matching medium such that little energy is reflected back from the enclosure's boundaries. In such cases all fields in the model will be required to satisfy the Sommerfeld radiation condition [44]:

$$\lim_{r \rightarrow \infty} r \left(\nabla \times \vec{E}_t^{\text{sct}}(\vec{r}) + jk_b \hat{r} \times \vec{E}_t^{\text{sct}}(\vec{r}) \right) = 0. \quad (2.28)$$

In this work three different configurations are studied: (i) two-dimensional transverse magnetic (2D TM), (ii) two-dimensional transverse electric (2D TE), and (iii) three-dimensional (3D) full-vectorial. In the next section the assumptions with each case, along with the field components are described. When necessary, any modifications for the wave equations are outlined.

2.3.1 Case 1: 2D Transverse Magnetic

For 2D transverse magnetic (TM) problems, the electrical properties as well as the fields are not varying in the \hat{z} -direction. In addition, the electric field is assumed to be z -polarized with no transverse components in the $x - y$ plane. Thus the incident field, scattered field and contrast source in wave equations (2.23) and (2.24) can be

represented as

$$\begin{aligned}\vec{E}_t^{\text{inc}}(\vec{r}) &= E_{t,z}^{\text{inc}}(\vec{r})\hat{z} \\ \vec{E}_t^{\text{sct}}(\vec{r}) &= E_{t,z}^{\text{sct}}(\vec{r})\hat{z} \\ \vec{w}_t(\vec{r}) &= w_{t,z}(\vec{r})\hat{z}.\end{aligned}\tag{2.29}$$

Here the position vector $\vec{r} = (x, y)$. With the electric field having only one longitudinal component in the \hat{z} -direction, the magnetic field will have two transverse components in the $x - y$ plane to satisfy Maxwell's equation; thus the configuration is known as transverse magnetic (TM).

Applying the above assumptions and conditions along with using the simplified wave equation (2.17), the wave equations can be written as

$$\nabla^2 E_{t,z}^{\text{sct}}(\vec{r}) + k_b^2(\vec{r})(\chi(\vec{r}) + 1)E_{t,z}^{\text{sct}}(\vec{r}) = -k_b^2(\vec{r})\chi(\vec{r})E_{t,z}^{\text{inc}}(\vec{r})\tag{2.30}$$

and

$$\nabla^2 E_{t,z}^{\text{sct}}(\vec{r}) + k_b^2(\vec{r})E_{t,z}^{\text{sct}}(\vec{r}) = -k_b^2(\vec{r})w_{t,z}(\vec{r}).\tag{2.31}$$

These equations are known as the scalar Helmholtz equations.

For conductive enclosures, the homogeneous Dirichlet BC given in (2.27) are simplified to

$$E_{t,z}^{\text{inc}}(\vec{r} \in \Gamma) = 0 \quad \text{and} \quad E_{t,z}^{\text{sct}}(\vec{r} \in \Gamma) = 0.\tag{2.32}$$

Similarly, the 2D Sommerfeld boundary conditions are given as

$$\lim_{r \rightarrow \infty} \sqrt{r} \left(\frac{\partial}{\partial r} E_{t,z}^{\text{sct}}(\vec{r}) + jk_b E_{t,z}^{\text{sct}}(\vec{r}) \right) = 0.\tag{2.33}$$

2.3.2 Case 2: 2D Transverse Electric

The electric field is polarized in the $x - y$ plane for 2D transverse electric (TE) problems, with no longitudinal component in the z -direction; thus the incident field, scattered field and contrast source have two components each and are given as

$$\begin{aligned}\vec{E}_t^{\text{inc}}(\vec{r}) &= E_{t,x}^{\text{inc}}(\vec{r})\hat{x} + E_{t,y}^{\text{inc}}(\vec{r})\hat{y} \\ \vec{E}_t^{\text{sct}}(\vec{r}) &= E_{t,x}^{\text{sct}}(\vec{r})\hat{x} + E_{t,y}^{\text{sct}}(\vec{r})\hat{y} \\ \vec{w}_t(\vec{r}) &= w_{t,x}(\vec{r})\hat{x} + w_{t,y}(\vec{r})\hat{y}.\end{aligned}\tag{2.34}$$

Further, the fields and electric properties of the OI and the background medium do not vary along the z -direction in 2D TE problems similar to 2D TM configurations.

The scattered electric field is governed by the vector wave equations (2.23) and (2.24), with any required boundary conditions defined in (2.27) and (2.28).

2.3.3 Case 3: 3D Full-Vectorial

In 3D full-vectorial problems, the field and the electric properties vary with respect to all space coordinates. Therefore, each field vector has three components, thus

$$\begin{aligned}\vec{E}_t^{\text{inc}}(\vec{r}) &= E_{t,x}^{\text{inc}}(\vec{r})\hat{x} + E_{t,y}^{\text{inc}}(\vec{r})\hat{y} + E_{t,z}^{\text{inc}}(\vec{r})\hat{z} \\ \vec{E}_t^{\text{sct}}(\vec{r}) &= E_{t,x}^{\text{sct}}(\vec{r})\hat{x} + E_{t,y}^{\text{sct}}(\vec{r})\hat{y} + E_{t,z}^{\text{sct}}(\vec{r})\hat{z} \\ \vec{w}_t(\vec{r}) &= w_{t,x}(\vec{r})\hat{x} + w_{t,y}(\vec{r})\hat{y} + w_{t,z}(\vec{r})\hat{z}.\end{aligned}\tag{2.35}$$

Similar to 2D TE, the vector wave equations (2.23) and (2.24) and the boundary conditions (2.27) and (2.28) are utilized to solve for the scattered electric field in the problem domain for 3D full-vectorial problems.

2.4 Integral Equation Formulation

The Helmholtz wave equations introduced earlier can be solved by the direct discretization of the PDE using techniques like the finite-difference (FD) method or the finite-element method (FEM). The discretization produces matrices representing the Helmholtz operator $\vec{\mathcal{H}}_b$ and the transformation operators $\vec{\mathcal{M}}_{\mathcal{S}}$, $\vec{\mathcal{M}}_{\mathcal{D}}$. In this thesis, the wave equations are solved using FEM, which is explained in detail in Chapter 3.

The alternative approach to formulating the wave equations is to represent the solution in integral equation form (IE) using the appropriate Green's function. The IE form of the electromagnetic problem is outlined herein to conveniently present the inverse scattering problem as will be explained later.

The integral solution of the the vector wave equation (2.24) can be written as [19]

$$\vec{E}_t^{\text{sct}}(\vec{r}) = \int_{\mathcal{D}} \bar{\bar{G}}_b(\vec{r}, \vec{r}') \cdot (-k_b^2(\vec{r}') \vec{w}_t(\vec{r}')) dv' \quad \text{for } \vec{r} \in \Omega \quad (2.36)$$

where the integration is performed over the domain \mathcal{D} , the support of the contrast source $\vec{w}_t(\vec{r}')$ (for $\vec{r}' \notin \mathcal{D}$, $\vec{w}_t(\vec{r}') = 0$); and $\bar{\bar{G}}_b(\vec{r}, \vec{r}')$ is the dyadic Green's function of the electric type that relates the field \vec{E}_t^{sct} and the contrast source variable \vec{w}_t .

The dyadic Green's function $\bar{\bar{G}}_b(\vec{r}, \vec{r}')$ has to satisfy the following inhomogeneous PDE [44]:

$$\nabla \times \nabla \bar{\bar{G}}_b(\vec{r}, \vec{r}') - k_b^2(\vec{r}) \bar{\bar{G}}_b(\vec{r}, \vec{r}') = \bar{\bar{I}} \delta(\vec{r} - \vec{r}') \quad \text{for } \vec{r}' \in \mathcal{D} \quad (2.37)$$

where k_b is a background medium wavenumber that can be inhomogeneous, $\delta(\vec{r} - \vec{r}')$

denotes the Dirac delta function and $\bar{\bar{I}}$ is the identity dyad given as

$$\bar{\bar{I}} = \begin{cases} \hat{z}\hat{z} & \text{2D TM} \\ \hat{x}\hat{x} + \hat{y}\hat{y} & \text{2D TE} \\ \hat{x}\hat{x} + \hat{y}\hat{y} + \hat{z}\hat{z} & \text{3D Full-Vectorial.} \end{cases} \quad (2.38)$$

The inhomogeneous PDE satisfied by $\bar{\bar{G}}_b(\vec{r}, \vec{r}')$ is associated with the same boundary conditions defined for the vector wave equation (2.24). In the TM illumination the Green's function has one component $G_{b,zz}\hat{z}\hat{z}$, in the TE polarization it has four components

$$\bar{\bar{G}}_b = G_{b,xx}\hat{x}\hat{x} + G_{b,xy}\hat{x}\hat{y} + G_{b,yx}\hat{y}\hat{x} + G_{b,yy}\hat{y}\hat{y} \quad (2.39)$$

and for 3D full-vectorial problems it has nine components

$$\begin{aligned} \bar{\bar{G}}_b = & G_{b,xx}\hat{x}\hat{x} + G_{b,yx}\hat{y}\hat{x} + G_{b,zx}\hat{z}\hat{x} + \\ & G_{b,xy}\hat{x}\hat{y} + G_{b,yy}\hat{y}\hat{y} + G_{b,zy}\hat{z}\hat{y} + \\ & G_{b,xz}\hat{x}\hat{z} + G_{b,yz}\hat{y}\hat{z} + G_{b,zz}\hat{z}\hat{z}. \end{aligned} \quad (2.40)$$

The dyadic components are independent from each other.

It is straight-forward to derive the analytical Green's function, $\bar{\bar{G}}_b(\vec{r}, \vec{r}')$, corresponding to an unbounded problem with a homogeneous background medium. Whereas if the problem's boundary is complicated (*e.g.* arbitrary and/or conducting) or if the background medium is inhomogeneous (*e.g.* multi-layered media), the derivation and the calculation of the Green's function can be a complex, computationally expensive process .

With the knowledge of the Green's function, the integral equation (2.36) is typically solved using the method-of-moments (MoM), which produces a dense system

of equations that can be a computational burden. The complexity of utilizing MoM depends on different factors that include the Green's function expression, the contrast of the OI relative to the background medium and the geometrical complexity of both the OI and the imaging domain \mathcal{D} . The acceleration of the MoM can be achieved, under certain assumptions, using various techniques like the conjugate-gradient fast Fourier transform (CG-FFT) [45, 46] and the fast multipole method (FMM) [47–49]. However, such techniques are not generally available for inhomogeneous background or problems with complicated boundaries.

2.4.1 Data and Domain Operators

The inverse scattering problem requires the scattered field values to be calculated on a measurement surface \mathcal{S} and within an imaging domain \mathcal{D} . Therefore two linear operators are introduced: the data operator and the domain operator [19, 34, 50]. Assuming $\vec{v}(\vec{r})$ exists for $\vec{r} \in \mathcal{D}$, the data operator is defined as

$$\mathcal{G}_{\mathcal{S}}\{\vec{v}\} = \int_{\mathcal{D}} \bar{\bar{G}}_b(\vec{r}, \vec{r}') \cdot (-k_b^2(\vec{r}') \vec{v}(\vec{r}')) dv' \quad \text{for } \vec{r} \in \mathcal{S} \quad (2.41)$$

and the domain operator as

$$\mathcal{G}_{\mathcal{D}}\{\vec{v}\} = \int_{\mathcal{D}} \bar{\bar{G}}_b(\vec{r}, \vec{r}') \cdot (-k_b^2(\vec{r}') \vec{v}(\vec{r}')) dv' \quad \text{for } \vec{r} \in \mathcal{D}. \quad (2.42)$$

Both integrals, (2.41) and (2.42), are taken over \mathcal{D} . A third linear operator $\mathcal{G}_{\mathcal{D}}^{\varphi}\{\vec{v}\}$ is defined as

$$\mathcal{G}_{\mathcal{D}}^{\varphi}\{\vec{v}\} = \int_{\mathcal{D}} \bar{\bar{G}}_b(\vec{r}, \vec{r}') \cdot (-k_b^2(\vec{r}') \vec{v}(\vec{r}') \varphi(\vec{r}')) dv' \quad \text{for } \vec{r} \in \mathcal{D} \quad (2.43)$$

where $\varphi(\vec{r}')$ is a scalar function. Note that the data operator \mathcal{G}_S returns the field values on a measurement surface \mathcal{S} , whereas the domain operator \mathcal{G}_D as well as the operator \mathcal{G}_D^φ return the field values within the imaging domain \mathcal{D} .

The operators presented herein return the same results as multiplying the outcome of the inverse Helmholtz operator $\vec{\mathcal{H}}_b$ (2.26) by the transformation operators $\vec{\mathcal{M}}_S$ and $\vec{\mathcal{M}}_D$. That is

$$\begin{aligned}\mathcal{G}_S \{\vec{v}\} &\equiv \vec{\mathcal{M}}_S \vec{\mathcal{H}}_b^{-1} \{\vec{v}\} \\ \mathcal{G}_D \{\vec{v}\} &\equiv \vec{\mathcal{M}}_D \vec{\mathcal{H}}_b^{-1} \{\vec{v}\}.\end{aligned}\tag{2.44}$$

2.4.2 Data and Domain Equations

The scattered field on the measurement surface \mathcal{S} due to a contrast source function \vec{w}_t can be written as

$$\vec{E}_t^{\text{sct}}(\vec{r}) = \mathcal{G}_S \{\vec{w}_t\}.\tag{2.45}$$

This equation is usually referred as the data equation. The total electric field, \vec{E}_t , within the imaging domain \mathcal{D} , can be calculated via

$$\vec{E}_t(\vec{r}) = \vec{E}_t^{\text{inc}}(\vec{r}) + \mathcal{G}_D \{\vec{w}_t\}.\tag{2.46}$$

This equation is usually called the domain equation.

Using the contrast source definition (2.25) and the operator given in (2.43), the domain equation can be rewritten as

$$(I - \mathcal{G}_D^\chi) \vec{E}_t(\vec{r}) = \vec{E}_t^{\text{inc}}(\vec{r})\tag{2.47}$$

where I is an identity operator. Thus, the total field inside the imaging domain \mathcal{D}

can be expressed as

$$\vec{E}_t(\vec{r}) = (I - \mathcal{G}_D^\chi)^{-1} \vec{E}_t^{\text{inc}}(\vec{r}) \quad (2.48)$$

where the superscript -1 denotes the inverse operator. Using (2.48) and the contrast source definition (2.25), the data equation can be rewritten as

$$\vec{E}_t^{\text{sct}}(\vec{r}) = \mathcal{G}_S \left\{ \chi (I - \mathcal{G}_D^\chi)^{-1} \left(\vec{E}_t^{\text{inc}} \right) \right\}. \quad (2.49)$$

Although the data and domain operators themselves are linear, the inverse operation within (2.49) is non-linear.

The equations outlined in this section will be used next to briefly explain the inverse scattering problem and the techniques utilized to solve it.

2.5 Inverse Scattering Problem

The objective of the inverse scattering problem is to estimate the contrast $\chi(\vec{r})$ inside the imaging domain \mathcal{D} from the scattered field measurements on the measurement surface \mathcal{S} . Let $\vec{E}_{\text{meas}}^{\text{sct}}(\vec{r})$ denote the measured scattered field on \mathcal{S} , then using (2.49), the contrast $\chi(\vec{r})$ is to be found from

$$\vec{E}_{\text{meas}}^{\text{sct}}(\vec{r}) = \mathcal{G}_S \left\{ \chi (I - \mathcal{G}_D^\chi)^{-1} \left(\vec{E}^{\text{inc}} \right) \right\}. \quad (2.50)$$

Here the incident field \vec{E}^{inc} is assumed to be known, whereas the operator \mathcal{G}_D^χ is unknown as the contrast χ is unknown.

The inverse operator in (2.50) is a mathematical representation of the nonlinearity associated with the inverse scattering problem. This is handled by casting the inverse problem as an optimization algorithm over variables representing the unknown elec-

trical properties of the OI which are to be reconstructed. The inversion algorithm objective is to utilize $\vec{E}_{\text{meas}}^{\text{sct}}(\vec{r})$ at several locations surrounding the OI to update estimates of the unknown contrast such as to minimize a given functional. The functional relates the measured data and the unknown attributes of the OI.

Most inversion algorithms are iterative techniques where estimates of the OI's electrical properties are updated starting from some initial guess. Broadly speaking, inversion algorithms can be divided into two types: conventional and modified-gradient [27]. The two approaches are distinguished by their use (or lack of use) of a forward solver, and the selection of the objective function.

2.5.1 Conventional Type Algorithms

The conventional type algorithm attempts to minimize a cost functional solely in terms of the scattered field outside the OI by updating the electrical properties of the OI at every iteration. Such inversion algorithms require that a forward solver be called several times at each iteration to calculate the scattered fields associated with each source for the current estimate of the OI's electrical properties; this can be a computational burden because the system of equations used to compute these scattered fields must be assembled at each iteration. Examples of such algorithms are the distorted Born iteration method (DBIM) [30], the Gauss-Newton inversion (GNI) [28], conjugate gradient [31] and global optimization techniques [13, 51]. Using the data equation expression in (2.49), the general conventional type inversion algorithm can be written as

$$\mathcal{C}^{\text{conv}}(\chi) = \frac{\sum_t \left\| \vec{E}_{t,\text{meas}}^{\text{sct}} - \mathcal{G}_S \left\{ \chi (I - \mathcal{G}_D^\chi)^{-1} \left(\vec{E}_t^{\text{inc}} \right) \right\} \right\|_S^2}{\sum_t \left\| \vec{E}_{t,\text{meas}}^{\text{sct}} \right\|_S^2} \quad (2.51)$$

where $\|\cdot\|$ notation represents the L_2 -norm (or the Euclidean norm) of the argument. Since the contrast χ is updated at every iteration, the operator $\mathcal{G}_{\mathcal{D}}^{\chi}$ has to be recalculated. The computation of the operator $(I - \mathcal{G}_{\mathcal{D}}^{\chi})^{-1}$ is equivalent to a forward solver call.

2.5.2 Modified-Gradient Type Algorithms

The modified-gradient type algorithm minimizes a cost functional in terms of both the scattered field outside of the OI, which is compared to the measured values, and the total field inside the imaging domain, which is expected to be consistent with the physics of the problem. Noting that the total field inside the imaging domain changes with respect to each transmitter, the number of unknown quantities can become extremely large. However, using modified-gradient algorithms forward solver calls are avoided.

Two different updating schemes within this approach have been suggested. The first scheme updates the contrast and the total field values corresponding to each transmitter simultaneously [52]. On the other hand, the second scheme treats the contrast and the total field (or the contrast sources) separately; when optimizing over the contrast, the total field (or the contrast sources) is assumed constant, and when updating the total field (or the contrast sources), the contrast is assumed to be known. The modified-gradient method (MGM) [53, 54] and the contrast source inversion (CSI) [55, 56] are the two well-known methods within the second updating scheme. As the CSI method is the most-known modified-gradient type, it is briefly explained for this class of inversion algorithms.

The CSI method formulates the MWI problem in terms of the contrast χ and the contrast source \vec{w}_t variables. Multiplying both sides of the domain equation (2.46)

by χ , results in

$$\vec{w}_t(\vec{r}) = \chi(\vec{r})\vec{E}_t^{\text{inc}}(\vec{r}) + \chi(\vec{r})\mathcal{G}_{\mathcal{D}}\{\vec{w}_t\} \quad (2.52)$$

which along with the data equation (2.45) is used to express the CSI functional as

$$\mathcal{C}^{\text{CSI}}(\chi, \vec{w}_t) = \frac{\sum_t \left\| \vec{E}_{t,\text{meas}}^{\text{sct}}(\vec{r}) - \mathcal{G}_{\mathcal{S}}\{\vec{w}_t\} \right\|_{\mathcal{S}}^2}{\sum_t \left\| \vec{E}_{t,\text{meas}}^{\text{sct}}(\vec{r}) \right\|_{\mathcal{S}}^2} + \frac{\sum_t \left\| \chi(\vec{r})\vec{E}_t^{\text{inc}}(\vec{r}) - \vec{w}_t(\vec{r}) + \chi(\vec{r})\mathcal{G}_{\mathcal{D}}\{\vec{w}_t\} \right\|_{\mathcal{D}}^2}{\sum_t \left\| \chi(\vec{r})\vec{E}_t^{\text{inc}}(\vec{r}) \right\|_{\mathcal{D}}^2}. \quad (2.53)$$

The contrast and the contrast source variables are updated successively by a conjugate gradient method.

In this thesis, the CSI method is selected as the algorithm to solve the MWI inverse problem and it is formulated using the finite-element method.

3

Solving the Forward Problem

The limitations of the human mind are such that it cannot grasp the behavior of its complex surroundings and creations in one operation. Thus the process of subdividing all systems into their individual components or ‘elements’, whose behavior is readily understood, and then rebuilding the original system for such components to study its behavior is a natural way in which the engineer, the scientist, or even the economist proceeds.

–Olgierd C. Zienkiewicz and Robert L. Taylor [57]

The microwave imaging problem can be divided into two parts: the forward problem and the inverse problem. The objective of the the forward problem, sometimes referred to as *the direct poblem*, is to predict the behavior of the field in the problem domain (Ω) for a given OI immersed in a known background medium. Historically, several numerical techniques have been developed to solve the forward problem associated with electromagnetics. These techniques generally fall under the title *computational electromagnetics*.

Practically speaking, computational electromagnetics can be categorized into either time-domain or frequency-domain techniques. Examples of time domain methods are the finite-difference time-domain (FDTD) [58], the finite-volume time-domain (FVTD) [59, 60] and the transmission-line matrix (TLM) [61] techniques. As time-domain methods are beyond the scope of the thesis they will not be discussed further.

Frequency-domain methods generally involve either the direct discretization of the PDEs associated with the electromagnetic problem or the discretization of some integral-form. As detailed in Section (2.4), the later technique will require either deriving or computing a Green's function that may be a complex and a computationally expensive process. The alternative is the direct discretization of the PDE and this can be easily performed using a finite-difference or a finite-element method.

In this chapter, the finite-element method (FEM) is reviewed and used to solve the forward problem for microwave imaging. The details of using FEM are outlined along with any necessary operators required for extracting information from the solution. The finite-element method is formulated for scalar two-dimensional problems, as well as for 2D and 3D vector problems.

3.1 The Finite Element Method

The finite-element method (FEM) is a numerical technique that was first proposed in the 1940s for solving boundary-value problems (BVPs) of mathematical physics. In this technique, the continuous space of the BVP is divided into a 'finite' number of parts ('elements') and solved; this is how the name of the technique originated, and the term was coined by Clough in 1960 [62]. The first practical use for FEM began in the 1950s for aircraft design; however it's first use in electrical engineering was not until 1965 when Winslow used it to solve for the magnetic field on an irregular mesh [63]. Currently, the applications of the finite element method extend to various engineering areas such as structural analysis, heat transfer, fluid mechanics, acoustics and electromagnetics.

The finite element method offers several advantages in comparison to other numerical techniques:

- Complex geometries with curvatures are easily modeled using triangular elements in 2D or tetrahedra in 3D.
- Material inhomogeneities are dealt with efficiently.
- Boundaries of different types, shapes and sizes are easily integrated within the FEM formulation.
- The discretization using FEM yields matrix equations that can be solved efficiently as the resultant matrices are sparse.

There are two approaches for formulating a problem using FEM: the Rayleigh-Ritz variational method and the method of weighted residuals (MoWR); herein the former one is used. The basic steps in solving a problem using FEM can be described as [44, 64]:

1. A boundary-value problem (BVP) is defined.
2. A variational expression (in the form of a functional) for solving the BVP is formulated. The variational expression is a function of the unknown variable being solved for in the BVP.
3. The first variation of the functional with respect to the unknown variable is set to zero. The stationary point of the functional is the solution of the BVP.
4. The problem domain is discretized into a finite number of elements and the elemental basis functions are selected.
5. The system of equations is built and solved.

3.2 Scalar Problems

3.2.1 The Boundary-Value Problem

For scalar wave problems, the goal is to calculate the scattered field ($E_{t,z}^{\text{sct}}$) by either solving (2.30) or (2.31) given the appropriate boundary conditions. Solving these scalar Helmholtz equations can be generalized to solving a BVP defined by the second-order partial differential equation (PDE)

$$\nabla^2 u(\vec{r}) + \alpha(\vec{r})u(\vec{r}) = \beta(\vec{r})f(\vec{r}) \quad (3.1)$$

where u is the unknown variable, α and β are known parameters associated with the physical properties of the problem domain (Ω), and f is the excitation function. Comparing to (2.30) and (2.31), $u = E_{t,z}^{\text{sct}}$ while the other parameters α , β and f vary depending on which Helmholtz equation is solved. The boundary conditions associated with the PDE are the Dirichlet BC

$$u(\vec{r}) = p(\vec{r}) \quad \text{on} \quad \Gamma_1 \quad (3.2)$$

and the Robin BC [65]

$$(\nabla u(\vec{r})) \cdot \hat{n} - \gamma(\vec{r})u(\vec{r}) = -q(\vec{r}) \quad \text{on} \quad \Gamma_2 \quad (3.3)$$

where $\Gamma_1 + \Gamma_2 = \Gamma$ is the boundary enclosing Ω , \hat{n} is an outward normal unit vector to Γ , and p , γ and q are parameters associated with the physical properties of the boundaries. When $\gamma = 0$, the Robin BC becomes the Neumann BC [44].

For calculating the scattered field ($E_{t,z}^{\text{sct}}$) inside a conductive enclosure, the ho-

homogeneous Dirichlet BC, 2.32, is applied on $\Gamma = \Gamma_1$, therefore we set $p = 0$. For unbounded MWI systems, the Robin BC can be used to approximate the Sommerfeld radiation condition on $\Gamma = \Gamma_2$.

3.2.2 The Variational Problem

In the Rayleigh-Ritz variational method, the BVP is replaced by a variational expression called the functional. The functional corresponds to a weak-form of the governing PDE under the given boundary conditions [64]. The approximate solution for the PDE is then obtained by finding the stationary point of the functional with respect to the unknown variables used to represent the solution.

Specifically, the BVP, (3.1)-(3.3), is converted to the variational problem [44]

$$\delta F(u) = 0 \quad \text{with} \quad u = p \quad \text{on} \quad \Gamma_1 \quad (3.4)$$

where the functional $F(u)$ is given by

$$F(u) = -\frac{1}{2} \int_{\Omega} (\nabla u \cdot \nabla u - \alpha u^2) \, dv + \int_{\Gamma_2} \left(\frac{\gamma}{2} u^2 - qu \right) \, ds - \int_{\Omega} \beta f u \, dv. \quad (3.5)$$

Here the Robin boundary condition (3.3) is incorporated in the second term of the functional $F(u)$, while the Dirichlet boundary condition (3.2) must be enforced explicitly [44]. The functional represents the core of the finite-element method; the next step is to discretize it.

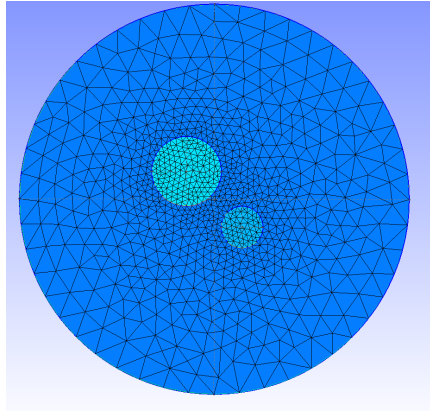


Figure 3.1: Example mesh created using GMSH [66]

3.2.3 Domain Discretization

The third step in solving a problem using FEM is to divide the problem domain (Ω) into a mesh of triangular elements defined by N nodes. Although other element shapes can be selected (*e.g.* rectangular), triangular elements have an advantage as they can model curved boundaries easily. Within the domain, the elements must not overlap and must have no gaps between them. The triangles are interconnected, and sharing nodes and edges.

For the final solution to be as accurate as possible, the triangles in the mesh should satisfy two conditions: (*i*) they should be as close to equilateral triangles as possible, (*ii*) they should be small in size with respect to the local wavelength and the gradient of the solution. While the former condition is easily realizable with most available mesh generators, the later condition will increase the computational complexity of the problem. A solution here is to create an adapted mesh, where the density of the elements is increased in regions where the solution gradient is expected to be high, for example where the material variation is anticipated to be high. An example mesh is shown in Figure 3.1.

3.2.4 Elemental Basis Functions

After the mesh is created, the unknown variable u is approximated within each triangular element. Here first-order linear basis functions are selected. Each triangle is defined by three nodes as depicted Figure 3.2 (a). Each node in the mesh is associated with two labels: a local number to indicate its location in a given triangle (as shown in Figure 3.2 (a)) and a global number to indicate its location relative to the entire mesh. Within a triangular element e , the unknown variable is given by

$$u^e(\vec{r}) = \sum_{l=1}^3 u_l^e \lambda_l^e(\vec{r}) \quad (3.6)$$

where l is a local index for each node on triangle e , u_l^e is the unknown function value at node l of triangle e , and the first-order linear basis function for node l is

$$\lambda_l^e(\vec{r}) = \frac{1}{2A^e}(a_l^e + b_l^e x + c_l^e y). \quad (3.7)$$

Here A^e is the area of triangle, a_l^e , b_l^e and c_l^e are coefficients dependent on the triangle geometry [44]. The area of a triangle e is calculated as

$$A^e = \frac{1}{2} \begin{vmatrix} 1 & x_1 & y_1 \\ 1 & x_2 & y_2 \\ 1 & x_3 & y_3 \end{vmatrix} \quad (3.8)$$

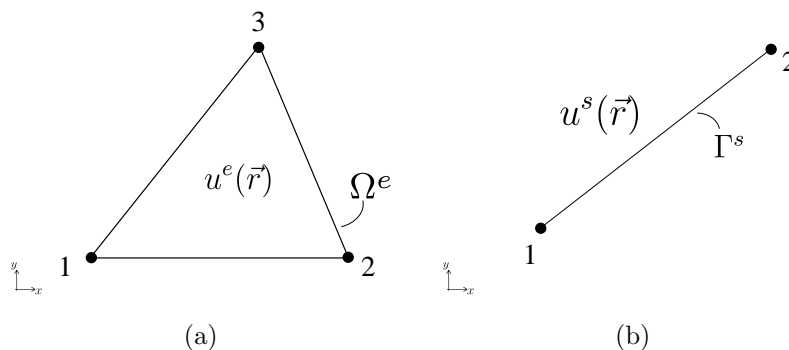


Figure 3.2: (a) First-order triangular element and (b) first-order line element

where $x_{1,2,3}^e$ and $y_{1,2,3}^e$ are the x - and y - coordinates of nodes $\{1, 2, 3\}$. For $l = 1$, the basis function coefficients are calculated as follows:

$$a_1^e = x_2^e y_3^e - y_2^e x_3^e, \quad (3.9)$$

$$b_1^e = y_2^e - y_3^e, \quad (3.10)$$

$$c_1^e = x_3^e - x_2^e. \quad (3.11)$$

The coefficients for $l = 2, 3$ are calculated by cyclic interchange of the subscripts in (3.9)-(3.11).

If variables α , β and f in (3.5) are defined on nodes, they can be approximated within a triangular element using the same basis function as u :

$$\alpha^e(\vec{r}) = \sum_{l=1}^3 \alpha_l^e \lambda_l^e(\vec{r}), \quad (3.12)$$

$$\beta^e(\vec{r}) = \sum_{l=1}^3 \beta_l^e \lambda_l^e(\vec{r}), \quad (3.13)$$

$$f^e(\vec{r}) = \sum_{l=1}^3 f_l^e \lambda_l^e(\vec{r}). \quad (3.14)$$

3.2.5 Boundary Basis Functions

The line integration in the second term of the functional $F(u)$ is performed along boundary Γ_2 ; thus, this boundary is discretized into 1D line elements. Each line element is defined by two nodes as shown in Figure 3.2 (b). Within a line segment s , the unknown variable is approximated by

$$u^s(\vec{r}) = \sum_{l=1}^2 u_l^s \lambda_l^s(\vec{r}) \quad (3.15)$$

where l is the local index for each node on the line segment, u_l^s is the unknown function value at node l of s and $\lambda_l^s(\vec{r})$ is the first-order linear boundary basis function. To ease the integration over the boundary, the line segment s is mapped to an isoparametric element that extends from zero to one, as depicted in Figure 3.3. Within the isoparametric element ζ^s , the unknown function is approximated by

$$u^s(\zeta) = \sum_{l=1}^2 u_l^s \lambda_l^{\zeta^s}(\zeta) \quad (3.16)$$

where ζ is the normalized distance from node 1 to node 2 on the line segment,

$$\lambda_1^{\zeta^s}(\zeta) = 1 - \zeta \quad \text{and} \quad \lambda_2^{\zeta^s}(\zeta) = \zeta. \quad (3.17)$$

The transformation to an isoparametric element ζ^s results in multiplying the integration performed over the element by l^s , the length of the line segment s

$$l^s = \sqrt{(x_2 - x_1)^2 + (y_2 - y_1)^2}. \quad (3.18)$$

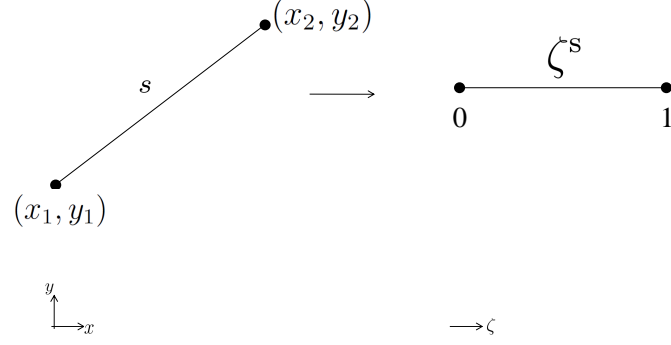


Figure 3.3: Transformation of line segment to an isoparametric element.

3.2.6 Functional Discretization

With the domain divided into N_e triangular elements and N_s line segments, the functional $F(u)$ can be written as

$$F(u) = \sum_{e=1}^{N_e} F^e(u^e) + \sum_{s=1}^{N_s} F^s(u^s) \quad (3.19)$$

where

$$F^e(u^e) = -\frac{1}{2} \int_{\Omega^e} (\nabla u^e \cdot \nabla u^e - \alpha^e (u^e)^2) dv - \int_{\Omega^e} \beta^e f^e u^e dv \quad (3.20)$$

$$F^s(u^s) = \int_{\Gamma_2^s} \left(\frac{\gamma^s}{2} (u^s)^2 - q^s u^s \right) ds. \quad (3.21)$$

As outlined in Appendix A, the approximations in (3.6), (3.12)-(3.14) and (3.16) are used in the above equations to evaluate the local matrices associated with each element in the mesh. Next, as described in Appendix B, the transformation from the local node indices to global indices is used to assemble the global FEM matrices.

This results in the formation of the following matrix equation

$$F(\underline{u}) = -\frac{1}{2}\underline{u}^T[\mathcal{S} - \mathcal{T}_\alpha]\underline{u} - \underline{u}^T\mathcal{T}_\beta\underline{f} - \underline{u}^T\underline{g} \quad (3.22)$$

where superscript T denotes the transpose; $\underline{u} \in \mathbb{C}^N$ is a vector of the values of the unknown function at the nodes; $\underline{f} \in \mathbb{C}^N$ is a vector of the excitation function f nodal values; $\underline{g} \in \mathbb{C}^N$ is a vector, which depends on the value of q ; $\mathcal{S} \in \mathbb{R}^{N \times N}$ is the stiffness matrix, which depends on the BCs; $\mathcal{T}_\alpha \in \mathbb{C}^{N \times N}$ is a mass matrix, which depends on the nodal values of α ; and $\mathcal{T}_\beta \in \mathbb{C}^{N \times N}$ is a mass matrix, which depends on the nodal values of β on the nodes.

Entries for the i^{th} row and j^{th} column of the stiffness matrix (not arising from the boundary-integral term) and the mass matrices are given by

$$\mathcal{S}_{i,j} = \int_{\Omega} \nabla \lambda_i \cdot \nabla \lambda_j \, dv \quad (3.23)$$

$$\mathcal{T}_{\alpha i,j} = \sum_{p=1}^{N_e} \int_{\Omega} \alpha_p \lambda_i \lambda_j \lambda_p \, dv \quad (3.24)$$

$$\mathcal{T}_{\beta i,j} = \sum_{p=1}^{N_e} \int_{\Omega} \beta_p \lambda_i \lambda_j \lambda_p \, dv \quad (3.25)$$

where λ_i , λ_j and λ_p are the linear basis functions defined at the i^{th} , j^{th} and p^{th} node respectively, ∇ is the spatial gradient operator, and α_p and β_b are the physical parameters at node p .

The stationary point of the discretized functional is found by setting the derivative of (3.22) with respect to \underline{u} to zero, yielding the matrix equation

$$[\mathcal{S} - \mathcal{T}_\alpha]\underline{u} = -\mathcal{T}_\beta\underline{f} - \underline{g}. \quad (3.26)$$

The matrices in (3.26) are sparse and symmetric, therefore the solution vector \underline{u} can be found efficiently using decomposition methods or iterative solvers designed for sparse matrices.

For BVPs with Dirichlet BCs, the values of u on the boundary are known; this results in changes to the structure of the matrix equation (3.26). However, this is not the case for BVPs with Robin BCs. With Robin BCs, changes occur only to the stiffness matrix \mathcal{S} . The effect of applying BCs to the FEM matrix equation are discussed in the next section.

3.2.7 Dirichlet Boundary Condition

For BVPs with inhomogeneous Dirichlet boundary conditions, the boundary $\Gamma = \Gamma_1$, and the boundary-integral term in (3.5) disappears. As shown in Appendix B, the matrix equation (3.26) can be written as

$$\begin{bmatrix} \mathcal{I}_{\text{BB}} & \mathbf{0}_{\text{BF}} \\ \mathcal{S}_{\text{FB}} - \mathcal{T}_{\alpha\text{FB}} & \mathcal{S}_{\text{FF}} - \mathcal{T}_{\alpha\text{FF}} \end{bmatrix} \begin{bmatrix} \underline{u}_{\text{B}} \\ \underline{u}_{\text{F}} \end{bmatrix} = - \begin{bmatrix} \mathcal{I}_{\text{BB}} & \mathbf{0}_{\text{BF}} \\ \mathcal{T}_{\beta\text{FB}} & \mathcal{T}_{\beta\text{FF}} \end{bmatrix} \begin{bmatrix} \underline{f}_{\text{B}} \\ \underline{f}_{\text{F}} \end{bmatrix}. \quad (3.27)$$

Here subscripts B and F refer to the B boundary nodes and the F free (interior) nodes in the mesh, thus $N = B + F$. The dimensions of the sub-matrices and vectors in (3.27) are indicated by their subscripts; for example sub-matrix $\mathcal{S}_{\text{FB}} \in \mathbb{C}^{\text{F} \times \text{B}}$ and $\underline{u}_{\text{B}} \in \mathbb{C}^{\text{B}}$. Further, sub-matrix $\mathcal{I}_{\text{BB}} \in \mathbb{R}^{\text{B} \times \text{B}}$ is an identity matrix, and sub-matrix $\mathbf{0}_{\text{BF}} \in \mathbb{R}^{\text{B} \times \text{F}}$ is a zero matrix. The sub-matrices \mathcal{S}_{FB} , $\mathcal{T}_{\alpha\text{FB}}$ and $\mathcal{T}_{\beta\text{FB}}$ describe the interaction between boundary nodes and free nodes.

The Dirichlet BC (3.2) sets $\underline{u}_{\text{B}} = \underline{p}$; therefore it can be seen from (3.27) that

$\underline{f}_B = -\underline{p}$. This simplifies the matrix equation (3.27) to

$$[\mathcal{S}_{\text{FF}} - \mathcal{T}_{\alpha\text{FF}}]\underline{u}_F = -\mathcal{T}_{\beta\text{FF}}\underline{f}_{\text{FF}} - [\mathcal{S}_{\text{FB}} - \mathcal{T}_{\alpha\text{FB}} - \mathcal{T}_{\beta\text{FB}}]\underline{p}. \quad (3.28)$$

In conductive enclosures, we apply homogeneous Dirichlet boundary conditions applies, *i.e.*

$$\underline{p} = 0, \quad (3.29)$$

therefore (3.28) becomes

$$[\mathcal{S}_{\text{FF}} - \mathcal{T}_{\alpha\text{FF}}]\underline{u}_F = -\mathcal{T}_{\beta\text{FF}}\underline{f}_{\text{FF}}. \quad (3.30)$$

Since the above matrix equation has only free (interior) nodes as unknowns, the subscript F can be dropped. Thus, the matrix equation to be solved becomes

$$[\mathcal{S} - \mathcal{T}_\alpha]\underline{u} = -\mathcal{T}_\beta\underline{f}. \quad (3.31)$$

3.2.8 Absorbing Boundary Condition

For unbounded problems, the domain (Ω) should be truncated by an artificial boundary to limit the size of the computational space. This numerical boundary should approximate the Sommerfeld radiation condition (2.33); in other words the boundary condition should make the boundary transparent to the impinging field, reducing nonphysical reflections to zero, if possible. Herein, the Robin BC is used to model the boundary with the coefficients selected so as to model the second-order absorbing boundary conditions (ABC) introduced by Bayliss-Gunzburger-Turkel [67].

This second-order ABC sets the coefficient $q = 0$ in (3.3) and the coefficient

$$\gamma = \gamma_1 + \gamma_2 \frac{\partial^2}{\partial \xi^2} \quad (3.32)$$

where [44, 64, 67]

$$\gamma_1 = -jk_b - \frac{\kappa}{2} + \frac{\kappa^2}{8(j\kappa - k_b)} \quad (3.33)$$

$$\gamma_2 = \frac{j}{2(j\kappa - k_b)}. \quad (3.34)$$

Here ξ is the arc length measured along the boundary and $\kappa(\xi)$ is the curvature of the boundary at ξ [44, p. 128]. The curvature of ξ is measured from the center of the problem domain Ω ; for circular boundaries the curvature is the reciprocal of the boundary radius, whereas for rectangular boundaries the curvature is zero. This Robin BC can be written as

$$\nabla u(\vec{r}) \cdot \hat{n} = \gamma_1 u(\vec{r}) + \gamma_2 \frac{\partial^2 u(\vec{r})}{\partial \xi^2} \quad \text{for } \vec{r} \in \Gamma \quad (3.35)$$

where \hat{n} denotes the outward-normal unit vector. The FEM formulation of the BCs leads to the boundary-integral term in (3.5) that contributes to the $(i,j)^{\text{th}}$ element of \mathcal{S} as [44]

$$\mathcal{S}_{i,j}^\Gamma = \int_\Gamma \left(\gamma_1 \lambda_i^\Gamma \lambda_j^\Gamma - \gamma_2 \frac{\partial \lambda_i^\Gamma}{\partial \xi} \frac{\partial \lambda_j^\Gamma}{\partial \xi} \right) ds. \quad (3.36)$$

Here $\lambda_i^\Gamma, \lambda_j^\Gamma$ are linear boundary basis functions defined for nodes i and j on Γ . For a boundary segment s the previous integral in terms of isoparametric coordinate ζ is given as

$$\mathcal{S}_{i,j}^s = \int_0^1 \left(\gamma_1 l^s \lambda_i^{\zeta^s} \lambda_j^{\zeta^s} - \frac{\gamma_2}{l^s} \frac{\partial \lambda_i^{\zeta^s}}{\partial \zeta} \frac{\partial \lambda_j^{\zeta^s}}{\partial \zeta} \right) d\zeta. \quad (3.37)$$

Finally, the FEM matrix equation in (3.26) simplifies to

$$[\mathcal{S} - \mathcal{T}_\alpha] \underline{u} = -\mathcal{T}_\beta \underline{f} \quad (3.38)$$

where \underline{g} in (3.26) is zero because $q = 0$, and the stiffness matrix is

$$\mathcal{S} = \mathcal{S}^\Omega - \mathcal{S}^\Gamma \quad (3.39)$$

where \mathcal{S}^Ω and \mathcal{S}^Γ are, respectively, the global matrices holding contributions from the domain nodes and the boundary nodes.

3.3 Vector Problems

3.3.1 The Boundary-Value Problem

Two-dimensional and three-dimensional EM vectorial problems can be formulated as a vector BVP defined by the second-order PDE

$$\nabla \times \nabla \times \vec{u}(\vec{r}) - \alpha(\vec{r})\vec{u}(\vec{r}) = \beta(\vec{r})\vec{f}(\vec{r}) \quad (3.40)$$

and the boundary conditions

$$\hat{n} \times \vec{u}(\vec{r}) = \vec{p}(\vec{r}) \quad \text{on} \quad \Gamma_1 \quad (3.41)$$

$$\hat{n} \times (\nabla \times \vec{u}(\vec{r})) + \gamma(\vec{r}) \hat{n} \times (\hat{n} \times \vec{u}(\vec{r})) = \vec{q}(\vec{r}) \quad \text{on} \quad \Gamma_2. \quad (3.42)$$

Here \vec{u} is the unknown spatial vector variable, α and β are known scalar parameters associated with the physical properties of the problem domain (Ω), and \vec{f} is the

excitation vector function. For the EM problem, comparing to (2.23) and (2.24), $\vec{u} = \vec{E}_t^{\text{sct}}$ while the other parameters α , β and \vec{f} vary depending on which vector Helmholtz equation is solved.

Considering the boundary conditions, Γ_1 defines the Dirichlet boundary whereas Γ_2 is a Robin boundary; with $\Gamma_1 + \Gamma_2 = \Gamma$, the boundary enclosing the problem domain Ω . The vector functions \vec{p} and \vec{q} along with the scalar function γ are parameters associated with the physical properties of the boundaries. When $\gamma = 0$, the Robin BC becomes the Neumann BC.

For calculating the scattered field (\vec{E}_t^{sct}) inside a conductive enclosure, the homogeneous Dirichlet BC, 2.27, is applied on $\Gamma = \Gamma_1$, therefore we set $\vec{p} = 0$. For unbounded MWI systems, the Robin BC is used to approximate the Sommerfeld radiation condition on $\Gamma = \Gamma_2$ [44].

3.3.2 Variational Problem

In accordance to the variational principle discussed in Section 3.2.2, the vector BVP herein can be formulated as the following variational problem

$$\delta F(\vec{u}) = 0 \quad \text{with} \quad \vec{u} = \vec{p} \quad \text{on} \quad \Gamma_1 \quad (3.43)$$

with the functional $F(\vec{u})$ given by

$$F(\vec{u}) = \frac{1}{2} \int_{\Omega} [(\nabla \times \vec{u}) \cdot (\nabla \times \vec{u}) - \alpha \vec{u} \cdot \vec{u}] dv + \int_{\Gamma_2} \left[\frac{\gamma}{2} (\hat{n} \times \vec{u}) \cdot (\hat{n} \times \vec{u}) + \vec{u} \cdot \vec{q} \right] ds - \int_{\Omega} \beta \vec{u} \cdot \vec{f} dv. \quad (3.44)$$

The Robin boundary condition (3.42) is included in the second term of the functional $F(\vec{u})$, while the Dirichlet boundary condition (3.41) must be enforced explicitly.

3.3.3 Domain Discretization

In the work presented herein, the vectorial problem is solved for both 2D and 3D configurations. For the 2D case, the problem domain (Ω) is divided into a mesh of triangular elements characterized by N nodes that are interconnected by a total number of E edges. The domain discretization scheme is similar to the one used in scalar 2D problems. An example mesh is shown in Figure 3.1.

In 3D problems, the domain Ω is divided into tetrahedral elements defined by N nodes that are interconnected by a total number of E edges. Although other element types can be selected (*e.g.* hexahedral or triangular prism), tetrahedra have an advantage as they can easily model curved boundaries. The tetrahedral elements within the volumetric domain must not overlap, must have no gaps between them, are interconnected and can share nodes and edges. With respect to the domain discretization, the solution accuracy in 3D FEM is improved when: (i) the tetrahedra are regular (*i.e.* the tetrahedra facets are equilateral triangles) and (ii) the tetrahedra have small volumes. The latter condition can cause the required computational sources of the problem to increase dramatically. A cross-section of an example three-dimensional mesh is shown in Figure 3.4 (a).

3.3.4 Elemental Basis Functions

For solving vectorial problems using FEM, the use of nodal-based elements exhibits shortcomings that can be overcome with the use of edge-based elements [64, 68, 69].

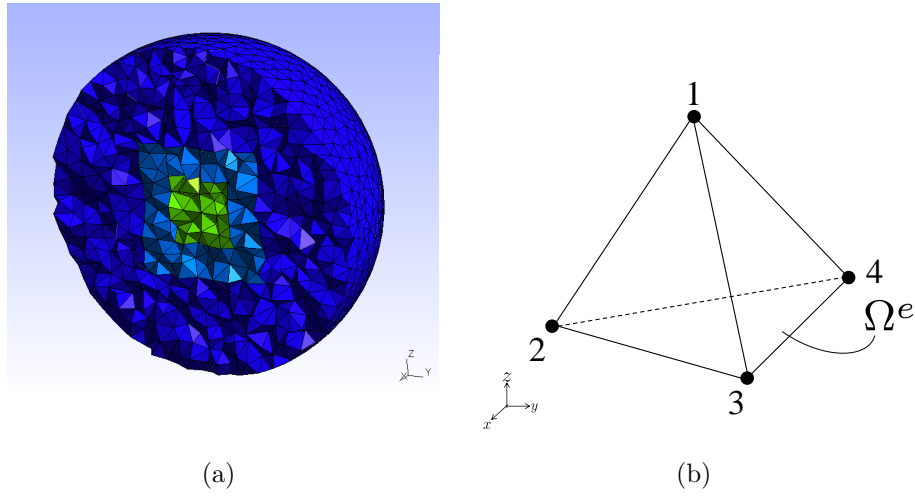


Figure 3.4: (a) A cross-section of a 3D mesh created using GMSH [66] (b) First-order tetrahedral element.

Using this approach, the FEM problem's degrees of freedom are assigned to the edges rather than to the nodes of the elements. Edge-based elements were first introduced by Whitney [70] and later discussed by Nédélec for their use in applications that solve Maxwell's equations [71]. Edge-based elements (associated with vector basis functions) eliminate spurious modes that can introduce errors in field calculations for near-field problems; these erroneous modes were observed by Csendes and Silvester when a vectorial problem was solved using nodal-basis functions [72]. In addition, with edge-based elements the tangential field continuity along the element boundaries is guaranteed which is important at the interface between dielectric discontinuities. Edge-based elements are thus standardly used for 2D, as well as for 3D, vectorial electromagnetic problems [73–75].

The vector basis functions for 2D triangular elements as well as for 3D tetrahedra are outlined in the next sections.

Table 3.1: Edge Numbering for a Triangular Element

Edge No. i	Node i_1	Node i_2
1	1	2
2	2	3
3	3	1

3.3.4.1 Triangular Edge-based Elements

We consider a triangular element e as depicted in Figure 3.2 (a). The nodes of the triangular element are joined together by three edges. Each edge in the mesh is paired with two labels: a local number to indicate its location in a given triangle and a global number to indicate its location with respect to the entire mesh.

Within a triangle e , each edge is associated with a vector-basis function (also known as a Whitney element [64]). The vector basis function for an edge i is given as

$$\vec{N}_i^e(\vec{r}) = l_i^e (\lambda_{i_1}^e(\vec{r}) \nabla \lambda_{i_2}^e(\vec{r}) - \lambda_{i_2}^e(\vec{r}) \nabla \lambda_{i_1}^e(\vec{r})) \quad (3.45)$$

where the edge number i is defined as lying between nodes i_1 and i_2 as specified in Table 3.1, l_i^e is the length of edge i , $\lambda_{i_1}^e$, $\lambda_{i_2}^e$ are the first-order nodal basis functions given in (3.7) and ∇ is the 2D spatial gradient operator.

Moreover, the vector field inside a triangular element e can be expanded as

$$\vec{u}^e(\vec{r}) = \sum_{i=1}^3 u_i^e \vec{N}_i^e(\vec{r}) \quad (3.46)$$

where u_i^e denotes the tangential field along the i^{th} edge.

Table 3.2: Edge Numbering for a Tetrahedral Element

Edge No. i	Node i_1	Node i_2
1	1	2
2	1	3
3	1	4
4	2	3
5	4	2
6	3	4

3.3.4.2 Tetrahedral Edge-based Elements

As previously stated, the problem domain, Ω , in 3D problems is divided into tetrahedral elements. Each element is defined by four nodes that are interconnected by six edges, as depicted in Figure 3.4 (b). As for 2D edge-elements, each edge is tagged with two numbers: a local number to denote its index in a given tetrahedron and a global number to indicate its index with respect to the entire mesh. The local edge numbering, as well as the associated nodes with each edge are defined in Table 3.2.

Similar to the two-dimensional case, the vector field inside a tetrahedron can be written as

$$\vec{u}^e(\vec{r}) = \sum_{i=1}^6 u_i^e \vec{N}_i^e(\vec{r}) \quad (3.47)$$

where u_i^e is the tangential field along edge i and $\vec{N}_i^e(\vec{r})$ is the vector basis function given again as in (3.46). Now $\lambda_{i_1}^e, \lambda_{i_2}^e$ are the three-dimensional linear nodal basis functions and ∇ is the 3D spatial gradient operator.

For a local node l belonging to tetrahedron e the nodal linear basis function is

$$\lambda_l^e(\vec{r}) = \frac{1}{6V_e} (a_l^e + b_l^e x + c_l^e y + d_l^e z) \quad (3.48)$$

Table 3.3: Local Indices to calculate Nodal Basis Functions

Node No. l	Node i	Node j	Node k
1	2	3	4
2	3	4	1
3	4	1	2
4	1	2	4

where V^e the volume of tetrahedron, and a_l^e , b_l^e , c_l^e and d_l^e are coefficients dependent on the tetrahedron geometry [44]. The volume of a tetrahedron e is calculated as

$$V^e = \frac{1}{6} \begin{vmatrix} 1 & x_1 & y_1 & z_1 \\ 1 & x_2 & y_2 & z_2 \\ 1 & x_3 & y_3 & z_3 \\ 1 & x_4 & y_4 & z_4 \end{vmatrix} \quad (3.49)$$

where $x_{1,2,3,4}^e$, $y_{1,2,3,4}^e$ and $z_{1,2,3,4}^e$ are the x -, y - and z - coordinates of nodes $\{1, 2, 3, 4\}$.

For a node l , the basis function coefficients are calculated as follows:

$$\begin{aligned} a_l^e &= (-1)^{l-1} (x_i y_j z_k - x_i y_k z_j - x_j y_i z_k + x_j y_k z_i + x_k y_i z_j - x_k y_j z_i) \\ b_l^e &= (-1)^l (y_i z_j - y_j z_i - y_i z_k + y_k z_i + y_j z_k - y_k z_j) \\ c_l^e &= (-1)^{l-1} (x_i z_j - x_j z_i - x_i z_k + x_k z_i + x_j z_k - x_k z_j) \\ d_l^e &= (-1)^l (x_i y_j - x_j y_i - x_i y_k + x_k y_i + x_j y_k - x_k y_j) \end{aligned} \quad (3.50)$$

where the nodal local indices $\{i, j, k\}$ associated with a node l are defined in a cyclic manner as shown in Table 3.3. This cyclic scheme assumes specific ordering of the local nodes around the tetrahedron, which is shown in Figure 3.4 (b).

3.3.4.3 Vector-basis functions Properties

It can be easily shown that the vector basis function, (3.45), exhibits the following two properties:

$$\begin{aligned}\nabla \cdot \vec{N}_i^e &= 0 \\ \nabla \times \vec{N}_i^e &= 2l_i^e \nabla \lambda_{i_1}^e \times \nabla \lambda_{i_2}^e.\end{aligned}$$

The first property shows that this basis function is ideal for representing vector fields in charge-free regions*. The second property indicates that the curl of any vector basis function evaluated at any given domain element is constant.

The third feature of the vector basis function is that its tangential component is constant along the edge it is associated with, whereas its normal component changes linearly along that edge. The tangential component is also continuous between elements. This property is important as it permits enforcing tangential continuity across elements without affecting the normal components. This mimics the behavior of field components along discontinuous material boundaries [44, 64, 76].

3.3.5 Boundary Basis Functions

3.3.5.1 1D Line Elements

The second term of the functional $F(\vec{u})$ (3.44) involves an integration performed along boundary Γ_2 ; thus this boundary is discretized into 1D line elements. Each line element, s , is a triangle's edge. If segment s is an edge i for triangle e , the vector

*For the work presented herein, the assumption (see Section 2.2) is that the problem domain is free of charge, hence $\nabla \cdot \vec{D} = 0$

field at the segment can be approximated by

$$\vec{u}^s(\vec{r}) = u^{e(s)} \vec{N}_i^{e(s)}(\vec{r}). \quad (3.51)$$

Here the superscript $e(s)$ is used to indicate that segment s is an edge for triangle e , $u^{e(s)}$ is the tangential field along segment s and $\vec{N}_i^{e(s)}(\vec{r})$ is the vector-basis function defined on that edge, as given in (3.45). Similar to 2D scalar problems, the line segment s is mapped to an isoparametric element (depicted in Figure 3.3) to ease the line integration.

3.3.5.2 2D Triangle Facets

For 3D problems, the boundary Γ_2 is a surface on which an integration is required as per the functional $F(\vec{u})$ given in (3.44). Analogous to 2D problems, this surface is divided into triangular facets. The vector field on each facet s can be approximated by

$$\vec{u}^s(\vec{r}) = \sum_{i=1}^3 u_i^{e(s)} \vec{N}_i^{e(s)}(\vec{r}) \quad (3.52)$$

where, again, the superscript $e(s)$ is utilized to associate facet s with tetrahedron e , and $u_i^{e(s)}$ is the tangential field along an edge i associated with a vector basis function $\vec{N}_i^{e(s)}(\vec{r})$. Since a surface triangle s is a facet that belongs to a tetrahedron e , the surface triangle and the tetrahedron will share three vector-basis functions. Hence, if triangle edges $\{1, 2, 3\}$ map to local tetrahedron edges $\{i, j, k\}$, then

$$\begin{aligned} u_1^{e(s)} &= u_i^e, & u_2^{e(s)} &= u_j^e, & u_3^{e(s)} &= u_k^e \\ \vec{N}_1^{e(s)} &= \vec{N}_i^e, & \vec{N}_2^{e(s)} &= \vec{N}_j^e, & \vec{N}_3^{e(s)} &= \vec{N}_k^e. \end{aligned} \quad (3.53)$$

The integration over the boundary can be simplified by mapping the surface triangle to an isoparametric element as depicted in Figure 3.5. The selected isoparametric element is an isosceles right-angled triangle with legs extending from zero to one in the $\xi - \eta$ plane. For the transformed element, the nodal linear basis functions at local triangle nodes are given as

$$\lambda_1^{\zeta^s}(\xi, \eta) = \xi \quad , \quad \lambda_2^{\zeta^s}(\xi, \eta) = \eta \quad , \quad \lambda_3^{\zeta^s}(\xi, \eta) = 1 - \xi - \eta \quad (3.54)$$

where $\{1, 2, 3\}$ are the local indices of the triangle nodes that can be projected to local tetrahedron nodes $\{n_1, n_2, n_3\}$. Further, the vector basis functions of the triangle s can be written in terms of the new isoparametric linear basis functions.

The transformation to an isoparametric element ζ^s results in multiplying an integration performed over the element by $2A^s$, where A^s is the area of the facet s

$$A^s = \frac{1}{2} \begin{vmatrix} 1 & x_1 & y_1 \\ 1 & x_2 & y_2 \\ 1 & x_3 & y_3 \end{vmatrix} . \quad (3.55)$$

3.3.6 Functional Discretization

After discretizing the problem into N_e domain elements with N_s boundary facets (or boundary line segments in 2D), the functional $F(\vec{u})$ can be written as

$$F(\vec{u}) = \sum_{e=1}^{N_e} F^e(\vec{u}^e) + \sum_{s=1}^{N_s} F^s(\vec{u}^s) \quad (3.56)$$

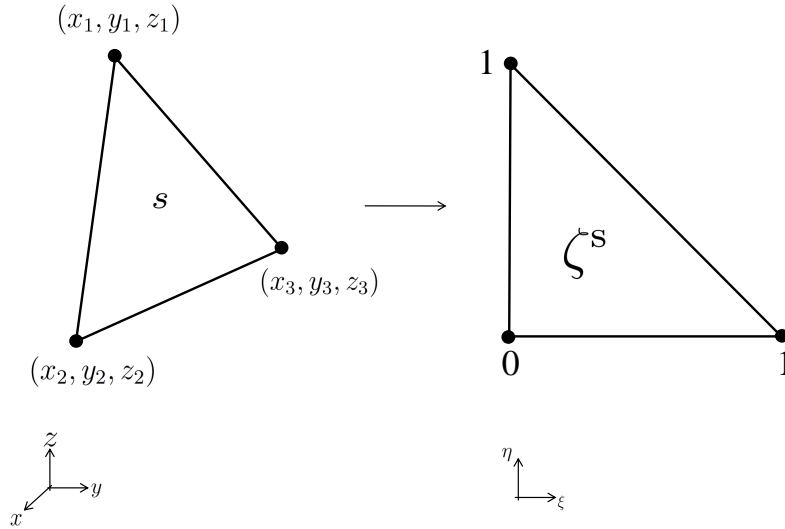


Figure 3.5: Transformation of a triangle element to an isoparametric element.

where

$$\begin{aligned}
 F^e(\vec{u}^e) &= \frac{1}{2} \int_{\Omega^e} [(\nabla \times \vec{u}^e) \cdot (\nabla \times \vec{u}^e) - \alpha^e \vec{u}^e \cdot \vec{u}^e] dv - \int_{\Omega^e} \beta^e \vec{u}^e \cdot \vec{f}^e dv \\
 F^s(\vec{u}^s) &= \int_{\Gamma_2^s} \left[\frac{\gamma^s}{2} (\hat{n} \times \vec{u}^s) \cdot (\hat{n} \times \vec{u}^s) + \vec{u}^s \cdot \vec{q}^s \right] ds.
 \end{aligned} \tag{3.57}$$

The approximations for the vector fields within the elements in (3.46), (3.51) for 2D and (3.47), (3.52) for 3D are used in the above equations to evaluate the local matrices associated with each element in the mesh. Next, the transformation from local edge indices to global indices is used to assemble the global FEM matrices (see Appendix A and B). This results in the formation of the following matrix equation

$$F(\underline{u}) = \frac{1}{2} \underline{u}^T [\mathbf{U} - \mathbf{V}_\alpha] \underline{u} - \underline{u}^T \vec{\mathcal{R}}_\beta \cdot \underline{\vec{f}} + \underline{u}^T \underline{g}. \tag{3.58}$$

where $\underline{u} \in \mathbb{C}^E$ is a vector of the unknown spatial-vector function \vec{u} along the mesh edges; $\underline{f} \in \mathbb{C}^{N_e}$ is a column vector that holds the excitation function spatial-vector fields located at the centroids of the domain elements; $\underline{g} \in \mathbb{C}^E$ is a vector, which depends on the values of \vec{q} in the BCs; $\mathbf{U} \in \mathbb{C}^{E \times E}$ is a stiffness matrix which depends on the BCs; $\mathbf{V}_\alpha \in \mathbb{C}^{E \times E}$ is a mass matrix, which depends on the centroidal values of α ; and $\vec{\mathcal{R}}_\beta \in \mathbb{C}^{E \times N_e}$ is a mass matrix which depends on the centroidal values of β , with each of its components being a spatial-vector with x - and y - components in 2D and an additional z -component in 3D.

Regardless of the BC type, the entries at the i^{th} row and j^{th} column of matrices \mathbf{U} and \mathbf{V}_α are given by

$$\begin{aligned} u_{i,j} &= \int_{\Omega} (\nabla \times \vec{N}_i) \cdot (\nabla \times \vec{N}_j) dv \\ v_{\alpha i,j} &= \int_{\Omega} \alpha \vec{N}_i \cdot \vec{N}_j dv \end{aligned} \quad (3.59)$$

where \vec{N}_i and \vec{N}_j are the linear vector basis functions defined at the i^{th} and j^{th} edge respectively and $\nabla \times$ is the curl operator.

The entry at the i^{th} row and k^{th} column of matrix $\vec{\mathcal{R}}_\beta$ is calculated as

$$\vec{\mathcal{R}}_{\beta i,k} = \int_{\Omega_k} \beta_k \vec{N}_i(\vec{r}) dv \quad (3.60)$$

where \vec{N}_i is the vector basis function defined at edge i belonging to the k^{th} domain element while Ω_k and β_k are, respectively, the domain covered by and the value of β assigned to the k^{th} triangle.

The stationary point of the discretized functional is found by setting the derivative

of (3.58) with respect to \underline{u} to zero, resulting in the matrix equation

$$[\mathbf{u} - \mathbf{v}_\alpha] \underline{u} = \vec{\mathcal{R}}_\beta \cdot \vec{\underline{f}} - \underline{g} \quad (3.61)$$

3.3.7 Dirichlet Boundary Condition

The treatment of the Dirichlet boundary conditions in edge-based FEM problems is very similar to node-based problems. Imposing inhomogeneous Dirichlet boundary condition (3.41) in vectorial BVPs, with boundary $\Gamma = \Gamma_1$, causes the boundary-integral term in (3.44) to vanish. As outlined in Appendix B, the matrix equation (3.61) can be segmented as

$$\begin{bmatrix} \mathcal{I}_{\text{BB}} & \mathbf{0}_{\text{BF}} \\ \mathbf{u}_{\text{FB}} - \mathbf{v}_{\alpha\text{FB}} & \mathbf{u}_{\text{FF}} - \mathbf{v}_{\alpha\text{FF}} \end{bmatrix} \begin{bmatrix} \underline{u}_{\text{B}} \\ \underline{u}_{\text{F}} \end{bmatrix} = \begin{bmatrix} \vec{\mathcal{R}}_{\beta\text{B}} \\ \vec{\mathcal{R}}_{\beta\text{F}} \end{bmatrix} \cdot \vec{\underline{f}}. \quad (3.62)$$

Here subscripts B and F refer to the B boundary edges and the F free (interior) edges in the mesh, with $E = \text{B} + \text{F}$. The dimensions of the sub-matrices and vectors in (3.62) are indicated by their subscripts; for example sub-matrix $\mathbf{u}_{\text{FB}} \in \mathbb{C}^{\text{F} \times \text{B}}$ and $\underline{u}_{\text{B}} \in \mathbb{C}^{\text{B}}$. The sub-matrices \mathbf{u}_{FB} and $\mathbf{v}_{\alpha\text{FB}}$ describe the interaction between boundary edges and free edges. The number of rows in sub-matrices $\vec{\mathcal{R}}_{\beta\text{B}}$ and $\vec{\mathcal{R}}_{\beta\text{F}}$ is indicated by the subscript B or F. The number of columns is N_e , the number of elements in the domain, which is also the size of column vector $\vec{\underline{f}}$. The Dirichlet BC sets $\underline{u}_{\text{B}} = \underline{p}$; therefore, the matrix equation (3.62) can be simplified to

$$[\mathbf{u}_{\text{FF}} - \mathbf{v}_{\alpha\text{FF}}] \underline{u}_{\text{F}} = \vec{\mathcal{R}}_{\beta\text{F}} \cdot \vec{\underline{f}} - [\mathbf{u}_{\text{FB}} - \mathbf{v}_{\alpha\text{FB}}] \underline{p}. \quad (3.63)$$

In conductive enclosures, the homogeneous Dirichlet boundary conditions applies, *i.e.*

$$\underline{p} = 0, \quad (3.64)$$

therefore (3.63) becomes

$$[\mathbf{u}_{\text{FF}} - \mathbf{v}_{\alpha\text{FF}}]\underline{u}_{\text{F}} = \vec{\mathcal{R}}_{\beta\text{F}} \cdot \underline{\vec{f}}. \quad (3.65)$$

Since the components of the above matrix equation depend only on free (interior) edges, the subscript F can be dropped. Thus, the matrix equation (3.65) becomes

$$[\mathbf{u} - \mathbf{v}_{\alpha}]u = \vec{\mathcal{R}}_{\beta} \cdot \underline{\vec{f}}. \quad (3.66)$$

3.3.8 Absorbing Boundary Condition

For unbounded problems, the domain (Ω) is truncated with an artificial boundary that approximates the Sommerfeld radiation condition (2.28). A Robin BC is used to implement the artificial boundary ($\Gamma = \Gamma_2$) with the coefficients selected so as to model the first-order vectorial ABC [44]. The first-order ABC sets the coefficient $\vec{q} = 0$ in (3.42) and the coefficient

$$\gamma = jk_b \quad (3.67)$$

and hence the Robin BC can be rewritten as

$$\hat{n} \times (\nabla \times \vec{u}(\vec{r})) = -jk_b \hat{n} \times (\hat{n} \times \vec{u}(\vec{r})) \quad \text{for } \vec{r} \in \Gamma. \quad (3.68)$$

The FEM formulation of the Robin BCs leads to the boundary-integral term that contributes to the $(i, j)^{\text{th}}$ element in \mathbf{u} as

$$\mathcal{U}_{i,j}^{\Gamma} = \int_{\Gamma} j k_b \left(\hat{n} \times \vec{N}_i \right) \cdot \left(\hat{n} \times \vec{N}_j \right) ds \quad (3.69)$$

where \vec{N}_i and \vec{N}_j are the boundary vector basis functions defined for edges i and j on Γ . For 2D problems the integral (3.69) can be written in terms of the isoparametric coordinate ζ as

$$\mathcal{U}_{i,i}^s = \int_0^1 j l^s k_b \left(\hat{n} \times \vec{N}_i \right) \cdot \left(\hat{n} \times \vec{N}_i \right) d\zeta \quad (3.70)$$

where s is a boundary edge and i is the global index of this edge. Similarly, for a boundary triangular facet s on a 3D surface, with respect to isoparametric coordinates (ξ, η) (3.69) is given as

$$\mathcal{U}_{i,j}^s = \int_0^1 \int_0^{1-\xi} j 2A^s k_b \left(\hat{n} \times \vec{N}_i \right) \cdot \left(\hat{n} \times \vec{N}_j \right) d\eta d\xi. \quad (3.71)$$

where $\{i, j\}$ are global edge indices. Eventually, the FEM matrix equation (3.61) simplifies to

$$[\mathbf{u} - \mathbf{v}_{\alpha}] \underline{u} = \vec{\mathcal{R}}_{\beta} \cdot \vec{f} \quad (3.72)$$

where \underline{g} is zero because $\vec{q} = 0$, and the stiffness matrix is

$$\mathbf{u} = \mathbf{u}^{\Omega} + \mathbf{u}^{\Gamma} \quad (3.73)$$

where \mathbf{u}^{Ω} and \mathbf{u}^{Γ} are the contributions of the domain edges and the boundary edges respectively.

3.4 Matrix Operators

Several matrix operators are introduced in this section which can be used to describe the inversion algorithms efficiently. They are also used in the forward problem to generate synthetic data.

3.4.1 Measurement Surface Operators

The fields of an electromagnetic problem are usually measured at R receiver locations positioned on a measurement surface \mathcal{S} . The first matrix operator, $\vec{\mathcal{M}}_{\mathcal{S}}$, introduced herein calculates the field at the receiver locations by operating on the solution obtained from the FEM solver.

For 2D TM scalar problems, the operator $\vec{\mathcal{M}}_{\mathcal{S}} \in \mathbb{C}^{R \times N}$ transforms field values from the N problem domain nodes to the R receiver locations on the measurement surface \mathcal{S} . The result of the transformation is z -polarized scalar field values, thus

$$\vec{\mathcal{M}}_{\mathcal{S}} = \mathcal{M}_{\mathcal{S},z} \hat{z}. \quad (3.74)$$

If the receiver locations are within the problem's mesh, the operator interpolates to these locations using the FEM nodal basis functions, while if the receivers are located outside the mesh (for example, in unbounded-region problems the receivers may be located in the far-field region), Huygens' principle is used to find the field at the receiver locations [44]. For 2D TM configurations, Huygens' principle says that the value of u at a receiver location \vec{r} is evaluated as

$$u(\vec{r}) = \oint_{\Gamma} \left[u(\vec{r}') \frac{\partial G_0(\vec{r}, \vec{r}')}{\partial n'} - G_0(\vec{r}, \vec{r}') \frac{\partial u(\vec{r}')}{\partial n'} \right] ds' \quad (3.75)$$

where \vec{r}' is the position vector for a location on boundary Γ , n' is the normal vector to Γ at \vec{r}' , and the 2D Green's function is

$$G_0(\vec{r}, \vec{r}') = \frac{1}{j^4} H_0^{(2)}(k_b |\vec{r} - \vec{r}'|). \quad (3.76)$$

Here $H_0^{(2)}$ is the zeroth-order Hankel function of the second kind.

For vector problems, the operator $\vec{\mathcal{M}}_{\mathcal{S}} \in \mathbb{C}^{R \times E}$ transforms field values along the E problem domain edges to the R receiver locations on the measurement surface \mathcal{S} . The result of the transformation in 2D TE problems is field vectors with x - and y -components; hence

$$\vec{\mathcal{M}}_{\mathcal{S}} = \mathcal{M}_{\mathcal{S},x} \hat{x} + \mathcal{M}_{\mathcal{S},y} \hat{y}. \quad (3.77)$$

For 3D vectorial problem, the transformation produces all three field components along the x -, y -, and z -axis, thus we write

$$\vec{\mathcal{M}}_{\mathcal{S}} = \mathcal{M}_{\mathcal{S},x} \hat{x} + \mathcal{M}_{\mathcal{S},y} \hat{y} + \mathcal{M}_{\mathcal{S},z} \hat{z}. \quad (3.78)$$

Analogous to scalar problems, if the receiver locations are within the problem's mesh the operator interpolates to these locations using the FEM vector basis functions, while if the receivers are located outside the mesh, Huygens' principle is employed. For vector problems, Huygens's principle says that the value of \vec{u} at a receiver location \vec{r} is calculated as

$$\vec{u}(\vec{r}) = \oint_{\Gamma} \left\{ [\hat{n}' \times \nabla' \times \vec{u}(\vec{r}')] G_0(\vec{r}, \vec{r}') + [\hat{n}' \cdot \vec{u}(\vec{r}')] \nabla' G_0(\vec{r}, \vec{r}') \right. \\ \left. + [\hat{n}' \times \vec{u}(\vec{r}')] \times \nabla' G_0(\vec{r}, \vec{r}') \right\} ds'. \quad (3.79)$$

For 3D problems the Green's function is

$$G_0(\vec{r}, \vec{r}') = \frac{e^{-jk_b|\vec{r}-\vec{r}'|}}{4\pi|\vec{r}-\vec{r}'|}. \quad (3.80)$$

3.4.2 Imaging Domain Operators

Most inversion algorithms require the field values within the imaging domain \mathcal{D} where the OI is located. The second operator $\vec{\mathcal{M}}_{\mathcal{D}}$ returns the field values inside the imaging domain \mathcal{D} by operating on the FEM solution defined everywhere in the problem domain Ω .

With respect to 2D scalar problems, the operator $\vec{\mathcal{M}}_{\mathcal{D}} \in \mathbb{R}^{I \times N}$ *selects* the field values at the I nodes within the imaging domain \mathcal{D} from the N problem domain nodes. Since the nodal values are z -polarized

$$\vec{\mathcal{M}}_{\mathcal{D}} = \mathcal{M}_{\mathcal{D},z} \hat{z}. \quad (3.81)$$

For vector problems, the operator $\vec{\mathcal{M}}_{\mathcal{D}} \in \mathbb{R}^{I \times E}$ is a matrix that transform field values along the E mesh edges to the I element centroids in the imaging domain \mathcal{D} . The transformations are performed by interpolation using the FEM vector basis functions. The results are field vectors with x - and y - components in 2D TE problems and an additional z -component in 3D full-vectorial problems; hence for 2D TE

$$\vec{\mathcal{M}}_{\mathcal{D}} = \mathcal{M}_{\mathcal{D},x} \hat{x} + \mathcal{M}_{\mathcal{D},y} \hat{y} \quad (3.82)$$

and for 3D full-vectorial

$$\vec{\mathcal{M}}_{\mathcal{D}} = \mathcal{M}_{\mathcal{D},x} \hat{x} + \mathcal{M}_{\mathcal{D},y} \hat{y} + \mathcal{M}_{\mathcal{D},z} \hat{z}. \quad (3.83)$$

3.4.3 Inverse FEM Matrix Operators

3.4.3.1 Scalar Problems

The algorithm for solving 2D scalar inverse problems (details of which will be discussed in Chapter 4) evaluates the z -polarized scattered field $E_{t,z}^{\text{sct}}$ given the contrast sources, $w_{t,z}$, within the imaging domain \mathcal{D} . Here, the scattered field is governed by the scalar Helmholtz equation (2.31); this equation can be solved using FEM. Comparing the BVP second-order PDE (3.1) with equation (2.31), the different terms in (3.1) become

$$u(\vec{r}) = E_{t,z}^{\text{sct}}(\vec{r}), \quad \alpha(\vec{r}) = k_b^2(\vec{r}), \quad (3.84)$$

$$\beta(\vec{r}) = -k_b^2(\vec{r}), \quad f(\vec{r}) = w_{t,z}(\vec{r}). \quad (3.85)$$

Thus, using the Rayleigh-Ritz formulation of FEM, the vectors and matrices in the matrix equation (3.26) map to

$$\underline{u} = \underline{E}_{t,z,\Omega}^{\text{sct}}, \quad \underline{f} = \underline{w}_{t,z,\Omega}, \quad (3.86)$$

$$\mathcal{T}_\alpha = \mathcal{T}_b, \quad \mathcal{T}_\beta = -\mathcal{T}_b. \quad (3.87)$$

Here $\mathcal{T}_b \in \mathbb{C}^{N \times N}$ is the mass matrix that depends on the background medium wavenumber k_b , and the vectors $\underline{E}_{t,z,\Omega}^{\text{sct}} \in \mathbb{C}^N$ and $\underline{w}_{t,z,\Omega} \in \mathbb{C}^N$ contain the nodal values of the scattered field and the contrast source for transmitter t . Moreover, as outlined in Sections 3.2.7 and 3.2.8, \underline{g} in (3.26) is equal to zero as a result of applying either the homogeneous Dirichlet BC or the second-order ABC over the whole boundary.

Substituting (3.86), (3.87) and $\underline{g} = 0$ in (3.26), the resulting FEM matrix equation

is

$$[\mathcal{S} - \mathcal{T}_b] \underline{E}_{t,z,\Omega}^{\text{sct}} = \mathcal{T}_b \underline{w}_{t,z,\Omega}. \quad (3.88)$$

The stiffness matrix $\mathcal{S} \in \mathbb{C}^{N \times N}$ depends on the boundary conditions in case of BVPs with Robin BC.

In the inversion algorithms to be considered, the contrast source variables $\underline{w}_{t,z} \in \mathbb{C}^I$ are available at nodes within the imaging domain (\mathcal{D}); however, the FEM matrix equation (3.88) requires the contrast source variables at all mesh nodes. The contrast source variables $\underline{w}_{t,z,\Omega} \in \mathbb{C}^N$, for all nodes in Ω are given by

$$\underline{w}_{t,z,\Omega} = \mathcal{M}_{\mathcal{D},z}^T \underline{w}_{t,z}. \quad (3.89)$$

Substituting (3.89) in the FEM matrix equation (3.88), a new operator $\mathcal{L}_z \in \mathbb{C}^{N \times I}$ to calculate the scattered field ($\underline{E}_{t,z,\Omega}^{\text{sct}}$) is defined as

$$\underline{E}_{t,z,\Omega}^{\text{sct}} = \mathcal{L}_z [\underline{w}_{t,z}] = \mathcal{K}_b^{-1} \mathcal{T}_b \mathcal{M}_{\mathcal{D},z}^T [\underline{w}_{t,z}] \quad (3.90)$$

where the matrix $\mathcal{K}_b = \mathcal{S} - \mathcal{T}_b$.

Inversion algorithms are tested using experimental datasets and synthetic datasets. The latter are generated by calculating the scattered field ($E_{t,z}^{\text{sct}}$) for an OI with known contrast (χ). This scattered field is governed by the scalar Helmholtz equation (2.30), which can also be solved using FEM. For this case, the terms of the second-order PDE (3.1) are

$$u(\vec{r}) = E_{t,z}^{\text{sct}}(\vec{r}), \quad \alpha(\vec{r}) = k_b^2(\vec{r})(\chi(\vec{r}) + 1), \quad (3.91)$$

$$\beta(\vec{r}) = -k_b^2(\vec{r})\chi(\vec{r}), \quad f(\vec{r}) = E_{t,z}^{\text{inc}}(\vec{r}). \quad (3.92)$$

Using the Rayleigh-Ritz formulation of FEM, the vectors and matrices in the matrix equation (3.26) become

$$\underline{u} = \underline{E}_{t,z,\Omega}^{\text{sct}}, \quad \underline{f} = \underline{E}_{t,z,\Omega}^{\text{inc}}, \quad (3.93)$$

$$\mathcal{T}_\alpha = \mathcal{T}_\chi + \mathcal{T}_b, \quad \mathcal{T}_\beta = -\mathcal{T}_\chi. \quad (3.94)$$

where $\mathcal{T}_\chi \in \mathbb{C}^{N \times N}$ is the mass matrix that depends on the OI contrast (χ) and the background wavenumber (k_b), and $\underline{E}_{t,z,\Omega}^{\text{inc}} \in \mathbb{C}^N$ is a vector that contains the nodal values of the incident field. Substituting (3.93), (3.94) and $\underline{g} = 0$ in (3.26), the resultant FEM matrix equation is

$$[\mathcal{S} - \mathcal{T}_b - \mathcal{T}_\chi] \underline{E}_{t,z,\Omega}^{\text{sct}} = \mathcal{T}_\chi \underline{E}_{t,z,\Omega}^{\text{inc}}. \quad (3.95)$$

To calculate the scattered field ($\underline{E}_{t,z,\Omega}^{\text{sct}}$), a new operator $\mathcal{L}_{z,\chi} \in \mathbb{C}^{N \times N}$ is defined as

$$\underline{E}_{t,z,\Omega}^{\text{sct}} = \mathcal{L}_{z,\chi} [\underline{E}_{t,z}^{\text{inc}}] = \mathcal{K}_\chi^{-1} \mathcal{T}_\chi [\underline{E}_{t,z}^{\text{inc}}] \quad (3.96)$$

where the matrix $\mathcal{K}_\chi = \mathcal{S} - \mathcal{T}_\chi - \mathcal{T}_b$.

3.4.3.2 Vector Problems

The inversion algorithm for vector problems (discussed in Chapter 4) calculates the scattered field \vec{E}_t^{sct} given the contrast sources \vec{w}_t within the imaging domain \mathcal{D} . The scattered field \vec{E}_t^{sct} satisfies the vector wave equation (2.24), which can be solved using edge-based FEM. By comparing the vector BVP (3.40) with equation (2.24),

the terms in (3.40) are identified as

$$\vec{u}(\vec{r}) = \vec{E}_t^{\text{sct}}(\vec{r}), \quad \alpha(\vec{r}) = k_b^2(\vec{r}), \quad (3.97)$$

$$\beta(\vec{r}) = k_b^2(\vec{r}), \quad \vec{f}(\vec{r}) = \vec{w}_t(\vec{r}). \quad (3.98)$$

Thus, using the Rayleigh-Ritz formulation of FEM, the vectors and matrices in the matrix equation (3.61) become

$$\underline{u} = \underline{E}_{t,\Omega}^{\text{sct}}, \quad \vec{f} = \vec{w}_{t,\Omega}, \quad (3.99)$$

$$\mathbf{V}_\alpha = \mathbf{V}_b, \quad \vec{\mathcal{R}}_\beta = \vec{\mathcal{R}}_b. \quad (3.100)$$

Here the data vector $\underline{E}_{t,\Omega}^{\text{sct}} \in \mathbb{C}^E$ contains the scattered vector field components along the edges of the mesh due to transmitter t , and $\vec{w}_{t,\Omega} \in \mathbb{C}^{N_e}$ is a column vector that holds the contrast source spatial-vector fields at the centroids of elements in Ω . Further, $\mathbf{V}_b \in \mathbb{C}^{E \times E}$ is the mass matrix that depends on the background medium wavenumber k_b , and $\vec{\mathcal{R}}_b \in \mathbb{C}^{E \times N_e}$ is a matrix which also depends on the background medium wavenumber but each of its entries is a spatial-vector. For 2D TE problems, the entries of \vec{w}_t and $\vec{\mathcal{R}}_b$ are spatial-vectors with x - and y - components; that is

$$\begin{aligned} \vec{w}_t &= w_{t,x} \hat{x} + w_{t,y} \hat{y} \\ \vec{\mathcal{R}}_b &= \mathcal{R}_{b,x} \hat{x} + \mathcal{R}_{b,y} \hat{y}. \end{aligned} \quad (3.101)$$

With respect to 3D full-vectorial problems each entry has an additional z -component, that is,

$$\begin{aligned} \vec{w}_t &= w_{t,x} \hat{x} + w_{t,y} \hat{y} + w_{t,z} \hat{z} \\ \vec{\mathcal{R}}_b &= \mathcal{R}_{b,x} \hat{x} + \mathcal{R}_{b,y} \hat{y} + \mathcal{R}_{b,z} \hat{z}. \end{aligned} \quad (3.102)$$

Next, \underline{g} in (3.61) is equal to zero as a result of applying either the homogeneous Dirichlet BC or the second-order ABC; this is outlined in Sections 3.3.7 and 3.3.8.

Substituting (3.99), (3.100) and $\underline{g} = 0$ in (3.61), the resultant FEM matrix equation is

$$[\mathbf{u} - \mathbf{v}_b] \underline{E}_{t,\Omega}^{\text{sct}} = \vec{\mathcal{R}}_b \cdot \vec{\underline{w}}_{t,\Omega}. \quad (3.103)$$

where the matrices depend on the boundary conditions as detailed in previous sections. Similar to scalar problems, the contrast source variables $\vec{\underline{w}}_t \in \mathbb{C}^I$ are located at the elements' centroids within the imaging domain \mathcal{D} ; therefore a new operator $\vec{\mathcal{L}} \in \mathbb{C}^{E \times I}$ is given as

$$\underline{E}_{t,\Omega}^{\text{sct}} = \vec{\mathcal{L}}[\vec{\underline{w}}_t] = \mathcal{K}_b^{-1} \vec{\mathcal{R}}_b \cdot \mathcal{M}_U^T[\vec{\underline{w}}_t] \quad (3.104)$$

where $\mathcal{K}_b = \mathbf{u} - \mathbf{v}_b$ and $\mathcal{M}_U \in \mathbb{R}^{I \times N_e}$ is a selection matrix that returns centroid values for only the elements located in the imaging domain \mathcal{D} , given centroid values for all the N_e elements in Ω . The inverse matrix operator can be written as

$$\vec{\mathcal{L}}[\vec{\underline{w}}_t] = \mathcal{L}_x[w_{t,x}] + \mathcal{L}_y[w_{t,y}] \quad (3.105)$$

for 2D TE problems, where $w_{t,x}$ and $w_{t,y}$ are the x - and y - components of the contrast source spatial-vector $\vec{\underline{w}}_t$. Similarly, for 3D full-vectorial problems

$$\vec{\mathcal{L}}[\vec{\underline{w}}_t] = \mathcal{L}_x[w_{t,x}] + \mathcal{L}_y[w_{t,y}] + \mathcal{L}_z[w_{t,z}] \quad (3.106)$$

where $w_{t,z}$ is the z - component of $\vec{\underline{w}}_t$.

The finite-element method is also used to solve the forward problem using the vector wave equation (2.23) when the contrast χ of a target relative to the background medium is provided. The field solution is used to generate synthetic data to test

inversion algorithms. The electric field along the mesh edges in the problem domain Ω is given as

$$\begin{aligned} \underline{E}_t^{\text{sct}} &= \vec{\mathcal{L}}_\chi[\vec{E}_t^{\text{inc}}] = \mathcal{K}_\chi^{-1} \left[\vec{\mathcal{R}}_\chi \cdot \vec{E}_t^{\text{inc}} \right] \\ &= (\mathbf{u} - \mathbf{v}_b - \mathbf{v}_\chi)^{-1} \left[\vec{\mathcal{R}}_\chi \cdot \vec{E}_t^{\text{inc}} \right]. \end{aligned} \quad (3.107)$$

Here $\mathbf{v}_\chi \in \mathbb{C}^{E \times E}$ and $\vec{\mathcal{R}}_\chi \in \mathbb{C}^{E \times N_e}$ are mass matrices that depends on the OI contrast, χ , and the background wavenumber, k_b , while $\vec{E}_t^{\text{inc}} \in \mathbb{C}^{N_e}$ is a column vector that holds the incident spatial-vector field at the centroids of the elements in Ω . The derivation of (3.107) is straight-forward by following the same steps outlined for obtaining (3.104).

4

The Inversion Algorithm

Really new ideas on inverse problems most times come from the collision between the needs and the accomplishments of people working in different areas.

–Pierre Sabatier [77]

A state-of-the-art modified-gradient algorithm that has had much success in solving inverse scattering problem is the contrast source inversion (CSI) technique [55]. In each iteration of CSI, two variables—the contrast and the contrast source—are updated successively using a conjugate gradient method. The CSI method has been formulated using integral-equations [20, 55], finite-differences [32, 78] and eigenfunction expansions [79].

The IE formulation of CSI is efficient if the Green’s function is available analytically and is such as to produce integral equation operators which can be efficiently discretized and evaluated. This is indeed the case if the background medium is homogeneous and if the boundary is such as to allow a closed-form Green’s function with the convolutional property (*e.g.* unbounded problem domains). To overcome these deficiencies in IE formulations, a finite-difference (FD) CSI method has been introduced in conjugation with a PDE formulation of the electromagnetic problem [32, 78]. The FD-CSI algorithm uses an effective uniform structured grid discretization of the

Helmholtz PDE. Using this technique one can incorporate an inhomogeneous background medium as well as various boundaries as long as these can be well approximated using the FD grid.

Despite its success, there are two major drawbacks inherent in FD-CSI. First, FD discretizations make it difficult to accurately model arbitrarily shaped boundaries, whether of the enclosure or of the unknown object, because of the use of structured rectangular grids requiring stair-stepping at curved boundaries. Although resolving the boundary is not an issue for unbounded-region configurations where absorbing boundary conditions are applied, it does become an issue for imaging configurations with conductive enclosures of arbitrary shape. Second, the use of structured rectangular grids becomes problematic when including prior information about the target because this usually requires the specification of electrical parameters on irregularly shaped regions [32, 78].

In this chapter, the CSI algorithm formulation using the finite-element method (FEM) is presented [29]. Unlike other CSI implementations, FEM-CSI offers several benefits that include: (*i*) performing the inversion on an arbitrary irregular grid of triangles or tetrahedra, (*ii*) incorporating an inhomogeneous medium as a background reference, (*iii*) controlling the density of the mesh adaptively within the problem domain, and (*iv*) easily incorporating radiating or arbitrarily-shaped conductive boundaries surrounding the MWI setup.

The first part of this chapter gives a general overview of the contrast source inversion (CSI) method where a description of the algorithm, along with the update procedure is outlined. In the second section of the chapter, a detailed formulation of the CSI method using FEM is presented. Here, the FEM-CSI algorithm is described for three problem configurations: 2D TM, 2D TE and 3D full-vectorial. Moreover,

any necessary terminologies and definitions that arise from the FEM problem discretization are outlined.

4.1 The Contrast Source Inversion Method

The CSI method formulates the optimization problem in terms of two variables, the contrast source, \vec{w}_t , and the contrast, χ . The CSI cost functional written with respect of these variables is given as [55]

$$\begin{aligned} \mathcal{C}^{\text{CSI}}(\chi, \vec{w}_t) &= \mathcal{C}^{\mathcal{S}}(\vec{w}_t) + \mathcal{C}^{\mathcal{D}}(\chi, \vec{w}_t) \\ &= \frac{\sum_t \|\vec{u}_t(\vec{r}) - \mathcal{G}_{\mathcal{S}}\{\vec{w}_t\}\|_{\mathcal{S}}^2}{\sum_t \|\vec{u}_t(\vec{r})\|_{\mathcal{S}}^2} + \frac{\sum_t \left\| \chi(\vec{r}) \vec{E}_t^{\text{inc}}(\vec{r}) - \vec{w}_t(\vec{r}) + \chi(\vec{r}) \mathcal{G}_{\mathcal{D}}\{\vec{w}_t\} \right\|_{\mathcal{D}}^2}{\sum_t \left\| \chi(\vec{r}) \vec{E}_t^{\text{inc}}(\vec{r}) \right\|_{\mathcal{D}}^2}. \end{aligned} \quad (4.1)$$

Here $\mathcal{C}^{\mathcal{S}}(\vec{w}_t)$ and $\mathcal{C}^{\mathcal{D}}(\chi, \vec{w}_t)$ are, respectively, the normalized data-error and domain-error functionals. The functionals are normalized to accommodate any imbalance between them.

In the CSI functional, \vec{u}_t is the measured scattered field on surface \mathcal{S} for each transmitter, $\mathcal{G}_{\mathcal{S}}$ is the data operator and $\mathcal{G}_{\mathcal{D}}$ is the domain operator. The data operator returns the scattered field on a measurement surface \mathcal{S} given the contrast source variable \vec{w}_t , while the domain operator returns the scattered field in the imaging domain \mathcal{D} from the contrast source variable \vec{w}_t . Both operators work on the contrast source variable \vec{w}_t depend on the environment that has been defined for the problem

domain. The L_2 -norms in (4.1) are defined as

$$\|\vec{x}\|_S^2 \triangleq \int_S \vec{x}(\vec{r})^* \cdot \vec{x}(\vec{r}) dv, \quad (4.2)$$

$$\|\vec{y}\|_D^2 \triangleq \int_D \vec{y}(\vec{r})^* \cdot \vec{y}(\vec{r}) dv, \quad (4.3)$$

where \vec{x} and \vec{y} are arbitrary functions, the superscript $*$ denotes the complex conjugate operator and \cdot represents the dot-product .

The CSI cost functional is minimized by updating two unknowns, the contrast, χ_n and the contrast source, $\vec{w}_{t,n}$, iteratively in an interlaced fashion. At the n^{th} iteration of the optimization, each variable is updated to minimize the cost functional while assuming the other unknown is constant. The contrast source sequence is updated using a conjugate-gradient (CG) algorithm, whereas the contrast variable is updated via a closed-form expression obtained analytically by minimizing the domain-error equation. The optimization process is terminated when the cost functional reaches a desired minimum.

4.2 The FEM-CSI Algorithm

Within the framework of the finite-element method, the discretization of the CSI functional results in the following cost functional over discrete vector unknowns:

$$\mathcal{F}^{\text{CSI}}(\underline{\chi}, \underline{\vec{w}}_t) = \mathcal{F}^S(\underline{\vec{w}}_t) + \mathcal{F}^D(\underline{\chi}, \underline{\vec{w}}_t). \quad (4.4)$$

Here the normalized data-error term $\mathcal{F}^S(\vec{w}_t)$ and the normalized domain-error term $\mathcal{F}^D(\underline{\chi}, \vec{w}_t)$ are given by

$$\mathcal{F}^S(\vec{w}_t) = \frac{\sum_t \left\| \vec{u}_t - \vec{\mathcal{M}}_S \vec{\mathcal{L}}[\vec{w}_t] \right\|_{\mathcal{S}}^2}{\sum_t \left\| \vec{u}_t \right\|_{\mathcal{S}}^2} \quad (4.5)$$

$$\mathcal{F}^D(\underline{\chi}, \vec{w}_t) = \frac{\sum_t \left\| \underline{\chi} \odot \vec{E}_t^{\text{inc}} - \vec{w}_t + \underline{\chi} \odot \vec{\mathcal{M}}_D \vec{\mathcal{L}}[\vec{w}_t] \right\|_{\mathcal{D}}^2}{\sum_t \left\| \underline{\chi} \odot \vec{E}_t^{\text{inc}} \right\|_{\mathcal{D}}^2}. \quad (4.6)$$

For a transmitter t , $\vec{u}_t \in \mathbb{C}^R$ is a vector of the measured vector scattered field data at the R receiver locations for each transmitter, $\underline{\chi} \in \mathbb{C}^I$ corresponds to a vector of contrast values located inside \mathcal{D} , and $\vec{E}_t^{\text{inc}} = \vec{\mathcal{M}}_D[\vec{E}_{t,\Omega}^{\text{inc}}]$ holds the incident field vector values inside \mathcal{D} . The notation $\underline{a} \odot \underline{b}$ denotes the Hadamard (*i.e.*, element-wise) product. The L_2 -norms calculated over the discretized domains \mathcal{S} and \mathcal{D} are defined in the next section.

For 2D TM problems the contrast source and contrast variables are located at the nodes of the imaging domain \mathcal{D} , whereas for 2D TE and 3D full-vectorial problems these variables are defined at the centroids of the elements inside \mathcal{D} , triangular elements in 2D TE and tetrahedra in 3D full-vectorial.

4.2.1 Norms and Inner Products

4.2.1.1 Nodal Variables, Nodal Unknowns

With the unknown variables located at the nodes of a mesh, the L_2 -norm and inner product in \mathcal{D} are calculated as

$$\|\underline{x}\|_{\mathcal{D}}^2 = \underline{x}^H \mathcal{T}_{\mathcal{D}} \underline{x} \quad \text{and} \quad \langle \underline{x}, \underline{y} \rangle_{\mathcal{D}} = \underline{y}^H \mathcal{T}_{\mathcal{D}} \underline{x} \quad (4.7)$$

where \underline{x} and \underline{y} are arbitrary vectors of size I with scalar entities, the superscript H denotes the Hermitian (complex conjugate transpose) and $\mathcal{T}_{\mathcal{D}} \in \mathbb{R}^{I \times I}$ is the mass matrix restricted to nodes lying within the imaging domain \mathcal{D} . The (i,j) th element of $\mathcal{T}_{\mathcal{D}}$ is given by

$$\mathcal{T}_{\mathcal{D}i,j} = \int_{\mathcal{D}} \lambda_i \lambda_j dv. \quad (4.8)$$

Assuming that the receiver locations on a surface \mathcal{S} are distributed uniformly, the L_2 -norm and the inner product on \mathcal{S} are given as

$$\|\underline{x}\|_{\mathcal{S}}^2 = \underline{x}^H \underline{x} \quad \text{and} \quad \langle \underline{x}, \underline{y} \rangle_{\mathcal{S}} = \underline{y}^H \underline{x} \quad (4.9)$$

where \underline{x} and \underline{y} are vectors of size R and have scalar elements.

4.2.1.2 Vector Variables, Centroidal Unknowns

Similar to the case with the unknowns defined at the nodes of the mesh, if the variables are located at the element centroids, the irregularity of the mesh should be accounted for when calculating the norms or inner products within the imaging domain. Let \vec{x} and \vec{y} be complex vectors of size I . The elements of each vector are associated with the centroids of geometries inside the imaging domain \mathcal{D} . Each of these elements is a spatial-vector field with an x -component and y -component in 2D problems and an additional z -component in 3D cases. The L_2 -norm and inner product in \mathcal{D} are calculated as

$$\|\vec{x}\|_{\mathcal{D}}^2 = \vec{x}^H \cdot \mathcal{T}_{\mathcal{D}} \vec{x} \quad \text{and} \quad \langle \vec{x}, \vec{y} \rangle_{\mathcal{D}} = \vec{y}^H \cdot \mathcal{T}_{\mathcal{D}} \vec{x}. \quad (4.10)$$

Here $\mathcal{T}_{\mathcal{D}} \in \mathbb{R}^{I \times I}$ is a diagonal matrix whose entities are the areas of the triangles inside \mathcal{D} for 2D problems, or the volumes of tetrahedra in \mathcal{D} for 3D configurations.

Similarly, let vectors $\underline{\vec{x}}$ and $\underline{\vec{y}}$ consist of spatial-vector field elements measured at equally distributed receiver locations R on \mathcal{S} . Then, the L_2 -norm and inner product on \mathcal{S} are given as

$$\|\underline{\vec{x}}\|_{\mathcal{S}}^2 = \underline{\vec{x}}^H \cdot \underline{\vec{x}} \quad \text{and} \quad \langle \underline{\vec{x}}, \underline{\vec{y}} \rangle_{\mathcal{S}} = \underline{\vec{y}}^H \cdot \underline{\vec{x}}. \quad (4.11)$$

4.2.2 The Contrast Source Variables Update

In CSI [55], the first step is to update contrast source variables $\underline{\vec{w}}_t$ by a conjugate-gradient (CG) method with Polak-Ribière search directions, while assuming the contrast variables $\underline{\chi}$ constant. In the second step, $\underline{\vec{w}}_t$ is assumed constant, and a modified form of the domain-error equation, $\mathcal{F}^{\mathcal{D}}(\underline{\chi}, \underline{\vec{w}}_t)$, is minimized (this second step has a closed form solution). The first update equation in the CSI method is

$$\underline{\vec{w}}_{t,n} = \underline{\vec{w}}_{t,n-1} + \alpha_{t,n} \underline{\vec{d}}_{t,n} \quad (4.12)$$

where subscript n is the iteration number, $\alpha_{t,n}$ is the update step-size and $\underline{\vec{d}}_{t,n}$ are Polak-Ribière search directions. The step-size $\alpha_{t,n}$ is determined as

$$\alpha_{t,n} = \arg \min_{\alpha} \left\{ \mathcal{F}^{\text{CSI}} \left(\underline{\vec{w}}_{t,n-1} + \alpha \underline{\vec{d}}_{t,n}, \underline{\chi}_{n-1} \right) \right\}, \quad (4.13)$$

for which a closed-form expression can be found by introducing $\underline{\vec{w}}_{t,n-1} + \alpha \underline{\vec{d}}_{t,n}, \underline{\chi}_{n-1}$ in (4.4) and setting the derivative with respect to α equal to zero. The result is

$$\alpha_{t,n} = \frac{\eta_{\mathcal{S}} \left\langle \underline{\vec{p}}_{t,n-1}, \underline{\vec{\mathcal{M}}}_{\mathcal{S}} \underline{\vec{\mathcal{L}}}[\underline{\vec{d}}_{t,n}] \right\rangle_{\mathcal{S}} + \eta_{\mathcal{D},n-1} \left\langle \underline{\vec{r}}_{t,n-1}, \underline{\vec{d}}_{n,t} - \underline{\chi}_{n-1} \odot \underline{\vec{\mathcal{M}}}_{\mathcal{D}} \underline{\vec{\mathcal{L}}}[\underline{\vec{d}}_{t,n}] \right\rangle_{\mathcal{D}}}{\eta_{\mathcal{S}} \left\| \underline{\vec{\mathcal{M}}}_{\mathcal{S}} \underline{\vec{\mathcal{L}}}[\underline{\vec{d}}_{t,n}] \right\|_{\mathcal{S}}^2 + \eta_{\mathcal{D},n-1} \left\| \underline{\vec{d}}_{n,t} - \underline{\chi}_{n-1} \odot \underline{\vec{\mathcal{M}}}_{\mathcal{D}} \underline{\vec{\mathcal{L}}}[\underline{\vec{d}}_{t,n}] \right\|_{\mathcal{D}}^2}. \quad (4.14)$$

Here the normalization factors η_S and $\eta_{\mathcal{D},n-1}$ are

$$\eta_S = \left(\sum_t \|\underline{\vec{u}}_t\|_S^2 \right)^{-1},$$

$$\eta_{\mathcal{D},n-1} = \left(\sum_t \left\| \underline{\chi}_{n-1} \odot \underline{\vec{E}}_t^{\text{inc}} \right\|_{\mathcal{D}}^2 \right)^{-1},$$

and the error terms $\underline{\vec{\rho}}_{t,n-1}$ and $\underline{\vec{r}}_{t,n-1}$ are

$$\underline{\vec{\rho}}_{t,n-1} = \underline{\vec{u}}_t - \underline{\vec{\mathcal{M}}}_S \underline{\vec{\mathcal{L}}}[\underline{\vec{w}}_{t,n-1}],$$

$$\underline{\vec{r}}_{t,n-1} = \underline{\chi}_{n-1} \odot \underline{\vec{E}}_t^{\text{inc}} - \underline{\vec{w}}_{t,n-1} + \underline{\chi}_{n-1} \odot \underline{\vec{\mathcal{M}}}_D \underline{\vec{\mathcal{L}}}[\underline{\vec{w}}_{t,n-1}].$$

The Polak-Ribière search directions $\underline{\vec{d}}_{t,n}$ are calculated by the following formula:

$$\underline{\vec{d}}_{t,n} = -\underline{\vec{g}}_{t,n} + \frac{\langle \underline{\vec{g}}_{t,n}, \underline{\vec{g}}_{t,n} - \underline{\vec{g}}_{t,n-1} \rangle_{\mathcal{D}}}{\left\| \underline{\vec{g}}_{t,n-1} \right\|_{\mathcal{D}}^2} \underline{\vec{d}}_{t,n-1} \quad (4.15)$$

where $\underline{\vec{g}}_{t,n}$ is the gradient of the cost function $\mathcal{F}^{\text{CSI}}(\underline{\chi}, \underline{\vec{w}}_t)$ with respect to the contrast sources $\underline{\vec{w}}_{t,n}$ and is given by

$$\underline{\vec{g}}_{t,n} = \underline{\vec{\mathcal{G}}}_S \cdot \underline{\vec{\rho}}_{t,n-1} + \underline{\vec{\mathcal{G}}}_D \cdot \underline{\vec{r}}_{t,n-1}. \quad (4.16)$$

Here the adjoint operators $\underline{\vec{\mathcal{G}}}_S$ and $\underline{\vec{\mathcal{G}}}_D$ are dyadic tensors whose elements (dyads) are dependent on the problem configuration being solved. The dyadic tensors expressions for each considered configuration is outlined next, with the full derivation of these expressions presented in Appendix C.

4.2.2.1 Case 1: 2D TM

For a 2D TM inversion problem, the electric field is assumed to be z -polarized with no transverse components in the $x - y$ plane. Therefore, the measured scattered field and the error terms have each only a z -component and are given as

$$\vec{u}_t = u_{t,z} \hat{z}, \quad \vec{\rho}_t = \rho_{t,z} \hat{z} \quad \text{and} \quad \vec{r}_t = r_{t,z} \hat{z}. \quad (4.17)$$

Further, the dyadic tensors, $\bar{\bar{\mathcal{G}}}_S$ and $\bar{\bar{\mathcal{G}}}_D$, have only one component each and are written as

$$\bar{\bar{\mathcal{G}}}_S = \mathcal{G}_{S,zz} \hat{z} \hat{z} \quad \text{and} \quad \bar{\bar{\mathcal{G}}}_D = \mathcal{G}_{D,zz} \hat{z} \hat{z} \quad (4.18)$$

where

$$\begin{aligned} \mathcal{G}_{S,zz} &= -2\eta_S \mathcal{T}_D^{-1} \mathcal{L}_z^H \mathcal{M}_{S,z}^H \\ \mathcal{G}_{D,zz} &= -2\eta_{D,n-1} \mathcal{T}_D^{-1} (\mathcal{I} - \mathcal{L}_z^H \mathcal{M}_{D,z}^H \mathcal{X}_{n-1}) \mathcal{T}_D. \end{aligned} \quad (4.19)$$

Here $\mathcal{I} \in \mathbb{R}^{I \times I}$ is an identity matrix and $\mathcal{X}_{n-1} = \text{diag}(\underline{\chi}_{n-1})$ is a diagonal matrix.

4.2.2.2 Case 2: 2D TE

In a 2D TE case the electric field is assumed to be polarized in the $x - y$ plane with no longitudinal component in the z -direction. Thus, the measured fields and

error terms are spatial vectors with two components each and are given as

$$\begin{aligned}
\vec{u}_t &= \underline{u}_{t,x} \hat{x} + \underline{u}_{t,y} \hat{y} \\
\vec{\rho}_t &= \underline{\rho}_{t,x} \hat{x} + \underline{\rho}_{t,y} \hat{y} \\
\vec{r}_t &= \underline{r}_{t,x} \hat{x} + \underline{r}_{t,y} \hat{y}.
\end{aligned} \tag{4.20}$$

The dyadic tensors used in calculating the gradient, $\underline{\underline{g}}_t$, are evaluated as

$$\begin{aligned}
\bar{\bar{\mathcal{G}}}_S &= \mathcal{G}_{S,xx} \hat{x} \hat{x} + \mathcal{G}_{S,yx} \hat{y} \hat{x} + \mathcal{G}_{S,xy} \hat{x} \hat{y} + \mathcal{G}_{S,yy} \hat{y} \hat{y} \\
\bar{\bar{\mathcal{G}}}_D &= \mathcal{G}_{D,xx} \hat{x} \hat{x} + \mathcal{G}_{D,yx} \hat{y} \hat{x} + \mathcal{G}_{D,xy} \hat{x} \hat{y} + \mathcal{G}_{D,yy} \hat{y} \hat{y}
\end{aligned}$$

where each term is given by

$$\begin{aligned}
\mathcal{G}_{S,xx} &= -2\eta_S \mathcal{T}_D^{-1} \mathcal{L}_x^H \mathcal{M}_{S,x}^H & \mathcal{G}_{S,xy} &= -2\eta^S \mathcal{T}_D^{-1} \mathcal{L}_x^H \mathcal{M}_{S,y}^H \\
\mathcal{G}_{S,yx} &= -2\eta_S \mathcal{T}_D^{-1} \mathcal{L}_y^H \mathcal{M}_{S,x}^H & \mathcal{G}_{S,yy} &= -2\eta^S \mathcal{T}_D^{-1} \mathcal{L}_y^H \mathcal{M}_{S,y}^H,
\end{aligned} \tag{4.21}$$

and

$$\begin{aligned}
\mathcal{G}_{D,xx} &= -2\eta_{D,n-1} \mathcal{T}_D^{-1} (\mathcal{I} - \mathcal{L}_x^H \mathcal{M}_{D,x}^H \mathcal{X}_{n-1}^H) \mathcal{T}_D \\
\mathcal{G}_{D,xy} &= 2\eta_{D,n-1} \mathcal{T}_D^{-1} \mathcal{L}_x^H \mathcal{M}_{D,y}^H \mathcal{X}_{n-1}^H \mathcal{T}_D \\
\mathcal{G}_{D,yx} &= 2\eta_{D,n-1} \mathcal{T}_D^{-1} \mathcal{L}_y^H \mathcal{M}_{D,x}^H \mathcal{X}_{n-1}^H \mathcal{T}_D \\
\mathcal{G}_{D,yy} &= -2\eta_{D,n-1} \mathcal{T}_D^{-1} (\mathcal{I} - \mathcal{L}_y^H \mathcal{M}_{D,y}^H \mathcal{X}_{n-1}^H) \mathcal{T}_D.
\end{aligned} \tag{4.22}$$

4.2.2.3 Case 3: 3D Full-Vectorial

For a 3D full-vectorial problem, there are three electric field components polarized along the x -, y -, and z - directions. Moreover, the measured field and error terms

are given as

$$\begin{aligned}
\vec{u}_t &= \underline{u}_{t,x} \hat{x} + \underline{u}_{t,y} \hat{y} + \underline{u}_{t,z} \hat{z} \\
\vec{\rho}_t &= \underline{\rho}_{t,x} \hat{x} + \underline{\rho}_{t,y} \hat{y} + \underline{\rho}_{t,z} \\
\vec{r}_t &= \underline{r}_{t,x} \hat{x} + \underline{r}_{t,y} \hat{y} + \underline{r}_{t,z} \hat{z}.
\end{aligned} \tag{4.23}$$

The dyadic tensors, $\bar{\bar{\mathcal{G}}}_S$ and $\bar{\bar{\mathcal{G}}}_D$ are written as

$$\begin{aligned}
\bar{\bar{\mathcal{G}}}_S &= \mathcal{G}_{S,xx} \hat{x} \hat{x} + \mathcal{G}_{S,yx} \hat{y} \hat{x} + \mathcal{G}_{S,zx} \hat{z} \hat{x} + \\
&\quad \mathcal{G}_{S,xy} \hat{x} \hat{y} + \mathcal{G}_{S,yy} \hat{y} \hat{y} + \mathcal{G}_{S,zy} \hat{z} \hat{y} + \\
&\quad \mathcal{G}_{S,xz} \hat{x} \hat{z} + \mathcal{G}_{S,yz} \hat{y} \hat{z} + \mathcal{G}_{S,zz} \hat{z} \hat{z}
\end{aligned} \tag{4.24}$$

and

$$\begin{aligned}
\bar{\bar{\mathcal{G}}}_{D,n-1} &= \mathcal{G}_{D,n-1,xx} \hat{x} \hat{x} + \mathcal{G}_{D,n-1,yx} \hat{y} \hat{x} + \mathcal{G}_{D,n-1,zx} \hat{z} \hat{x} + \\
&\quad \mathcal{G}_{D,n-1,xy} \hat{x} \hat{y} + \mathcal{G}_{D,n-1,yy} \hat{y} \hat{y} + \mathcal{G}_{D,n-1,zy} \hat{z} \hat{y} + \\
&\quad \mathcal{G}_{D,n-1,xz} \hat{x} \hat{z} + \mathcal{G}_{D,n-1,yz} \hat{y} \hat{z} + \mathcal{G}_{D,n-1,zz} \hat{z} \hat{z}
\end{aligned} \tag{4.25}$$

where each term is given by

$$\mathcal{G}_{S,uv} = -2\eta_S \mathcal{T}_D^{-1} (\mathcal{L}_u^H \mathcal{M}_{S,v}^H) \tag{4.26}$$

and

$$\mathcal{G}_{D,n-1,uv} = \begin{cases} -2\eta_{D,n-1} \mathcal{T}_D^{-1} (\mathcal{I} - \mathcal{L}_u^H \mathcal{M}_{D,v}^H \mathcal{X}_{n-1}^H) \mathcal{T}_D & \text{for } u = v \\ 2\eta_{D,n-1} \mathcal{T}_D^{-1} \mathcal{L}_u^H \mathcal{M}_{D,v}^H \mathcal{X}_{n-1}^H \mathcal{T}_D & \text{for } u \neq v. \end{cases} \tag{4.27}$$

Here subscripts u, v are selected to represent either x, y or z .

4.2.3 The Contrast Variables Update

After updating the contrast source variables, $\underline{\chi}$ is evaluated by minimizing the modified domain equation $\mathcal{F}_m^{\mathcal{D}}(\underline{\chi})$ given by

$$\begin{aligned}\mathcal{F}_m^{\mathcal{D}}(\underline{\chi}) &= \sum_t \left\| \underline{\chi} \odot \vec{E}_t^{\text{inc}} - \vec{w}_t + \underline{\chi} \odot \vec{\mathcal{M}}_{\mathcal{D}} \vec{\mathcal{L}}[\vec{w}_t] \right\|_{\mathcal{D}}^2 \\ &= \sum_t \left\| \underline{\chi} \odot \vec{E}_t - \vec{w}_t \right\|_{\mathcal{D}}^2.\end{aligned}\tag{4.28}$$

Here the total field vector $\vec{E}_t = \vec{E}_t^{\text{inc}} + \vec{\mathcal{M}}_{\mathcal{D}} \vec{\mathcal{L}}[\vec{w}_t]$. The contrast source variables \vec{w}_t are assumed constant in this minimization.

The derivation of the minimizer can be simplified by introducing a diagonal matrix $\vec{\mathcal{E}}_t \in \mathbb{C}^{I \times I}$ whose diagonal entities are the elements of vector \vec{E}_t ; the diagonal matrix replaces the Hadamard element-wise product, thus the modified domain equation can be rewritten as

$$\mathcal{F}_m^{\mathcal{D}}(\underline{\chi}) = \sum_t \left\| \vec{\mathcal{E}}_t \underline{\chi} - \vec{w}_t \right\|_{\mathcal{D}}^2.\tag{4.29}$$

As derived in Appendix D, at the n^{th} iteration, the minimizer for $\mathcal{F}_m^{\mathcal{D}}(\underline{\chi})$ requires then the solution of the following sparse matrix equation for $\underline{\chi}_n$:

$$\left(\sum_t \vec{\mathcal{E}}_{t,n}^H \cdot \mathcal{T}_{\mathcal{D}} \vec{\mathcal{E}}_{t,n} \right) \underline{\chi}_n = \sum_t \vec{\mathcal{E}}_{t,n}^H \cdot \mathcal{T}_{\mathcal{D}} \vec{w}_{t,n}.\tag{4.30}$$

Since $\vec{\mathcal{E}}_{t,n}$ is a diagonal matrix and $\mathcal{T}_{\mathcal{D}}$ is sparse, the minimizer $\underline{\chi}_n$ can be calculated efficiently.

4.2.4 Initializing the Algorithm

The initial guess of the contrast source variables cannot be set to zero since the cost functional is undefined for a zero contrast source. As in the standard CSI algorithm, the initial guess for the FEM-CSI is evaluated by calculating the contrast source variables that will minimize the data-error equation, $\mathcal{F}^S(\underline{\vec{w}}_t)$. This minimizer is taken to be the result of applying the method of steepest descent to $\mathcal{F}^S(\underline{\vec{w}}_t)$. As shown in Appendix E, this initial guess can be given in closed-form as

$$\underline{\vec{w}}_{t,0} = \frac{\text{Re} \left\langle \vec{\mathcal{M}}_S \vec{\mathcal{L}}[\vec{\mathcal{G}}_S \cdot \underline{\vec{u}}_t], \vec{f}_t \right\rangle_S \vec{\mathcal{G}}_S \cdot \underline{\vec{u}}_t}{\left\| \vec{\mathcal{M}}_S \vec{\mathcal{L}}[\vec{\mathcal{G}}_S \cdot \underline{\vec{u}}_t] \right\|_S^2} \quad (4.31)$$

After evaluating $\underline{\vec{w}}_{t,0}$, the initial guess for the contrast variables $\underline{\chi}$ is calculated using (4.30) and the initial Polak-Ribière search directions $\vec{d}_{t,0}$ are set to zero.

5

Multiplicative Regularization

We come now to the question: what is a priori certain or necessary, respectively in geometry (doctrine of space) or its foundations? Formerly we thought everything; nowadays we think nothing. Already the distance-concept is logically arbitrary; there need be no things that correspond to it, even approximately.

–Albert Einstein

Microwave imaging inverse problems exhibit two properties: nonlinearity and ill-posedness. The nonlinearity of the problem is tackled using various optimization algorithms, while several regularization techniques are used to account for the ill-posedness.

Different regularization methods have been reported in the literature and have been successfully applied for various applications [12]. A successful regularization technique which has been used is the weighted L_2 -norm total variation multiplicative regularization (MR), which has been incorporated into both GNI and CSI [3, 12, 28, 32, 56, 78, 80, 81]. Not only has it been shown to enhance the outcome of the inversion algorithm, *i.e.* regularize the optimization, but it also has other desirable features: (i) its edge-preserving characteristic, and (ii) its capacity for suppressing noise in measured data.

Multiplicative regularization is formulated in the continuous domain and must be discretized for application. In the first part of this chapter, a novel technique for incorporating multiplicative regularization in the FEM-CSI algorithm is introduced. In typical MR-CSI inversion algorithms that have been developed previously the unknowns are located on a uniform grid of either rectangular cells (in 2D configurations) or cuboids (in 3D problems). In such methods, finite-difference approximations for the gradient and divergence operators used in multiplicative regularization can be easily applied. As we have seen, when FEM is used to discretize the electromagnetic field problem, the unknown variables are located on either the nodes of an irregular mesh or the centroids of elements (triangles in 2D, tetrahedra in 3D); thus applying MR using finite-differences becomes difficult. In this chapter new techniques are introduced to perform the gradient and divergence operators on a triangular or a tetrahedral mesh.

In the second part of this chapter, an improvement to the multiplicative regularization applied to CSI is proposed. The enhancement accounts for the imbalance between the real and imaginary components of the OI's contrast that can occur in some MWI applications, *e.g.* biomedical imaging [82]. The proposed method retains the advantages of MR-CSI, in addition to improving the reconstruction of the imaginary part of the OI. The scaling factor defined in the balanced multiplicative regularization (BMR) is dependent on the ratio of the real to the imaginary components' magnitude of the OI's relative permittivity. The balanced multiplicative regularization can be applied to either CSI formulations based on integral-equations [20, 80] or other forms that result from the direct discretization of the partial differential equations (PDE) associated with MWI [29, 32, 78]. Herein, BMR is applied to FEM-CSI [83].

5.1 Multiplicatively Regularized FEM-CSI

The CSI inversion results may be significantly enhanced through the use of a total-variation based regularizer [3, 7, 56, 80, 84, 85]. In general, the total variation (TV) regularization attempts to penalize contrasts which have a large total variation, *i.e.* when there is significant variation from pixel to pixel in the inversion domain. For a differentiable function h the total-variation is defined as,

$$\text{TV}(h(\vec{r})) = \int_{\mathcal{D}} |\nabla h(\vec{r})| dv \quad (5.1)$$

where ∇ is the spatial gradient operator and $\vec{r} \in \mathcal{D}$.

Total-variation based regularizers were first introduced to image processing to correct for the presence of noise in the images [86]. Inspired by their success, TV regularizers were adapted to CSI in different forms [56, 80]. Initially, these regularizers were tested as an additive regularizer [56], but this required the choice of a parameter used to balance the effect of the total-variation term and the regular CSI cost functional (4.1). The parameter selection process may be avoided by applying the total-variation based regularizer as a multiplicative term [80]. Different multiplicative regularizers have been tested and evaluated for the CSI method [80]. The weighted L_2 -norm total variation multiplicative regularizer (MR) had the best performance amongst all the different implementations.

With the MR term, the cost functional at the n^{th} iteration becomes

$$\mathcal{C}_n(\chi, \vec{w}_t) = \mathcal{C}_n^{\text{MR}}(\chi) \times \mathcal{C}^{\text{CSI}}(\chi, \vec{w}_t) \quad (5.2)$$

where the regularization term $\mathcal{C}_n^{\text{MR}}(\chi)$ is given by

$$\mathcal{C}_n^{\text{MR}}(\chi) = \int_{\mathcal{D}} b_n^2(\vec{r}) (|\nabla \chi(\vec{r})|^2 + \delta_n^2) dv. \quad (5.3)$$

Here

$$b_n(\vec{r}) = (V (|\nabla \chi_{n-1}(\vec{r})|^2 + \delta_n^2))^{-1/2} \quad (5.4)$$

where $V = \int_{\mathcal{D}} dv$, χ_n^{CSI} is the CSI update of the contrast variable at the n^{th} iteration, and $\delta_n^2 = \mathcal{C}^{\mathcal{D}}(\chi_n^{\text{CSI}}, w_{t,n}) \bar{A}^{-1}$ is the steering factor for the MR term in which \bar{A} is the mean area of inversion pixel facets in imaging domain \mathcal{D} .

The discretized form of the continuous functional in MR-FEMCSI is

$$\mathcal{F}_n(\underline{\chi}, \underline{\vec{w}}_t) = \mathcal{F}_n^{\text{MR}}(\underline{\chi}) \times \mathcal{F}^{\text{CSI}}(\underline{\chi}, \underline{\vec{w}}_t) \quad (5.5)$$

where the regularization term $\mathcal{F}_n^{\text{MR}}(\underline{\chi})$ is given by

$$\mathcal{F}_n^{\text{MR}}(\underline{\chi}) = \|\underline{b}_n \odot \nabla \underline{\chi}\|_{\mathcal{D}}^2 + \delta_n^2 \|\underline{b}_n\|_{\mathcal{D}}^2. \quad (5.6)$$

Here

$$\underline{b}_n = \left(V \left(|\nabla \underline{\chi}_n^{\text{CSI}}|^2 + \delta_n^2 \right) \right)^{-1/2} \quad \text{and} \quad \delta_n^2 = \mathcal{F}^{\mathcal{D}}(\underline{\chi}_n^{\text{CSI}}, \underline{\vec{w}}_{t,n}) \bar{A}^{-1} \quad (5.7)$$

where $\underline{\chi}_n^{\text{CSI}}$ is the CSI update of the contrast variable at the n^{th} iteration. For 2D problems, V is the total area of domain \mathcal{D} and \bar{A} is the mean area of mesh triangles; for 3D configurations, V is the total volume of the domain \mathcal{D} and \bar{A} is the mean area of the tetrahedral facets in \mathcal{D} .

The spatial gradient operator, ∇ , is a matrix operator that returns the compo-

nents of the gradient calculated at either the nodes or the centroids of the elements within \mathcal{D} , depending on the location of the contrast vector, $\underline{\chi}$, entries. If the vector $\underline{\chi}$ elements are defined on the nodes of an irregular mesh, the gradient operator ∇ returns the spatial gradient at the centroids of the elements within the imaging domain \mathcal{D} . On the other hand, if $\underline{\chi}$ values are located on the centroids of the mesh elements, the gradient matrix operator ∇ returns the components of the spatial gradient at the nodes within the imaging domain. The calculations performed by the gradient operator for either 2D or 3D problems will be detailed in the next section.

Next, let $\underline{\mathcal{X}}$ be an arbitrary data vector where each of its elements is a spatial-vector field with x and y components in 2D and an additional z -component in 3D. The operation $|\underline{\mathcal{X}}|^2$ used in (5.7) (and later on) returns a vector of the same size as $\underline{\mathcal{X}}$ but with scalar entries. The i^{th} value of the resulting vector is

$$|\underline{\mathcal{X}}_i|^2 = |\mathcal{X}_{x,i}|^2 + |\mathcal{X}_{y,i}|^2 \quad (5.8)$$

for 2D and

$$|\underline{\mathcal{X}}_i|^2 = |\mathcal{X}_{x,i}|^2 + |\mathcal{X}_{y,i}|^2 + |\mathcal{X}_{z,i}|^2 \quad (5.9)$$

for 3D. Here the subscripts x , y and z indicate the spatial components of element i .

5.1.1 Updating the Contrast Variables

Since $\mathcal{F}_n^{\text{MR}}(\underline{\chi}_n^{\text{CSI}}) = 1$, the update procedure for the contrast source variables \underline{w}_t remains unchanged; however, this is not the case for the contrast variables $\underline{\chi}$. After calculating the contrast variables using FEM-CSI, they are updated by a CG method using Polak-Ribière search directions \underline{d}_n^{χ} as follows:

$$\underline{\chi}_n = \underline{\chi}_n^{\text{CSI}} + \alpha_n^{\chi} \underline{d}_n^{\chi}. \quad (5.10)$$

Here $\underline{\chi}_n^{\text{CSI}}$ is the update from the CSI algorithm (4.30) and α_n^{χ} is an update step-size.

The search directions \underline{d}_n^{χ} are calculated as

$$\underline{d}_n^{\chi} = -\underline{g}_n^{\chi} + \frac{\langle \underline{g}_n^{\chi}, \underline{g}_n^{\chi} - \underline{g}_{n-1}^{\chi} \rangle_{\mathcal{D}}}{\|\underline{g}_{n-1}^{\chi}\|_{\mathcal{D}}^2} \underline{d}_{n-1}^{\chi} \quad (5.11)$$

where \underline{g}_n^{χ} is the preconditioned gradient of $\mathcal{F}_n(\underline{\chi}, \vec{w}_t)$ with respect $\underline{\chi}$ [32, 80], as is now explained.

For MR-FEMCSI, the gradient \underline{g}_n^{χ} evaluated at $\underline{\chi} = \underline{\chi}_n^{\text{CSI}}$ is

$$\underline{g}_n^{\chi} = \left(\underline{g}_{\text{MR},n}^{\chi} \times \mathcal{F}^{\text{CSI}}(\underline{\chi}_n^{\text{CSI}}, \vec{w}_{t,n}) + \underline{g}_{\mathcal{D},n}^{\chi} \times \mathcal{F}^{\text{MR}}(\underline{\chi}_n^{\text{CSI}}) \right) \odot \underline{P}_n \quad (5.12)$$

where $\underline{g}_{\text{MR},n}^{\chi}$ and $\underline{g}_{\mathcal{D},n}^{\chi}$ are, respectively, the gradients of the MR term and the CSI cost functional with respect to the contrast $\underline{\chi}$ at the n^{th} iteration and are calculated as (see Appendix F for derivation details),

$$\begin{aligned} \underline{g}_{\text{MR},n}^{\chi} &= -2\nabla \cdot \left(\underline{b}_n^2 \odot \nabla \chi_n^{\text{CSI}} \right) \\ \underline{g}_{\mathcal{D},n}^{\chi} &= 2\eta_{\mathcal{D},n-1} \sum_t \mathcal{T}_{\mathcal{D}}^{-1} \vec{\mathcal{E}}_{t,n}^H \cdot \mathcal{T}_{\mathcal{D}} \vec{\mathcal{L}}_{t,n}. \end{aligned} \quad (5.13)$$

The divergence operator, $\nabla \cdot$, in $\underline{g}_{\text{MR},n}^{\chi}$ is a matrix operator that takes the result of $(\underline{b}_n^2 \odot \nabla \chi_n)$ and returns the spatial divergence calculated within the imaging domain \mathcal{D} . If $\underline{\chi}$ elements are defined on the nodes, the vector $(\underline{b}_n^2 \odot \nabla \chi_n)$ has its entries on the elemental centroids in \mathcal{D} and further the result of the divergence operator $\nabla \cdot$ is returned on the nodes within \mathcal{D} . Similarly, if $\underline{\chi}$ entries are located on the centroids,

the vector $(\underline{b}_n^2 \odot \nabla \chi_n)$ elements are evaluated on the nodes and eventually the result of matrix operator $\nabla \cdot$ is calculated at the centroids of elements in \mathcal{D} . The evaluations performed by the divergence operator will be discussed in the next section.

The preconditioner in (5.12) is calculated as $\underline{P}_n = \left(\sum_t |\vec{E}_{t,n}|^2 \right)^{-1}$ where $\vec{E}_{t,n} \triangleq \vec{E}_t^{\text{inc}} + \vec{\mathcal{M}}_{\mathcal{D}} \vec{\mathcal{L}}[\vec{w}_{t,n}]$ is the total field for transmitter t ; the notation $|\cdot|^2$ is explained towards the end of Section 5.1. In equation (5.13), $\vec{\mathcal{E}}_{t,n}$ and $\vec{r}_{t,n}$ are the total field diagonal matrix and the residual of the domain-error equation respectively given as,

$$\begin{aligned} \vec{\mathcal{E}}_{t,n} &= \text{diag}(\vec{E}_{t,n}) \\ \vec{r}_{t,n} &= \vec{\mathcal{E}}_{t,n} \underline{\chi}_n^{\text{CSI}} - \vec{w}_{t,n}. \end{aligned} \quad (5.14)$$

Due to the fact that the $\underline{\chi}_n^{\text{CSI}}$ is a minimizer of a modified form of the domain-error equation $\mathcal{F}^{\mathcal{D}}$ (see Section 4.2.3), the gradient \underline{g}_n^{χ} evaluated at $\underline{\chi} = \underline{\chi}_n^{\text{CSI}}$ vanishes to zero. Thus, the gradient expression (5.12) can be simplified to

$$\underline{g}_n^{\chi} = \left(-2 \nabla \cdot \left(\underline{b}_n^2 \odot \nabla \underline{\chi}_n^{\text{CSI}} \right) \times \mathcal{F}^{\text{CSI}}(\underline{\chi}_n^{\text{CSI}}, \vec{w}_{t,n}) \right) \odot \underline{P}_n. \quad (5.15)$$

The update step-size, α_n^{χ} , is calculated analytically as

$$\alpha_n^{\chi} = \arg \min_{\alpha^{\chi}} \left\{ \mathcal{F}_n \left(\vec{w}_{t,n}, \underline{\chi}_n^{\text{CSI}} + \alpha^{\chi} \underline{d}_n^{\chi} \right) \right\} \quad (5.16)$$

which involves finding the roots of a cubic polynomial. As outlined in Appendix G, this yields one real root along with a complex-conjugate pair; the real root is taken as the step-size [56, 80].

5.2 Spatial Derivatives on Arbitrary Meshes

Accurate evaluation of the spatial gradient and divergence of the contrast at the unknown locations of an arbitrary mesh, required in (5.6) and (5.15), is not as straightforward as when using a uniform rectangular grid.

For 2D TM problems, the contrast variables are defined at nodal locations of an arbitrary triangular FEM mesh. The unknown contrast is represented using linear basis functions with a gradient which is constant over each triangle and is discontinuous between triangles. The divergence of the gradient at each node is not easily defined. If quadratic elements are used, the gradient would be a linear function over each element but the divergence would still be discontinuous between elements. Therefore, some form of averaging is required.

For 2D TE cases, the contrast variables are located at the centroids of the mesh triangular elements. Similarly, for 3D full-vectorial problems the contrast variables are positioned at the centroids of the mesh tetrahedra. In both cases the contrast is discontinuous between elements, hence the gradient and divergence calculations are indirect and specially tailored techniques have to be devised to calculate them.

For each problem configuration, methods that combine the use of first-order linear basis functions within an FEM element and the creation of a *dual-mesh* to perform some form of averaging over a defined stencil have been created to evaluate the spatial gradient and divergence. These techniques are outlined next.

5.2.1 Case 1: 2D TM

For 2D TM cases the contrast variables are located at the nodes of the triangular mesh and are represented using linear basis functions. Consequently, the spatial

gradient of the contrast can be calculated numerically over each triangle in the mesh using the first-order basis functions. In FEM, the contrast within a triangle e at the n^{th} iteration is given by

$$\chi_n^e(\vec{r}) = \sum_{l=1}^3 \chi_{l,n}^e \lambda_l^e(\vec{r}) \quad (5.17)$$

where l is a local index for each node on triangle e , $\chi_{l,n}^e$ is the contrast value at node l of triangle e , and the first-order linear basis function for node l is

$$\lambda_l^e(\vec{r}) = \frac{1}{2A^e} (a_l^e + b_l^e x + c_l^e y). \quad (5.18)$$

Here A^e is the area of triangle e and the coefficients a_l^e , b_l^e and c_l^e are dependent only on the triangle geometry [44].

The spatial gradient of the contrast within triangle e is then calculated as

$$\begin{aligned} \nabla \chi_n^e &= \sum_{l=1}^3 \chi_{l,n}^e \nabla \lambda_l^e(\vec{r}) \\ &= \frac{1}{2A^e} \sum_{l=1}^3 \chi_{l,n}^e (b_l^e \hat{x} + c_l^e \hat{y}) \end{aligned} \quad (5.19)$$

where \hat{x} and \hat{y} are the Cartesian unit vectors.

The spatial gradient in (5.19) is also used to calculate the coefficients b_n^2 for each triangle in \mathcal{D} and then to evaluate the multiplicative regularization term $\mathcal{F}_n^{\text{MR}}(\underline{\chi})$.

To update the contrast variables $\underline{\chi}$, the gradient \underline{g}_n^{χ} has to be evaluated at each node in \mathcal{D} . For each node i let us define $\zeta_{i,n}$ as follows:

$$\begin{aligned} \zeta_{i,n} &= \nabla \cdot \vec{\xi}_{i,n} \\ &= \nabla \cdot (\xi_{i,n}^x \hat{x} + \xi_{i,n}^y \hat{y}) \\ &= \hat{x} \cdot \nabla \xi_{i,n}^x + \hat{y} \cdot \nabla \xi_{i,n}^y \end{aligned} \quad (5.20)$$

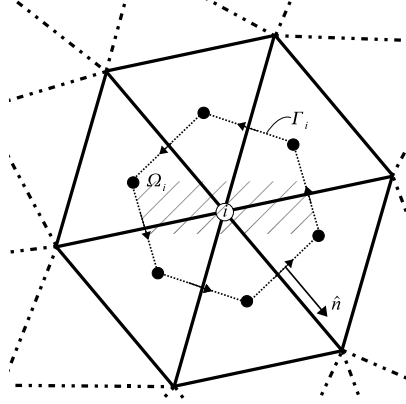


Figure 5.1: Region surrounding node i to approximate the spatial derivatives. The “•” in the diagram represents the centroid of a triangle.

where $\vec{\xi}_{i,n} = b_{i,n}^2 \nabla \chi_{i,n}$. Since b_n^2 and $\nabla \chi_n$ are calculated for each triangle rather than each node, the spatial divergence for each node in (5.20) needs to be approximated.

Let us define a region Ω_i around node i as depicted in figure 5.1. The vertices of this region are the centroids of triangles sharing node i . Using the divergence theorem, it can be shown that

$$\begin{aligned} \hat{x} \cdot \nabla \xi_{i,n}^x &\approx \langle \hat{x} \cdot \nabla \xi_n^x(\vec{r}) \rangle_{\Omega_i} \\ &= \frac{1}{A_i} \oint_{\Gamma_i} \xi_n^x(\vec{r}) \hat{x} \cdot \hat{n} ds \end{aligned} \quad (5.21)$$

where $\langle \cdot \rangle_{\Omega_i}$ denotes the average value over region Ω_i , A_i is the area of Ω_i , Γ_i is the boundary of Ω_i and \hat{n} is outward normal vector to Γ_i .

Similarly the second term in (5.20) is approximated as

$$\hat{y} \cdot \nabla \xi_{i,n}^y \approx \frac{1}{A_i} \oint_{\Gamma_i} \xi_n^y(\vec{r}) \hat{y} \cdot \hat{n} ds. \quad (5.22)$$

Since the values of $\xi_n(\vec{r})$ are known at the vertices of region Ω_i , the line integrals

in (5.21) and (5.22) can be easily evaluated numerically. Here the trapezoidal rule is used to calculate the integral over each segment in region Ω_i .

5.2.2 Case 2: 2D TE

The contrast variables are located on the mesh triangle centroids for 2D TE problems and they are discontinuous across elements; hence an averaging scheme similar to the one used to approximate the divergence for 2D TM problems is required to calculate the spatial gradient. The required gradient is approximated at each node in the mesh using the same dual-mesh scheme as for the 2D TM case depicted in Figure 5.1. Using (5.21) and (5.22) at a node i , the x -component of the gradient can be approximated as

$$\frac{\partial \chi_{i,n}}{\partial x} = \hat{x} \cdot \nabla \chi_{i,n} = \frac{1}{A_i} \oint_{\Gamma_i} \chi_n(\vec{r}) \hat{x} \cdot \hat{n} ds \quad (5.23)$$

and the y -component as

$$\frac{\partial \chi_{i,n}}{\partial y} = \hat{y} \cdot \nabla \chi_{i,n} = \frac{1}{A_i} \oint_{\Gamma_i} \chi_n(\vec{r}) \hat{y} \cdot \hat{n} ds. \quad (5.24)$$

With the spatial gradient values approximated at the nodes, the coefficients b_n^2 can be calculated for each node in imaging domain \mathcal{D} and thus the MR term $\mathcal{F}^{\text{MR}}(\underline{\chi})$ can be evaluated.

Next, the calculation of the divergence of $b_n^2 \nabla \chi$ at the centroid of each triangle in \mathcal{D} is done with the aid of the FEM first-order basis functions. For a triangle e let

$$\xi_n^e = \sum_{l=1}^3 (\xi_{x,l,n}^e \hat{x} + \xi_{y,l,n}^e \hat{y}) \lambda_l^e(\vec{r}) \quad (5.25)$$

where for a node l in triangle e

$$\xi_{x,l,n}^e = (b_{n,l}^e)^2 \frac{\partial \chi_{l,n}^e}{\partial x} \quad , \quad \xi_{y,l,n}^e = (b_{n,l}^e)^2 \frac{\partial \chi_{l,n}^e}{\partial y} \quad (5.26)$$

and λ_l^e is the basis function given in (5.18). The divergence of $b_n^2 \nabla \chi$ calculated at the centroid of triangle e is

$$\begin{aligned} (\nabla \cdot b_n^2 \nabla \chi)_n^e &= \frac{\partial \xi_n^e}{\partial x} \cdot \hat{x} + \frac{\partial \xi_n^e}{\partial y} \cdot \hat{y} \\ &= \frac{1}{2A^e} \sum_{l=1}^3 (\xi_{x,l,n}^e b_l^e + \xi_{y,l,n}^e c_l^e) . \end{aligned} \quad (5.27)$$

The values of $\xi_{x,l,n}^e$ and $\xi_{y,l,n}^e$ have been evaluated already using the dual-mesh scheme at the nodes of the imaging domain, thus expression (5.27) is a straightforward calculation. Thus, the gradient $\underline{g}_{\text{MR},n}^x$ needed in (5.12) to update the contrast variables χ can be readily obtained.

5.2.3 Case 3: 3D Full-Vectorial

The techniques to calculate the spatial gradient and divergence for 3D problems are very similar to those utilized for 2D TE configurations, as the contrast variables are defined at the centroids of the mesh tetrahedra. First, the gradient is approximated at the nodes of the imaging domain \mathcal{D} using a 3D dual-mesh technique analogous to the 2D scheme presented in figure 5.1. For 3D problems, the region Ω_i is a volume surrounding node i . The surface of volume Ω_i is constructed of triangular patches whose vertices are the centroids of tetrahedra sharing the node.

Let ζ represent a space-component in the Cartesian coordinates (either x , y or z).

For a node i , the ζ -component of the spatial gradient can be approximated as

$$\begin{aligned} \frac{\partial \chi_{i,n}}{\partial \zeta} &= \hat{\zeta} \cdot \nabla \chi_{i,n} \\ &\approx \left\langle \hat{\zeta} \cdot \nabla \chi_n(\vec{r}) \right\rangle_{\Omega_i} \\ &= \frac{1}{V_i} \oint_{\Gamma_i} \chi_n(\vec{r}) \hat{\zeta} \cdot \hat{n} \, ds \end{aligned} \quad (5.28)$$

where $\hat{\zeta}$ is a constant unit vector, $\langle \cdot \rangle_{\Omega_i}$ denotes the average value over the volumetric region Ω_i , V_i is the volume of Ω_i , Γ_i is the contour (surface) of Ω_i and \hat{n} is outward normal vector to Γ_i . As the $\chi_n(\vec{r})$ values are known at the vertices of surface Γ_i , the integration in (5.28) can be performed numerically.

After approximating the spatial gradients at the nodes of \mathcal{D} , the coefficients b_n^2 are calculated and the value of the MR term $\mathcal{F}^{\text{MR}}(\underline{\chi})$ at the n^{th} iteration is evaluated.

The next step is to calculate the divergence at the centroid of each tetrahedral so as to evaluate the search directions \underline{g}_n^x . The 3D FEM scalar first-order linear basis functions defined within a tetrahedron element are used. For a given tetrahedral e let

$$\xi_n^e = \sum_{l=1}^4 (\xi_{x,l,n}^e \hat{x} + \xi_{y,l,n}^e \hat{y} + \xi_{z,l,n}^e \hat{z}) \lambda_l^e(\vec{r}) \quad (5.29)$$

where for a node l in tetrahedral e

$$\xi_{\zeta,l,n}^e = (b_{n,l}^e)^2 \frac{\partial \chi_{l,n}^e}{\partial \zeta} \quad (5.30)$$

for any Cartesian component ζ , and λ_l^e is a 3D scalar linear basis function given as

$$\lambda_l^e(\vec{r}) = \frac{1}{6V_e} (a_l^e + b_l^e x + c_l^e y + d_l^e z). \quad (5.31)$$

Here V^e is the volume of element e and the coefficients a_l^e , b_l^e , c_l^e and d_l^e are only dependent on the tetrahedron geometry [44].

The spatial divergence within a tetrahedron e is then calculated as

$$\begin{aligned} (\nabla \cdot b_n^2 \nabla \chi)_n^e &= \frac{\partial \xi_n^e}{\partial x} \cdot \hat{x} + \frac{\partial \xi_n^e}{\partial y} \cdot \hat{y} + \frac{\partial \xi_n^e}{\partial z} \cdot \hat{z} \\ &= \frac{1}{6V^e} \sum_{l=1}^3 (\xi_{x,l,n}^e b_l^e + \xi_{y,l,n}^e c_l^e + \xi_{z,l,n}^e d_l^e). \end{aligned} \quad (5.32)$$

Utilizing the calculated values of $\xi_{x,l,n}^e$, $\xi_{y,l,n}^e$ and $\xi_{z,l,n}^e$ on the nodes using the dual-mesh scheme (5.28), the divergence values at the centroids of the imaging domain are found and used to calculate \underline{g}_n^x to update the contrast variables $\underline{\chi}$.

5.2.4 Spatial Derivatives Calculation Summary

In the preceding sections, the evaluations of the spatial gradients and divergence were demonstrated for different configurations. To ease the calculation of the search directions \underline{g}_n^x used to update the contrast $\underline{\chi}$, the techniques to perform the spatial derivatives can be implemented as matrix operators ∇ for the gradient and $\nabla \cdot$ for the divergence.

For 2D TM, the matrix operator ∇ operates on a vector of nodal values of χ , $\underline{\chi}$ and returns the components of the spatial gradient calculated at the centroids of the triangles within the imaging domain \mathcal{D} . After calculating b_n^2 at each centroid, the divergence operator $\nabla \cdot$ takes the centroid values of $b_n^2 \nabla \chi$ and returns the approximate value of $\nabla \cdot b_n^2 \nabla \chi$ at the nodes.

For 2D TE and 3D, the matrix operator ∇ returns the components of the gradient calculated at the nodes within \mathcal{D} by operating on a vector of centroid values of χ , $\underline{\chi}$. Then at each node b_n^2 is calculated. Next, the divergence matrix $\nabla \cdot$ operates on the

nodal values of $b_n^2 \nabla \chi$ to calculate the approximate value of $\nabla \cdot b_n^2 \nabla \chi$ at the centroids.

5.3 Balanced MR-FEMCSI

A major drawback of the standard MR implementation is that the real and imaginary parts of the contrast are weighted similarly. For applications where there is an imbalance between the real and imaginary components of the contrast, the application of MR to CSI can result in an erroneous reconstruction of the imaginary part, as the inversion algorithm will favor the real part of the contrast. This can be improved by scaling the real and imaginary updates of the contrast in the MR functional differently, as proposed in [87]. Essentially, by modifying the MR term, the imbalance in the contrast can be compensated to achieve a reconstruction that is more accurate for both the real and imaginary parts of the contrast. The balanced multiplicative regularization (BMR) term is given as

$$\mathcal{C}_n^{\text{BMR}}(\chi) = \int_{\mathcal{D}} b_n(\vec{r})^2 (|\nabla \chi_{\text{R}}(\vec{r})|^2 + Q(\vec{r})^2 |\nabla \chi_{\text{I}}(\vec{r})|^2 + \delta_n^2) dv \quad (5.33)$$

Here χ_{R} and χ_{I} are the real and imaginary components of the contrast, Q is a balancing factor, and

$$b_n(\vec{r}) = \left(V (|\nabla \chi_{\text{R},n-1}(\vec{r})|^2 + Q(\vec{r})^2 |\nabla \chi_{\text{I},n-1}(\vec{r})|^2 + \delta_n^2) \right)^{-1/2}. \quad (5.34)$$

With the inclusion of the balanced multiplicative regularization term, the cost functional at the n^{th} iteration becomes

$$\mathcal{C}_n(\chi, \vec{w}_t) = \mathcal{C}_n^{\text{BMR}}(\chi) \times \mathcal{C}^{\text{CSI}}(\chi, \vec{w}_t). \quad (5.35)$$

The discretized form of the functional in BMR-FEMCSI is written as

$$\mathcal{F}_n(\underline{\chi}, \underline{\vec{w}}_t) = \mathcal{F}_n^{\text{BMR}}(\underline{\chi}) \times \mathcal{F}^{\text{CSI}}(\underline{\chi}, \underline{\vec{w}}_t) \quad (5.36)$$

where the balanced regularized term $\mathcal{F}^{\text{BMR}}(\underline{\chi})$ is given by

$$\mathcal{F}^{\text{BMR}}(\underline{\chi}) = \|\underline{b}_n \odot \nabla \underline{\chi}_R\|_{\mathcal{D}}^2 + \|\underline{b}_n \odot \underline{Q} \odot \nabla \underline{\chi}_I(\vec{r})\|_{\mathcal{D}}^2 + \delta_n^2 \|\underline{b}_n\|_{\mathcal{D}}^2. \quad (5.37)$$

Here

$$\underline{b}_n = \left(V \left(|\nabla \underline{\chi}_{R,n-1}|^2 + \underline{Q}^2 \odot |\nabla \underline{\chi}_{I,n-1}|^2 + \delta_n^2 \right) \right)^{-1/2}. \quad (5.38)$$

Since $\mathcal{F}_n^{\text{BMR}}(\underline{\chi}_{n-1}) = 1$, the update procedure for the contrast source variable $\underline{\vec{w}}_t$ remains unchanged; however, this is not the case for the contrast variable $\underline{\chi}$. The real and imaginary components of the contrast, $\underline{\chi}_R$ and $\underline{\chi}_I$, are updated independently in BMR-CSI. The analytical CSI update (4.30) for the contrast variables is no longer performed in BMR-CSI, rather the real and imaginary components of the contrast are updated by a conjugate-gradient method as follows:

$$\begin{aligned} \underline{\chi}_{R,n} &= \underline{\chi}_{R,n-1} + \alpha_n^{\text{XR}} \underline{d}_n^{\text{XR}} \\ \underline{\chi}_{I,n} &= \underline{\chi}_{I,n-1} + \alpha_n^{\text{XI}} \underline{d}_n^{\text{XI}}. \end{aligned} \quad (5.39)$$

The search directions $\underline{d}_n^{\text{XR}}$ and $\underline{d}_n^{\text{XI}}$ are calculated using the Polak-Ribière search di-

rections, and are given by

$$\begin{aligned} \underline{d}_n^{\chi_R} &= -\underline{g}_n^{\chi_R} + \frac{\langle \underline{g}_n^{\chi_R}, \underline{g}_n^{\chi_R} - \underline{g}_{n-1}^{\chi_R} \rangle_{\mathcal{D}}}{\left\| \underline{g}_{n-1}^{\chi_R} \right\|_{\mathcal{D}}^2} \underline{d}_{n-1}^{\chi_R} \\ \underline{d}_n^{\chi_I} &= -\underline{g}_n^{\chi_I} + \frac{\langle \underline{g}_n^{\chi_I}, \underline{g}_n^{\chi_I} - \underline{g}_{n-1}^{\chi_I} \rangle_{\mathcal{D}}}{\left\| \underline{g}_{n-1}^{\chi_I} \right\|_{\mathcal{D}}^2} \underline{d}_{n-1}^{\chi_I} \end{aligned} \quad (5.40)$$

where $\underline{g}_n^{\chi_R}$ and $\underline{g}_n^{\chi_I}$ are the preconditioned gradients of $\mathcal{F}_n(\underline{\chi}, \vec{w}_t)$ with respect to $\underline{\chi}_R$ and $\underline{\chi}_I$ respectively and are given by

$$\begin{aligned} \underline{g}_n^{\chi_R} &= \left(\underline{g}_{\text{MR},n}^{\chi_R} \times \mathcal{F}^{\text{CSI}}(\underline{\chi}_{n-1}, \vec{w}_{t,n}) + \underline{g}_{\mathcal{D},n}^{\chi_R} \times \mathcal{F}^{\text{BMR}}(\underline{\chi}_{n-1}) \right) \odot \underline{P}_n \\ \underline{g}_n^{\chi_I} &= \left(\underline{g}_{\text{MR},n}^{\chi_I} \times \mathcal{F}^{\text{CSI}}(\underline{\chi}_{n-1}, \vec{w}_{t,n}) + \underline{g}_{\mathcal{D},n}^{\chi_I} \times \mathcal{F}^{\text{BMR}}(\underline{\chi}_{n-1}) \right) \odot \underline{P}_n \end{aligned} \quad (5.41)$$

where

$$\begin{aligned} \underline{g}_{\text{MR},n}^{\chi_R} &= -2 \nabla \cdot \left(\underline{b}_n^2 \odot \nabla \underline{\chi}_{R,n-1} \right) \\ \underline{g}_{\text{MR},n}^{\chi_I} &= -2 \nabla \cdot \left(\underline{Q}^2 \odot \underline{b}_n^2 \odot \nabla \underline{\chi}_{I,n-1} \right) \end{aligned} \quad (5.42)$$

and

$$\begin{aligned} \underline{g}_{\mathcal{D},n}^{\chi_R} &= \text{Re} \left(2\eta_{\mathcal{D},n-1} \sum_t \mathcal{T}_{\mathcal{D}}^{-1} \vec{\mathcal{E}}_{t,n}^H \cdot \mathcal{T}_{\mathcal{D}} \vec{l}_{t,n} \right) \\ \underline{g}_{\mathcal{D},n}^{\chi_I} &= \text{Im} \left(2\eta_{\mathcal{D},n-1} \sum_t \mathcal{T}_{\mathcal{D}}^{-1} \vec{\mathcal{E}}_{t,n}^H \cdot \mathcal{T}_{\mathcal{D}} \vec{l}_{t,n} \right). \end{aligned} \quad (5.43)$$

The update step-sizes $\alpha_n^{\chi_R}$ and $\alpha_n^{\chi_I}$ in (5.39) are calculated analytically based on the

following minimization:

$$\begin{aligned}\alpha_n^{\chi_R} &= \arg \min_{\alpha^{\chi_R}} \left\{ \mathcal{F}_n \left(\vec{w}_{t,n}, \underline{\chi}_{R,n-1} + \alpha^{\chi_R} \underline{d}^{\chi_{R,n}}, \underline{\chi}_{I,n-1} \right) \right\} \\ \alpha_n^{\chi_I} &= \arg \min_{\alpha^{\chi_I}} \left\{ \mathcal{F}_n \left(\vec{w}_{t,n}, \underline{\chi}_{R,n-1}, \underline{\chi}_{I,n-1} + \alpha^{\chi_I} \underline{d}^{\chi_{I,n}} \right) \right\},\end{aligned}\tag{5.44}$$

which involves finding the roots of two cubic polynomials. As outlined in Appendix G, this yields one real root along with a complex-conjugate pair for each polynomial; the real roots are the step-sizes [56, 80].

5.3.1 Balancing and the Domain-Error Equation

Although the domain-error equation, $\mathcal{C}^{\mathcal{D}}(\chi, \vec{w}_t)$, in the CSI functional (4.1) is a function of the contrast variables χ , the balancing factor is not applied to the imaginary component of the contrast. As outlined in [55, 88], the domain-error equation (also known as the state equation) arises from the physics underlying the MWI problem, and it enforces Maxwell's equations. Multiplying the imaginary part of the contrast by the balancing factor would cause Maxwell's equations to not be satisfied. Thus, it is inappropriate to have a balancing factor in the domain-error equation.

6

Implementation and Evaluation

*Do all the good you can,
By all the means you can,
In all the ways you can,
In all the places you can,
At all the times you can,
To all the people you can,
As long as ever you can.*

–John Wesley [89]

In this chapter the FEM-CSI algorithm is validated by inverting synthetic datasets as well as experimental data. The chapter begins with a brief description of the implementation along with a discussion of the methods used in solving the FEM matrix equations.

The second part of the chapter is dedicated to the inversion of synthetic data. The section begins by exploring the different advantages of the FEM-CSI algorithm using 2D TM examples. Next, different examples are utilized to demonstrate the features of the multiplicative regularization (MR) implemented with FEM-CSI. Imaging resulting using the MR enhancement, balanced multiplicative regularization (BMR) are presented next. This first set of imaging results, including MR and BMR, are for the 2D TM cases so that they can be compared against an IE-CSI algorithm which was solely available for 2D TM problems [27].

For 2D TE, the examples are selected to again outline some of the FEM-CSI advantages, also comparing the TM and the TE reconstructions for the same targets. Due to the computational complexity associated with 3D FEM, the examples to demonstrate FEM-CSI for full-vectorial problems are chosen to be relatively simple with the OI located in an unbounded homogeneous background medium. The purpose of these simple examples is solely to show the functionality of the algorithm.

The third part of the chapter employs the FEM-CSI algorithm to invert experimental datasets. The experimental data are available from the electromagnetic imaging laboratory at the University of Manitoba (UofM) [22, 26, 90, 91]; the Universitat Politècnica de Catalunya (UPC) Barcelona, Spain [92]; and the Institut Fresnel, France [38, 39]. The UofM datasets consist of data collected in an air-filled microwave tomography (MWT) imaging system [22] as well as a similar MWT setup where different matching fluids of varying salt concentrations are used. Regardless of the background medium, the collected data are assumed to be 2D with TM polarization. The single UPC Barcelona dataset was collected using a microwave scanner system filled with distilled water [92]. Again, the system model is assumed to be 2D with TM polarization. The Institut Fresnel datasets were measured with the receiving antennas in the far-field region; furthermore, the data collection was done inside an anechoic chamber [38, 39]. The datasets consist of 2D TM and TE measurements as well as 3D. Details on each experimental setup are provided in this chapter along with the inversion results obtained.

6.1 Implementation

The FEM solver and the inversion algorithms presented in this work have been implemented in MATLAB[®], running on a PC workstation with two Intel[®] Xeon[®]

quad-core 2.8 GHz processors and 18 GB of physical memory. The codes have been highly-optimized using the various data-vectorization techniques in MATLAB, along with the various packages that can handle sparse matrices and data-structures efficiently. The code has been designed to make use of the available multi-core processors.

Using MATLAB, the inverse operator $\vec{\mathcal{L}}$ in FEM is calculated using an efficient LU decomposition algorithm designed for sparse and symmetric matrices. The algorithm is the Unsymmetric-Pattern Multifrontal Package (UMFPACK) with column pre-ordering [93, 94]. For a given problem, the LU decomposition is performed once and the resulting matrices are stored and recalled as necessary. Then, for solving the linear matrix equation, efficient matrix factorization algorithms included with UMFPACK are used.

Another direct solver package that can be used for sparse matrix LU decomposition and factorization is PARDISO (Parallel Sparse Direct Linear Solver). Although it is a direct solver, PARDISO supports a combination of direct and iterative methods to accelerate the linear solution process [95]. PARDISO often uses less memory than UMFPACK however it was not used or tested for the work presented in this thesis.

A disadvantage of using sparse LU decomposition algorithms is that they require more memory, which make their use quite problematic for 3D problems that require a large number of unknowns. An alternative would be using iterative solvers like GMRES (Generalized Minimal RESidual method) [96] and CG (conjugate gradient). Although they are more memory-efficient, iterative solvers are sometimes unstable and can have slow convergence; therefore appropriate preconditioning techniques have to be tested and used. A brief study that compares between the use of direct and iterative methods for solving 3D FEM problems was undertaken and the results are provided herein.

For finite-element mesh generation the third party freeware GMSH [66] is used. For all the results to ensure accurate calculations of the electric field, the characteristic mesh length (CL) of the different meshes is selected to be less than $\lambda/10$ where λ is the smallest expected wavelength for a given problem.

6.2 Synthetic Results

6.2.1 Inverse Crime

The term ‘‘Inverse Crime’’ has been coined to describe the cases where the synthetic datasets are generated using the same solver and numerical grid that is used by the inversion algorithm [97]. For the examples presented herein, the FEM forward solvers used to create the datasets share the same theoretical formulation as the solvers used in the inversion algorithm. Thus, to avert an inverse crime two techniques are used. First, the meshes used to generate the synthetic datasets are different from those used by the inversion algorithm. Next, noise is added to all the synthetic scattered fields obtained from the forward solver as follows [98]:

$$\underline{u}_\zeta^{\text{noisy}} = \underline{u}_\zeta + \|\underline{u}_\zeta\|_\infty \frac{\eta}{\sqrt{2}} (\tau_1 + j\tau_2), \quad (6.1)$$

where \underline{u}_ζ is a data-vector holding the ζ -component of the synthetically generated scattered field on the domain \mathcal{S} due to all the transmitters T , $\|\underline{u}_\zeta\|_\infty$ is the maximum magnitude of the data-vector complex entries, τ_1 and τ_2 are uniformly distributed random numbers between -1 and 1 , and η is the desired noise level. If 5% noise is added to the synthetic datasets, for example, $\eta = 0.05$.

6.2.2 Algorithm Evaluation

The implemented inversion algorithms can be evaluated, broadly speaking, in terms of the quality of the algorithm reconstructions relative to the actual profile, and the runtime of the algorithm. While the reconstruction quality can be measured using various metrics (*e.g.* vector norms, mean, standard deviation, *etc.*), the measurement of the computational time is dependent on different factors like the development environment, the programming efficiency and the inversion problem size. Herein, the average time per algorithm iteration (t_{iter}) is measured using MATLAB built-in functions. Along with the iteration time, the following information for each inverted dataset are tabulated as required: the frequencies of operation (f), the number of transmitters (T) per frequency, the number of elements (N_e) in the problem domain Ω , the number of nodes (N) or edges (E) in Ω and the number of unknowns (I) in the imaging domain \mathcal{D} .

The quality of the synthetic data reconstructions are assessed by calculating the L_1 , L_2 and L_∞ vector error-norms for each dataset based on the exact relative permittivity profile, $\epsilon_r^{\text{exact}}(\vec{r})$. Since the actual profile and the inversion results are located on different arbitrary unstructured meshes, it is necessary to interpolate them to the same uniform grid to calculate the vector error-norms. This uniform grid is discretized to finer and finer cells until the calculated error-norms converge. The vector error-norms are normalized by the norm of the exact relative permittivity interpolated to a uniform grid ($\underline{\epsilon}_r^{\text{exact}}$) and are calculated as

$$L_p = \frac{\|\underline{\epsilon}_r^{\text{exact}} - \underline{\epsilon}_r^{\text{reconst}}\|_p}{\|\underline{\epsilon}_r^{\text{exact}}\|_p} \quad (6.2)$$

where $\underline{\epsilon}_r^{\text{reconst}}$ is the reconstructed relative permittivity interpolated to a uniform grid.

The vector error-norms are presented in tabular form for each synthetic dataset, along with the logarithm of the data-error equation \mathcal{F}^S after the last iteration.

6.2.3 FEM-CSI: 2D TM

In this section, synthetic datasets are generated and inverted for 2D problems with TM polarization. For unbounded problems, the transmitters are assumed to be 2D electric point sources (line sources in 3D) with the incident field produced by transmitter t calculated as

$$\vec{E}_t^{\text{inc}}(\vec{r}) = \frac{1}{j4} H_0^{(2)}(k_b |\vec{r} - \vec{r}_t|) \hat{z}. \quad (6.3)$$

Here $H_0^{(2)}$ is the zeroth-order Hankel function of the second kind, k_b is the wavenumber of the background medium and \vec{r}_t is the position vector of the transmitter.

If the problem domain is enclosed by a PEC surface, the sources are still 2D electric point sources, but the incident field within the chamber is calculated as explained in Appendix I.

The data are generated using an FEM solver where 3% noise is added to the scattered data collected on the measurement surface \mathcal{S} using the method described in (6.1). First, a comparison between the inversion results from FEM-CSI and IE-CSI is performed using the same synthetic dataset. Next, several datasets are utilized to show the FEM-CSI algorithm advantages. Unless otherwise specified, the algorithms are allowed to run for 1024 iterations to ensure convergence. In addition, the predicted contrast after each iteration is constrained to remain within physical bounds (*i.e.* the real part of the relative permittivity is kept greater than 1, and the conductivity is constrained to be a positive value).

A summary of the inversions in this section is provided in Table 6.2, while the vector error-norms are given in Table 6.3.

6.2.3.1 Comparison between FEM-CSI and IE-CSI

For comparing FEM-CSI and IE-CSI, we consider the U-umlaut (\ddot{U}) profile depicted in Figures 6.1 (a) and (b). In this profile, the OI consists of scatterers arranged in the ‘ \ddot{U} ’ shape having the same relative permittivity of $\epsilon_r = 2 - j1$. The OI is located in an unbounded homogeneous background medium with relative permittivity $\epsilon_b = 1$. The OI is illuminated by 16 transmitters at a frequency of $f = 2$ GHz and the data are collected using 16 receivers per transmitter. The transmitting and receiving points are evenly spaced and co-located on a circle of radius 0.225 m. The synthetic dataset was generated using an FEM solver.

In both FEM-CSI and IE-CSI, the inversion domain \mathcal{D} is a square region centered in the middle of the problem domain with side-length equal to 0.15 m. In FEM-CSI, the inversion mesh consists of unstructured arbitrarily oriented triangles with 3,139 nodes within \mathcal{D} . The IE-CSI inversion grid consists of 100×100 cells confined within the boundaries of \mathcal{D} .

The reconstruction results using FEM-CSI are shown in Figures 6.1(c) and (d) and for IE-CSI in Figures 6.1 (e) and (f). The convergence of the cost functionals using FEM-CSI and IE-CSI are shown in Figure 6.8 (a). Comparing the reconstructions, the results of both FEM-CSI and IE-CSI are similar. The relative error for FEM-CSI $L_2^{\text{FEM-CSI}} = 18.22\%$ while for IE-CSI $L_2^{\text{IE-CSI}} = 17.78\%$. Both algorithms were able to resolve the different features of the OI; however both reconstructions of the real and imaginary relative permittivity values are higher than the true values.

Differences between FEM-CSI and IE-CSI reconstructions arise because FEM-CSI

is performed on an irregular mesh of arbitrary triangular elements while in IE-CSI the inversion domain is a regular uniform grid of square cells. These differences can be reduced by using a uniform mesh of equilateral triangles in FEM-CSI, applying a spatial filtering technique on FEM-CSI result at each iteration [99], or using multiplicative regularization. Furthermore, the cost functionals of FEM-CSI and IE-CSI converge to different values because the synthetic dataset is generated using FEM, the numerical noise floor of both algorithms is different (FEM-CSI implemented in MATLAB while IE-CSI in C++), and again the inversion domain properties are not the same.

6.2.3.2 Microwave Tomography in PEC Enclosures of Various Shapes

As previously mentioned, one advantage of FEM-CSI is the ability to perform imaging in different PEC enclosure shapes without any modification to the algorithm. The novelty of near-field microwave imaging in circular chambers with PEC boundaries was introduced before using IE-CSI in [20]. The concept of imaging inside enclosures of arbitrary shapes was further developed using a Gauss-Newton Inversion (GNI) algorithm in [23, 100]. To illustrate this feature in FEM-CSI, we consider an OI which consists of three circular regions with electrical properties that resemble biological tissues. One of the circular regions has a radius of 0.06 m with a relative permittivity of $\epsilon_r = 12$. The other two circular regions are embedded in this region. The two regions have the same radius of 0.015 m with relative permittivities of $\epsilon_r = 40 - j10$ and $\epsilon_r = 30 - j15$ at a frequency of $f = 1$ GHz. This OI has been used in other publications such as [29, 79]. The target configuration is shown in Figures 6.2 (a) and (b).

The OI is centered within three different PEC enclosures of different shapes: a

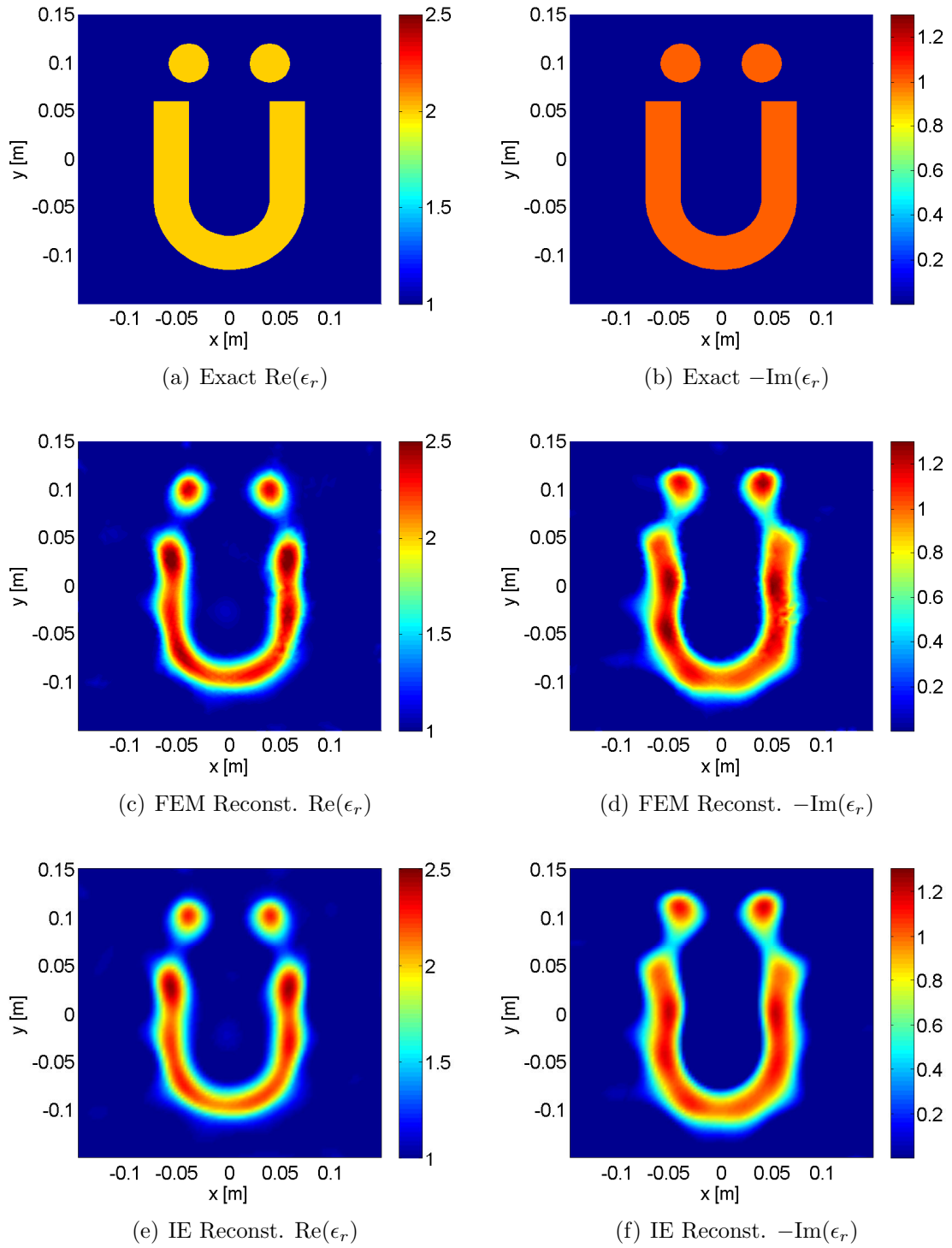


Figure 6.1: (a)-(b) \ddot{U} exact profile and reconstructions at $f = 2$ GHz using (c)-(d) FEM-CSI and (e)-(f) IE-CSI.

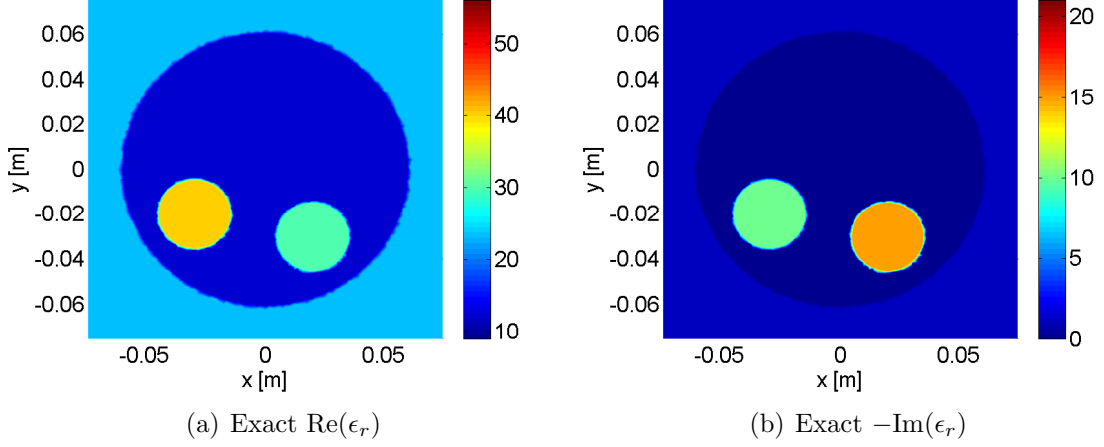


Figure 6.2: Exact profile of circular targets with lossy background at a frequency of $f = 1$ GHz.

circle of radius 0.12 m, a square with side-length of 0.24 m, and an equilateral triangle of side-length equal to 0.42 m. The dimensions of each enclosure are depicted in Figures 6.3 (a), (d) and (g). In all enclosures, the OI is surrounded by a background medium of relative permittivity $\epsilon_b = 23.4 - j1.13$ at a frequency of $f = 1$ GHz. The OI is interrogated by 32 transmitters at a frequency of $f = 1$ GHz and the scattered field data are collected at 32 receivers per transmitter. For all enclosures, the transmitting and receiving points are evenly spaced and co-located on a circle of radius 0.1 m.

The inversion domain \mathcal{D} is a square centered in the middle of the enclosures with the square's side-length equal to 0.15 m. The number of unknowns in \mathcal{D} are approximately 6,000 for all cases. For any enclosure, the unknowns are positioned on the vertices of triangles in an unstructured arbitrary mesh. The reconstructions after 1024 iterations are shown in Figures 6.3 (b) and (c) for the circular, (e) and (f) for the square, and (h) and (i) for the triangular enclosures, and the cost functional convergence is given in Figure 6.8 (b). The L_2 -norm relative errors for the reconstructions in the three different enclosures are quite similar with $L_2^{\text{circle}} = 18.25\%$,

Table 6.1: Relative Dielectric Permittivities of Brain Model at $f = 1$ GHz

Skin	Skull	CSF	GM	WM	Stroke
$46 - j15$	$12.8 - j2.4$	$69.3 - j42.8$	$52.8 - j16.9$	$38.6 - j9.0$	$61.1 - j28.5$

$L_2^{\text{square}} = 19.22\%$ and $L_2^{\text{triangle}} = 19.28\%$. The OI features are well resolved using any of the PEC enclosure shapes.

6.2.3.3 Biological Imaging with an Inhomogeneous Background

To demonstrate the capability of FEM-CSI to employ prior information as an inhomogeneous background, the third OI is selected as a simplified model of a brain exhibiting symptoms of a stroke. This brain model is based on that published in [4] and similar such models have been used in [28, 78]. It consists of an outer skin region followed by the skull, the cerebral-spinal-fluid (CSF), the gray matter (GM) and the white matter (WM). A stroke region representing a blood clot is located at the left side of the white matter region. The relative permittivities of the different biological regions in the model are summarized in Table 6.1 for a frequency of $f = 1$ GHz. The permittivity values of the model are based on the results of a study reported in [101].

The brain model is located in a background medium of permittivity $\epsilon_b = 45 - j13$. The target is irradiated by 32 transmitters evenly spaced on a circle of radius 0.11 m at a frequency of $f = 1$ GHz. The data are collected at 32 receivers per transmitter where the receiver locations are the same as the transmitter locations. The inversion domain \mathcal{D} is a square centered in the problem domain with its side-length equal to 0.20 m. The number of unknowns (located at the mesh nodes) within \mathcal{D} is 12,131 nodes. The inversion algorithm is run three successive times. In the first run, blind inversion is performed with no prior information given to the algorithm. For the second simulation, the prior data depicted in Figures 6.4(c) and (d) is given

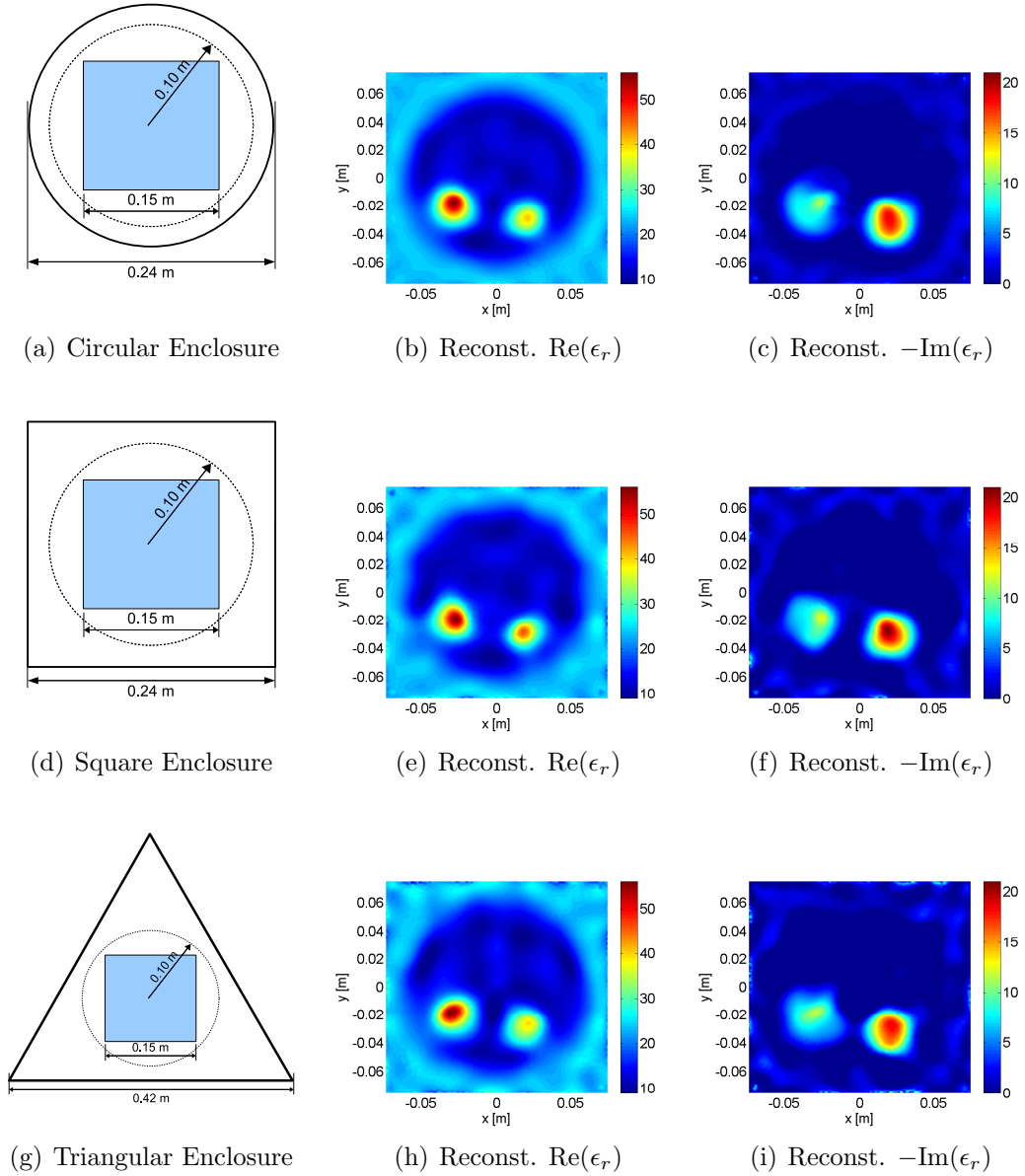


Figure 6.3: PEC enclosure configurations and FEM-CSI reconstructions at $f = 1$ GHz for (a)-(c) a circular domain, (d)-(f) a square domain and (g)-(i) a triangular domain.

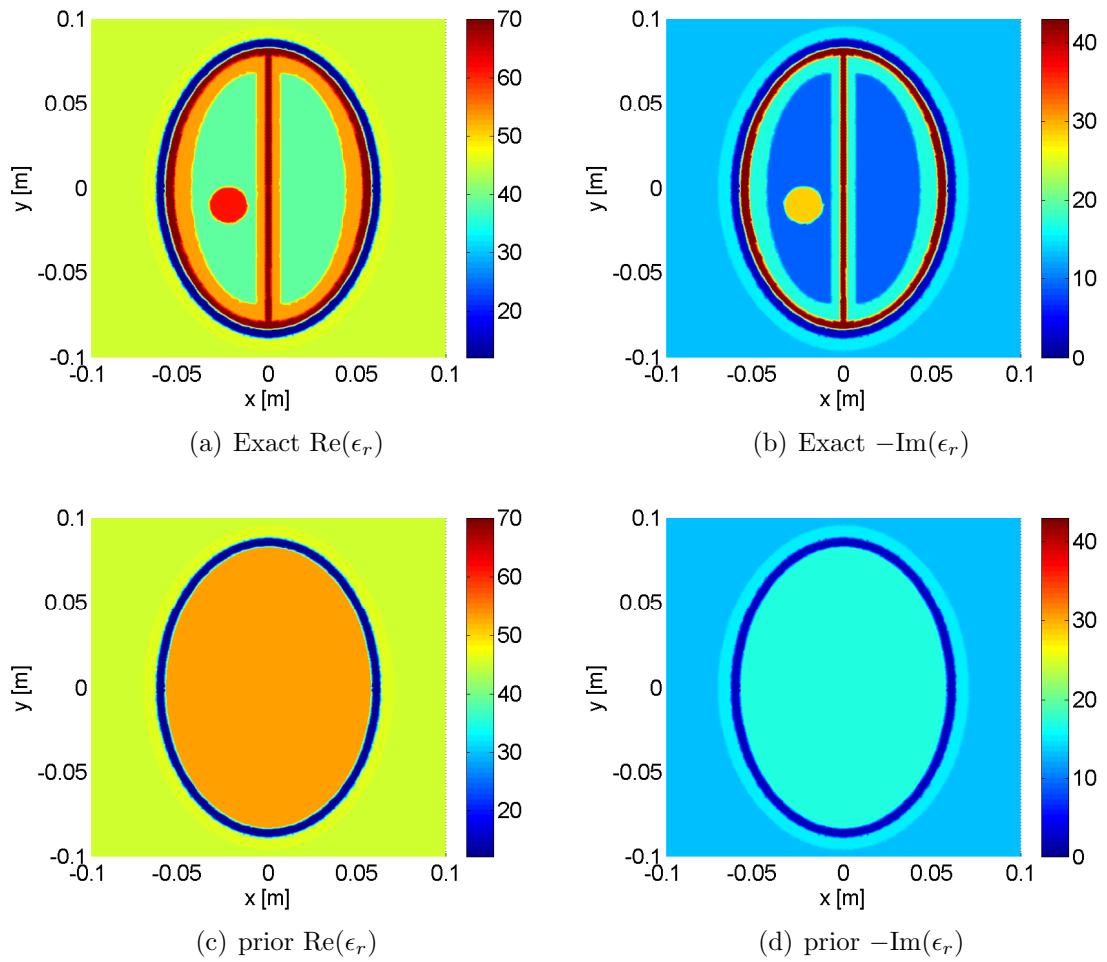


Figure 6.4: (a)-(b) Brain exact profile and (c)-(d) given prior information at $f = 1$ GHz.

to the algorithm as an initial guess. The third simulation was executed using the prior information as an inhomogeneous background by incorporating this information within the $\mathcal{L}[\cdot]$ operator.

The reconstruction results after 1024 iterations are shown in Figures 6.5 (a), (b) for blind inversion, (c), (d) when the prior information is used as an initial guess, and (e), (f) when the prior information is used as the inhomogeneous background. The FEM-CSI cost functional convergence for each case is given in Figure 6.8 (c). The features of the brain model with the stroke are resolved in all three cases; however, the best reconstruction is obtained with the prior information used as an inhomogeneous background (inhomog. bkg.). The L_2 -norm relative errors for the different runs are $L_2^{\text{blind}} = 22.49\%$, $L_2^{\text{initial}} = 14.54\%$ and $L_2^{\text{inhomog}} = 13.91\%$. The relative errors verify that using the prior information as an inhomogeneous background for the inversion gives the best results.

6.2.3.4 Adaptive Meshing

The fourth synthetic dataset example demonstrates the benefit of using adaptive meshing to improve the quality of the reconstruction while keeping the computational complexity to a minimum. For this example three different inversion meshes are utilized: a coarse mesh, an adapted mesh and a fine mesh (see Figure 6.7). For coarse and fine meshes the triangular elements are of relatively uniform size. For the adapted mesh, regions where OI inhomogeneities are *detected* are refined with more triangular elements. The inhomogeneities are *detected* using the FEM-CSI reconstructions on the coarse mesh, and this is the only purpose of using a coarse mesh.

The OI is composed of two targets embedded within a circular region as depicted in Figure 6.6. The circular region has a relative permittivity of $\epsilon_r = 5$. The left and right

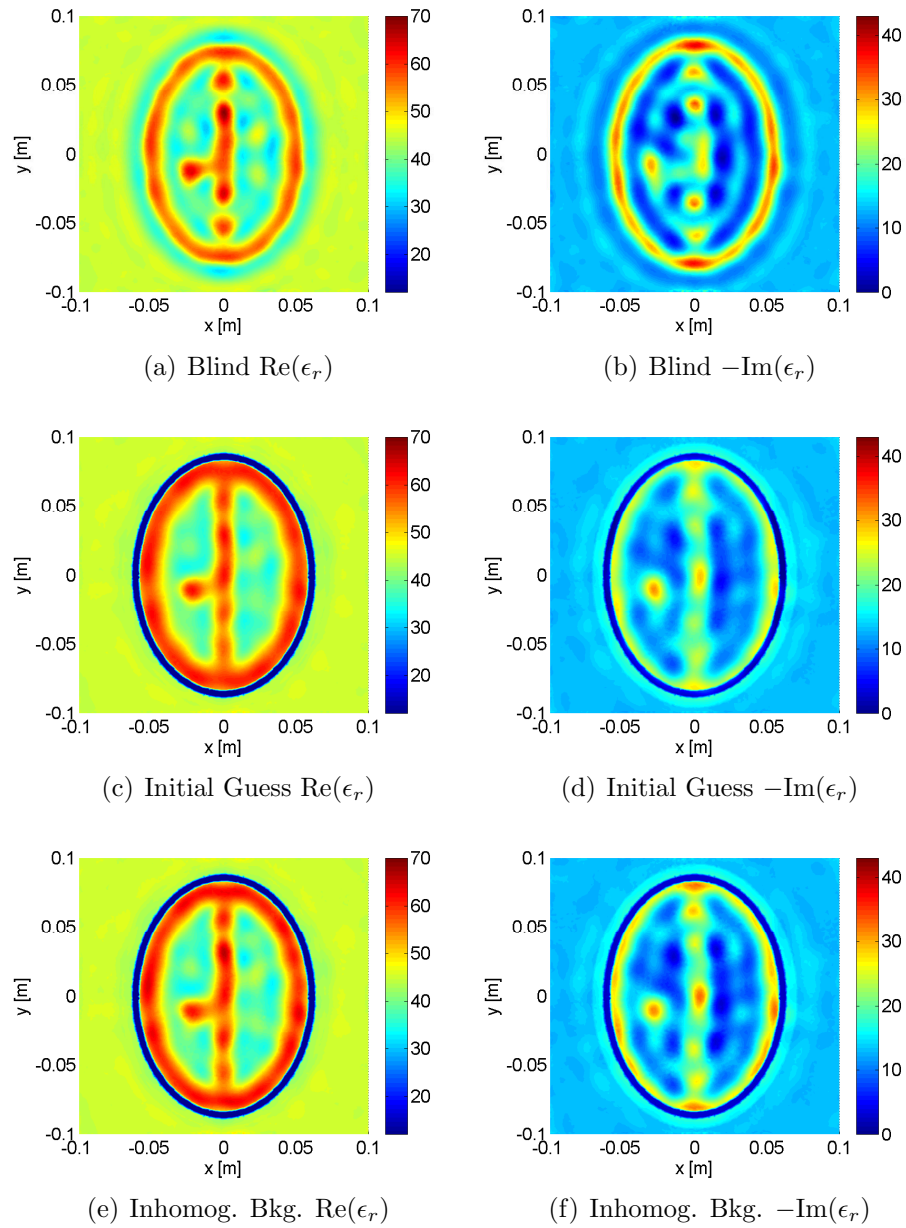


Figure 6.5: FEM-CSI reconstructions at $f = 1$ GHz (a)-(b) when no prior information is given, (c)-(d) when prior information is utilized as initial guess, and (e)-(f) when prior information is used as background.

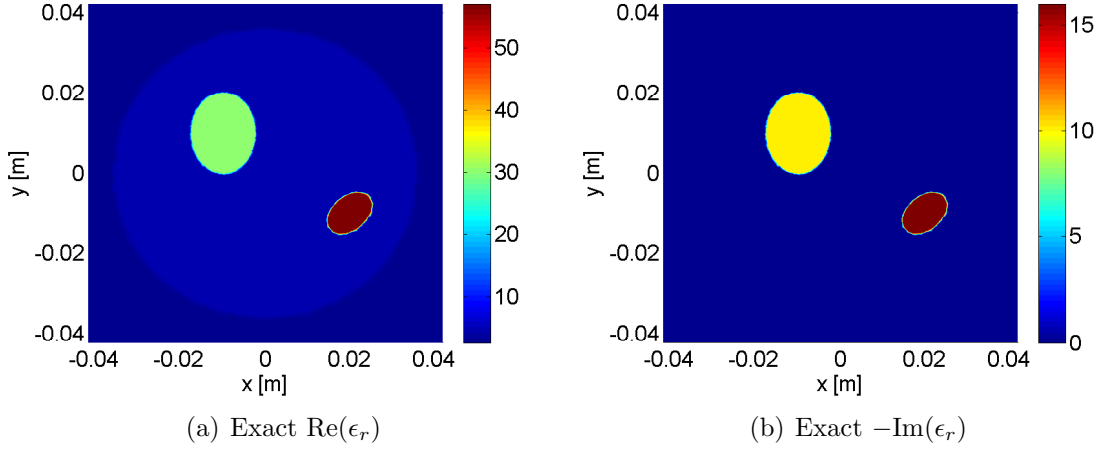


Figure 6.6: Exact relative permittivity of OI (a) Real and (b) Imaginary

inner targets relative permittivities at $f = 2$ GHz are $\epsilon_r = 30 - j10$ and $\epsilon_r = 57 - j16$ respectively. The OI is illuminated by 32 transmitters at a frequency of $f = 2$ GHz and the data are collected using 32 receivers per transmitter. The transmitters and the receivers are evenly spaced and co-located on a circle of radius 0.05 m. The MWT setup along with the OI are surrounded by an unbounded homogeneous background medium with relative permittivity $\epsilon_b = 2.6$. The inversion domain \mathcal{D} is a square centered in the domain with side-length equal to 0.042 m. The number of nodes N in Ω and unknowns I per inversion mesh, along with t_{iter} are given in Table 6.2. The reconstruction results using different meshes are shown in Figure 6.7, while the algorithm cost functional convergence for each case is given in Figure 6.8 (d). The vector error-norms are given in Table 6.3.

From the tabulated results it is obvious that a considerable reduction in the computational resources (time and memory) is obtained without compromising the image quality when an adapted mesh is utilized compared to a uniform fine mesh. This is well-demonstrated in the vector error-norms and the data-error given in the tables, as well as the reconstructions shown in Figure 6.7.

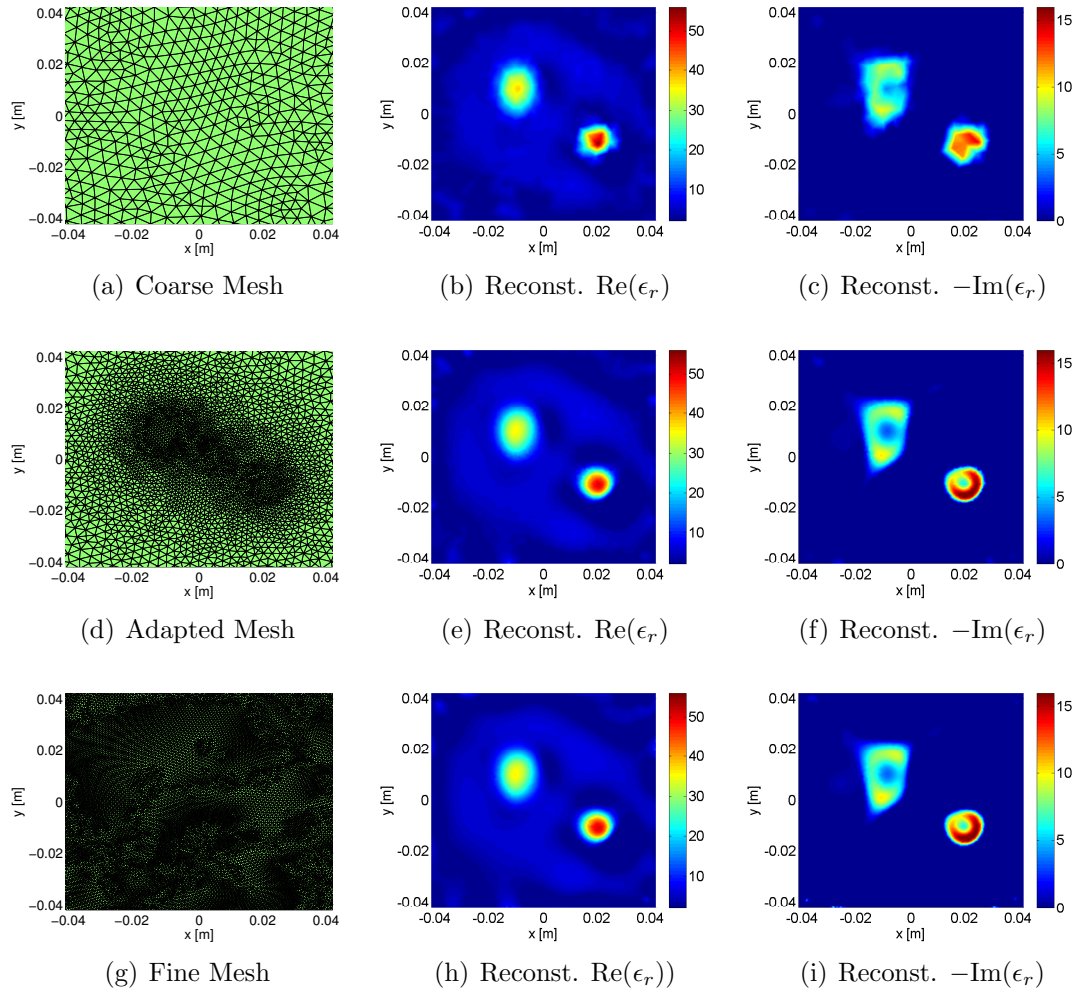


Figure 6.7: The reconstructions at $f = 2$ GHz with (a)-(c) a coarse mesh, (d)-(f) an adapted mesh and (g)-(i) a fine mesh.

Table 6.2: Summary of 2D TM Inversion Examples

Example	f (GHz)	T	N_e	N	I	t_{iter} (s)
FEM-CSI vs. IE-CSI	2	16				
FEM-CSI			26696	13539	3139	1.00
IE-CSI			10000	10000	10000	1.00
PEC Enclosures	1	32				
Circular			24338	12352	6027	2.51
Square			30702	15584	5936	2.79
Triangular			40159	20382	5951	3.28
Brain Model	1	32	42892	21689	12131	5.96
Adaptive Meshing	2	32				
Coarse			1778	940	394	0.11
Adapted			7580	3841	3050	0.80
Fine			38116	19258	8703	4.20
Low-Contrast Concentric Squares	1	30	24236	12213	7008	2.77
Breast Model	1.6	24	34882	17630	7804	1.33
Human Forearm Model	1	24	59434	29998	9950	3.45
Lossy E-phantom	2	24	36208	18324	8010	2.15

6.2.3.5 Section Conclusion

The results of applying the FEM-CSI algorithm to synthetic 2D TM datasets have been demonstrated by applying it to MWI setups using PEC enclosures of various shapes as well as using prior information in the form of an inhomogeneous background for the inverse problem. The ability to use adaptive non-uniform meshes with finer resolution in regions exhibiting large gradients in the dielectric contrast is also a possibility using this algorithm and has been tested. The use of adaptive meshes provides a reduction in the computational resources required while maintaining the reconstruction quality.

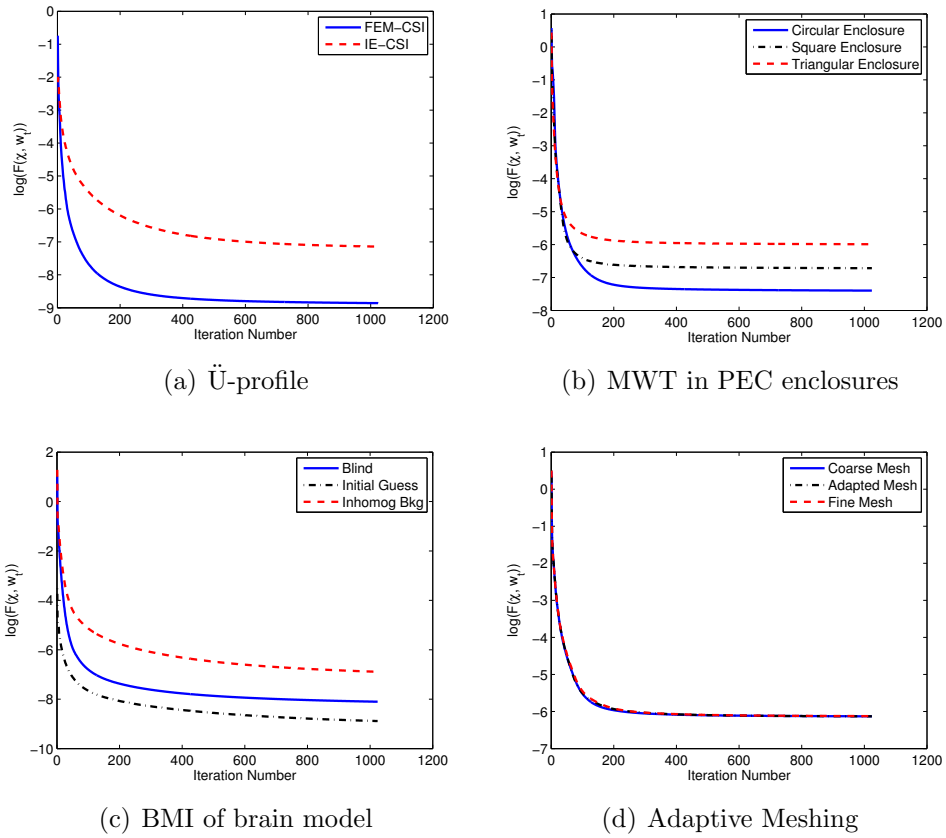


Figure 6.8: The FEM-CSI cost functional versus the iteration number for (a) \ddot{U} -profile, (b) MWT in PEC enclosures, (c) BMI of brain model and (d) adaptive meshing dataset reconstructions.

6.2.4 MR-FEMCSI: 2D TM

The benefits of adding multiplicative regularization to FEM-CSI are studied in this section. The incident field transmitters are again 2D electric point sources. For the synthetically generated data, 5% noise is added. The first example in the study outlines the edge-preserving characteristic of multiplicative regularization as well as its ability to suppress noise in the data. In this example, the results from MR-FEMCSI are compared against IE-MRCSI results. The second example shows not only the advantages of MR, but also those acquired from using FEM-CSI. A summary of the examples' parameters are given in Table 6.1, with the error analysis presented in Table 6.2. The cost functional convergence for each example is shown in Figure 6.14.

6.2.4.1 Low-Contrast Concentric Squares

For the first synthetic dataset, the OI consists of low-contrast concentric squares positioned in the center of the problem domain Ω as depicted in Figure 6.9. The inner and outer squares have side-lengths equal to λ and 2λ respectively where λ is the free-space wavelength at the operating frequency $f = 1$ GHz. The relative permittivity of the inner square is $\epsilon_r = 1.6 - j0.2$ and $\epsilon_r = 1.3 - j0.4$ for the outer square. The OI is illuminated by 30 transmitters equidistant on a circle of radius 2.33λ . For each transmitter, the measured synthetic data are collected by 30 receivers evenly spaced on a circle of radius 2.17λ . The tomography setup and the OI are located in an unbounded homogeneous background medium with relative permittivity $\epsilon_b = 1$. The inversion domain \mathcal{D} is a square centered in the domain with side-length equal to 3λ . The number of unknowns located in \mathcal{D} is approximately 7,000. The dataset is inverted using FEM-CSI and MR-FEMCSI. The algorithms are allowed to run for

Table 6.3: Errors for 2D TM Inversion Examples

Example	L_1	L_2	L_∞	$\log(\mathcal{F}^S(\underline{\vec{w}}_t))$
FEM-CSI vs. IE-CSI				
FEM-CSI	8.96%	18.22%	63.25%	-10.95
IE-CSI	8.94%	17.78%	58.42%	-7.63
PEC Enclosures				
Circular	12.01%	18.25%	58.29%	-7.63
Square	13.41%	19.22%	56.00%	-6.89
Triangular	14.07%	19.28%	53.81%	-6.18
Brain Model				
Blind	13.51%	22.49%	47.72%	-10.40
Initial Guess	8.84%	14.54%	36.99%	-12.07
Inhomog Bkg	8.19%	13.91%	35.96%	-9.70
Adaptive Meshing				
Coarse	37.74%	46.60%	97.66%	-6.24
Adapted	36.47%	42.42%	77.63%	-6.24
Fine	35.47%	41.98%	80.00%	-6.24
Low-Contrast Concentric Squares				
FEM-CSI	4.95%	7.67%	31.00%	-7.71
MR-FEMCSI	2.89%	6.74%	32.42%	-7.71
Breast Model				
FEM-CSI	28.13%	37.59%	110.12%	-10.45
MR-FEMCSI	18.35%	32.82%	81.00%	-10.24
Human Forearm Model				
MR-FEMCSI	4.10%	7.20%	39.98%	-8.82
BMR-FEMCSI $Q = 5$	3.68%	7.01%	45.14%	-8.79
BMR-FEMCSI $Q = 20$	4.20%	7.64%	43.46%	-8.65
E-phantom				
MR-FEMCSI	3.59%	6.20%	33.93%	-9.78
BMR-FEMCSI $Q = 10$	3.09%	6.19%	34.88%	-9.54
BMR-FEMCSI $Q = 30$	3.41%	6.30%	33.20%	-9.16
BMR-FEMCSI Q -map	3.15%	6.25%	33.72%	-9.39

1024 iterations to ensure convergence. The cost functional convergence is shown in Figure 6.14 (a).

The reconstruction results using FEM-CSI are shown in Figure 6.9 (c) and (d) while MR-FEMCSI results are given in Figure 6.9 (e) and (f). A one-dimensional cross-section at $y = 0$ is plotted in Figure 6.10 to compare the reconstruction of both algorithms relative to the actual profile. As is clear from the inversion results, the quality of MR-FEMCSI reconstructions are better than those of FEM-CSI. With the incorporation of the MR term, the edges of the squares are reconstructed well and any unwanted oscillations are smoothed out.

The purpose of this example is to demonstrate the advantages of applying multiplicative regularization to FEM-CSI. Nevertheless, the same example is inverted using IE-MRCSI [27] and the results are shown in Figure 6.11. The reconstructions from the two algorithms are similar (unwanted reconstruction artifacts are visible in both). In IE-MRCSI the edges of the squares are sharper because the inversion domain is a uniform square grid whereas for MR-FEMCSI the inversion domain is a mesh of arbitrarily oriented triangles.

6.2.4.2 Breast Model

In the second example two advantages of the MR-FEMCSI algorithm are shown: the ease of incorporating a conductive enclosure to surround the problem domain, and the algorithm's capability of employing prior information as an inhomogeneous background. The selected OI is a 2D slice of a *mostly fatty* breast model to which an elliptically-shaped tumor is added. The length of the tumor's major axis is 1.5 cm, while its minor axis is 1.0 cm. The breast model along with the tumor are shown in Figures 6.12 (a) and (b) for a frequency of $f = 1.6$ GHz. The 2D slice is taken from

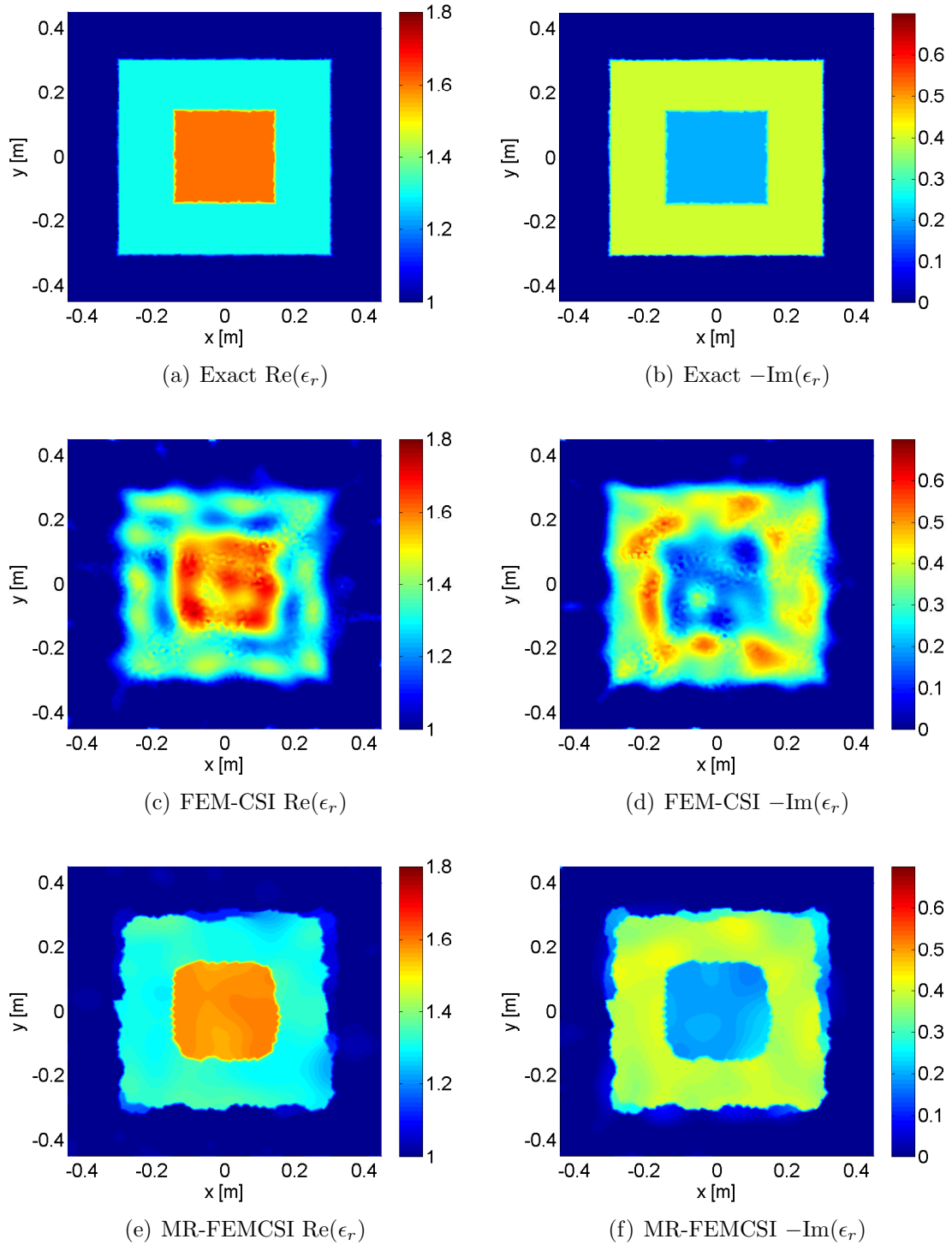


Figure 6.9: (a)-(b) Low-contrast concentric squares exact profile, (c)-(d) FEM-CSI reconstruction and (e)-(f) MR-FEMCSI reconstruction at frequency $f = 1$ GHz.

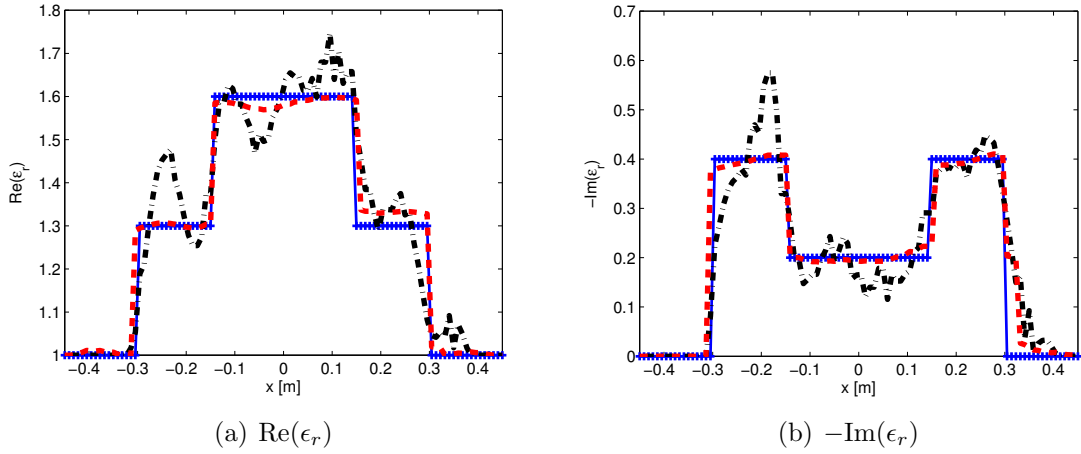


Figure 6.10: A cross-section at $y = 0$ for the exact profile (solid blue), FEM-CSI reconstruction (dash-dot black) and MR-FEMCSI (dash red).

the University of Wisconsin-Madison three-dimensional (3D) breast model, which is derived from anatomically realistic MRI data [102]. The complex permittivities of different tissues in the model are based on the studies outlined in [103]. The complex permittivity of the tumor region is taken from the 75th percentile group given in [103]. The mean relative permittivities of the different biological tissues in the model are summarized in Table 6.4. The OI is immersed in a low-loss matching medium of relative permittivity $\epsilon_b = 23.4 - j1.13$ surrounded by a circular conductive enclosure of radius 0.12 m. The OI is interrogated by 24 transmitters evenly distributed on a circle of radius 0.069 m at a frequency of $f = 1.6$ GHz. The scattered data are collected at 24 receivers per transmitter where the receiver locations are the same as the transmitter locations.

The inversion domain \mathcal{D} is a 0.12 m \times 0.094 m rectangular region centered in the middle of the problem domain. Within \mathcal{D} the number of unknowns is approximately 7800. The prior information, depicted in Fig. 6.12 (c) and (d), is used as an inhomogeneous background and is incorporated within the $\mathcal{L}[\cdot]$ operator. The

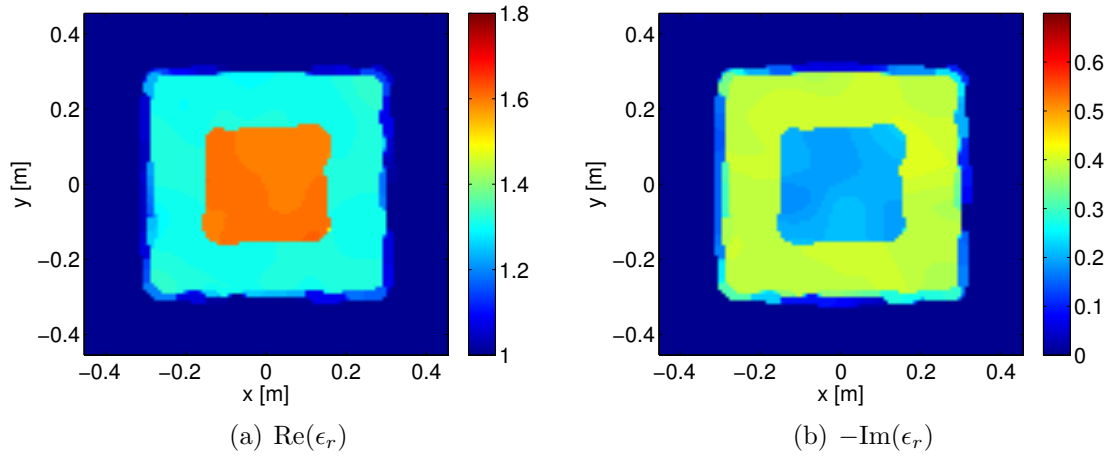


Figure 6.11: Low-contrast concentric squares reconstructions using IE-MRCSI.

prior information consists of the skin's location and complex permittivity at $f = 1.6$ GHz [101], along with assigning the inside of the breast a complex permittivity of $\epsilon_r = 6 - j1$. The prior value for the inside of the breast is an approximation for the relative permittivity of fatty tissues, the main breast constituent for the 75th percentile group. For the algorithms to converge they were run for 2048 iterations. The reconstruction results are shown in Figures 6.13 (a) and (b) for FEM-CSI and in Figures 6.13 (c) and (d) for MR-FEMCSI. The cost functional convergence is shown in Figure 6.14 (b). The results from both algorithms predict the presence of two main scatterers within the interior of the breast, which are the elliptical tumor and the fi-

Table 6.4: Relative Dielectric Permittivities of Breast Model at $f = 1.6$ GHz

Biological Tissue	Relative Permittivity
Skin	$45.00 - j11.75$
Muscle	$54.74 - j12.66$
Fat	$5.50 - j0.88$
Fibroglandular	$43.98 - j11.05$
Tumor	$59.51 - j15.85$

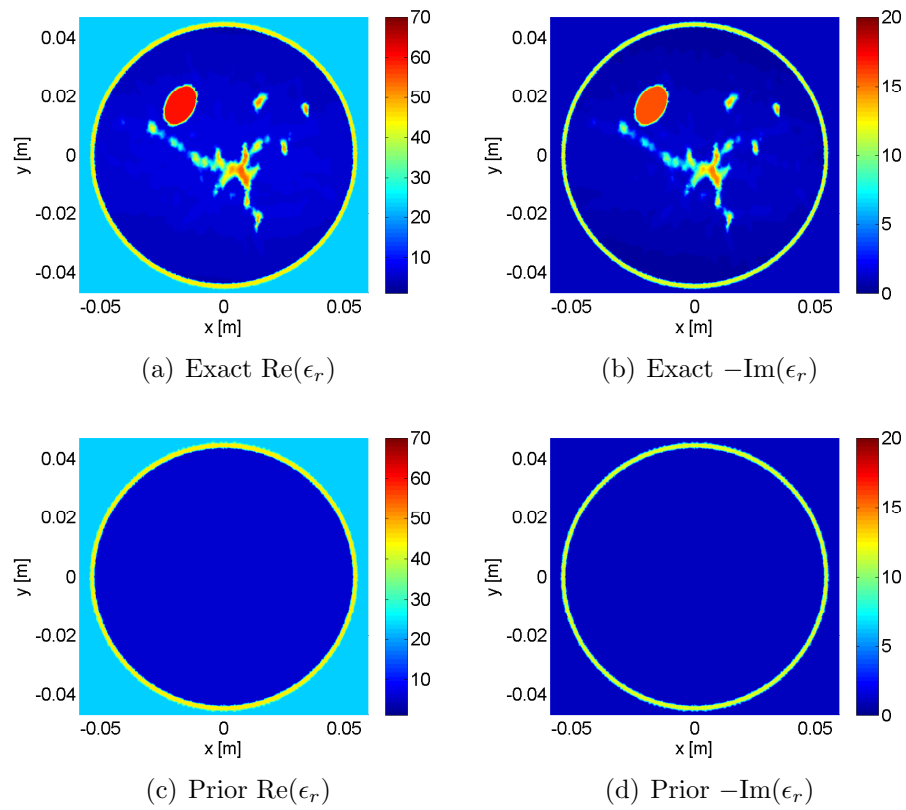


Figure 6.12: (a)-(b) Breast Model exact profile and (c)-(d) given prior information at frequency $f = 1.6$ GHz.

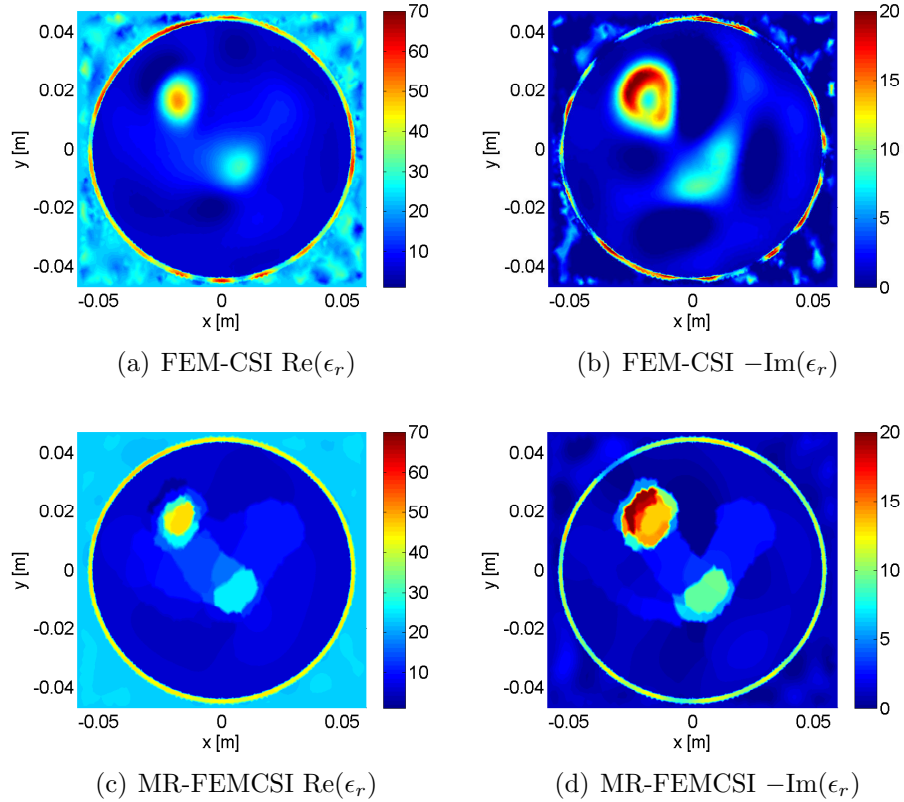


Figure 6.13: Reconstructions at $f = 1.6$ GHz using (a)-(b) FEM-CSI and (c)-(d) MR-FEMCSI.

brogladular tissue. The MR-FEMCSI algorithm correctly reconstructs the location and orientation of the tumor within the breast while preserving the skin; FEM-CSI fails to maintain the skin correctly. The predicted complex permittivity of the tumor is underestimated by both algorithms. Both algorithms fail to accurately estimate the shape and permittivity of the fibroglandular tissue; however the algorithms estimate the fibroglandular tissue's location correctly and they both assign the tissue a lower complex permittivity value compared to that of tumor, which is correct. Overall, the inclusion of multiplicative regularization enhanced the quality of the reconstruction.

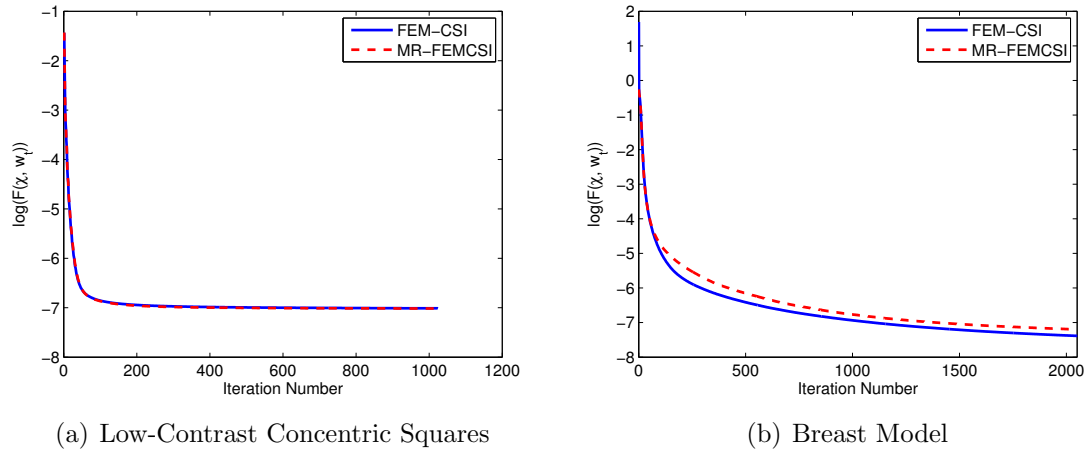


Figure 6.14: The cost functional versus the iteration number for (a) low-contrast concentric squares and (b) breast model synthetic datasets reconstruction.

6.2.4.3 Section Conclusion

A multiplicatively regularized finite-element method contrast source inversion (MR-FEMCSI) algorithm has been validated for 2D microwave imaging under the TM approximation of the fields. The algorithm retains the advantages of FEM-CSI, such as the ability to invert data on an arbitrary triangular mesh, allowing a non-uniform discretization of the imaging domain, as well as the ability to utilize prior information to introduce an inhomogeneous background into the inversion process. The addition of multiplicative regularization adds noise suppression to the inversion and enhances the edges of the reconstructed images while flattening regions of constant contrast.

6.2.5 Balanced MR-FEMCSI: 2D TM

In this section, the BMR-FEMCSI algorithm is tested using synthetic datasets for 2D TM problems. The datasets are selected to demonstrate how the new algorithm

out-performs the conventional MR-FEMCSI, along with outlining a methodology in selecting the balancing factor, Q . In the inversion for each dataset, the results are constrained to remain within physical bounds (*i.e.* $\text{Re}(\epsilon_r) \geq 1$ and $\text{Im}(\epsilon_r) \leq 0$). Unless otherwise specified, the algorithm is allowed to run for 1024 iterations to ensure convergence. A summary of the examples is given in Table 6.1, while the error vector-norms are presented in Table 6.2. The cost functional convergence for each example is shown in Figure 6.21.

6.2.5.1 Human Forearm Model

For biological tissues, the ratio of the real to the imaginary component of the relative permittivity is large. This degrades the reconstruction quality of the imaginary part of the contrast when using unbalanced MR-FEMCSI. In this example, synthetic scattered data from an OI depicting a human forearm is inverted to demonstrate BMR-FEMCSI's potential in producing better reconstructions in MWI for biomedical applications.

The synthetic model is a human forearm, as depicted in Figures 6.15 (a) and (b), with the relative complex permittivities given by $\epsilon_r^{\text{skin}} = 46.0 - j15$, $\epsilon_r^{\text{bone}} = 13.0 - j2.3$ and $\epsilon_r^{\text{muscle}} = 55 - j16$ [101]. The frequency of operation is $f = 1$ GHz. The OI is surrounded by a salty water solution with relative permittivity $\epsilon_b = 76.56 - j15.04$. The human forearm is interrogated by 24 transmitters and the data are collected by 24 receivers per transmitter. The transmitters and receivers are co-located and equally spaced on a circle of radius 0.094 m. To prevent an inverse crime, the synthetic dataset is generated using an MoM solver along with adding 10% noise to the scattered data. The inversion domain \mathcal{D} is a square centered in the problem domain Ω with side-length equal to 0.10 m.

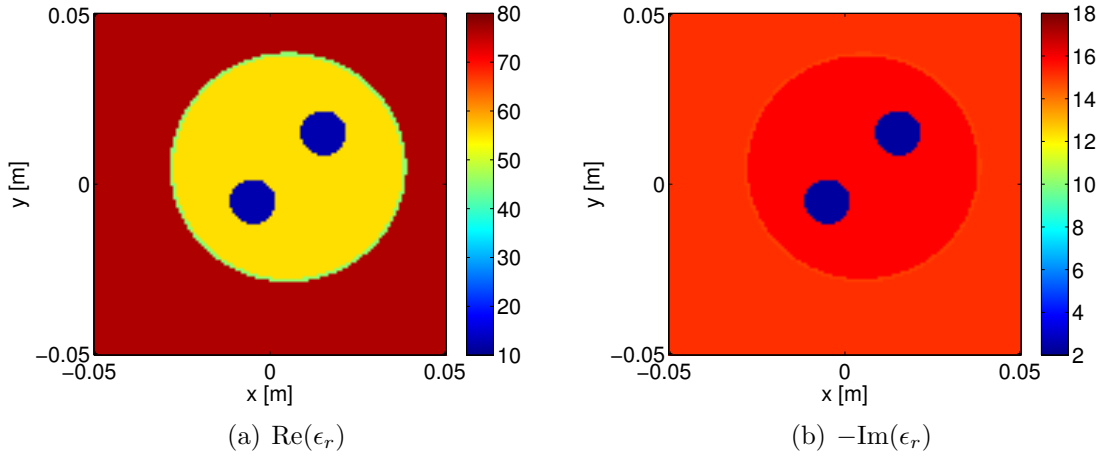


Figure 6.15: Synthetic arm exact profile at a frequency $f = 1$ GHz.

The results of using MR-FEMCSI are shown in Figures 6.16 (a) and (b). The reconstructions using BMR-FEMCSI are shown in Figures 6.16 (c) and (d) for $Q = 5$ and Figures 6.16 (e) and (f) for $Q = 20$. The cost functional convergence is shown in Figure 6.21 (a).

The real part reconstructions using MR-FEMCSI and BMR-FEMCSI for $Q = 5$ are very similar, but degrades when using $Q = 20$ in BMR-FEMCSI. In all three reconstructions, the real part of the bone's relative permittivity is overshoot to an average of 22. The imaginary part reconstruction using MR-FEMCSI is oscillatory with poor reconstruction of the arm's contour. However, as shown in Figures 6.16 (d) and (f), using BMR-FEMCSI the shape of the human forearm is preserved and distinguishable from the background medium. For BMR-FEMCSI, the imaginary part reconstruction using $Q = 5$ is better than using $Q = 20$, with the imaginary component of the bone more overshoot in the later case. Further, for $Q = 20$ an erroneous halo of $-\text{Im}(\epsilon_r) = 13$ is formed around the forearm muscle, with its value less than the expected imaginary part of the skin as well as thicker.

From the results presented herein, we speculate that the selection of the Q -factor

is dependent on the expected ratio of the real to the imaginary components for the different material parameters constituting the OI (i.e., $\mathcal{R} = |\text{Re}(\epsilon_r)/\text{Im}(\epsilon_r)|$). Using the actual values of the complex relative permittivity, for the different objects in the imaging domain \mathcal{D} the ratios are: $\mathcal{R}^{\text{skin}} \approx 3.1$, $\mathcal{R}^{\text{bone}} \approx 5.7$, $\mathcal{R}^{\text{muscle}} \approx 3.4$ and $\mathcal{R}^{\text{background}} \approx 5.1$. With the ratios' average being $\mathcal{R}^{\text{average}} \approx 4.3$, it is not a surprise that the best reconstruction result is obtained using BMR-FEMCSI for $Q = 5$.

6.2.5.2 E-Phantom

The purpose of this numerical example is to demonstrate how the selection of the balancing factor, Q , will alter the results significantly. The OI presented herein consists of an “e-phantom” with a circular inclusion embedded within it [87, 104]. As depicted in Figures 6.17 (a) and (b), the relative complex permittivity of the inclusion and the right-most feature of the OI is $\epsilon_r = 33 - j5$ at a frequency $f = 2$ GHz, while the rest of the “e-phantom” has a permittivity of $\epsilon_r = 33 - j1.2$. The OI is immersed in a low-loss background with relative permittivity of $\epsilon_b = 23 - j1$ and is illuminated by 24 transmitters successively. The resultant scattered field is collected at 24 receivers per transmitter. The transmitters and receivers are evenly distributed on a circle of radius 0.1 m.

The collected synthetic field is inverted using MR-FEMCSI and BMR-FEMCSI. The imaging domain \mathcal{D} is a square centered in the problem domain Ω with side-length equal to 0.14 m. The number of unknowns in \mathcal{D} is 8010 and they are located at the nodes of a triangular arbitrary mesh. The reconstruction results using MR-FEMCSI are shown in Figures 6.18 (a) and (b). The BMR-FEMCSI results are shown in Figures 6.18 (c) and (d) for $Q = 10$ and Figures 6.18 (e) and (f) for $Q = 30$. The cost functional convergence for each algorithm run is shown in Figure 6.21 (b).

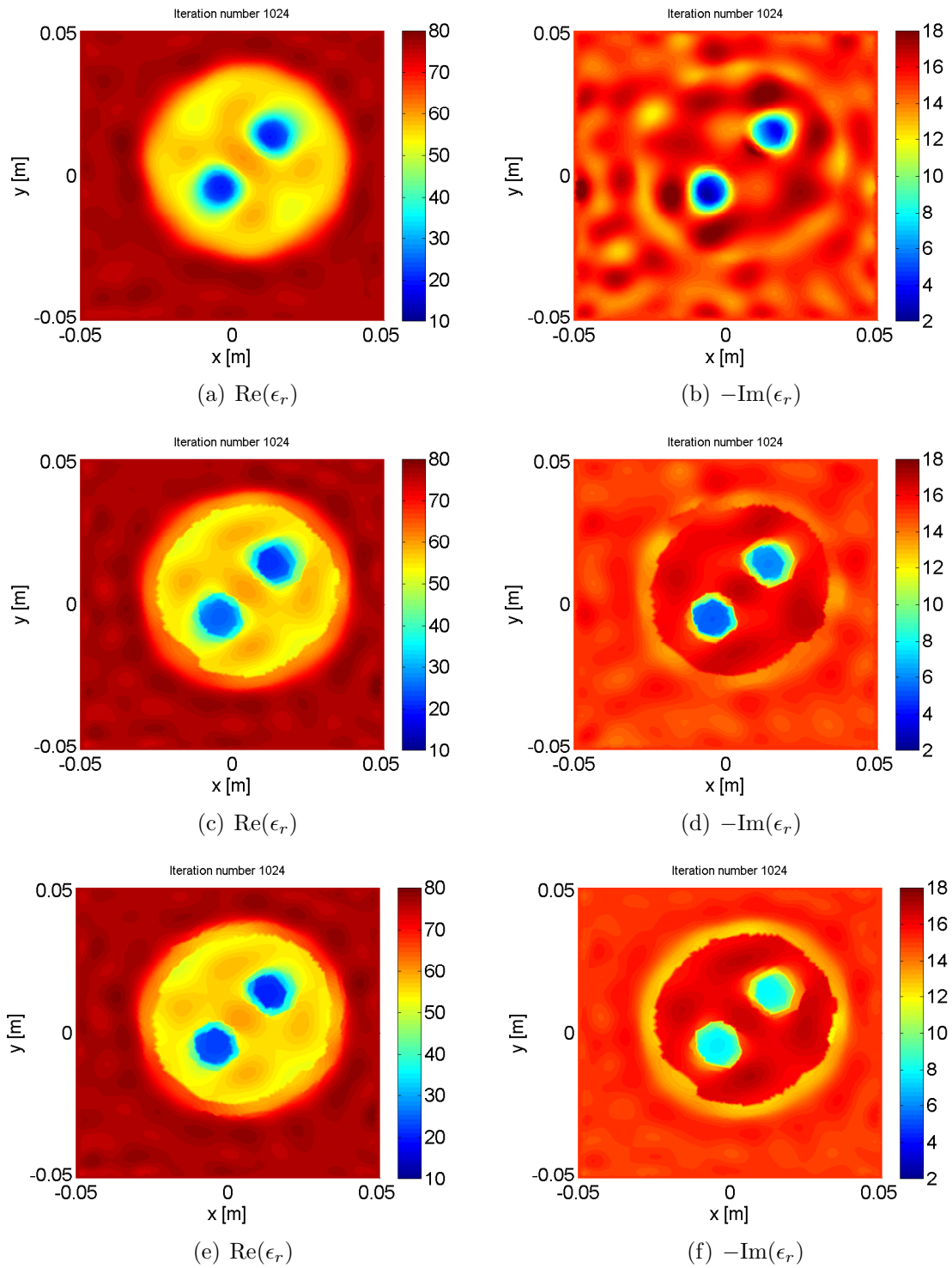


Figure 6.16: Human forearm model reconstructions using (a)-(b) MR-FEMCSI and (c)-(d) BMR-FEMCSI for $Q = 5$ and (e)-(f) for $Q = 20$.

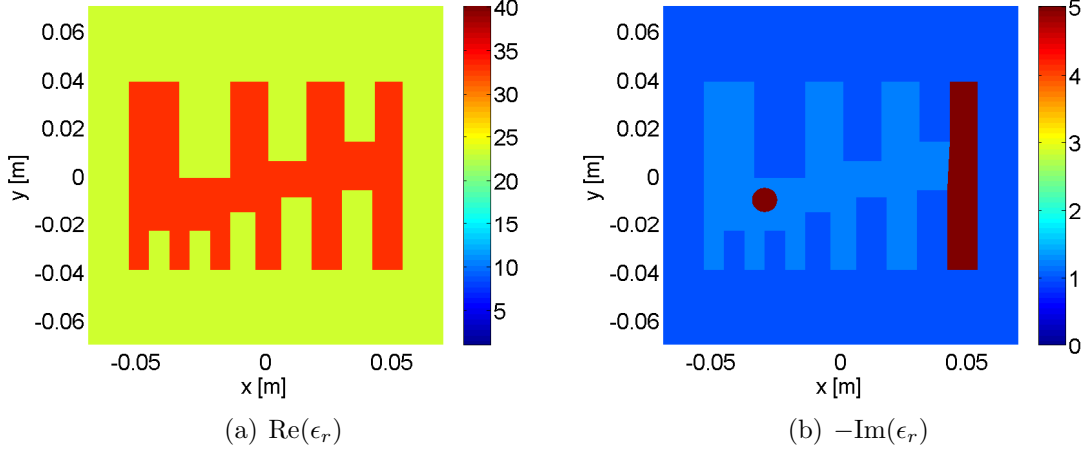


Figure 6.17: The “e-phatom” with circular inclusion exact profile at a frequency $f = 2$ GHz.

For this example, statistical analysis is performed to compare the quality of the reconstructions. This analysis includes calculating the mean and variance of the real and imaginary components of the reconstructions for each region in the imaging domain.

The reconstructions of the real component within the imaging domain are accurate and are similar almost independently of the chosen Q . The real component of the reconstructed permittivity has an approximate mean value of 32.5, while for the background medium this mean is 23.3, independent of Q . Further, the variances, $\sigma_{\text{Re}(\epsilon_r)}^2$, are 3.6 and 1.3 for the OI and the background medium respectively, independent of the selected Q .

The quality of the imaginary part reconstructions is analyzed for each separate region of the exact OI with the aid of the error-bar plots shown in Figure 6.19 and the statistical results are summarized in Table 6.5. For a given Q , the imaginary reconstruction, $-\text{Im}(\epsilon_r)$, of each region in \mathcal{D} is represented by a line whose mid-point is the mean of the reconstruction with a length of two times the variance, $\sigma_{-\text{Im}(\epsilon_r)}^2$.

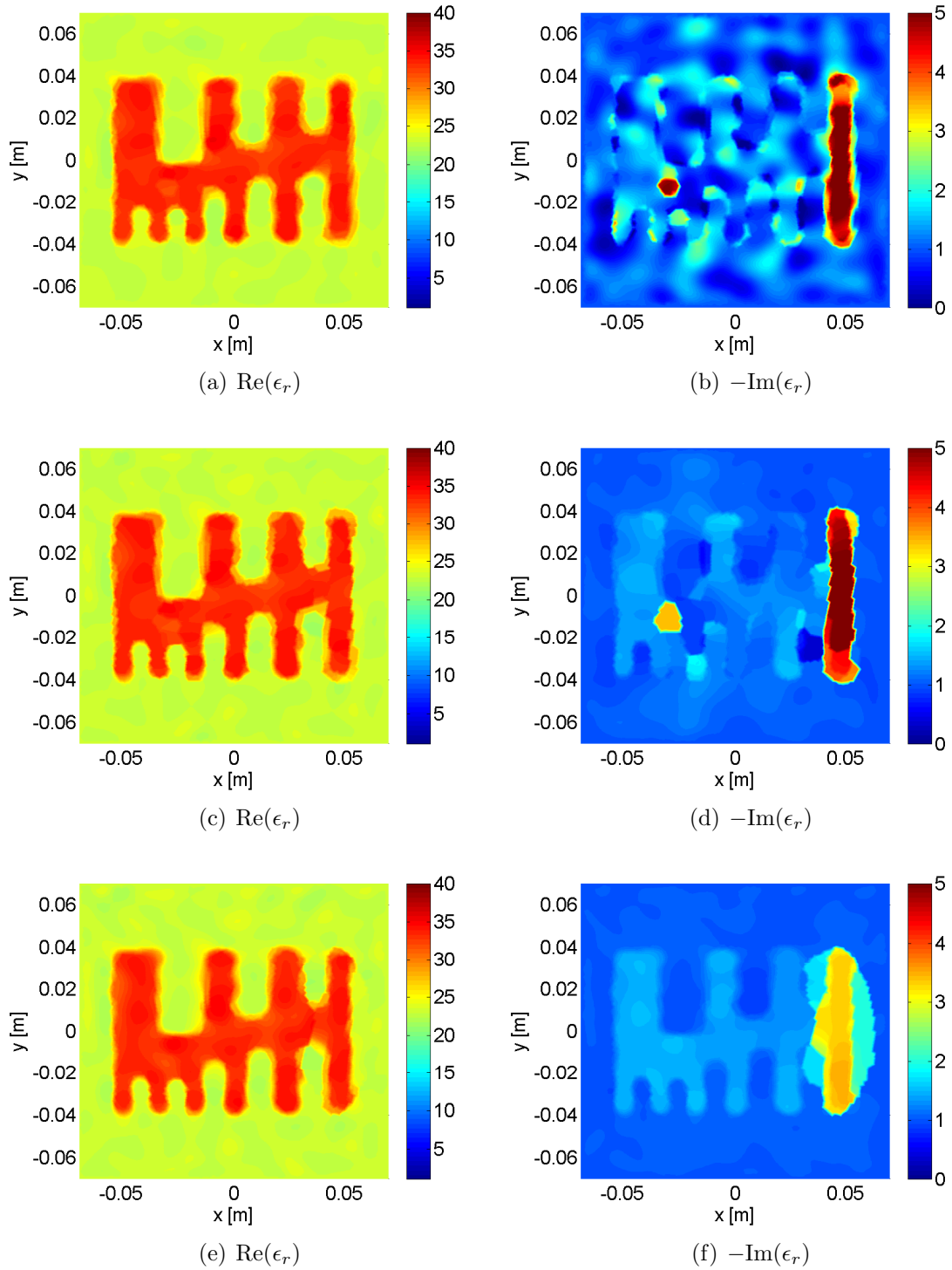


Figure 6.18: The “e-phantom” with circular inclusion reconstructions using (a)-(b) MR-FEMCSI and (c)-(d) BMR-FEMCSI for $Q = 10$ and (e)-(f) for $Q = 30$.

Considering MR-FEMCSI ($Q = 1$), the reconstruction is the most accurate of the four inversions with respect to the mean value, but it has the largest variance. This is visible in Figure 6.18 (b) as the oscillatory behavior of the reconstruction, particularly for the “e-phantom” region. Except for the inclusion region and right-most feature of the “e-phantom”, most of the imaginary part of the OI is indistinguishable from the background.

The BMR-FEMCSI algorithm with $Q = 10$ was more successful in attaining the different features of the OI with better reconstruction of the right-most OI feature. This is clear from the error-bar plots as the different variances are lower for the $Q = 10$ reconstruction in comparison the MR-FEMCSI estimates. For $Q = 30$ the low-loss features of the OI are better reconstructed with an average predicted value of $-\text{Im}(\epsilon_r) = 1.4$; nevertheless from Table 6.5 the variance for the low-loss “e-phantom” feature is larger for $Q = 30$ in comparison to $Q = 10$, which is due to the feature estimates near the lossy arm being overshoot for $Q = 30$. Moreover the value of the imaginary component of the right-most feature is undershot to approximately 3, while the circular inclusion is not detected at all; the later explains why the mean of the circular inclusion estimates is far off from the actual expected value. Finally, artifacts are visible around the right-most arm of the “e-phantom”, which will affect the mean and the variance of the background medium estimates as observed in Figure 6.19 and Table 6.5.

The different results obtained for various balancing factors, Q , are due to the differences in the ratio \mathcal{R} amongst the OI components. For the circular inclusion and the right-most OI element $\mathcal{R} = 6.6$, thus the imaginary part reconstruction of these features are better using MR-FEMCSI ($Q = 1$) and BMR-FEMCSI with $Q = 10$. For the low-loss features in the “e-phantom” the ratio $\mathcal{R} = 27.5$; thus a

Table 6.5: Statistical Analysis of results

Region	$\frac{ \text{Im}(\epsilon_r^{\text{reconstr.}}) - \text{Im}(\epsilon_r^{\text{actual}}) }{ \text{Im}(\epsilon_r^{\text{actual}}) }$	$\sigma_{-\text{Im}(\epsilon_r)}^2$
Background Medium		
MR-FEMCSI ($Q = 1$)	8.24%	0.196
$Q = 10$	6.67%	0.088
$Q = 30$	9.06%	0.073
Q -map	5.66%	0.028
Low-loss E-phantom		
MR-FEMCSI ($Q = 1$)	5.93%	0.300
$Q = 10$	7.35%	0.080
$Q = 30$	18.47%	0.091
Q -map	14.28%	0.026
High-loss E-phantom Arm		
MR-FEMCSI ($Q = 1$)	8.73%	1.146
$Q = 10$	9.25%	0.635
$Q = 30$	36.37%	0.189
Q -map	16.97%	0.953
High-loss Circular Inclusion		
MR-FEMCSI ($Q = 1$)	25.42%	1.458
$Q = 10$	32.76%	0.024
$Q = 30$	70.50%	0.001
Q -map	44.93%	0.038

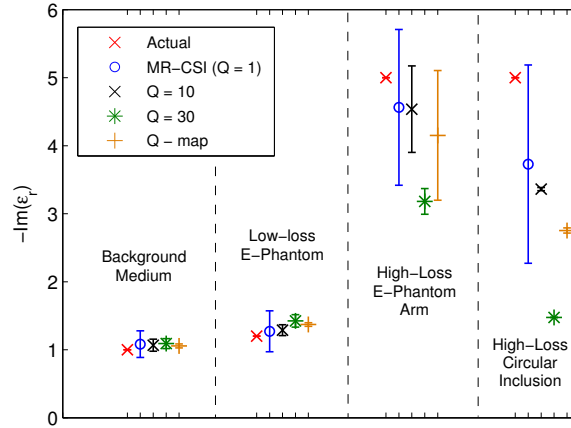


Figure 6.19: Statistical analysis of the $-\text{Im}(\epsilon_r)$ reconstructions using different Q -factors.

better reconstruction for these features is obtained using BMR-FEMCSI with $Q = 30$, degrading the reconstruction of the high-loss parts of the OI. These observations motivated us to have a location-dependent mapping of Q across the imaging domain \mathcal{D} . This mapping is built using prior information about the OI as well as results from previous BMR-FEMCSI runs. A rectangular region is created inside the imaging domain where the location of the OI is predicted. Within this rectangular region, two regions are embedded: a circular region of 6 mm radius centered at the estimated location of the inclusion, and a small rectangular region at the estimated location of the right-most feature of the OI. The location and size of the different regions are estimated using the BMR-FEMCSI runs. A Q -factor of 6 is assigned to the two embedded regions. The Q -factor for the remainder of the rectangle in \mathcal{D} is set to 28. The rest of the imaging domain \mathcal{D} has a $Q = 23$. The different values of Q are based on the various ratios \mathcal{R} calculated earlier. The final mapping of Q throughout \mathcal{D} is depicted in Figure 6.20 (a).

The use of the location-dependent Q -map results in better imaginary part re-

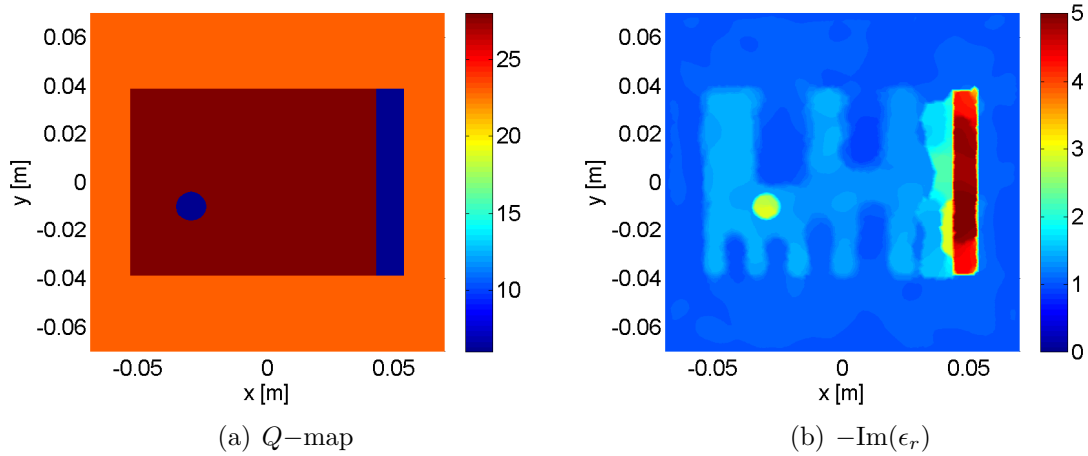


Figure 6.20: (a) Map of balancing factor Q inside the imaging domain and (b) the imaginary part reconstruction using BMR-FEMCSI at $f = 2$ GHz.

constructions for the background medium and the low-loss “e-phantom” feature in comparison to those achieved using a fixed value of Q . This is clear in Figure 6.19 as these features have mean values close to the expected actual values, with the variance of the estimates being the smallest in comparison to the reconstructions with different fixed Q -factors. For the circular inclusion, the variance of the estimate is low but the mean value is smaller than expected; however, the accuracy is still better than the case with $Q = 30$. The small variance suggests a smooth reconstruction as shown in Figure 6.20 (b). The lossy arm reconstruction is again better than the $Q = 30$ estimate and is closer to the result obtained using $Q = 10$. The reconstruction of the real component of the OI is not shown here as it is similar to the ones estimated by MR-FEMCSI and BMR-FEMCSI with fixed Q .

In this example, the information used to create the Q -map was extracted from the actual profile of the OI as well as the previous BMR-FEMCSI runs. Nevertheless, for other problems the ratio of the real to the imaginary components of the OI can be estimated using studies of the electrical properties for the materials being imaged, *e.g.*

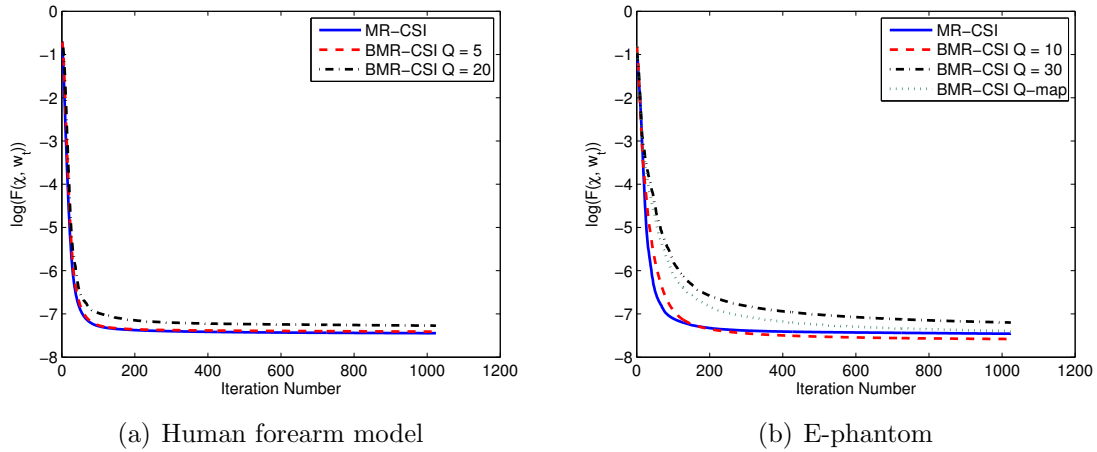


Figure 6.21: The cost functional versus the iteration number for (a) human forearm model and (b) “e-phantom” synthetic datasets reconstruction.

biological tissues permittivity models [101, 102]. As for the location and the shape of different inhomogeneities in the OI, they can be predicted using other imaging modalities, *e.g.* magnetic resonance imaging (MRI) or ultrasound.

6.2.5.3 Section Conclusion

It has been shown in this section that BMR-FEMCSI can provide a better reconstruction for the imaginary part of the relative complex permittivity when there is a large imbalance between the real and imaginary parts of the OI’s relative permittivity. From the examples, it can be deduced that the selection of the balancing factor will have an influence on the reconstruction, and the choice of Q is dependent on the ratio of the real to the imaginary components of the OI’s relative complex permittivity. Using prior information about the OI along with the results from BMR-FEMCSI for fixed Q s, a map of balancing factor can be formed across the imaging domain to improve the quality of the reconstructions. A future improvement would be to create the Q -map using no prior information.

6.2.6 Inversion of 2D TE Datasets

In this section, the MR-FEMCSI algorithm for 2D TE problems is tested using synthetically generated data. The incident electric field is produced by an imposed 2D magnetic point sources. For a transmitter t , the incident field of such a source is given by

$$\vec{E}_t^{\text{inc}}(\vec{r}) = \frac{Z_b}{4} H_1^{(2)}(k_b |\vec{r} - \vec{r}_t|) \frac{[(y - y_t)\hat{x} - (x - x_t)\hat{y}]}{|\vec{r} - \vec{r}_t|} \quad (6.4)$$

where $Z_b = \sqrt{\mu_0/(\epsilon_0\epsilon_b)}$ is the intrinsic impedance of the background, $H_1^{(2)}$ is the second-kind Hankel function of order one and $\vec{r}_t = x_t\hat{x} + y_t\hat{y}$ is the position vector of transmitter t .

An inverse crime is avoided by adding 3% additive white noise to the scattered field data [98]. The noise is added to each spatial component of the field separately. In addition, the synthetic data is generated using meshes that are different from the ones used to perform the inversion. As for TM cases, during the inversion process the estimates at each iteration are constrained to lie within physical bounds, that is $\text{Re}(\epsilon_r) \geq 1$ and $\text{Im}(\epsilon_r) \leq 0$. For each example, the inversion algorithm is run for 2048 iterations to ensure convergence. A summary is provided in Table 6.6 and the calculated error vector-norms are provided in Table 6.7. The cost functional convergence for each example is shown in Figures 6.26.

6.2.6.1 Imaging inside a Conductive Enclosure

As previously discussed, one advantage of using an FEM-based inversion algorithm is the ability to perform imaging in different conductive enclosure shapes without any modifications to the algorithm itself [29, 100]. In this section, microwave imaging for the TE case is done in a triangular conductive enclosure.

The OI in this example is the same as the OI described in Section 6.2.3.2. The

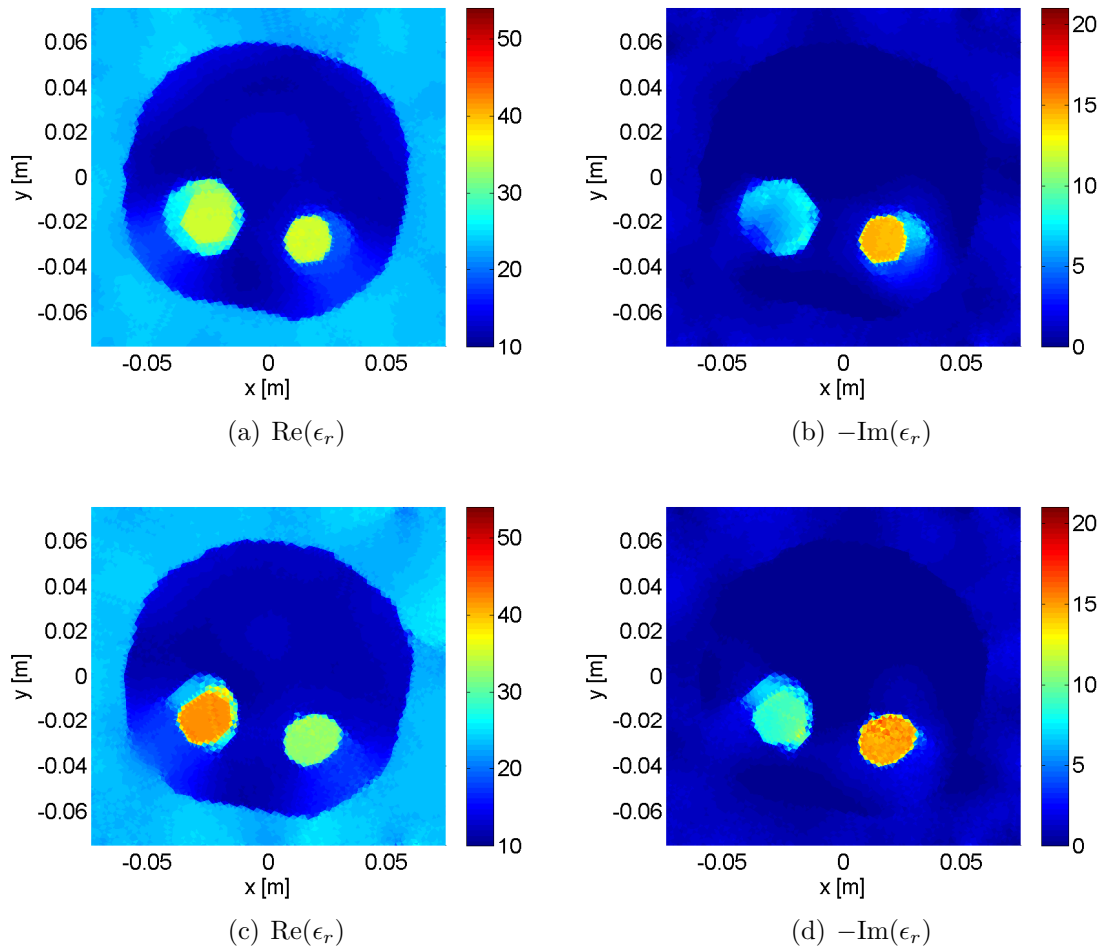


Figure 6.22: The MR-FEMCSI reconstructions of a frequency $f = 1$ GHz for (a)-(b) an unbounded domain problem and for (c)-(d) a domain enclosed by triangular conductive boundary.

target configuration is shown in Figure 6.2. The OI is centered within a conductive enclosure shaped as an equilateral triangle of side-length equal to 0.42 m, and it is surrounded by a background medium of relative permittivity $\epsilon_b = 23.4 - j1.13$ at a frequency $f = 1$ GHz. The OI is interrogated by 32 transmitters and the scattered data are collected at 32 receivers per transmitter, co-located with the transmitters. The transmitters are magnetic line sources. The x and y components of the TE scattered field are collected. The transmitting and receiving points are evenly spaced on a circle of radius 0.1 m. For comparison purposes, imaging is performed also with the OI immersed in an unbounded homogeneous region.

The inversion domain is a square centered in the middle of the problem domain with side-length equal to 15 cm. The inversion domain consists of approximately 12,000 unstructured arbitrarily oriented triangles. The unknown contrast, $\underline{\chi}$, and contrast source, $\underline{\vec{w}}_t$, variables in the inversion algorithm are located at the centroids of these triangles. Recall that the electric field is solved using edge elements for the TE case.

The reconstructions after 2048 iterations are shown in Figure 6.22. For both configurations, the unbounded and the triangular conductive enclosure, the features

Table 6.6: Summary of 2D and 3D Vectorial Inversion Examples

Example	f (GHz)	T	N_e	E	I	t_{iter} (s)
Circular Lossy Targets (2D)	1	32				
Triangular Conductive Enclosure			40159	60540	12238	9
Unbounded			24338	36689	12375	6
Lossy E-phantom (2D)	0.9	16	20974	31626	7651	
Transverse Electric						2.7
Transverse Magnetic						0.7
Heterogeneous Lossy Cube (3D)	1	72	36767	45176	18656	149

Table 6.7: Errors for 2D and 3D Vectorial Inversion Examples

Example	L_1	L_2	L_∞	$\log(\mathcal{F}^S(\underline{\vec{w}}_t))$
Circular Lossy Targets (2D)				
Triangular Conductive Enclosure	8.70%	19.39%	77.10%	-5.64
Unbounded	9.27%	19.25%	63.92%	-5.63
Loss E-phantom (2D)				
Transverse Electric				
MR-FEMCSI	2.09%	2.74%	10.09%	-6.91
BMR-FEMCSI $Q = 20$	1.70%	2.38%	9.95%	-6.94
Transverse Magnetic				
MR-FEMCSI	1.72%	2.41%	10.03%	-11.87
BMR-FEMCSI $Q = 20$	1.54%	2.26%	9.67%	-11.86
Heterogeneous Lossy Cube (3D)				
FEMCSI	4.87%	15.33%	71.33%	-8.65
MR-FEMCSI	4.73%	15.01%	70.87%	-8.63

of the OI are reconstructed successfully. In both configurations, the estimated real and imaginary relative permittivity values are close to the true values.

6.2.6.2 Lossy E-phantom: TM-TE comparison

The next OI, considered for purposes of comparing TM with TE reconstructions, is the “e-phantom” which consists of multiple concave features as depicted in Figure 6.23. The complex relative permittivity of the OI is $\epsilon_r = 70 - j17$, and it is immersed in an unbounded homogeneous background with complex relative permittivity of $\epsilon_b = 77.5 - j20.0$. The OI is illuminated by 16 transmitters at a frequency of $f = 0.9$ GHz and the scattered data are collected using 16 receivers per transmitter. The transmitters are electric line sources in TM case and magnetic line sources in the TE case. The z component of the scattered field is collected in the TM case and the x and y components are collected in the TE case. The transmitting and receiving

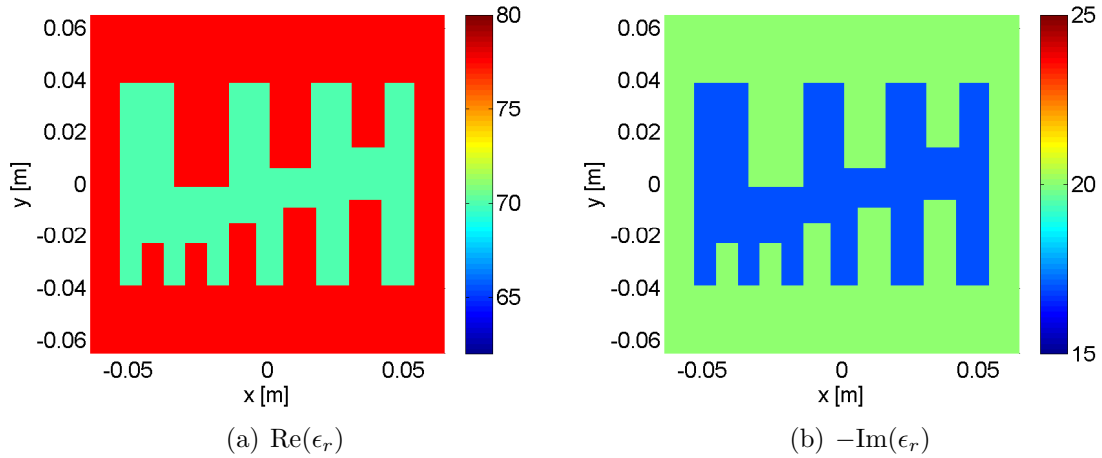


Figure 6.23: The exact profile of “e-phantom” at a frequency $f = 0.9$ GHz.

points are evenly spaced on a circle of radius 0.1 m.

In both cases, the inversion domain is a square centered in the middle of the problem domain with side-length equal to 13 cm. The inversion domain consists of 7651 unstructured arbitrarily oriented triangles. The unknown contrast, $\underline{\chi}$, and contrast source, \vec{u}_t , variables are located at the centroids of these triangles. The TM and TE datasets are inverted using MR-FEM-CSI with inversion results for TE and TM cases shown in Figure 6.24.

The reconstruction results for the TE case are shown in Figures 6.24 (a) and (b), while Figures 6.24 (c) and (d) show results for the TM case. The cost functional convergence is shown in Figure 6.26 (b). For both polarizations, the value of the complex relative permittivity of the target is estimated accurately, but all of the features show up only for the TE case. The smallest “finger” of the phantom does not show up well in the TM reconstruction. This is consistent with the conclusion arrived at by Mojabi and LoVetri [35] who speculated that more accurate reconstructions may be obtained using TE data than using TM data, especially with only a few transmitters and receivers being used. The imaginary component reconstructions

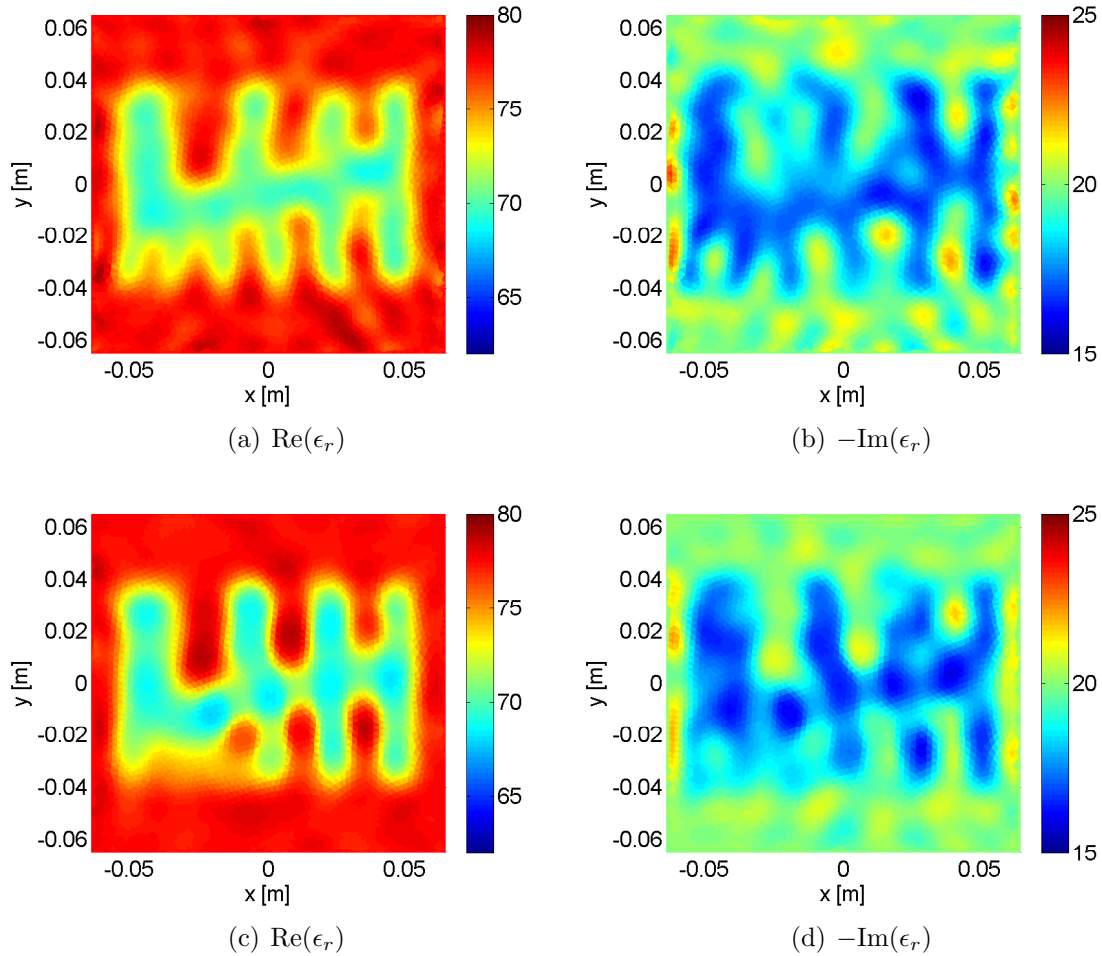


Figure 6.24: MR-FEMCSI reconstructions at $f = 0.9$ GHz for (a)-(b) the TE case and (c)-(d) the TM case.

show oscillatory artifacts for both the TM and TE cases, and this is due to the imbalance between the relative permittivity's real and imaginary components for the background medium and the OI. This problem can be ameliorated using the balanced MR-FEMCSI algorithm, as the results shown in Figure 6.25 demonstrate.

As listed in Table 6.6, the time per iteration is 3.5 times more for the TE case than the TM case. This is expected as more computations are required at each iteration for the TE inversion.

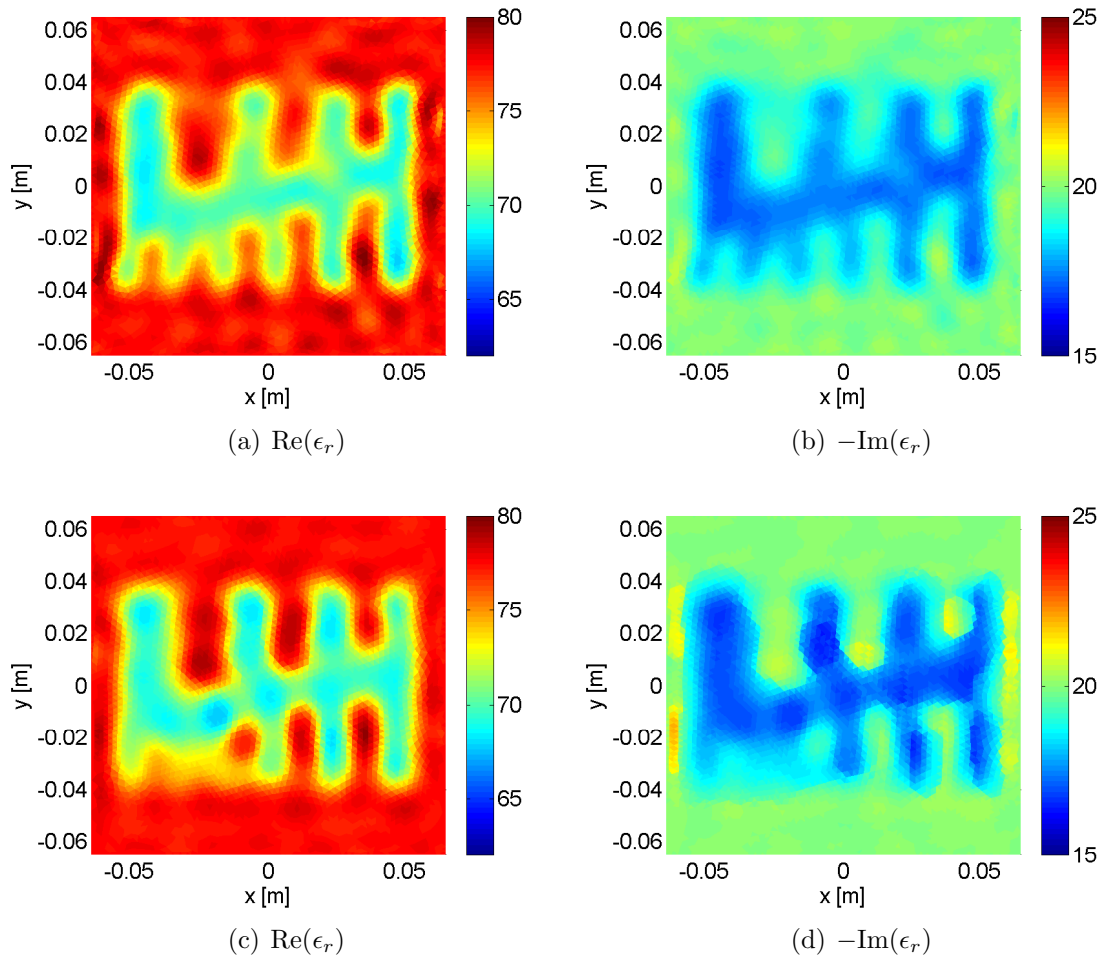


Figure 6.25: BMR-FEMCSI reconstructions for $Q = 20$ at $f = 0.9$ GHz for (a)-(b) the TE case and (c)-(d) the TM case.

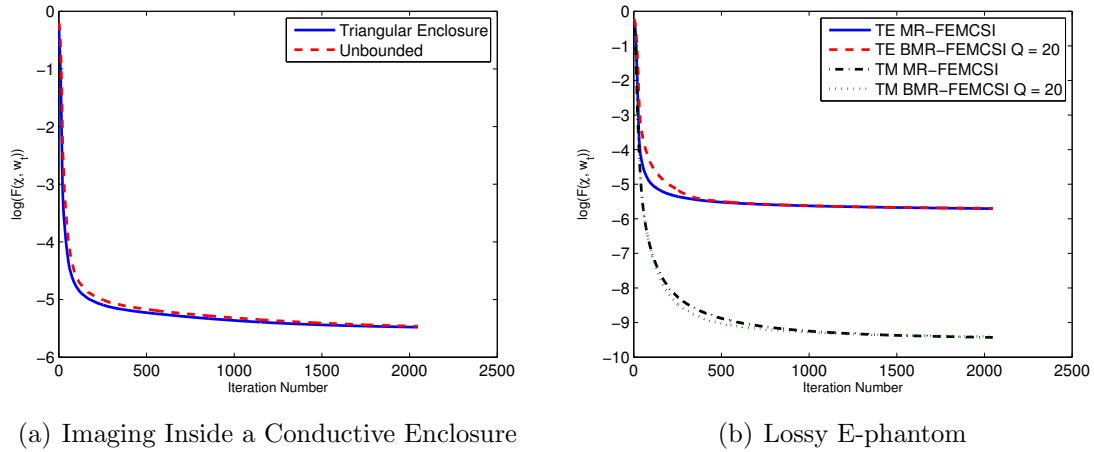


Figure 6.26: The cost functional versus the iteration number for (a) imaging inside a conductive enclosure and (b) lossy E-phantom synthetic datasets reconstruction.

6.2.6.3 Section Conclusion

The FEM-CSI algorithm and its variants have been validated for 2D microwave imaging under the TE approximation of the fields. The algorithm retains the advantages of FEM-CSI, such as the ability to invert on an unstructured triangular mesh, as well as the ease of modeling different boundary types and shapes. In addition to testing the algorithm, the last example which was considered shows that better reconstructions are obtained using TE data in comparison to TM data, confirming the conclusions of previous publications.

6.2.7 Inversion of 3D Datasets

In this section, the FEM-CSI algorithm and its multiplicative regularized form are tested using a 3D full-vectorial problem. Due to the computational complexity associated with three-dimensional problems, a simple example is selected to demonstrate the functionality of the algorithm. As well as testing the method, a brief study

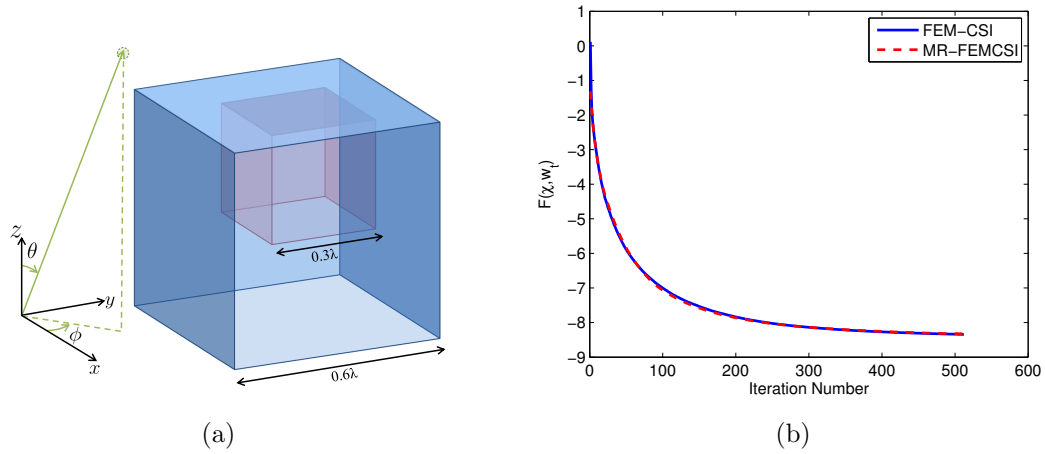


Figure 6.27: (a) The coordinates configuration and the OI depiction. (b) The cost functional progress for the inversion of 3D synthetic dataset.

that outlines the use of different techniques to solve the FEM matrix equations is presented in this section.

6.2.7.1 A Heterogeneous Lossy Dielectric Cube

The OI consists of two cubes: an outer cube with side-length equal to $0.6\lambda_b$ centered at the origin of the problem domain Ω , and an inner cube with side-length equal to $0.3\lambda_b$ with its center having coordinates $(0.05\lambda_b, 0.05\lambda_b, 0.05\lambda_b)$. Here λ_b is the background medium wavelength at the operating frequency $f = 1$ GHz. In this example, the background medium is free-space, hence $\epsilon_b = 1$. The outer cube is lossless and it has a relative permittivity of $\epsilon_r = 1.5$. The inner cube is lossy and has a complex relative permittivity of $\epsilon_r = 2 - j2$. The OI is depicted in Figure 6.27 (a), while two-dimensional cross-sections of the OI's real and imaginary relative permittivity at different planes are shown in Figures 6.28 (a)-(c) and Figures 6.29 (a)-(c). This same target and configuration was used to test a 3D GNI technique in [105].

The OI is illuminated with single plane waves incident at a multitude of directions. The plane waves' incident polar angle θ varies from 25° to 155° in 26° steps. For each polar angle, the azimuthal angle ϕ varies from -150° to 180° in 30° increments. Hence the total number of incident directions is 72. The orientation of the spherical coordinate system is given in Figure 6.27 (a). The incident plane waves are selected to have a magnitude of 1 and a phase angle of 0 at $(0, 0, 0)$. The electric field associated with each incident plane wave is polarized such that it has equal θ - and ϕ - components:

$$\begin{aligned}\vec{E}_t^{\text{inc}}(\vec{r}) &= E_{t,\theta}^{\text{inc}}\hat{\theta} + E_{t,\phi}^{\text{inc}}\hat{\phi} \\ &= [\hat{\theta} + \hat{\phi}]\frac{e^{jk_b\hat{k}_t\cdot\vec{r}}}{\sqrt{2}}\end{aligned}\tag{6.5}$$

where $\vec{r} = x\hat{x} + y\hat{y} + z\hat{z}$ is the position vector of an observation point, k_b is the wavenumber of the background medium and

$$\hat{k}_t = \sin(\theta_t)\cos(\phi_t)\hat{x} + \sin(\theta_t)\sin(\phi_t)\hat{y} + \cos(\theta_t)\hat{z}.\tag{6.6}$$

Here θ_t and ϕ_t denote the polar and azimuthal angles of an incident plane wave produced by a transmitter t . We say that the plane-wave is incoming from the (θ_t, ϕ_t) direction. In Cartesian coordinates, the incident electric field is written as

$$\begin{aligned}\vec{E}_t^{\text{inc}}(\vec{r}) &= E_{t,x}^{\text{inc}}\hat{x} + E_{t,y}^{\text{inc}}\hat{y} + E_{t,z}^{\text{inc}}\hat{z} \\ &= (\hat{x}[\cos(\theta_t)\cos(\phi_t) - \sin(\phi_t)] + \hat{y}[\cos(\theta_t)\sin(\phi_t) + \cos(\phi_t)] - \hat{z}\sin(\theta_t)) \\ &\quad \times \frac{e^{jk_b\hat{k}_t\cdot\vec{r}}}{\sqrt{2}}.\end{aligned}\tag{6.7}$$

For each transmitter, the scattered field data are collected at 72 receivers points distributed on the surface of a sphere with radius $2\lambda_b$ centered around the target. The receiver points are specified using θ and ϕ in the spherical coordinate system. Thus for each dataset, the total number of measurements is $72 \times 72 = 5,184$. For each scattered field measurement, all three Cartesian components are collected.

The synthetic datasets are generated using an FEM solver where 3% noise is added according to (6.1). The noise is added to each spatial component of the vector field separately. The mesh used to generate the synthetic data is different from the inversion mesh. The algorithms are allowed to run for 512 iterations to ensure convergence. The contrast estimates after each iteration are constrained to lie within physical bounds, *i.e.* $\text{Re}(\epsilon_r) > 1$ and $-\text{Im}(\epsilon_r) > 0$. The inversion domain is selected as a sphere with radius 0.165 m and centered at the origin. The unknowns are located at the centroids of 18,656 tetrahedra. A summary of the inversion problem is given in Table 6.6 and the cost functional convergence is shown in Figure 6.27 (b). A 1-D cross-section of the reconstruction across the plane $y = 0.015$ m is shown in Figure 6.30.

The FEM-CSI and MR-FEMCSI imaging results at planes $x = 0.015$ m, $y = 0.015$ m and $z = 0.015$ m are shown in Figures 6.28 (d)-(i) for the real part of the reconstructions and Figures 6.29 (d)-(i) for the imaginary part. The results are cross-sections through the tetrahedral mesh; hence the triangular faceted nature of the image. The expected borders of the two cubes are depicted with solid white lines in each plot. The L_p error vector-norms for this example are given in Table 6.7.

The inversion algorithms are able to detect the location and the dimensions of the cubes; nevertheless their shapes are deformed, especially the inner cube. The close to *spherical* shape of the inner cube is due to the reconstruction being performed on

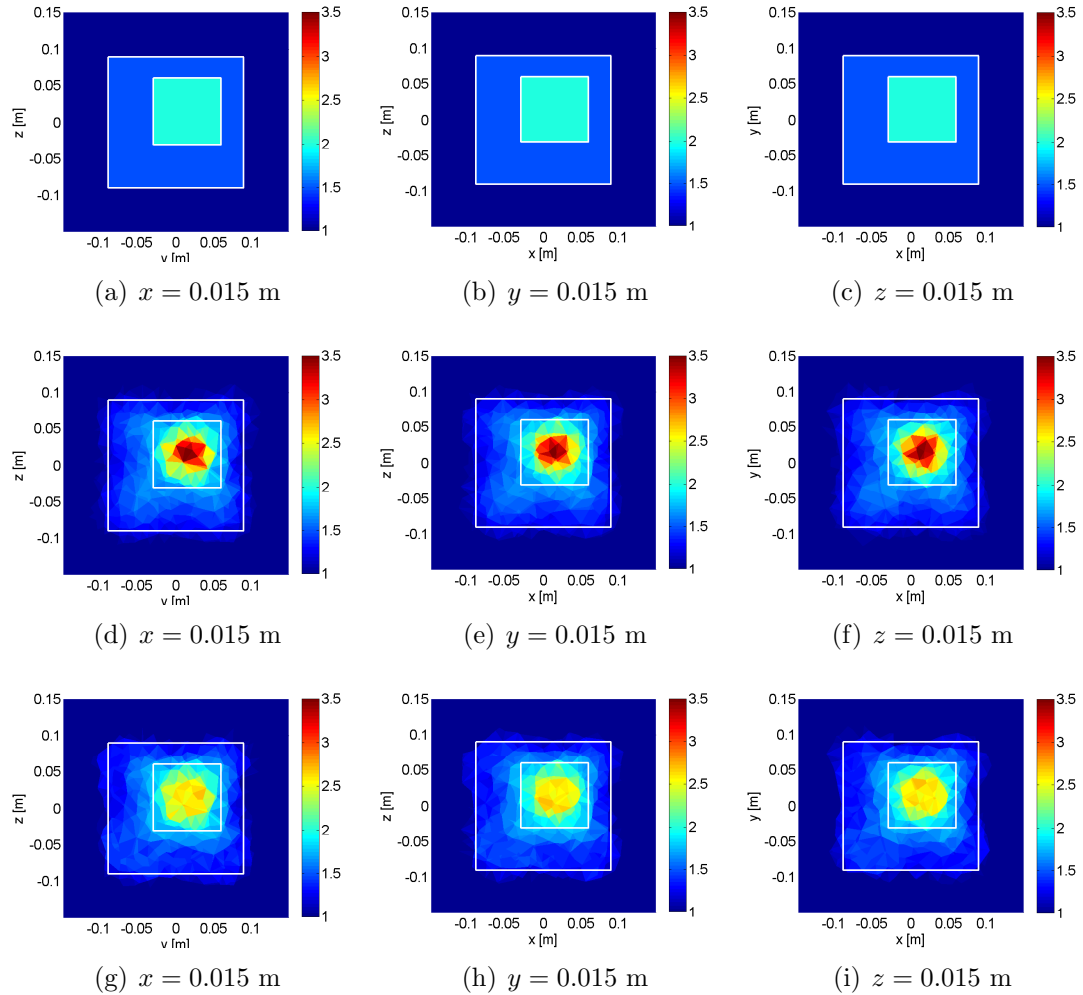


Figure 6.28: The real component $\text{Re}(\epsilon_r)$ of the (a)-(c) the actual OI, the reconstructions using (d)-(f) FEM-CSI and (g)-(i) MR-FEMCSI at planes $x = 0.015\text{m}$, $y = 0.015\text{m}$ and $z = 0.015\text{m}$.

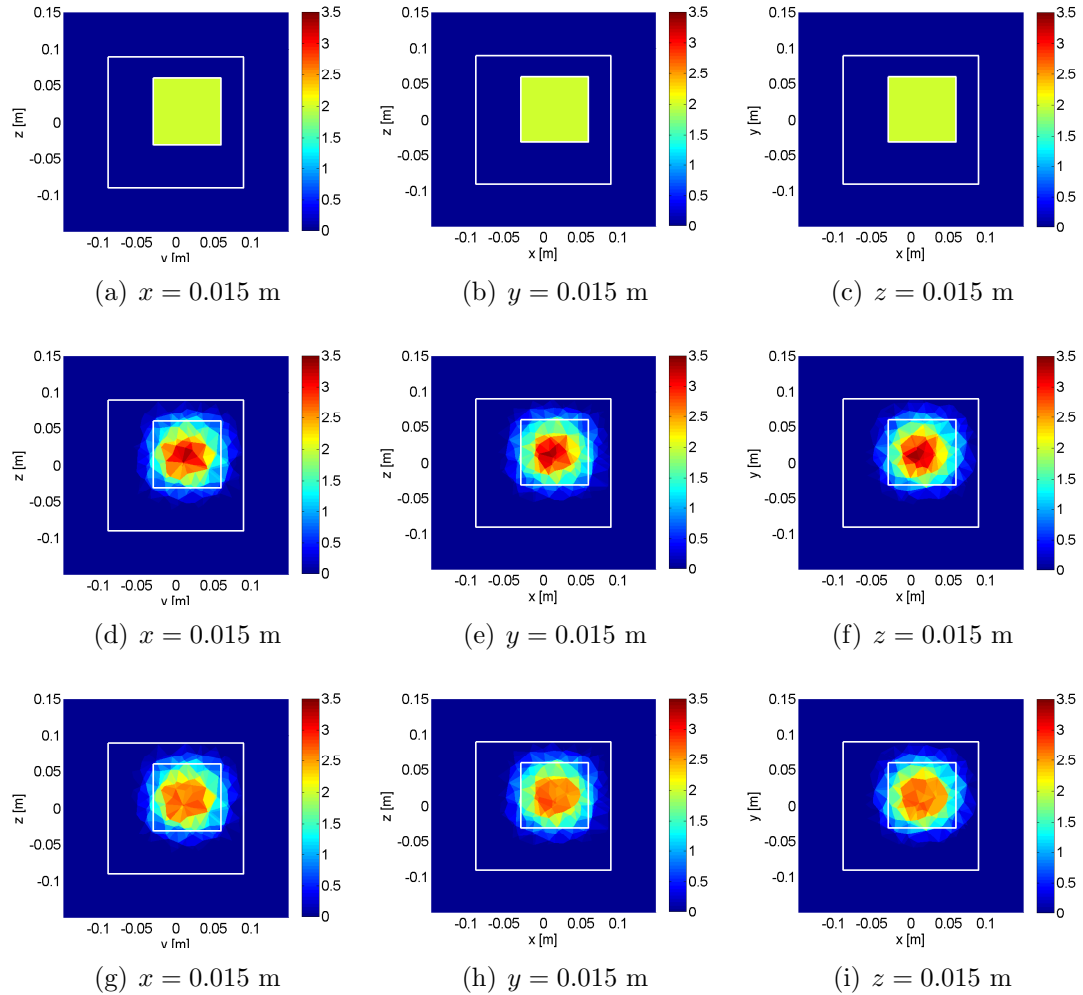


Figure 6.29: The imaginary component $-\text{Im}(\epsilon_r)$ of the (a)-(c) the actual OI, the reconstructions using (d)-(f) FEM-CSI and (g)-(i) MR-FEMCSI at planes $x = 0.015$ m, $y = 0.015$ m and $z = 0.015$ m.

a mesh with arbitrarily oriented tetrahedra; thus the edges of the tetrahedra will, *most probably*, not line up with the cube edges. This can be fixed by increasing the number of tetrahedral elements in the mesh, but this will cause an increase in the computational resources required to solve the problem. Such resources are not currently available given the serial nature of the implementation.

The results using multiplicative regularization are smoother and less oscillatory and one can easily distinguish the two objects. With respect to the permittivity values, both algorithms tend to correctly predict that the outer cube is lossless. The real component of the outer cube is smooth but underestimated to an average value of 1.33 using MR. As for the FEM-CSI reconstruction, the outer cube's real part increases from 1 to 1.75 as can be seen from Figure 6.30 (a). The inner cube is better predicted with the inclusion of the L_2 weighted norm; the FEM-CSI algorithm overestimates the imaginary part of the relative permittivity to values as high as 3.5. This can be observed from the 1-D plot in Figure 6.30 (b). The real part of the inner cube is overestimated by both algorithms, however the FEM-CSI prediction is larger than 3 whereas the MR-FEMCSI has an average of approximately 2.3.

Due to the mesh's unstructured nature, the 2D plots shown in Figures 6.28 and 6.29 do not appear aesthetically pleasing. This can be resolved by interpolating the results to a 3D cubical grid and then smoothing them spatially using a convolutional filter*. A 2D slice at $z = 0.015$ m for the MR-FEMCSI reconstruction interpolated to a 3D grid and then filtered is shown in Figure 6.31. The left column contains the interpolated results, whereas the right column shows the interpolated results after filtering. The procedure does not change the estimated values nor the dimensions of the reconstruction as can be seen by comparing the filtered results at $z = 0.015$ m with

*The MATLAB built-in function *smooth3* was used to create the spatial convolutional filter.

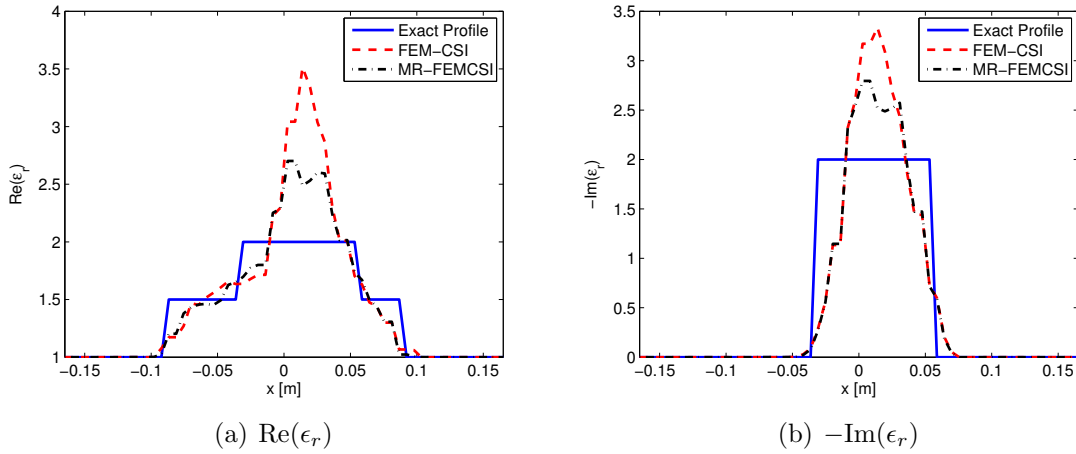


Figure 6.30: A 1-D cross-section across the plane $y = 0.015$ m for the exact profile (solid blue), FEM-CSI reconstruction (dash red) and MR-FEMCSI (dash-dot black).

Figures 6.28 (i) and 6.29 (i). It simply makes the results more aesthetically appealing. Reconstructions for all subsequent 3D datasets in this thesis will be presented after post-processing them using the described method.

6.2.7.2 Comparison of Computational Resource using Different Solvers

The current implementation of the 3D algorithms utilizes sparse matrix LU-decomposition with column pre-ordering to calculate the inverse FEM operator $\vec{\mathcal{L}}$. This technique incurs large memory requirements, and so an alternative with lower memory requirements would be to use iterative techniques like GMRES. Here a brief description of the computational time and memory usage of LU-decomposition verses GMRES is studied. The study is undertaken using MATLAB, thus the time and memory usage are measured using built-in MATLAB functions. The objective of the study is not to compare the accuracy of the results from the two methods nor to recommend a particular technique, but merely to justify why, within the scope and the time-frame of the thesis, LU decomposition was selected over an iterative technique.

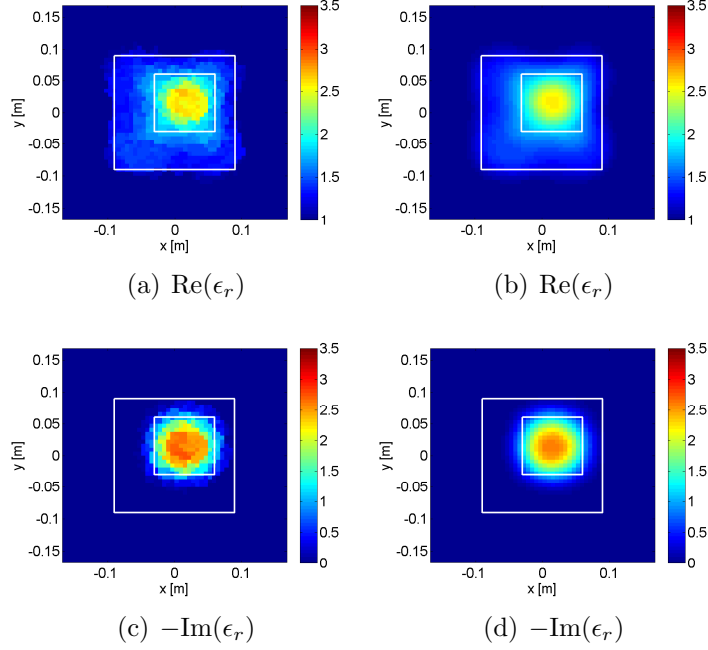


Figure 6.31: The MR-FEMCSI reconstruction at plane $z = 0.015$ m interpolated to a cubic grid (a), (c) without spatial filtering and (b), (d) with spatial filtering.

Let us consider a 3D mesh with $N_e = 34,505$ tetrahedral elements interconnected via $E = 42,552$ edges. The FEM matrix equation can be written as

$$\mathcal{K}_\chi[\underline{E}_t^{\text{sct}}] = \vec{\mathcal{R}}_\chi \cdot \vec{E}_t^{\text{inc}}. \quad (6.8)$$

where $\mathcal{K}_\chi \in \mathbb{C}^{E \times E}$ and $\vec{\mathcal{R}}_\chi \in \mathbb{C}^{E \times N_e}$ are sparse symmetric matrices dependent on the problem boundary as well as the background wavenumber and the contrast of the OI. For this example, the OI is the system of cubes presented in Section 6.2.7.1 surrounded by free-space within a domain Ω truncated by absorbing boundaries. The data vectors $\underline{E}_t^{\text{sct}} \in \mathbb{C}^E$ and $\vec{E}_t^{\text{inc}} \in \mathbb{C}^{N_e}$ are, respectively, the scattered field values along the mesh edges and the incident field spatial-vectors at the centroids of the mesh tetrahedra. The goal of the matrix equation is to solve for the tangential scattered

field values $\underline{E}_t^{\text{sct}}$, hence the FEM equation can be rewritten as

$$\underline{E}_t^{\text{sct}} = \vec{\mathcal{L}} \left[\underline{\vec{E}}_t^{\text{inc}} \right] = \mathcal{K}_\chi^{-1} \left[\vec{\mathcal{R}}_\chi \cdot \underline{\vec{E}}_t^{\text{inc}} \right] \quad (6.9)$$

where $\vec{\mathcal{L}}$ is the inverse FEM matrix. Thus, to calculate the scattered field vector $\underline{E}_t^{\text{sct}}$ the inverse of matrix \mathcal{K}_χ is required. Practically, this is not feasible as the inverse of a sparse matrix is not sparse, and will therefore require a very large amount of memory and will take a long time to compute. The alternative is to resort to solving equation (6.8) whenever required using direct or iterative methods.

The direct method used in this study involves computing the LU-decomposition of the sparse, symmetric matrix \mathcal{K}_χ using UMFPACK and then using back-substitution techniques to calculate the scattered field as required. The iterative method selected for this study is GMRES using no preconditioner at first, and then testing it with diagonal and incomplete LU preconditioning. For GMRES, the algorithm inputs are \mathcal{K}_χ and the evaluation of $\vec{\mathcal{R}}_\chi \cdot \underline{\vec{E}}_t^{\text{inc}}$. The setup parameters for GMRES are the initial guess, the maximum number of inner and outer iterations and an error tolerance. The initial guess is selected to be zero, the error tolerance is set to 0.001 and the maximum number of inner and outer iterations are 20 and 100, respectively. Furthermore, when incomplete LU is used as a preconditioner additional parameters need to be set. The GMRES parameters are selected *ad-hoc* by *trial-and-error* to ensure an acceptable convergence. The results of the study are summarized in Table 6.8.

Whether LU or GMRES with preconditioning is utilized, the required matrices are computed once, saved and recalled when necessary. Amongst the different techniques, LU-decomposition required the largest amount of memory. Nevertheless, after calculating the decomposition matrices \mathbf{L} and \mathbf{U} along with the pre-ordering matrices \mathbf{P} and \mathbf{Q} , this method calculated the solution in the least amount of time compared to

Table 6.8: Computational Resources Required for Different Solvers

Solver	Time and Iterations	Memory ^[1]	Error ^[2]
LU with back-substitution			
Decomposition	35.17 s	L : 455 MB U : 455 MB P : 1 MB Q : 1 MB	
Solving (6.8)	0.69 s		
GMRES			
No Preconditioner	107.4 s 76 iterations		0.11%
Diagonal Preconditioner			
Constructing matrices	0.03 s	$\mathcal{K}_{\chi,diag}$ ^[3] 1.30 MB	
Solving (6.8)	68.17 s 48 iterations		0.12%
Incomplete LU			
Constructing matrices	111.52 s	L _{inc} ^[3] 148 MB U _{inc} : 148 MB	
Solving (6.8)	2.78 s 14 iterations		0.14%

^[1] Here, the extra memory required to compute the problem using a certain solver is only noted.

^[2] The error is calculated as $\left(\|\underline{x}^{\text{GMRES}} - \underline{x}^{\text{LU}}\|^2 / \|\underline{x}^{\text{LU}}\|^2\right)$ where $\underline{x}^{\text{LU}}$ and $\underline{x}^{\text{GMRES}}$ are the LU and GMRES solutions respectively.

^[3] The abbreviations *diag* and *inc* stand for diagonal and incomplete.

GMRES with the different preconditioners. With GMRES, the best time was achieved using incomplete LU preconditioning however it had to calculate the matrices \mathbf{L}_{inc} and \mathbf{U}_{inc} beforehand.

The calculation times shown in Table 6.8 are for a single transmitter. Given T transmitters for a particular problem, at each inversion algorithm iteration a minimum of $6 \times T$ evaluations equivalent to (6.8) are required. In the work presented in the thesis, the 3D mesh densities are kept to within feasible limits, such that it is more time-efficient to use LU-decomposition techniques and get satisfactory results. The memory requirement can be handled as the workstation used to develop the algorithm has 18 GB of physical memory.

Nevertheless, if the number of elements within the mesh increases, the memory requirement would surge to an amount which could not be handled by a typical workstation. The solution would then be to use iterative methods, the parallelization of which is beyond the scope of the thesis. Further details about iterative methods for sparse systems can be found in [106].

Table 6.9: Summary of 2D Experimental Datasets

Example	f (GHz)	T	N_e	N^*	I	t_{iter} (s)
University of Manitoba						
E-Phantom	5	24	38496	19390	13706	2.90
Wood-Nylon	3	24	15826	8060	4522	0.85
Human Forearm	0.8, 1, 1.2	24	64360	32387	11455	4.00
UPC	2.33	64	101520	55127	22582	39.81
Institut Fresnel 2D			40982		17887	
TM				20726		
<i>FoamDielInt</i>	2 – 10	8				21
<i>FoamDielExt</i>	2 – 10	8				21
<i>FoamTwinDiel</i>	2 – 10	18				40
<i>FoamMetExt</i>	2 – 18	18				80
TE				61707		
<i>FoamDielInt</i>	2 – 10	8				27
<i>FoamDielExt</i>	2 – 10	8				27
<i>FoamTwinDiel</i>	2 – 10	18				42
<i>FoamMetExt</i>	2 – 18	18				90

* For the TE case, this is the number of edges E in the inversion mesh.

6.3 Experimental Results

6.3.1 UofM Microwave Tomography System

The research group at the University of Manitoba (UofM) has constructed a microwave imaging system with a Plexiglas casing [22], as well as a prototype with a metallic enclosure [21]. A picture of the system with the Plexiglas casing is shown in Figure 6.32 (a), and with the conductive enclosure in Figure 6.33 (a). Despite the 3D nature of the actual system, the inversion of the measurement datasets obtained from the system is performed under the 2D TM assumption, *i.e.* $\vec{E}_t^{\text{sct}} = E_{t,z}^{\text{sct}} \hat{z}$ and

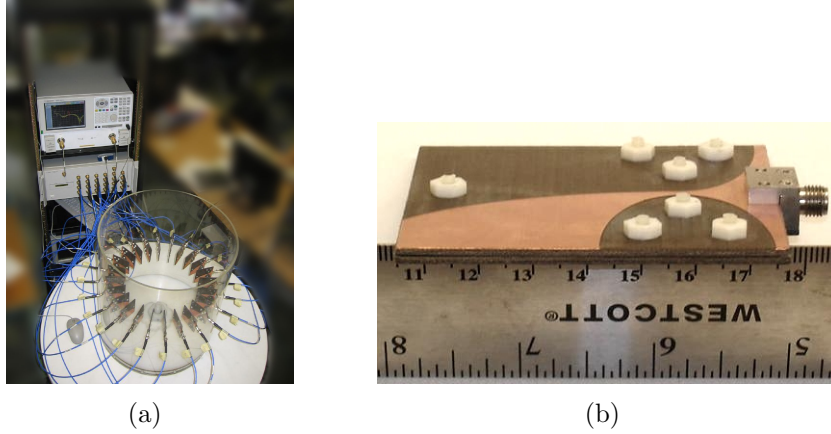


Figure 6.32: (a) The MWT system with the Plexiglas casing. (b) A Vivaldi antenna.

$$\vec{E}_t^{\text{inc}} = E_{t,z}^{\text{inc}} \hat{z}.$$

The microwave imaging system consists of a vector network analyzer (VNA), an Agilent PNA E8363, used as a microwave source and receiver. The VNA is connected to the antennas via a 24 matrix switch (Agilent 87050A-K24). The experimental apparatus is controlled via a computer workstation which is connected through a local-ethernet device. As transducers (transmitters/receivers), the system employs twenty-four antennas arranged at even intervals of 15° in a circular array at the midpoint height along the inside of the enclosures. At a single frequency, 23 data points are collected per transmitter, thus the total number of measurements is $23 \times 24 = 552$ per dataset.

The background medium for the Plexiglas system is free-space ($\epsilon_b = 1$). The air-filled system uses Vivaldi antennas as transmitters and receivers [107]. A picture of a Vivaldi antenna is shown in Figure 6.32 (b). The design bandwidth of the antennas is from 3 GHz to 10 GHz. The optimum operational frequencies of this system were chosen utilizing a frequency-selection procedure outlined in [22]. The Vivaldi antennas are assumed to be evenly spaced on a circle of ≈ 13.0 cm radius for

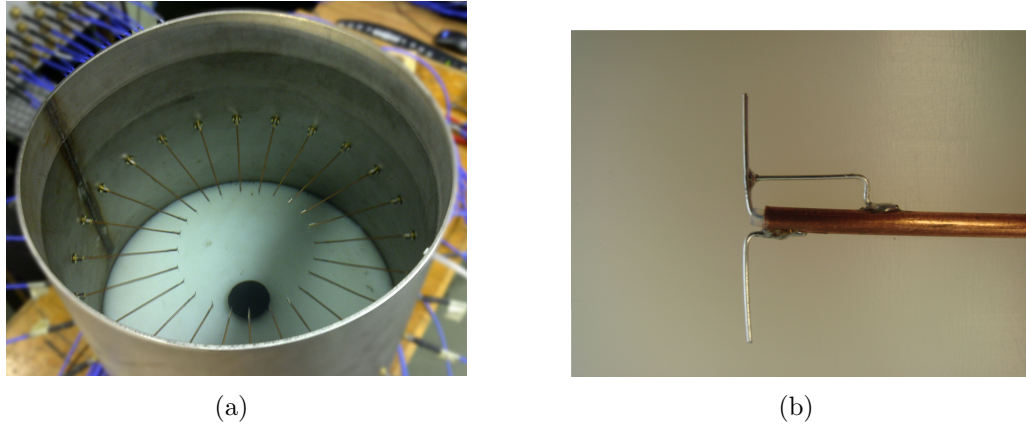


Figure 6.33: (a) The metallic enclosure. (b) A dipole antenna with quarter wavelength balun.

the inversion algorithms. The Plexiglas cylinder has a radius of ≈ 22 cm and is 50.8 cm in height.

For the metallic enclosure system, the main purpose is to image biological targets, hence the system uses a fluid of deionized water and table salt as a background medium. The matching fluid is selected to decrease the image contrast, as well as to reduce the modeling error between the assumed computational model and the actual system. The system utilizes 24 dipole antennas with a quarter-wavelength balun. A picture of a single dipole is shown in Figure 6.33 (b). The antennas are located at a radius of 9.4 cm from the center of the chamber. The metallic enclosure has a radius of 22.4 cm and is filled, to a height of 44.4 cm, with a matching fluid. The system is capable of imaging from approximately 0.8 GHz to 1.2 GHz in a salt/deionized water background. A study of the matching fluid selection as well as a full description of the system are detailed in [91].

For a transmitter t , the VNA system measures the S -parameter $S_{r,t}$ which is the ratio of the voltage measured at a receiver port r to the voltage transmitted via port t . As the inversion algorithms require scattered field measurements, the *raw*

S -parameter data must be calibrated. For each dataset three S -parameter measurements are collected: the measurements without the presence of the OI and are labeled as incident data; the measurements with the unknown target in the system and are denoted as the OI total data; and the measurements with a reference object in the system and are called the reference total data. The scattered data due to the OI is calculated by subtracting the incident data from the OI total data; this is called $S_{r,t}^{\text{sct,OI}}$. Similarly, the scattered data due to the reference is evaluated by taking the difference between the incident and the reference total data; this is denoted as $S_{r,t}^{\text{sct,ref}}$. Assuming a 2D line source model for the incident field, the scattered electric field data from the known reference, $E_{r,t}^{\text{sct,ref}}$, can be calculated analytically for the model. The reference object typically used in the UofM system is a metallic cylinder. Finally, the calibrated measured fields, $E_{r,t}^{\text{sct}}$, for the unknown OI are calibrated using

$$E_{r,t}^{\text{sct}} = \frac{E_{r,t}^{\text{sct,ref}}}{S_{r,t}^{\text{sct,ref}}} S_{r,t}^{\text{sct,OI}}. \quad (6.10)$$

This method of calibration eliminates any measurement errors which are *constant* over the two scattered data measurements, $S_{r,t}^{\text{sct,ref}}$ and $S_{r,t}^{\text{sct,OI}}$. Examples of the removable errors include cable losses, phase shifts and mis-matches at the connectors. This method is not capable of removing errors due to the coupling of the antennas in the system, and it has limited capacity to remove modeling error: the error introduced into the inversion process because the inversion model does not match the actual system. Further details of calibrating the UofM system are discussed in [22, 25, 91].

6.3.1.1 Inversion of UofM Datasets

Three UofM datasets are inverted using the inversion algorithms presented in this work. The inversion algorithms assume the incident field is produced by a 2D electric

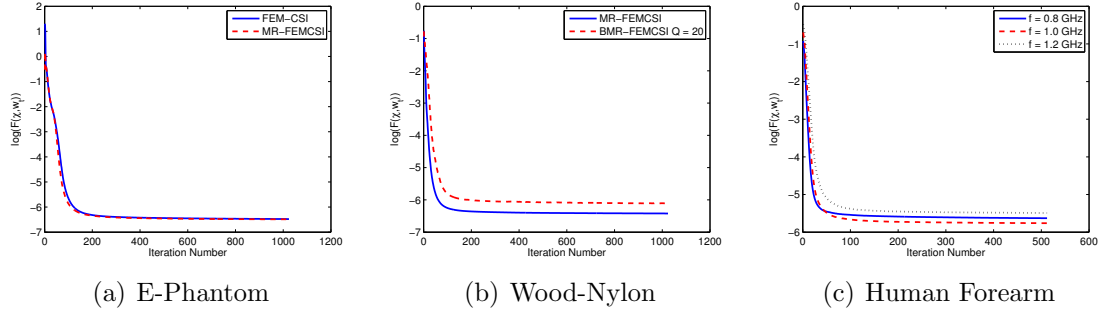


Figure 6.34: The cost functional versus the iteration number for (a) the E-Phantom, (b) wood-nylon and (c) volunteer one forearm experimental datasets reconstruction.

line source given by (6.3). Unless otherwise specified, the algorithms are allowed to run for 1024 iterations to ensure convergence. In the inversion for each dataset the results are constrained to remain within the regions defined by $1 < \text{Re}(\epsilon_r) < 83$ and $0 < -\text{Im}(\epsilon_r) < 30$. The cost functional convergence for the each dataset are shown in Figure 6.34. A summary of the examples is given in Table 6.9.

6.3.1.2 E-Phantom

As the first example, an “e-phantom” with multiple concave features is used as the target in the UofM air-filled MWT system. A side-view of the actual target is shown in Figure 6.35 (a), while the exact permittivity profile is depicted in Figure 6.35 (b). The “e-phantom” is constructed of ultrahigh-molecular-weight (UHMW) polyethylene which is a lossless material of relative permittivity $\epsilon_r = 2.3$ [108]. The inversion domain \mathcal{D} is selected to be a square centered in the problem domain Ω with side-length equal to 0.13 m.

The computational complexity of the inversion algorithm is reduced by adapting the inversion mesh such that the mesh is denser within the imaging domain \mathcal{D} in comparison to outside \mathcal{D} . This results in the number of unknowns in \mathcal{D} to be 13,706

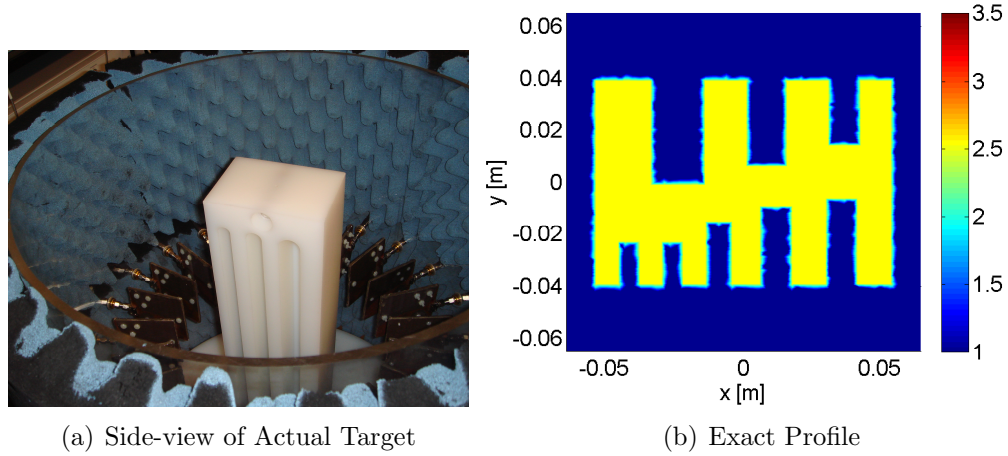


Figure 6.35: The “e-phantom” (a) inside the imaging setup, (b) its exact profile at $f = 5$ GHz.

nodes, while the total number of nodes N in problem domain Ω is 19,390. The ability to control the mesh density demonstrates an advantage of FEM-CSI in comparison to other CSI formulations.

The real parts of the relative permittivity using FEM-CSI and MR-FEMCSI are shown in Figures 6.36 (a) and (b) (the imaginary parts are omitted because the background and the target are close to being lossless). Using multiplicative regularization the shape and edges of the target is well reconstructed; however features of the “e-phantom” smaller than 8 mm (approx. $2\lambda/15$, where λ is the free-space wavelength) are not resolved. This result is similar to that obtained using MR-GNI on a uniform grid as reported in [90]. The MR-FEMCSI reconstruction is more homogeneous within the target contour in comparison to the FEM-CSI result; in addition the value of the permittivity is not overshoot by MR-FEMCSI.

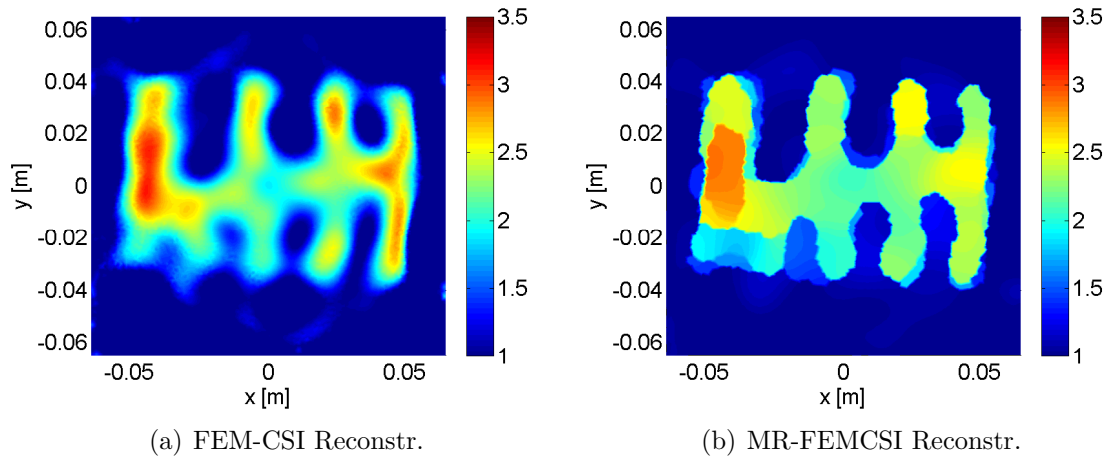


Figure 6.36: The “e-phantom” reconstruction results using (a) FEM-CSI and (b) MR-FEMCSI.

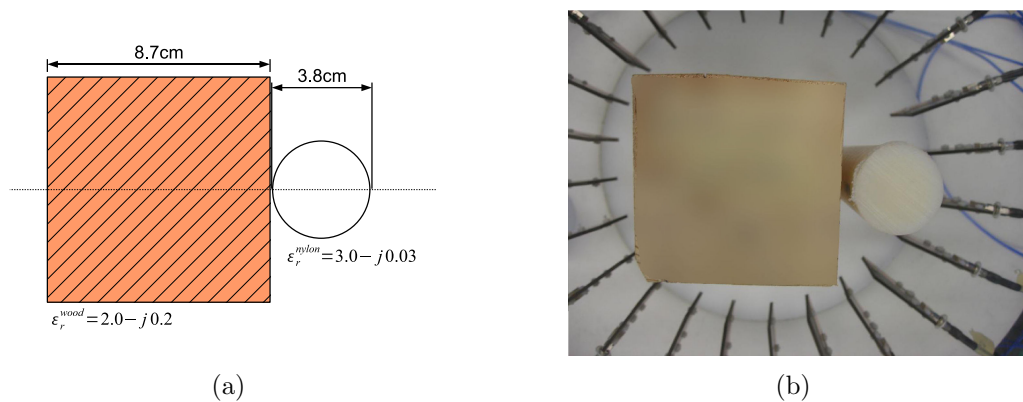


Figure 6.37: The OI consisting of a wooden block and a nylon cylinder.

6.3.1.3 Wood-Nylon Target

The next lossy dielectric example consists of a wooden block and a nylon cylinder as depicted in Figure 6.37. The relative complex permittivities are $\epsilon_r^{\text{wood}} = 2.0 - j0.2$ and $\epsilon_r^{\text{nylon}} = 3.0 - j0.03$ at a frequency $f = 3$ GHz (as measured using the Agilent 85070E dielectric probe kit). The dataset for this target is collected in the UofM air-filled system. The imaging domain \mathcal{D} is selected to be a square centered in the problem domain Ω with side-length equal to 0.24 m. The calibrated measurements are inverted using MR-FEMCSI and BMR-FEMCSI [29]. The number of unknowns in \mathcal{D} is 4,522 and they are located at the nodes of an unstructured triangular mesh. The MR-FEMCSI reconstructions are shown in Figures 6.38 (a) and (b), along with the BMR-FEMCSI results for $Q = 20$ in Figures 6.38 (c) and (d).

The reconstruction results for the real component of the OI are similar using either MR or BMR; both regularizations predicted the real component of the OI accurately. Using MR, the imaginary part reconstruction is not satisfactory; on the other hand, with BMR for $Q = 20$ the algorithm reconstructs the imaginary component of the dielectric constant for the wooden block properly with an average value of 0.11 for $-\text{Im}(\epsilon_r)$; this is slightly less than the value measured by the dielectric probe. As for the nylon cylinder, considering it is almost lossless and the MWI system used has a limited signal-to-noise ratio as well as dynamic range, the reconstruction of the cylinder's imaginary part is difficult. The obtained reconstruction is very similar to that obtained using the balanced version of GNI, PMR-GNI [87].

6.3.1.4 Human Forearm

Under a University of Manitoba Biomedical Research Ethics Board approved protocol, the UofM system with the metallic enclosure and dipole antennas was used

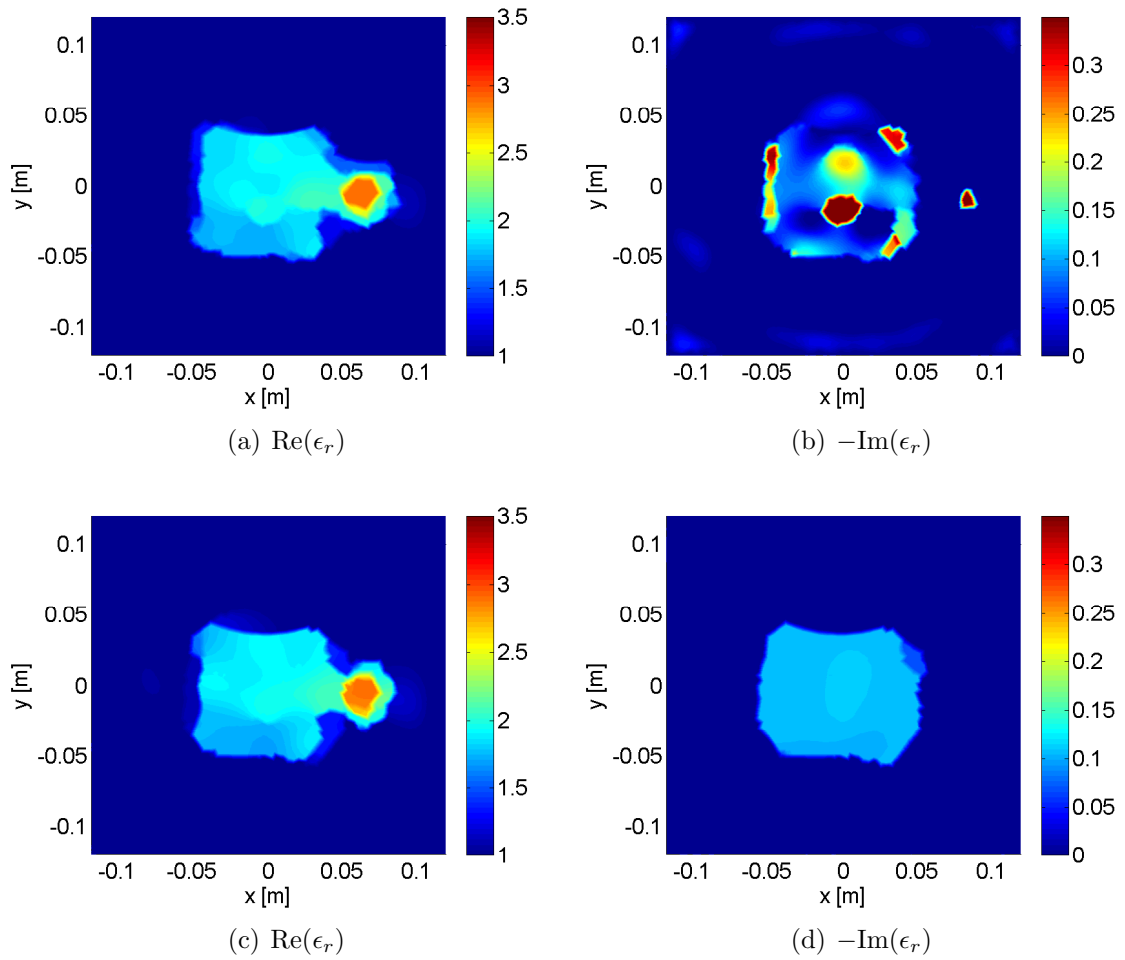


Figure 6.38: The reconstructions at a frequency $f = 3$ GHz using (a)-(b) MR-FEMCSI and (c)-(d) BMR-FEMCSI for $Q = 20$.

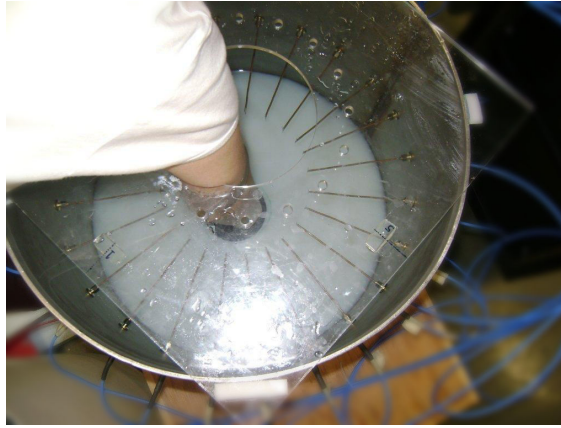


Figure 6.39: A volunteer's forearm in the microwave imaging system.

to image the forearms of 5 adult volunteers. A picture of a volunteer's forearm in the MWI system is shown in Figure 6.39. To provide a base-line on each volunteer's anatomy, each volunteer was also imaged with a 0.2 T Esaote E-scan XQ MRI machine, using a forearm coil. The MRI scan occurred less than 1 hour after the collection of the microwave data. Herein, the MWI inversion results for *Volunteer 1* at three frequencies 0.8 GHz, 1.0 GHz, and 1.2 GHz are shown. The associated MRI is also shown. A detailed discussion of the study and more results are provided in [26].

The metallic enclosure was filled with approximately 70 litres of fluid with the amount of salt added being approximately 3.1 grams/litre. A plot of the permittivity of the matching fluid is shown in Figure 6.40. At 1 GHz, the relative permittivity of the matching fluid is $\epsilon_b \approx 77 - j15$. The data for each frequency were independently inverted using the balanced MR-FEMCSI method. The balance factor was set to $Q = 5$. This factor was selected based on our experience with obtaining the best images with human forearm tissues. The inversion domain \mathcal{D} was a square with side-length of 9 cm and center $(1.5, -1.5)$ cm. The unknowns were located on 11,455 nodes within \mathcal{D} . The MRI scan along with the MWI reconstruction results for *Volunteer 1*

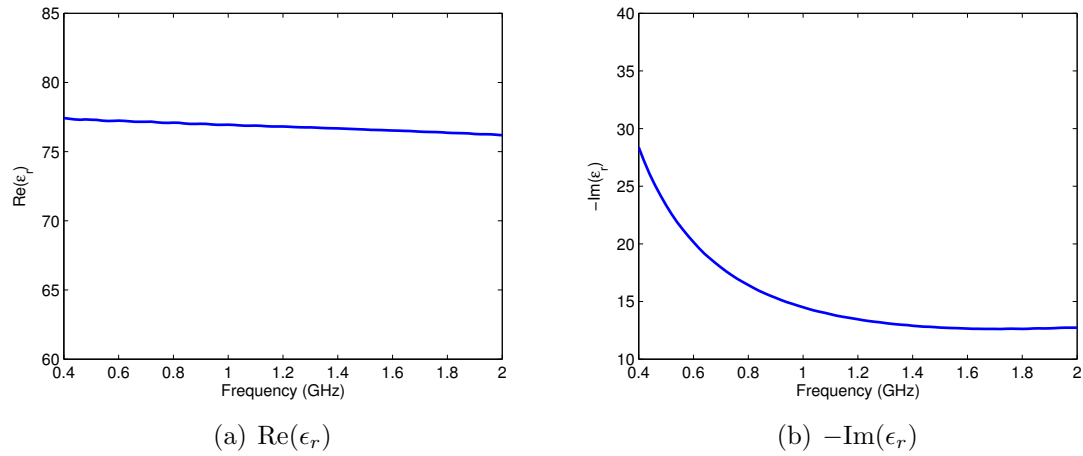


Figure 6.40: The complex relative permittivity of the matching fluid used for microwave imaging.

are shown in Figure 6.41.

For this volunteer, both bones are visible at all three frequencies. The real part of the permittivity of the muscle tissue varies between 56 – 67 (approx.) for all three frequencies, while the average imaginary part of the permittivity of the muscle drops steadily as the frequency increases (approximately 28, 23, 21 for 0.8, 1 and 1.2 GHz). This agrees with the trends seen in the permittivity values in the literature [101]: the real part of the permittivity of muscle and blood is relatively constant across this frequency range, whereas the imaginary part is expected to be inversely proportional to the frequency. The exact agreement between the literature and the measured values are not expected because of the differences between *in-vivo* and *ex-vivo* measurements [109].

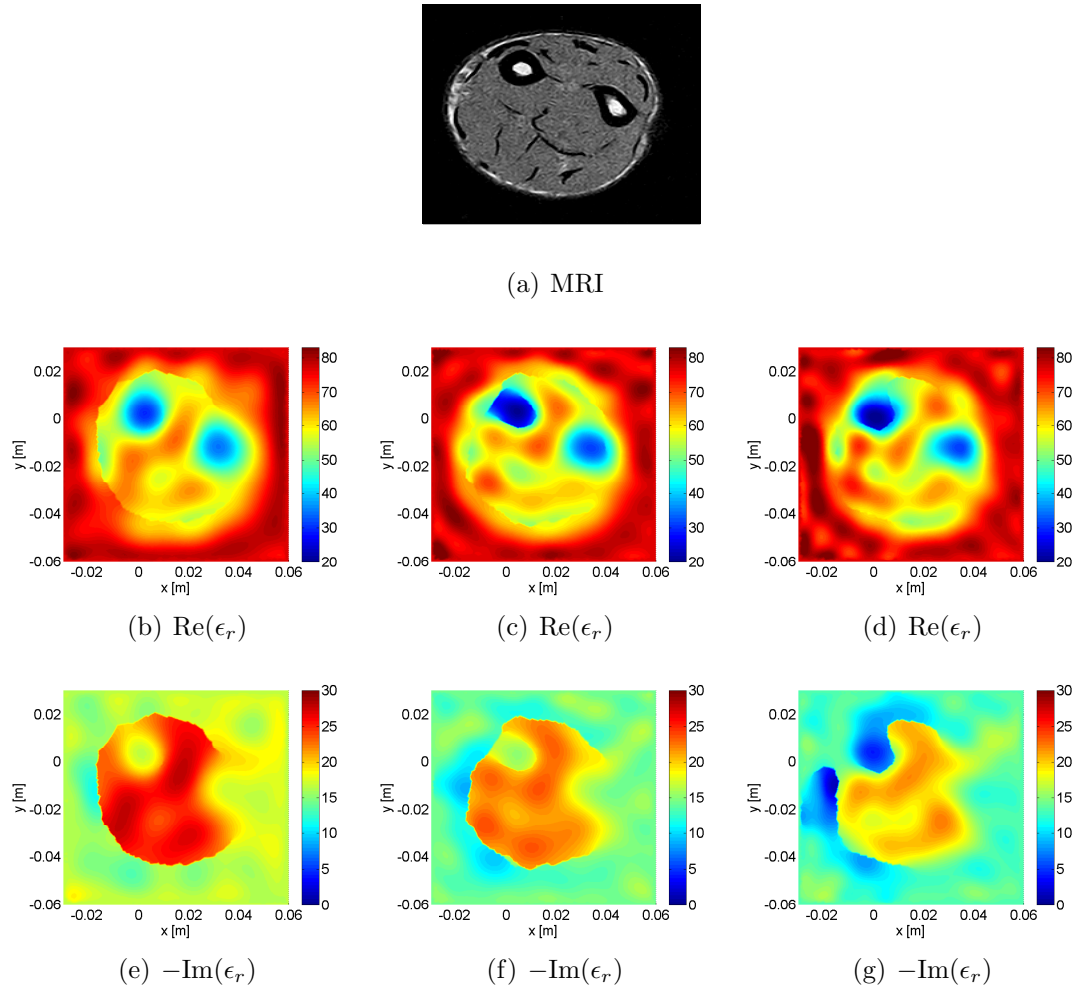


Figure 6.41: (a) The MRI of a volunteer's arm and the MWI reconstructions at frequencies (b), (e) $f = 0.8$ GHz, (c), (f) $f = 1.0$ GHz and (d), (g) $f = 1.2$ GHz.

6.3.2 UPC Barcelona Datasets

The UPC Barcelona datasets were collected in 1991 using a near-field 2.33 GHz microwave scanner system [92]. This system consists of 64 horn antennas distributed equally on a circular array of radius 0.125 m. Each antenna can operate as either a transmitter or a receiver. When using one of the 64 antennas as a transmitter, the 33 antennas in front of it are active as receivers. Not all antennas are used as receivers due to the isolation limitations of the system circuitry. The horn antennas produce and measure electric field parallel to the z -axis; hence the fields are assumed to have a TM polarization.

The measured scattered field due to a target was calibrated to that of a model incident field taken to be a unit line source directed in the z -axis. The model incident field was taken to be

$$E_t^{\text{inc}}(\vec{r}) = -\frac{j2\pi f\mu_0}{4} H_0^{(2)}(k_b |\vec{r} - \vec{r}_t|) \quad (6.11)$$

where k_b is the background medium wavenumber and \vec{r}_t is the location of transmitter t . The data collection tank was filled with a background medium of water with relative permittivity $\epsilon_b = 77.3 - j8.66$ at 2.33 GHz. Only calibrated data is available in the dataset.

For the inversion of these experimental datasets, the imaging domain \mathcal{D} is selected to be circular with radius 4.7 cm. The number of unknowns in \mathcal{D} is approximately 22,000. For each dataset the inversion algorithms are run for 1024 iterations to ensure convergence. In addition, at each iteration the inversion results are constrained to lie within the region defined by $0 \leq \text{Re}(\epsilon_r) \leq 80$ and $0 \leq -\text{Im}(\epsilon_r) \leq 20$. Each dataset is inverted using FEM-CSI, MR-FEMCSI, and BMR-FEMCSI with $Q = 5$ and $Q = 10$.

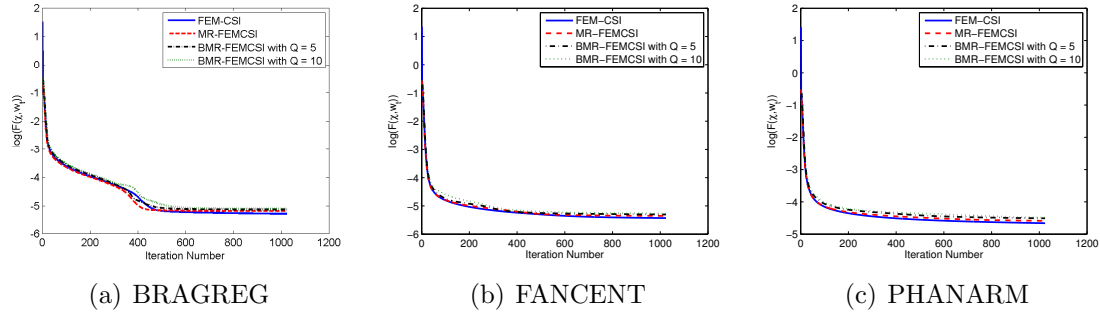


Figure 6.42: The cost functional versus the iteration number for (a) BRAGREG, (b) FANCENT and (c) PHANARM experimental datasets inversion.

A summary of the inversions is provided in Table 6.9, while the convergence of the cost functional for each dataset is shown in Figure 6.42.

6.3.2.1 Human Forearm

The first experimental dataset collected by UPC is known as BRAGREG. The scattering object is a human forearm, which is immersed in the tank and is surrounded by the antennas. The forearm has expected permittivities of $\epsilon_r = 12 - j2.5$ for bone and $\epsilon_r = 54 - j11$ for muscle at a frequency $f = 2.33$ GHz [101]. The reconstruction results are shown in Figure 6.44 and the cost functional progress is demonstrated in Figure 6.42 (a). The worst reconstruction is obtained using FEM-CSI with no multiplicative regularization. Although the arm contour is visible in Figure 6.44 (a), the reconstruction is oscillatory with the overall features of the arm being blurred. Using either the normal or the balanced form of MR, the contours of the the bones and muscle tissue as well as that of the forearm are clear and distinguishable. The imaginary component of the reconstruction is least oscillatory and smoothest using the balanced MR-FEMCSI with $Q = 5$. The relative permittivity of the muscle is well estimated, however the relative permittivity of the bones are above their expected

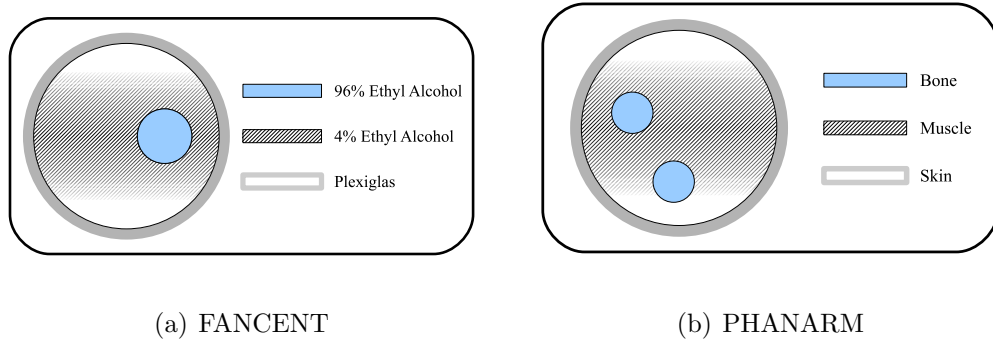


Figure 6.43: (a) FANCENT and (b) PHANARM target configurations.

values; it is speculated that this is due to the low dynamic range of the system [3,28,110]. The results obtained using MR-FEMCSI are similar to the reconstructions using MR-FDCSI [78] and MR-IECSI [27].

6.3.2.2 Cylindrical Phantom

The OI for the second UPC dataset consists of two Plexiglas cylinders filled with different concentrations of ethyl alcohol as depicted in Figure 6.43. The smaller cylinder was filled with 96% ethyl alcohol solution with a relative complex permittivity of $\epsilon_r = 10 - j8.3$. The bigger cylinder contained a solution of 4% ethyl alcohol with $\epsilon_r = 73 - j11$. The Plexiglas had a relative permittivity of $\epsilon_r = 2.73 - j0.01$. This dataset is referred to as FANCENT. The reconstruction results are given in Figure 6.45, while the convergence of the cost functional is shown in Figure 6.42 (b). Similar to the BRAGREG dataset, it can be observed that the smoothest reconstructions with the least fluctuations are obtain using the balanced MR. The contour of the Plexiglas is visible, nevertheless its relative permittivity value is overshoot. For the bigger cylinder, the complex relative permittivity is well-estimated using BMR with $Q = 10$. As for the smaller cylinder, its circular contour is clear using either variants

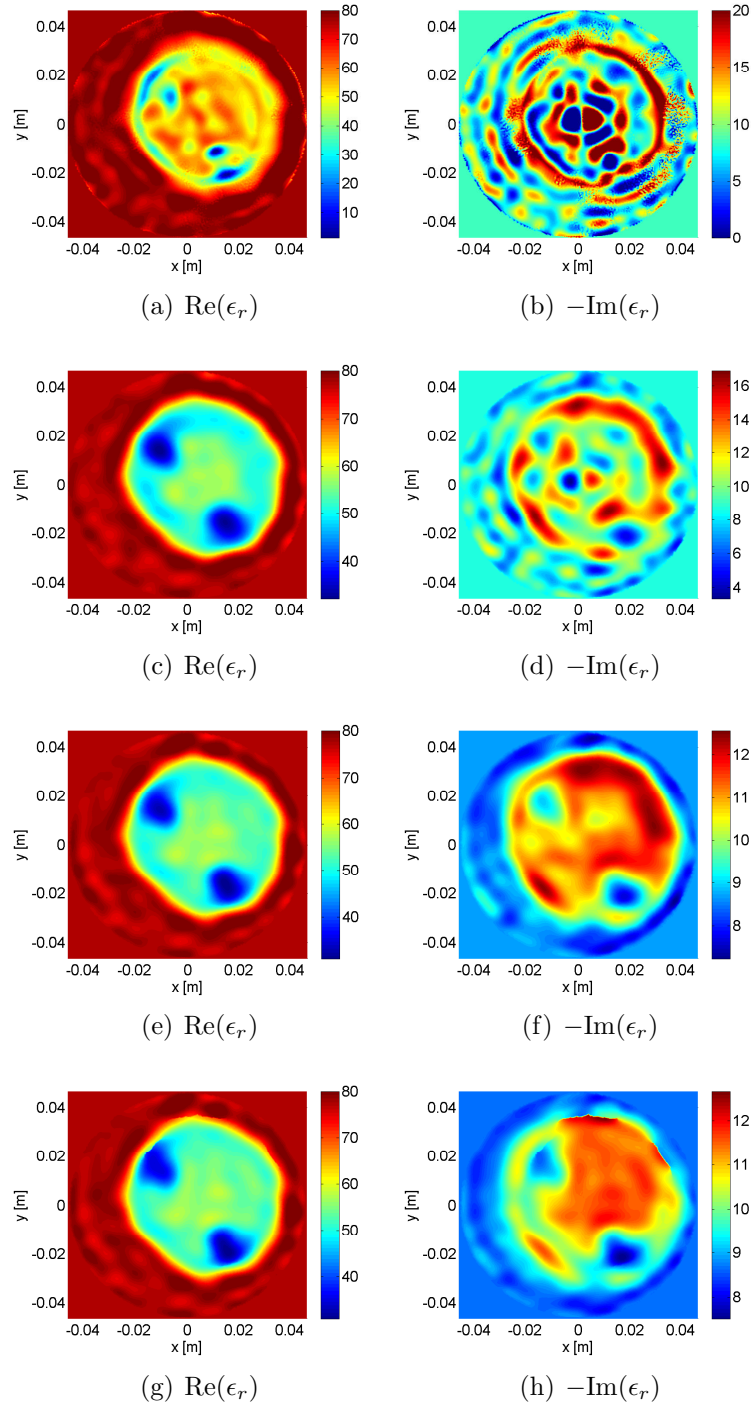


Figure 6.44: Inversion of BRAGREG dataset using (a)-(b) FEM-CSI, (c)-(d) MR-FEMCSI and BMR-FEMCSI for (e)-(f) $Q = 5$ and (g)-(h) $Q = 10$.

of MR; however using BMR, the imaginary part reconstruction is better. The best relative permittivity estimate for the liquid in the small cylinder is obtained using BMR with $Q = 5$, although it is higher than expected; again it is expected that this is due to the low dynamic range of the system.

6.3.2.3 Human Arm Phantom

The last dataset, known as PHANARM, is collected for a human arm phantom. The phantom configuration is depicted in Figure 6.43. The skin and the bones of the OI were made with PVC with complex permittivity $\epsilon_r = 2.73 - j0.01$ and the muscle was made from a material with $\epsilon_r = 54.5 - j17.2$. The reconstruction results are shown in Figure 6.46 and the convergence of the inversion algorithms' functional is given in Figure 6.42 (c). As observed with previous datasets, the results obtained using the balanced MR-FEMCSI are notably better than those obtained using FEM-CSI and its MR counterpart. The quality of the reconstructions using BMR are good as the phantom arm features are clear. Nevertheless, quantitatively the relative permittivity values are not as expected for the different arm constituents. As a matter of fact, the imaginary part of the reconstructed permittivity for one of the bones is completely wrong. Similar results were obtained using MR-IECSI for this OI [3].

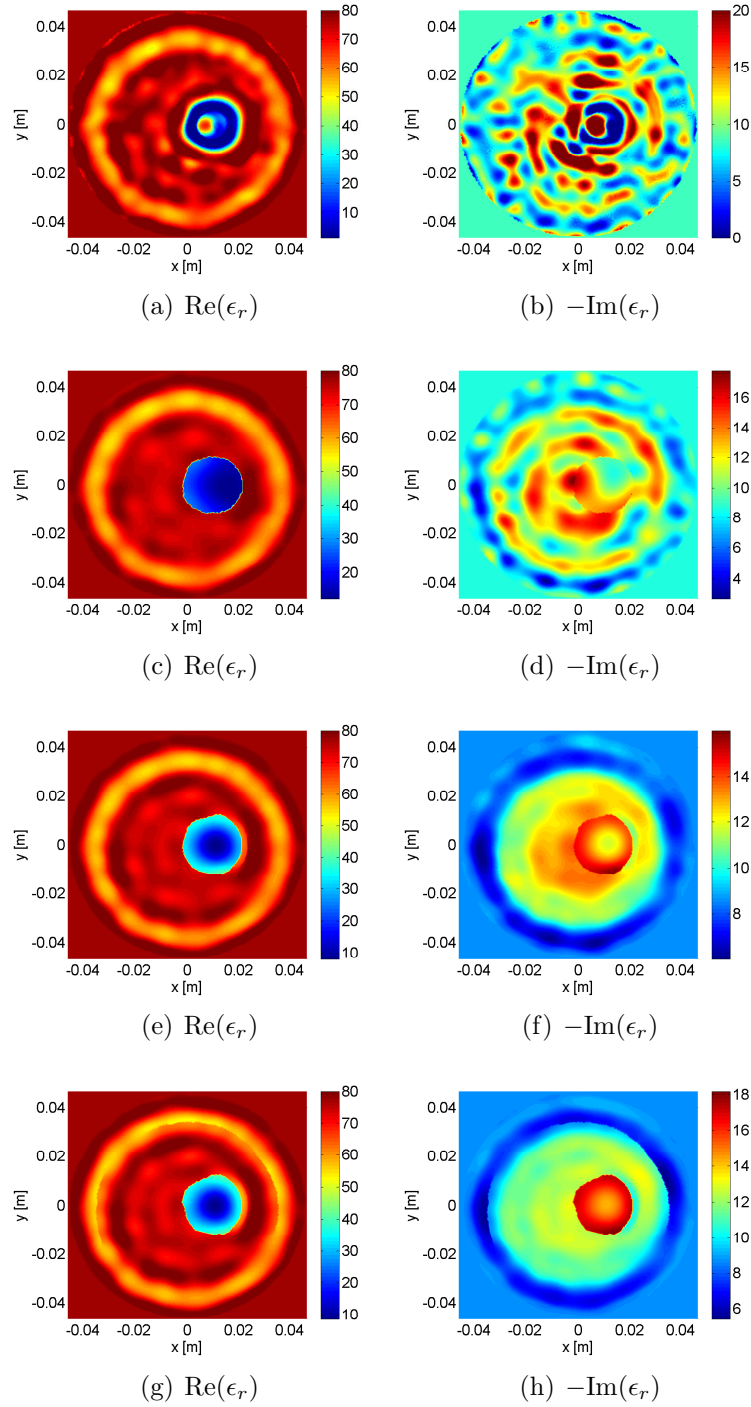


Figure 6.45: Inversion of FANCENT dataset using (a)-(b) FEM-CSI, (c)-(d) MR-FEMCSI and BMR-FEMCSI for (e)-(f) $Q = 5$ and (g)-(h) $Q = 10$.

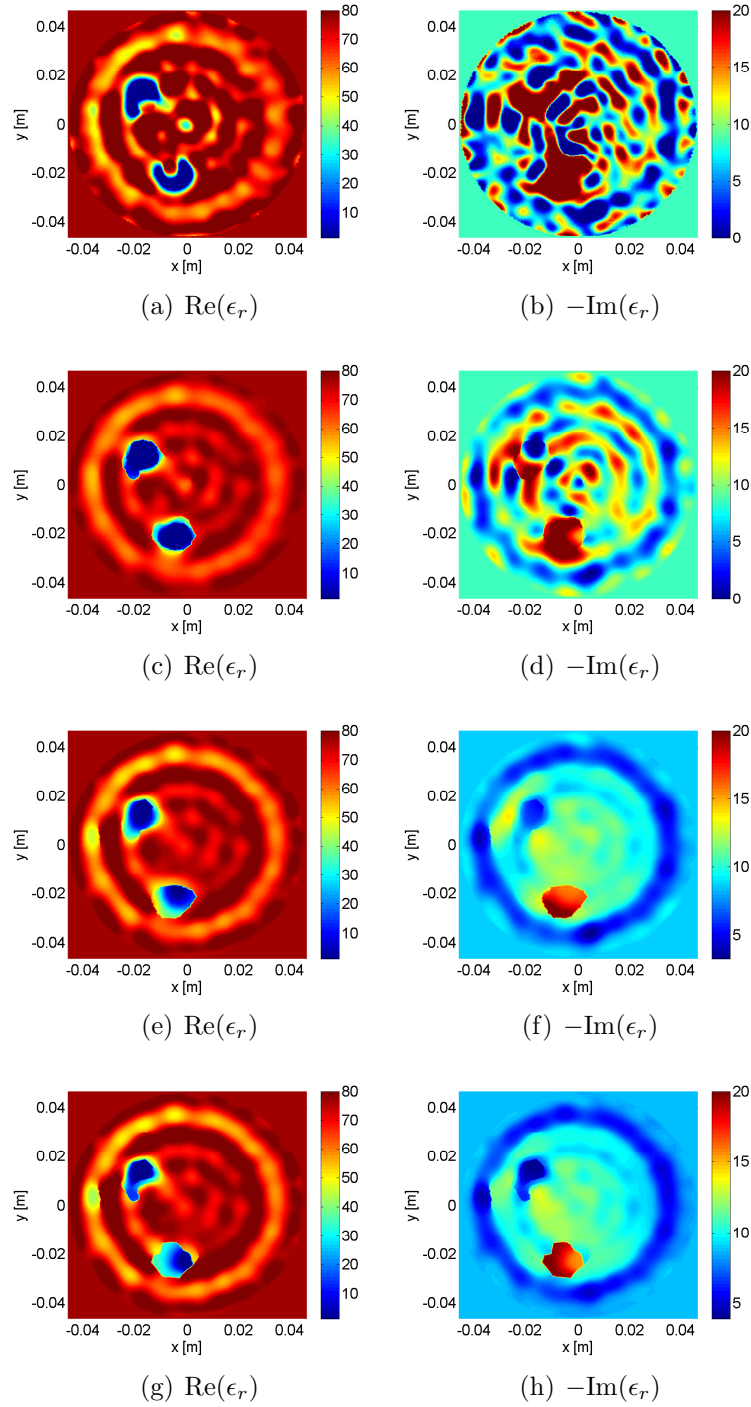


Figure 6.46: Inversion of PHANARM dataset using (a)-(b) FEM-CSI, (c)-(d) MR-FEMCSI and BMR-FEMCSI for (e)-(f) $Q = 5$ and (g)-(h) $Q = 10$.

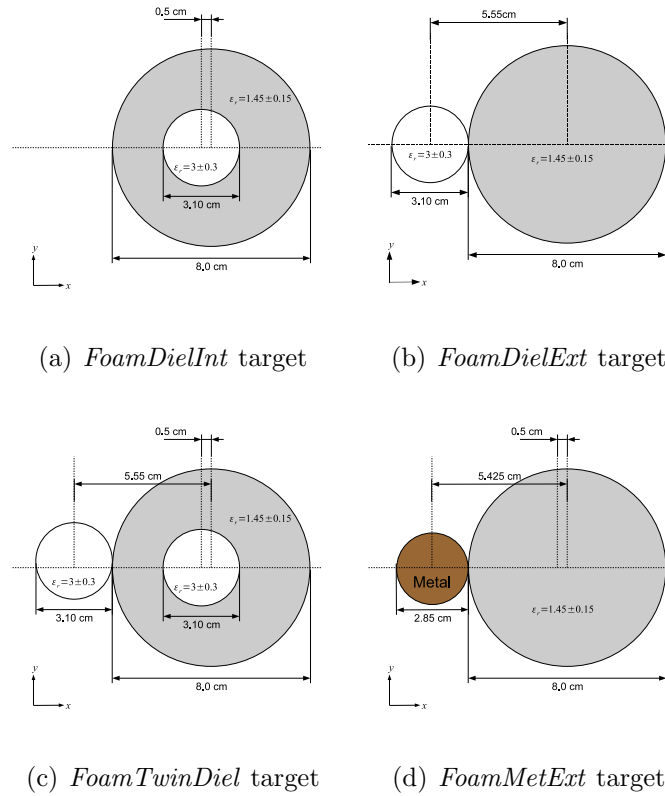


Figure 6.47: The targets of the 2D Fresnel dataset (a) *FoamDielInt* (b) *FoamDielExt* (c) *FoamTwinDiel* (d) *FoamMetExt*.

6.3.3 Institut Fresnel 2D Datasets

For the 2005 Institut Fresnel experimental dataset [38], TM and TE multifrequency experimental data were collected for different inhomogeneous targets depicted in Figure 6.47: *FoamDieInt*, *FoamDielExt*, *FoamTwinDiel* and *FoamMetExt*.

In these datasets, the transmitting and receiving antennas are both wide-band horn antennas positioned on a circle having a 1.67 m radius and located inside an anechoic chamber. The targets are all circular cylinders with no variation in the longitudinal z -direction; hence a 2D model is appropriate. For all the targets, the background medium is free-space with $\epsilon_b = 1$. In the TM illumination the z -component of the

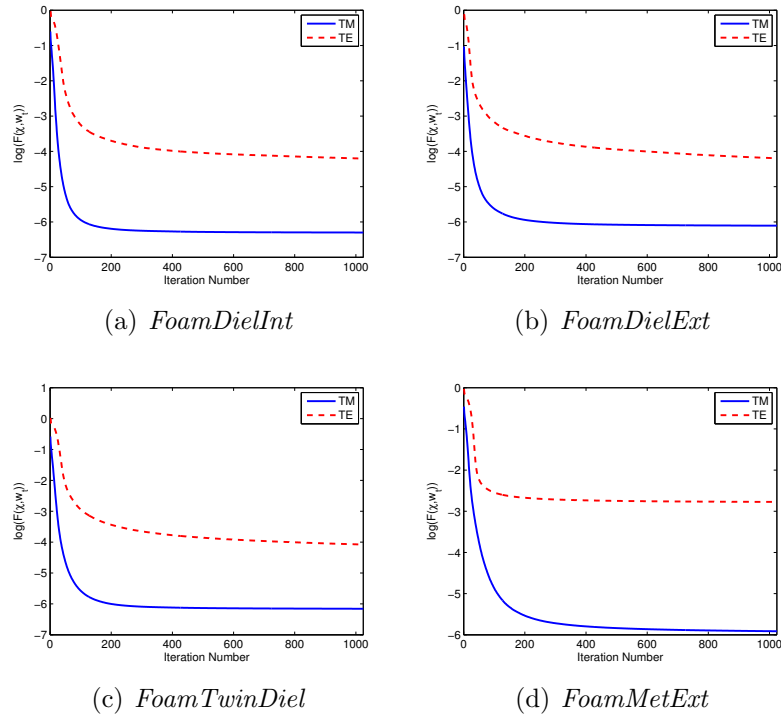


Figure 6.48: The cost functional progress for (a) *FoamDielInt*, (b) *FoamDielExt*, (c) *FoamTwinDiel* and (d) *FoamMetExt* TM and TE experimental datasets inversions.

scattered field is collected and calibrated. For the TE illumination, the ϕ -component of the scattered field is measured and calibrated, then converted to the x - and y -components to be used by the inversion algorithm. The measured data were calibrated assuming the model of the incident field to be a 2D electric point source for the TM case and a 2D magnetic point source for the TE case. The data calibration process is detailed in [111].

The *FoamDielInt* and *FoamDielExt* targets are interrogated by 8 transmitters and the measured data are collected at 9 different frequencies from 2 GHz to 10 GHz with a step of 1 GHz at 241 receiver points per transmitter. The *FoamTwinDiel* target is illuminated by 18 transmitters and the number of frequencies and receivers is the same as the previous two targets. For the *FoamMetExt* target, while the number of

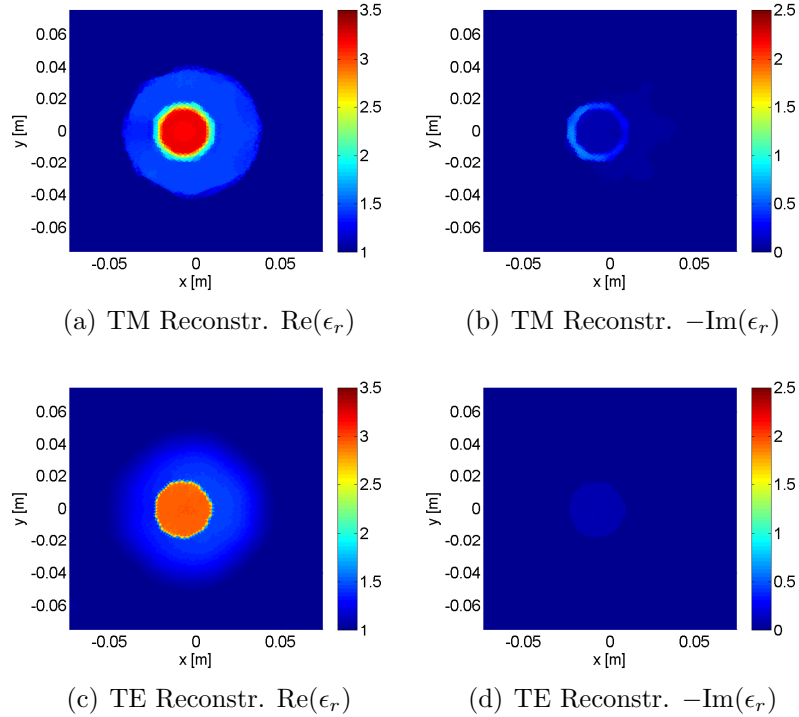


Figure 6.49: The reconstruction of the *FoamDieInt* target at $f = 2$ GHz using simultaneous-frequency MR-FEMCSI for (a)-(b) the TM case and (c)-(d) the TE case.

transmitters and receivers is the same as the *FoamTwinDiel* datasets, the object is irradiated at 17 different frequencies in the range from 2 GHz to 18 GHz with 1 GHz step.

For both TM and TE cases, the data for the different frequencies are inverted simultaneously using the MR-FEMCSI algorithm. The extension of the algorithm allowing it to deal simultaneously with multi-frequency datasets, for a lossless background, is relatively simple to incorporate. Some of the details of this extension can be found in [111, 112]. The inversion domain \mathcal{D} is a square centered in the problem domain Ω with the side-length equal to 15 cm. For both TM and TE cases, the unknown variables are located at the centroids of 17, 887 triangles. To ensure convergence, the

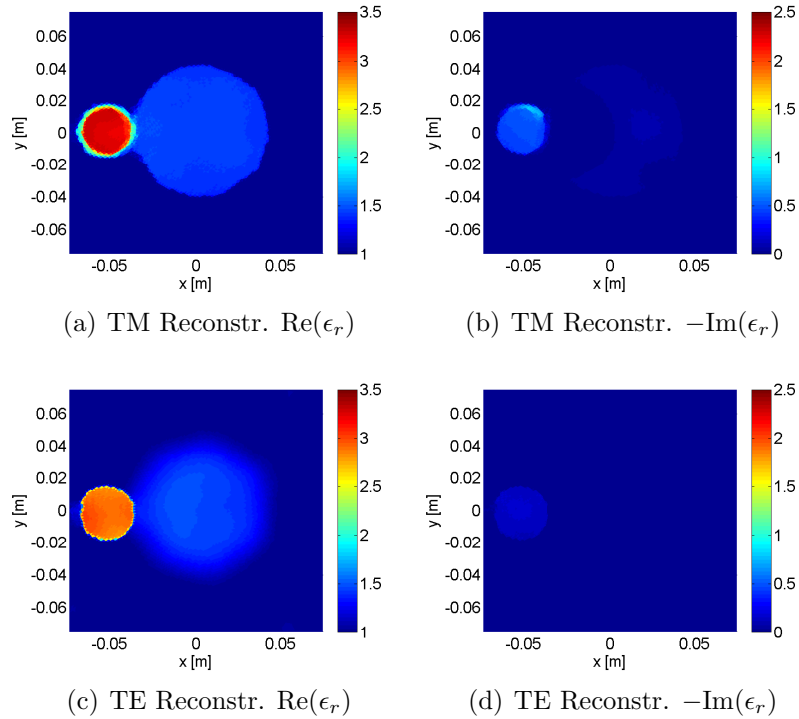


Figure 6.50: The reconstruction of the *FoamDielExt* target at $f = 2$ GHz using simultaneous-frequency MR-FEMCSI for (a)-(b) the TM case and (c)-(d) the TE case.

algorithm was run for 1024 iterations. The real and imaginary components of the relative permittivity were constrained to $1 < \text{Re}(\epsilon_r) < 100$ and $0 < -\text{Im}(\epsilon_r) < 100$. A summary of the inversions is provided in Table 6.9, while the convergence of the cost functional for each dataset is shown in Figure 6.48.

The reconstruction results for the different datasets at the lowest frequency ($f = 2$ GHz) are shown in Figures 6.49–6.52. The results achieved using simultaneous frequency inversion using the MR-FEMCSI algorithm are quite similar to those obtained using MR-IECSI [111]. The foam cylinder with diameter 8 cm is reconstructed well for all the datasets with an average relative permittivity of $\epsilon_r = 1.4$. For the *FoamDielExt*, *FoamDielInt* and *FoamTwinDiel* datasets, the location and the shape of the plastic

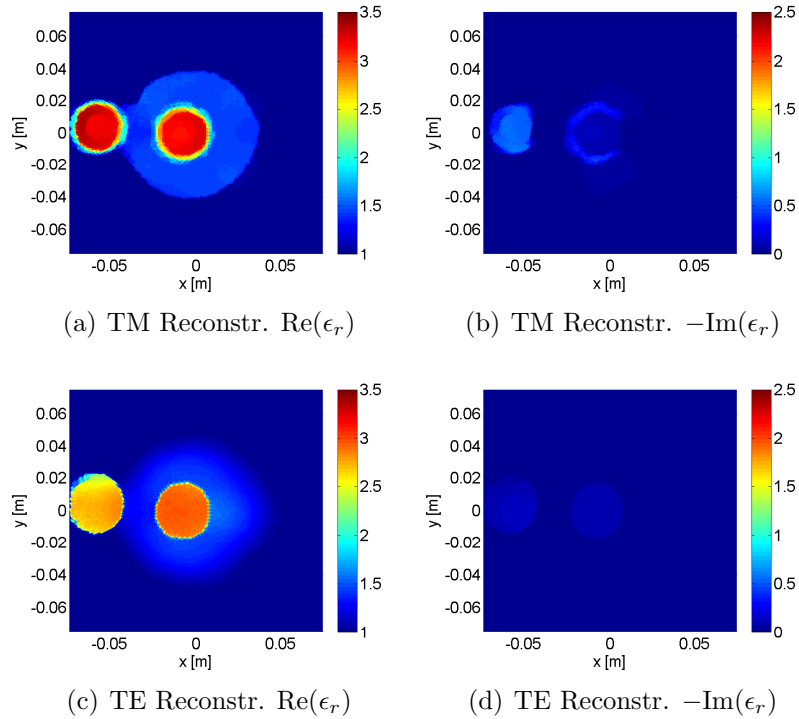


Figure 6.51: The reconstruction of the *FoamTwinDiel* target at $f = 2$ GHz using simultaneous-frequency MR-FEMCSI for (a)-(b) the TM case and (c)-(d) the TE case.

cylinders with diameter 3.1 cm are estimated correctly. For the TE case, the average relative permittivity for the plastic cylinder reconstructions is $\epsilon_r = 2.9 - j0.11$, although the object is close to lossless. For the TM case, the average relative permittivity is $\epsilon_r = 3.1 - j0.4$. An incorrect prediction of the imaginary part was also obtained using the Gauss-Newton inversion algorithm [35]. Comparing the TM and TE reconstructions, the contour of the plastic cylinders are better defined for the TE case; additionally, the imaginary part errors are less for the TE case than for the TM case.

The reconstructions for the *FoamMetExt* datasets are shown in Figure 6.52. The inversion result of the TM dataset shows that the location of the metallic cylinder

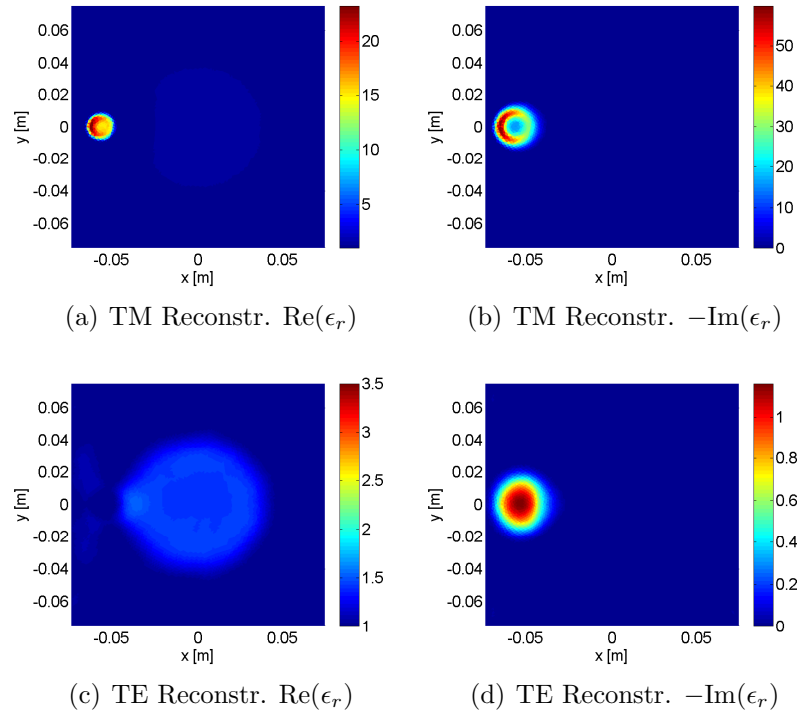


Figure 6.52: The reconstruction of the *FoamMetExt* target at $f = 2$ GHz using simultaneous-frequency MR-FEMCSI for (a)-(b) the TM case and (c)-(d) the TE case.

is accurately retrieved with the real and imaginary components of its relative permittivity having the same order of magnitude (greater than 10). The reconstruction of the metallic cylinder indicates the presence of an object with high conductivity; however the result is ambiguous, in that it can't differentiate between a high real or high imaginary part [111]. Theoretically, the inversion of a perfectly conducting cylinder should only obtain the boundary of the object. The contrast sources inside the metallic cylinder are invisible, consequently the reconstructed real component of the contrast inside the object is arbitrary and is merely an artifact of the inversion algorithm. This can be fixed by enforcing smaller constraints on the components of the reconstructed permittivity as will be outlined later.

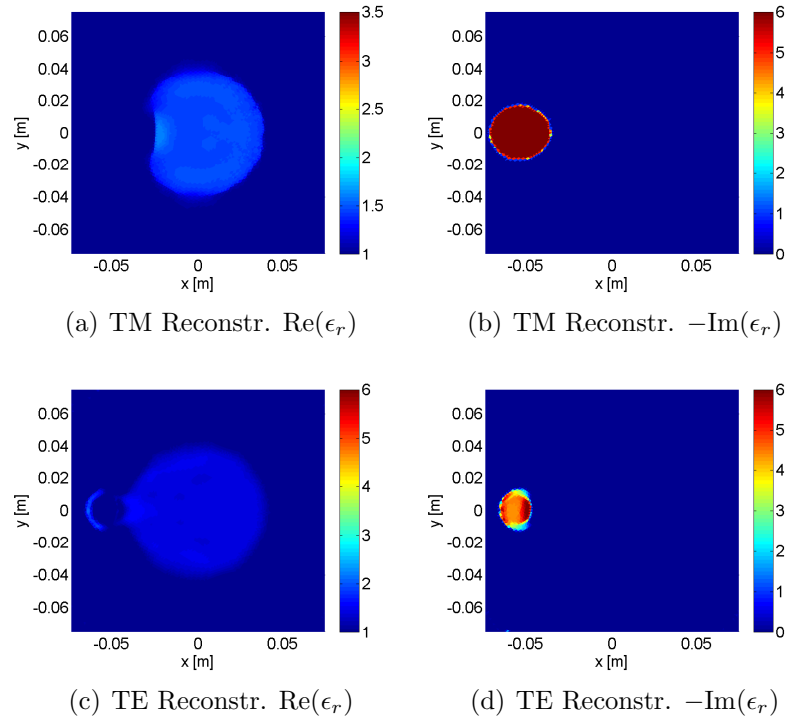


Figure 6.53: The reconstruction of the *FoamMetExt* target at $f = 2$ GHz with $\max |\text{Im}(\epsilon_r)| < 6$ using simultaneous-frequency MR-FEMCSI for (a)-(b) the TM case and (c)-(d) the TE case.

As for the TE case, the metallic cylinder with diameter 2.85 cm is constructed with the real part of its relative permittivity close to 1, whereas its imaginary part indicates an object with loss but with values less than those obtained using the TM dataset.

The MR-FEMCSI algorithm was run again for the *FoamMetExt* dataset with the components of the relative permittivity constrained to lie in the region defined by $1 < \text{Re}(\epsilon_r) < 6$ and $0 < -\text{Im}(\epsilon_r) < 6$. The reconstruction results are shown in Figure 6.53. For the TM dataset, the metallic cylinder was reconstructed as an object with the real part of its permittivity equal to 1 and its imaginary part equal to the maximum constraint, *i.e.* $-\text{Im}(\epsilon_r) = 6$. As for the TE case, with the new

constraints the metallic cylinder was estimated as a circle with a smaller diameter as well as higher loss than obtained using the first set of constraints; furthermore the contour of the metallic cylinder is visible in the real component reconstruction. Finally, the reconstruction of the foam cylinder is better in the TE case than in the TM case, regardless of the constraints applied. In the TM case the shape of the foam is distorted in the proximity of the metallic cylinder.

6.3.4 Institut Fresnel 3D Datasets

Three-dimensional data were collected for several targets at the Institut Fresnel of Marseille in 2009 [39]. In a special issue of *Inverse Problems* [113], the collected datasets were inverted using different methods like MR-IECSI [114], DBIM [115] and GNI [116]. The inversion algorithms were based on the integral-equation formulation of the electromagnetic problem. Herein, the datasets are inverted using the 3D MR-FEMCSI algorithm. The final reconstructions using the algorithm are similar to those reported in literature using other methods.

The experimental setup consisted of a parabolic antenna as a transmitter and a ridged-horn antenna as a receiver, both located inside an anechoic chamber. The antennas moved around the targets on a spherical surface of radius 1.796 m. For the transmitting antenna, the azimuthal angle, ϕ , varied from 20° to 340° with steps of 40° and the polar angle, θ , ranged from 30° to 150° with steps of 15° . The definition of the coordinate system is shown in Figure 6.54. According to the system design, the receiving antenna positions were restricted to a single azimuthal plane at $\theta = 90^\circ$. In addition, for technical reasons the location of the receiving antenna could not be closer than 50° from the azimuth angle position of the transmitter. Hence, the azimuthal angle of the receiver varied from 0° to 350° with steps of 10° , with the exclusion of

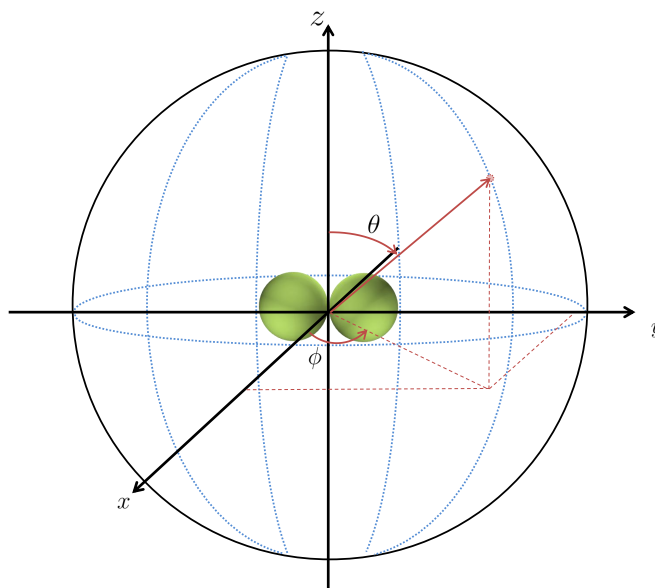


Figure 6.54: The coordinates configuration of the Institut Fresnel 3D setup.

$\pm 50^\circ$ of the transmitter's azimuthal angle. Furthermore, for each dataset the receiver positions opposite to the transmitter were unusable due to the saturation of network analyzer receiver.

The measured data were collected at 21 frequencies ranging from 3 to 8 GHz with a 0.25 GHz step. For each target, two polarization cases were measured: in the first case, the transmitter and the receiver were polarized along the θ -direction; in the second case, the transmitting antenna was polarized along the ϕ -direction whereas the receiving antenna was again polarized along the θ -direction. The collected data at each polarization were calibrated using the techniques described in [39].

In the work presented here, the two polarization measurements are merged by applying the reciprocity theorem, where the roles of the transmitting and receiving antennas are switched. Because the receiving antenna is always at $\theta = 90^\circ$ plane, using reciprocity, the incident field can be modeled as a z -polarized plane wave with

magnitude -1 and phase 0 at the origin $(0, 0, 0)$. The model incident field is given as

$$\vec{E}_t^{\text{inc}}(\vec{r}) = -e^{jk_b(x \cos(\phi'_t) + y \sin(\phi'_t))} \hat{z}. \quad (6.12)$$

where ϕ'_t denotes the azimuthal angle of the reciprocal transmitter, which is equal to a receiver's azimuthal angle ϕ_r in the actual measurement setup. The plane wave model of the incident field is valid as the transmitters and receivers in the experimental setup is more than 10λ away from the targets (the far-field region), where λ is the free-space wavelength at a frequency $f = 3$ GHz.

The receiver locations in the reciprocal system are taken to be at the source positions in the actual measurement setup. The receiver position (ϕ'_r, θ'_r) corresponds to the transmitter location (ϕ_t, θ_t) in the actual system. The receivers are located on a sphere of radius 1.796 m.

Let $E_{\theta\theta}^{\text{sct}}$ and $E_{\phi\theta}^{\text{sct}}$ be the measured scattered fields at the actual receiver with the transmitting antenna polarized along the θ - and the ϕ -directions respectively. The spatial components of the scattered field vector at the reciprocal receiver location (ϕ'_r, θ'_r) are

$$\begin{aligned} E_x^{\text{sct}} &= \cos(\theta'_r) \cos(\phi'_r) E_{\theta\theta}^{\text{sct}} - \sin(\phi'_r) E_{\phi\theta}^{\text{sct}} \\ E_y^{\text{sct}} &= \cos(\theta'_r) \sin(\phi'_r) E_{\theta\theta}^{\text{sct}} + \cos(\phi'_r) E_{\phi\theta}^{\text{sct}} \\ E_z^{\text{sct}} &= -\sin(\theta'_r) E_{\theta\theta}^{\text{sct}}. \end{aligned} \quad (6.13)$$

The multi-frequency reciprocal datasets are inverted using a frequency-hopping approach [117]. With the frequency-hopping technique, the data from each frequency are inverted independently, and the solution from the lower frequency is used to calculate the initial guess for the next higher frequency. At each frequency the algorithm

Table 6.10: Summary of 3D Experimental Datasets

Example	f (GHz)	T	N_e	N	I	t_{iter} (s)
Institute Fresnel 3D						
Two Sphere	3 – 5	36	69913	85112	41865	201
Two Cubes	3 – 8	36	77675	93010	19044	210
Cube of Spheres	3 – 8	36	80742	95905	38851	210
<i>Myster</i>	3 – 8	36	70850	84344	35809	130

was run for 75 iterations to ensure its convergence, except at the last frequency where it was allowed to run for 512 iterations. For the work presented herein, increasing the maximum number of iterations per frequency to beyond 75 did not alter the final result. The predicted contrast after each iteration is constrained to remain within physical bounds ($\text{Re}(\epsilon_r) \geq 1$ and $-\text{Im}(\epsilon_r) \geq 0$). For comparison purposes the results for each dataset are presented with and without the use of multiplicative regularization. The imaginary part of the reconstructions are not shown as the targets are lossless. A summary of the inversions is given in Table 6.10.

6.3.4.1 Two Spheres

The first target consists of two dielectric spheres 50 mm in diameter aligned along the x -axis. The target is depicted in Figure 6.55 (a). The relative permittivity of both spheres is $\epsilon_r = 2.6$. The imaging domain \mathcal{D} is defined as a sphere 120 mm in diameter, centered around the origin $(0, 0, 0)$. The unknown variables are located at the centroids of approximately 42,000 tetrahedra within \mathcal{D} . The frequency-hopping approach is applied to the multi-frequency data at 3, 4 and 5 GHz. It was observed that the use of data for frequencies greater than 5 GHz corrupted the reconstructions, so they were omitted. The results at 5 GHz are shown in Figure 6.56 using FEM-CSI, and in Figure 6.57 adding MR. For each inversion algorithm, a 3D isosurface plot,

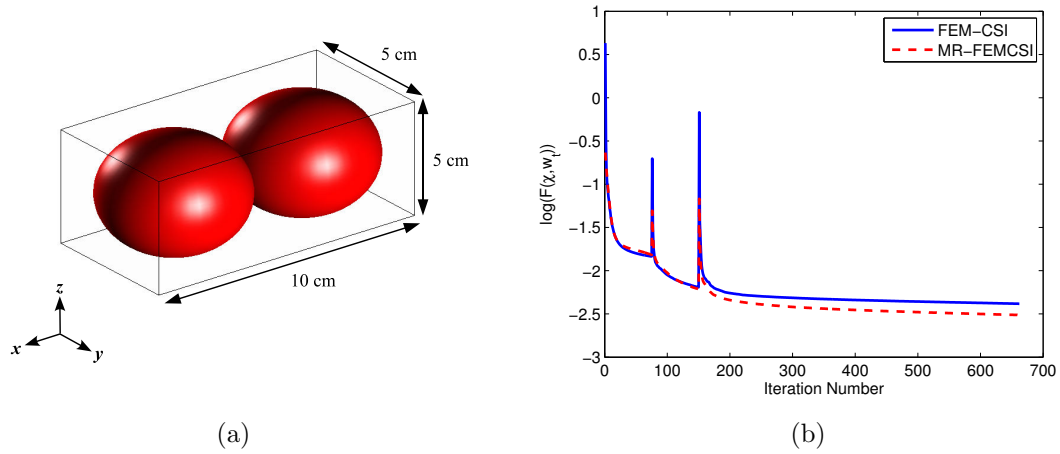


Figure 6.55: (a) The two spheres target configuration and (b) the cost functional convergence.

a 3D slice plot and 2D cross-sectional plots at planes $x = 0$, $y = 0$ and $z = 0$ are presented. The level of the isosurface plot is set to 2.0. White-solid lines outline the expected locations of the spheres in the $y = 0$ and $z = 0$ 2D cross-section plots. The cost functional convergence is shown in Figure 6.55 (b).

The results obtained using the multiplicatively regularized FEM-CSI are smooth and not overshoot in comparison to the reconstructions when no MR is utilized. Without MR, the relative permittivity values overshoot to approximately 3.5 and there are holes at the sphere centres. This can be observed in Figures 6.56 (e) and 6.57 (e). Both algorithms predict the size and location of the spheres accurately. This can be deduced from the isosurface plots as well as from the cross-sectional figures. It can be observed from the cost functional convergence in Figure 6.55 (b) that the algorithms converged; note that the sudden jumps in the progress is due to the transition from one frequency to the next after 75 iterations. The cost functional convergence for the inversion of the other experimental datasets is similar to that of the two spheres.

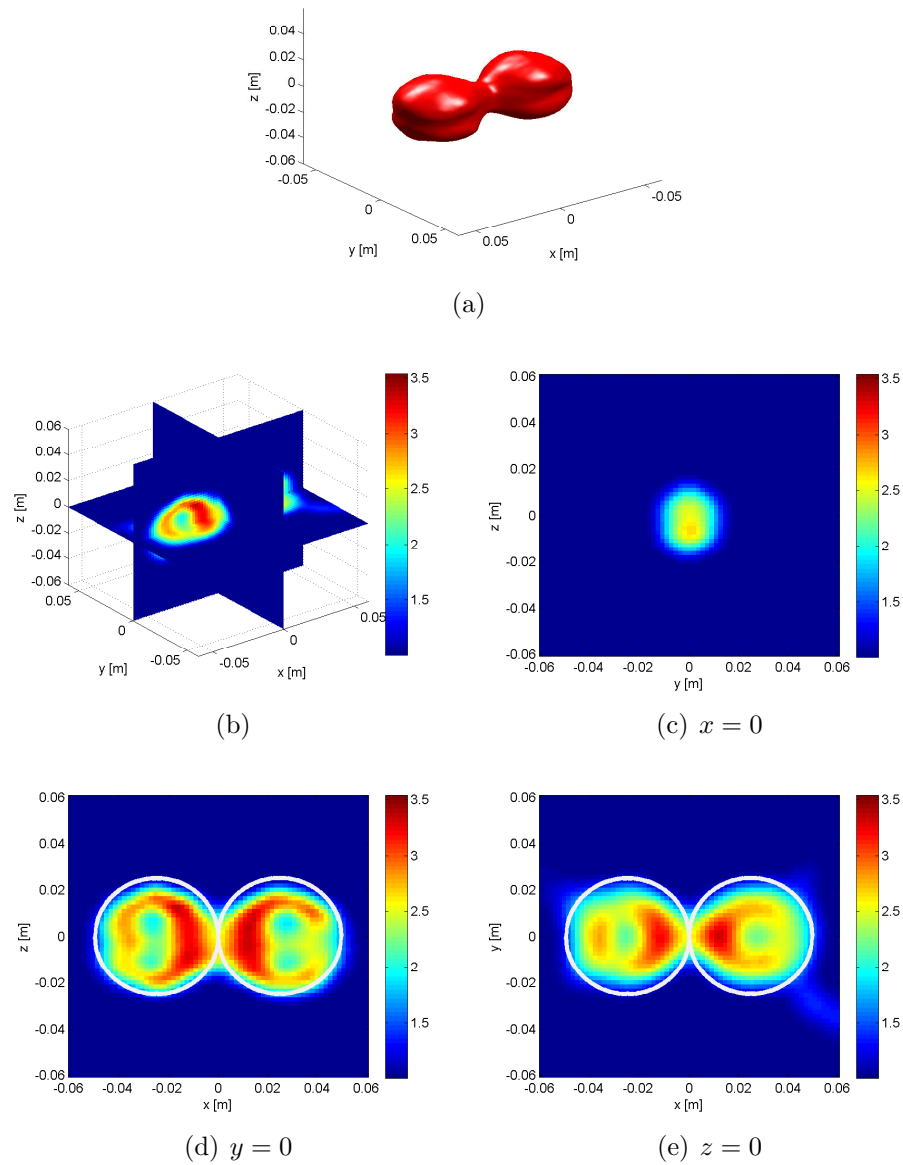


Figure 6.56: The reconstructions at $f = 5$ GHz for the two spheres target using frequency-hopping FEM-CSI . (a) The isosurface plot (level = 2.0), (b) the 3D slice plot, and the 2D cross-section plots at planes (c) $x = 0$, (d) $y = 0$ and (e) $z = 0$.

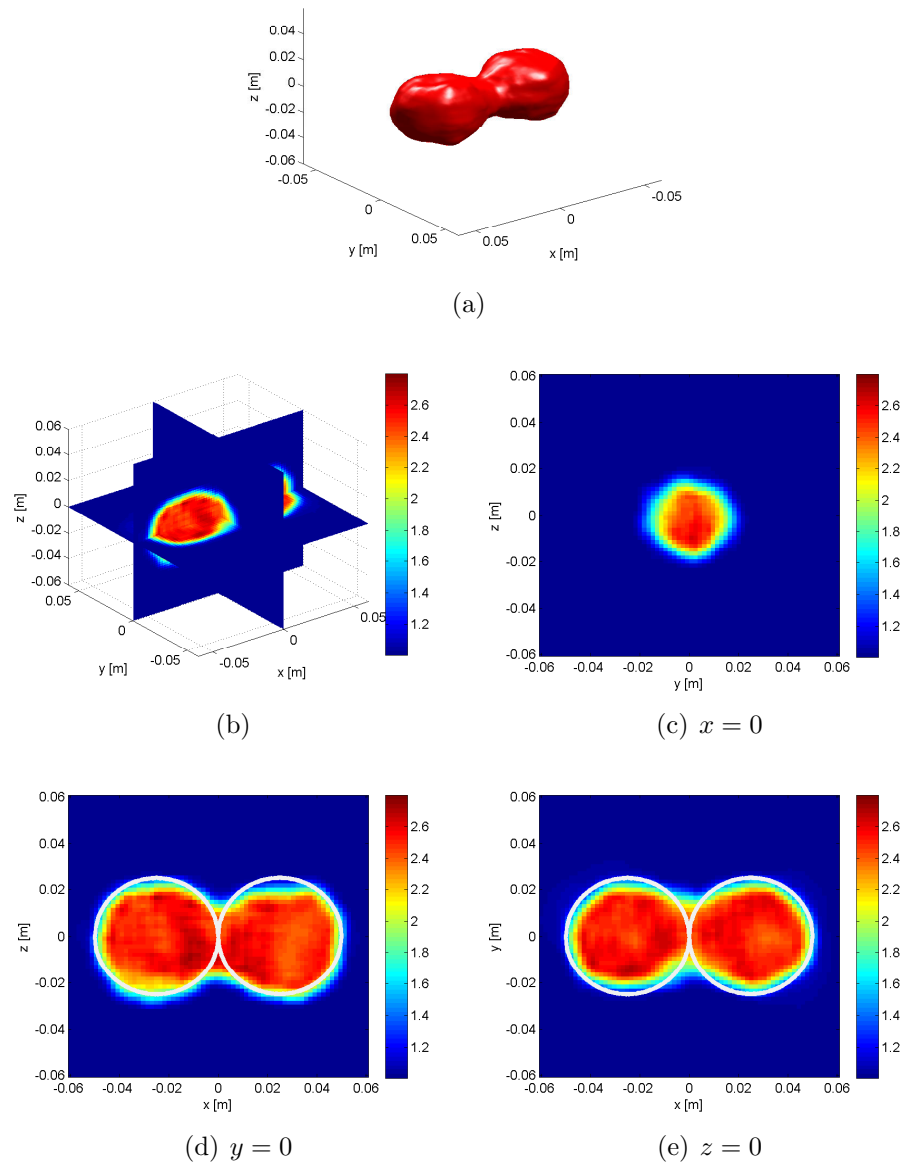


Figure 6.57: The reconstructions at $f = 5$ GHz for the two spheres target using frequency-hopping MR-FEMCSI. (a) The isosurface plot (level = 2.0), (b) the 3D slice plot, and the 2D cross-section plots at planes (c) $x = 0$, (d) $y = 0$ and (e) $z = 0$.

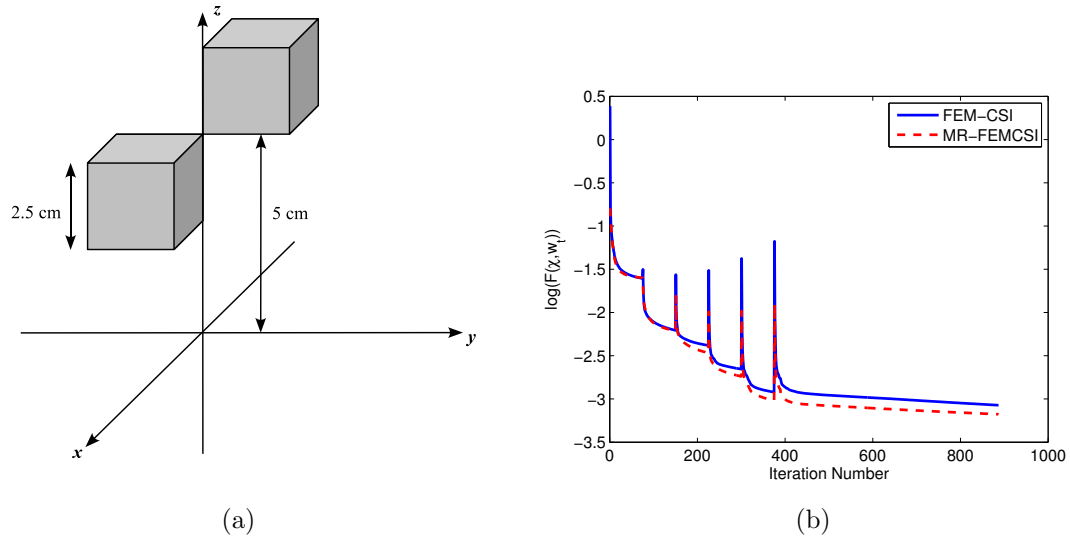


Figure 6.58: (a) The two-cubes target configuration and (b) the cost functional conversion.

6.3.4.2 Two Cubes

The second target has two dielectric cubes of side-length equal to 25 mm and relative permittivity $\epsilon_r = 2.3$. The cubes are located 25 mm and 50 mm above the plane $z = 0$ as shown in Figure 6.58. The imaging domain \mathcal{D} is selected as a rectangular prism with length and width equal to 90 mm and a height of 95 mm. The prism center is located at point $(0, 0, 52.5)$ mm. The multi-frequency data from 3 GHz to 8 GHz with a step of 1 GHz are used to reconstruct the OI using the frequency-hopping approach. The number of unknowns in \mathcal{D} is approximately 19,000.

The inversion results at $f = 8$ GHz are given in Figure 6.59, while the cost functional convergence is shown in Figure 6.58 (b). The reconstruction results for each inversion algorithm include the isosurface plot with the level set to 1.5, and the 2D slice plots at planes $x = [-14, 14]$ mm, $y = [-14, 14]$ mm and $z = [30, 64]$ mm. The expected location of the cubes are indicated with solid-white lines on each slice.

The locations and relative sizes of the cubes are predicted correctly by the inversion

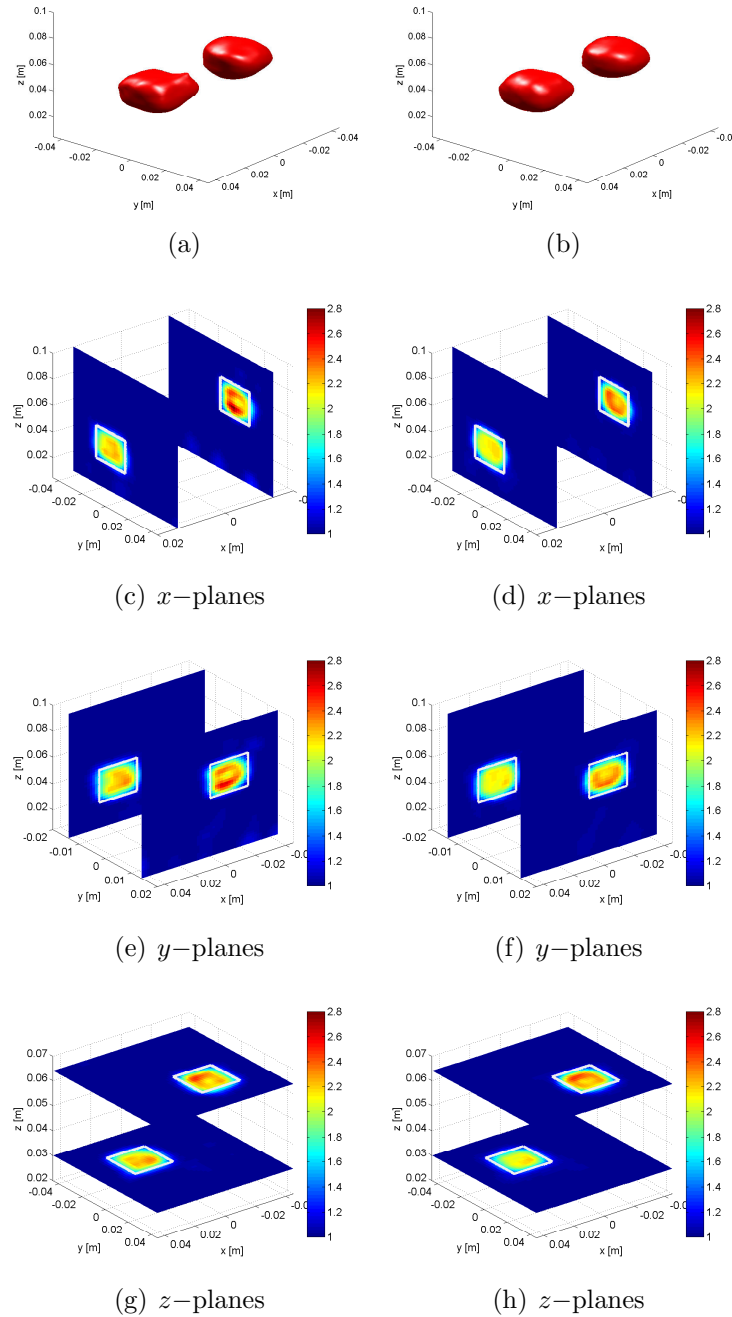


Figure 6.59: (a)-(b) The isosurface plot (level = 1.5) at $f = 8$ GHz of the two cubes target and the 2D slice plots of the reconstruction at planes (c)-(d) $x = [-14, 14]$ mm, (e)-(f) $y = [-14, 14]$ mm and (f)-(g) $z = [30, 64]$ mm. The figures on the left are the FEM-CSI reconstructions while those on the right are the MR-FEMCSI results. The results are obtained using a frequency-hopping approach.

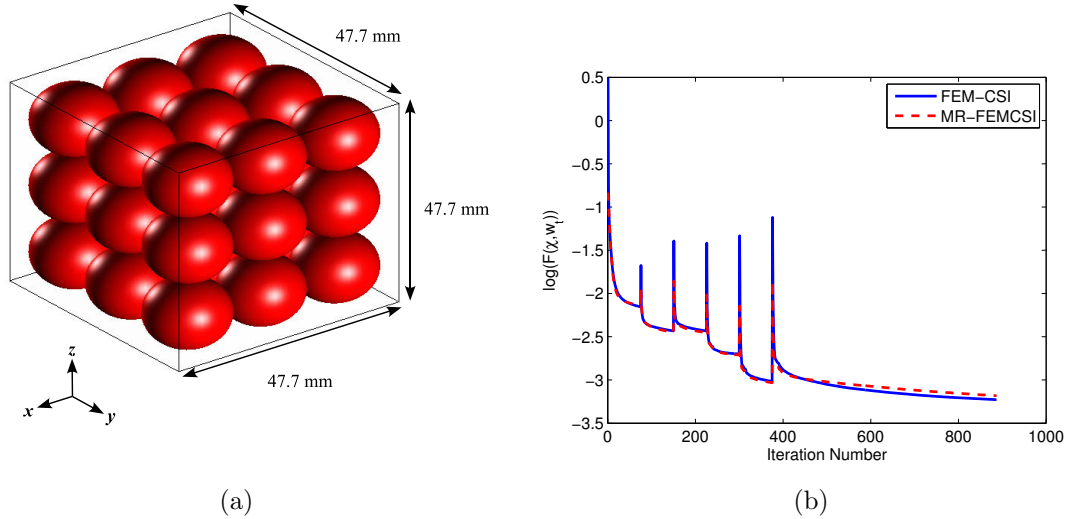


Figure 6.60: (a) The cube of spheres target configuration and (b) the cost functional convergence.

algorithms as can be noticed from the slice plots. Using multiplicative regularization, the reconstructions are smoother as well as more homogeneous, and the estimated relative permittivity values are close to 2.3. From the isosurface plots, the inversion algorithm did not produce cubic solids, rather it estimated the targets as irregularly shaped objects. This is because the unknowns are located in an irregular tetrahedral mesh. The shape reconstruction can be improved by increasing the number of elements in the imaging domain; however this will increase the required computational resources for the algorithm.

6.3.4.3 Cube of Spheres

The third OI is an aggregate of 27 dielectric spheres arranged in a cube as depicted in Figure 6.60 (a). Each sphere has a diameter of 15.9 mm and a relative permittivity of $\epsilon_r = 2.6$. The inversion domain \mathcal{D} is a cube centered in the problem domain Ω with side-length equal to 98 mm. The unknowns are located at the centroids

of approximately 39,000 tetrahedra within \mathcal{D} . The frequency-hopping technique is applied to the multi-frequency data from 3 GHz to 8 GHz in 1 GHz steps.

The convergence of the inversion algorithms' cost functional is shown in Figure 6.60 (b) and the reconstruction results at 8 GHz are given in Figure 6.61. The results in the left column of Figure 6.61 are the FEM-CSI reconstructions, and those in the right column are the MR-FEMCSI estimates. For each inversion algorithm the following figures are shown: a 3D isosurface plot with its level set to 1.9 and 2D cross-sections of the reconstruction at planes $x = 0$ mm, $y = 0$ mm and $z = 12.5$ mm. The circles with the solid-white circumferences depict the expected location of the spheres in the 2D slices.

The 3D isosurface plots at 8 GHz (Figures 6.61 (a) and (b)) show 9 strips parallel to the z -axis. The vertical separation between the spheres is not visible; this is also evident from the 2D cross-sections at $x = 0$ and $y = 0$. Nevertheless, with the 2D cross-section at $z = 12.5$ mm, the presence of a 3-by-3 array of circles is clearly visible. The location of the circles align with the white-solid contours. The estimated permittivity values do not exceed 2.6. Without MR, the free-space in between the spheres is clear; multiplicative regularization tends to smooth out the reconstruction and fill-in the space as shown in Figure 6.61 (d).

6.3.4.4 *Myster*

The *Myster* target is a group of 12 spheres, 23.8 mm diameter each. They are arranged together to compose the geometry shown in Figure 6.62 (a). The sphere centers are situated along the vertices of an *icosahedron*, as depicted in Figure 6.62 (b). Each sphere has a relative permittivity of $\epsilon_r = 2.6$. The inversion domain \mathcal{D} is a square box with its center point located at (0,0,10) mm. The length and width

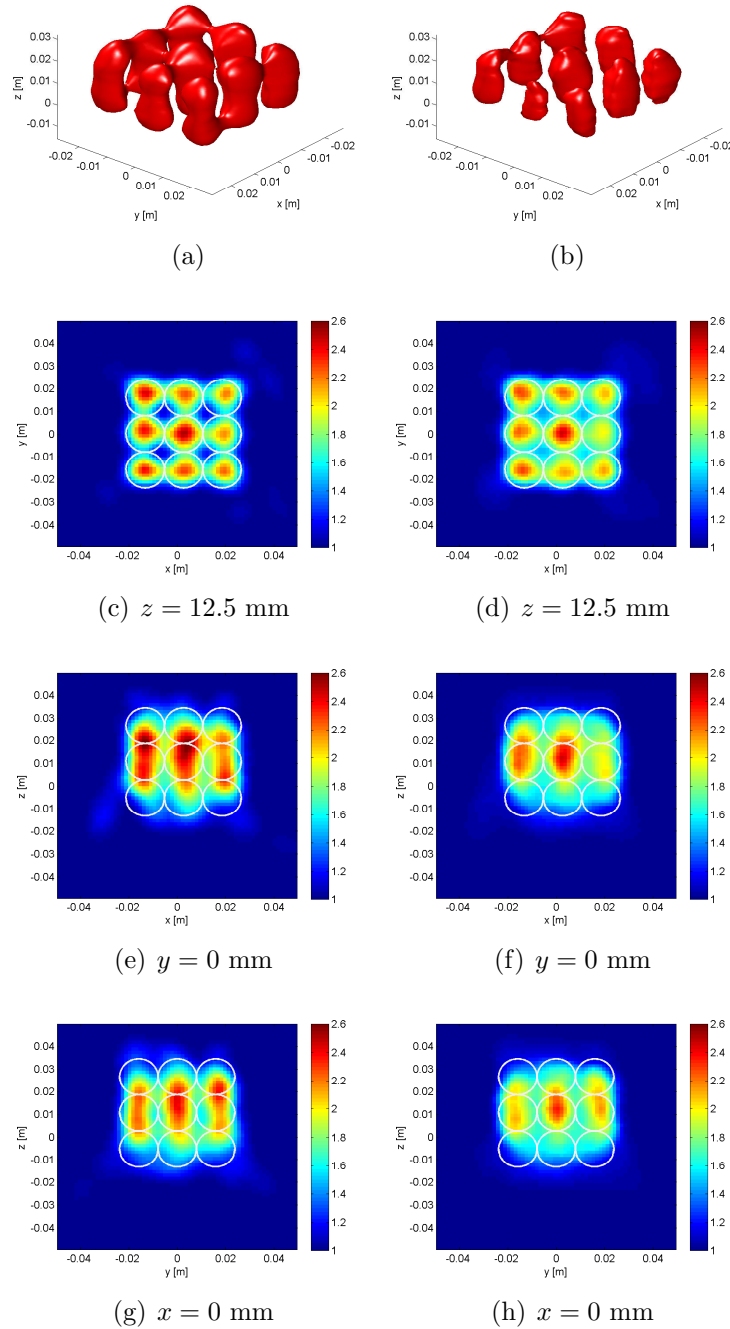


Figure 6.61: (a)-(b) The isosurface plot (level = 1.9) at $f = 8$ GHz of the cube of spheres target and the 2D slice plots of the reconstruction at planes (c)-(d) $z = 12.5$ mm, (e)-(f) $y = 0$ mm and (f)-(g) $x = 0$ mm. The figures on the left are the FEM-CSI reconstructions while those on the right are the MR-FEMCSI results. The results are obtained using a frequency-hopping approach.

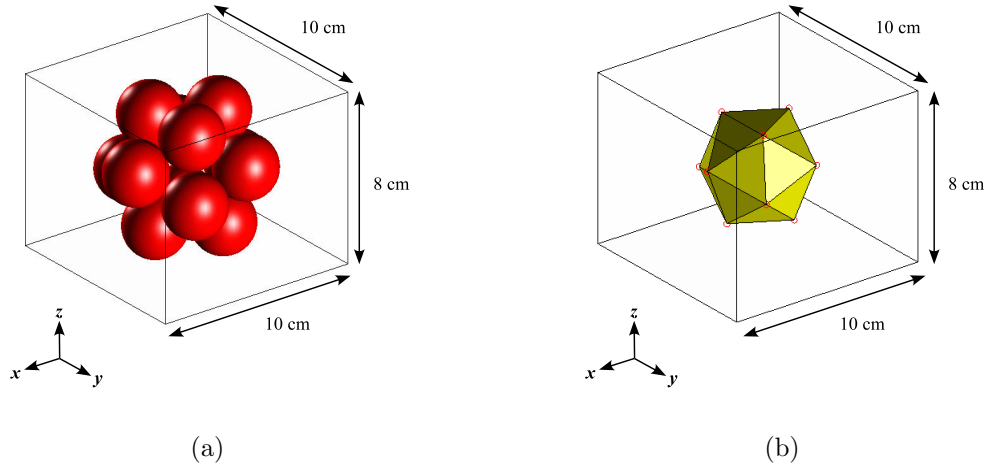


Figure 6.62: (a) *Myster* target configuration and (b) an icosahedron. The red circles at the vertices of the icosahedron are the sphere centers of the *Myster* target.

of the box are equal to 100 mm. Its height is 80 mm. The number of unknowns is approximately 36,000 located at the tetrahedral centroids in \mathcal{D} . Similar to the last two datasets, a frequency-hopping approach is applied using data from 3 GHz to 8 GHz with a frequency increment of 1 GHz.

The reconstruction results are presented in Figures 6.64–6.66. The plots in Figure 6.64 are the isosurface plots (level = 1.5) and the 2D slice plots at planes $x = [-11.12, -6.87]$ mm and $y = [-4.1, 19.25]$ mm. The left column of Figure 6.64 contains the FEM-CSI reconstructions and the right column has the MR-FEMCSI results. The 2D slices in Figure 6.65 are the FEM-CSI results at six z -planes ranging from $z = 4.40$ mm to $z = 35.97$ mm. The MR-FEMCSI z -plane cross-sections are shown in Figure 6.66. All the shown results are the reconstructions at a frequency $f = 8$ GHz. The convergence of the cost functional is given in Figure 6.63.

The algorithms predicted the overall shape and location of the *Myster* object accurately. The L_2 -weighted regularizer tends to smooth and fuse the spheres together as can be deduced from Figure 6.66; nevertheless it does not over-estimate the relative

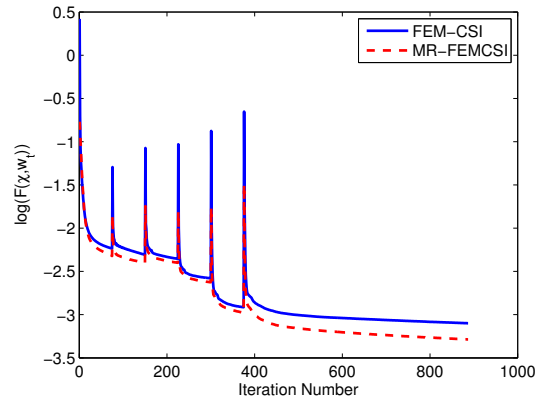


Figure 6.63: The cost functional convergence for the *Myster* dataset inversion.

permittivity value of the spheres. Without multiplicative regularization, the gaps in-between the spheres are more visible as is the location of the individual spheres within the *Myster* structure; however the estimated values of the permittivity exceed the expectation.

6.3.4.5 Section Conclusion

The FEM-CSI algorithm along with its variant, which incorporates MR, were tested using the 3D experimental datasets collected by the Institut Fresnel of France. The inversion algorithms were successful in predicting the location and size of the targets. The reconstructed relative permittivity values for the targets were overshoot by FEM-CSI; the inclusion of MR fixed that however it caused small spaces between the constituents of some targets to smooth out and be filled.

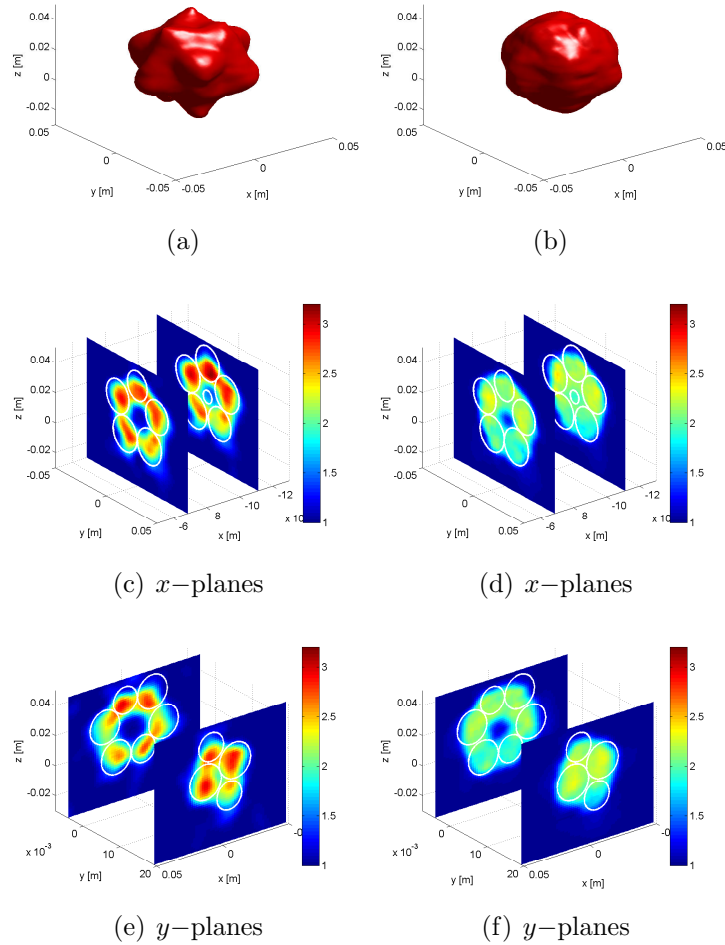


Figure 6.64: (a)-(b) The isosurface plot (level = 1.5) at $f = 8$ GHz of the *Myster* target and the 2D slice plots of the reconstruction at planes (c)-(d) $x = [-11.12, -6.87]$ mm and (e)-(f) $y = [-4.10, 19.25]$ mm. The figures on the left are the FEM-CSI reconstructions while those on the right are the MR-FEMCSI results. The results are obtained using a frequency-hopping approach.

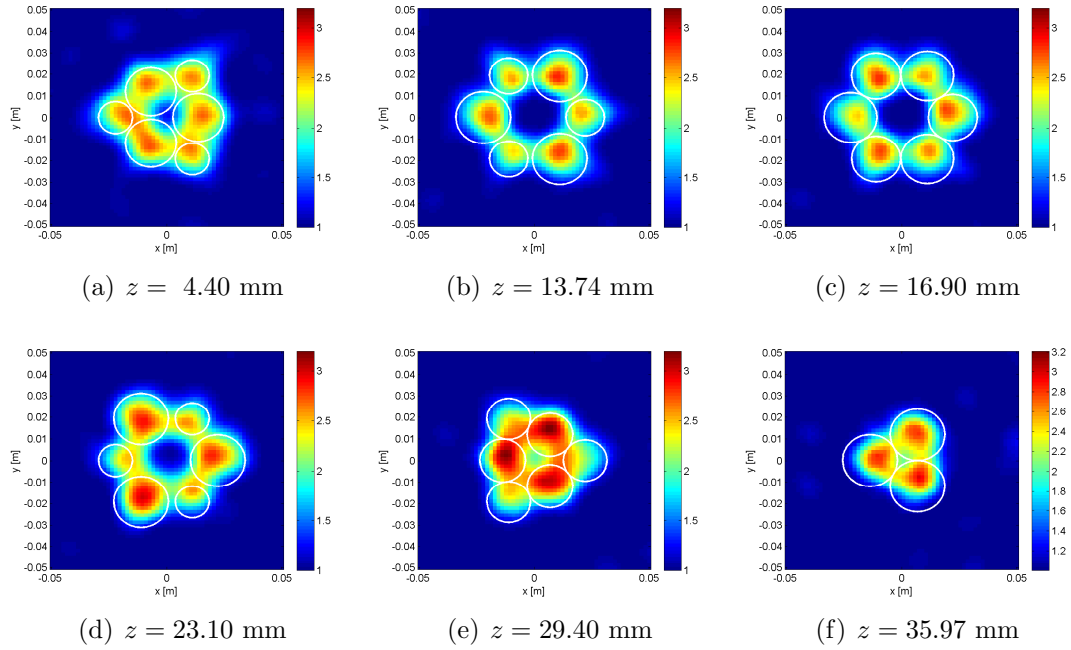


Figure 6.65: The *Myster* dataset frequency-hopping FEM-CSI reconstructions at different z -planes for $f = 8$ GHz.

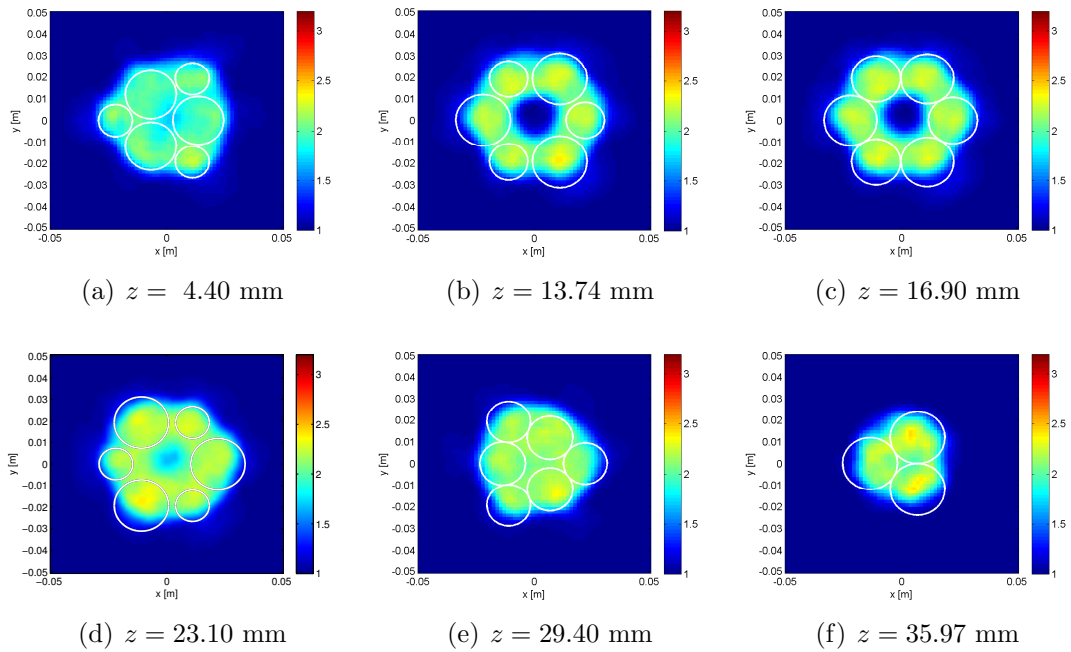


Figure 6.66: The *Myster* dataset frequency-hopping MR-FEMCSI reconstructions at different z -planes for $f = 8$ GHz.

7

Conclusions and Future Work

Aut non tentaris, aut perfice. (Either don't attempt it, or carry it through the end.)

–Ovid

The formulation as well as the implementation of the state-of-the-art contrast source inversion using the finite element method for microwave imaging applications was completed:

- The full derivation of a new CSI algorithm incorporating the flexibility of the finite-element method to discretize the appropriate EM forward operators of the electromagnetic problem has been given. The formulation was presented for scalar as well as vectorial, 2D and 3D problems.
- The weighted L_2 -norm total variation multiplicative regularization was incorporated to the algorithm, along with an enhancement to account for the imbalance between the real and imaginary components of the OI's relative permittivity in some applications. A novel technique to calculate the gradient and divergence operators required for multiplicative regularization on arbitrary meshes was introduced.

- For 2D problems, extensive testing using synthetic examples was undertaken to emphasize the advantages offered by the algorithm. Due to computational complexities, simple synthetic examples were used to test the functionality of the FEM-CSI algorithm in 3D. Further, the matrix solver used was chosen by comparing the computation time and the memory usage of different methods, so as to make the 3D inverse problem feasible given the computational resources available.
- The algorithm was successful in inverting experimental datasets from the UofM microwave imaging systems, as well as datasets from other setups in France and Spain. Due to the lack of various vectorial experimental datasets, the algorithm was tested with vectorial data collected in free-space only.

7.1 Future Work

- The accuracy of the finite-element method can be improved by either refining the problem mesh or by resorting to higher-order basis functions. While the first method increases the computational complexity of problem, the later technique would provide better accuracy with a fewer number of elements [44]. The drawback of using higher-order elements is the mathematical complications associated with it, especially for three-dimensional problems.
- Currently, the electric field and the electric properties of the OI are computed on the same mesh. Although the electric field computation may require a finely discretized mesh to ensure accurate calculations, the properties of the OI may be uniformly distributed and can be reconstructed well on a coarse mesh. An improvement to the inversion algorithm would be to detach the field compu-

tation mesh from the reconstruction mesh resulting in a dual-mesh scheme as implemented in [33]. This can be readily implemented within the framework of the current inversion algorithm and would mostly only require changing some of the matrix transformation operators.

- It has been shown that the use of adaptive meshing reduces the computational resources required to obtain the same image quality as when a uniformly fine mesh is used. The meshing technique was performed manually after a visual inspection of the coarse-mesh reconstructions; future work could include the use of a fully automatic adaptively refinement procedure [118].
- The use of inhomogeneous backgrounds as prior information for biomedical experimental data can be further investigated. Such a study might require integrating measurements from other modalities, *e.g.* ultrasound and MRI, into the microwave imaging algorithm.
- The presented formulation of the CSI algorithm is not restricted to the use of FEM as a computational tool. Other techniques like the finite-volume [60] and the discontinuous Galerkin [119] frequency-domain methods can be integrated into the inversion algorithm. The only required modifications to the inversion algorithm would be the matrix operators that implement from the FEM discretization. The use of the finite-volume technique might be advantageous due to the availability of accurate models for thin-wires and circuits [60]. In addition, the finite-volume method computes both the electric and magnetic fields within the mesh.
- The image quality of the reconstructions may be improved by utilizing other types of regularization techniques like shape and location methods [120, 121].

-
- The 3D full-vectorial form of the algorithm has to be tested with more complicated configurations, for example with the OI inside a chamber having conductive walls or with the OI immersed in a lossy background medium. Such further testing of the algorithm would require a more efficient implementation of the FEM-CSI algorithm in 3D.
 - The algorithm implementation can be accelerated or parallelized via distributed computing using graphics processing units (GPU) or computer clusters. Furthermore, the algorithms can be ported to another computer language for more efficient memory handling and for better speed of execution.

Appendix

No other question has ever moved so profoundly the spirit of man; no other idea has so fruitfully stimulated his intellect; yet no other concept stands in greater need of clarification than that of the infinite.

–David Hilbert [[122](#)]

A

Derivation of FEM Local Matrices

A.1 Scalar Problems: Two-Dimensional Case

With the domain divided into N_e triangular elements and N_s line segments, the functional $F(u)$ in (3.5) can be written as

$$F(u) = \sum_{e=1}^{N_e} F^e(u^e) + \sum_{s=1}^{N_s} F^s(u^s) \quad (\text{A.1})$$

where

$$F^e(u^e) = -\frac{1}{2} \int_{\Omega^e} \left(\nabla u^e \cdot \nabla u^e - \alpha^e (u^e)^2 \right) dv - \int_{\Omega^e} \beta^e f^e u^e dv \quad (\text{A.2})$$

$$F^s(u^s) = \int_{\Gamma_2^s} \left(\frac{\gamma^s}{2} (u^s)^2 - q^s u^s \right) ds. \quad (\text{A.3})$$

Using the approximations in (3.6), (3.12)-(3.14) and (3.16), the above equations can be written as

$$F^e(u^e) = -\frac{1}{2} (\underline{u}^e)^T \mathcal{S}^e(\underline{u}^e) + \frac{1}{2} (\underline{u}^e)^T \mathcal{T}_\alpha^e(\underline{u}^e) - (\underline{u}^e)^T \mathcal{T}_\beta^e(\underline{f}^e) \quad (\text{A.4})$$

$$F^s(u^s) = \frac{1}{2} (\underline{u}^s)^T \mathcal{S}^s(\underline{u}^s) - \frac{q^s l^s}{2} (\underline{u}^s)^T (\underline{f}^s). \quad (\text{A.5})$$

where l^s is the length of line segment s , vectors \underline{u}^e , \underline{f}^e , \underline{u}^s and \underline{f}^s are

$$\underline{u}^e = \begin{bmatrix} u_1^e \\ u_2^e \\ u_3^e \end{bmatrix}, \quad \underline{f}^e = \begin{bmatrix} f_1^e \\ f_2^e \\ f_3^e \end{bmatrix}, \quad \underline{u}^s = \begin{bmatrix} u_1^s \\ u_2^s \end{bmatrix}, \quad \underline{f}^s = \begin{bmatrix} 1 \\ 1 \end{bmatrix} \quad (\text{A.6})$$

and matrices \mathcal{S}^e , \mathcal{T}_α^e , \mathcal{T}_β^e and \mathcal{S}^s are

$$\mathcal{S}^e = \int_{\Omega^e} \begin{bmatrix} \nabla \lambda_1^e \cdot \nabla \lambda_1^e & \nabla \lambda_1^e \cdot \nabla \lambda_2^e & \nabla \lambda_1^e \cdot \nabla \lambda_3^e \\ \nabla \lambda_2^e \cdot \nabla \lambda_1^e & \nabla \lambda_2^e \cdot \nabla \lambda_2^e & \nabla \lambda_2^e \cdot \nabla \lambda_3^e \\ \nabla \lambda_3^e \cdot \nabla \lambda_1^e & \nabla \lambda_3^e \cdot \nabla \lambda_2^e & \nabla \lambda_3^e \cdot \nabla \lambda_3^e \end{bmatrix} dv, \quad (\text{A.7})$$

$$\mathcal{T}_\alpha^e = \int_{\Omega^e} \begin{bmatrix} \lambda_1^e \lambda_1^e \nu_\alpha^e & \lambda_1^e \lambda_2^e \nu_\alpha^e & \lambda_1^e \lambda_3^e \nu_\alpha^e \\ \lambda_2^e \lambda_1^e \nu_\alpha^e & \lambda_2^e \lambda_2^e \nu_\alpha^e & \lambda_2^e \lambda_3^e \nu_\alpha^e \\ \lambda_3^e \lambda_1^e \nu_\alpha^e & \lambda_3^e \lambda_2^e \nu_\alpha^e & \lambda_3^e \lambda_3^e \nu_\alpha^e \end{bmatrix} dv, \quad (\text{A.8})$$

$$\mathcal{T}_\beta^e = \int_{\Omega^e} \begin{bmatrix} \lambda_1^e \lambda_1^e \nu_\beta^e & \lambda_1^e \lambda_2^e \nu_\beta^e & \lambda_1^e \lambda_3^e \nu_\beta^e \\ \lambda_2^e \lambda_1^e \nu_\beta^e & \lambda_2^e \lambda_2^e \nu_\beta^e & \lambda_2^e \lambda_3^e \nu_\beta^e \\ \lambda_3^e \lambda_1^e \nu_\beta^e & \lambda_3^e \lambda_2^e \nu_\beta^e & \lambda_3^e \lambda_3^e \nu_\beta^e \end{bmatrix} dv, \quad (\text{A.9})$$

$$\mathcal{S}^s = \gamma^s \int_{\Gamma_2^s} \begin{bmatrix} \lambda_1^s \lambda_1^s & \lambda_1^s \lambda_2^s \\ \lambda_2^s \lambda_1^s & \lambda_2^s \lambda_2^s \end{bmatrix} ds, \quad (\text{A.10})$$

where $\nu_\alpha^e \triangleq \lambda_1^e \alpha_1^e + \lambda_2^e \alpha_2^e + \lambda_3^e \alpha_3^e$ and $\nu_\beta^e \triangleq \lambda_1^e \beta_1^e + \lambda_2^e \beta_2^e + \lambda_3^e \beta_3^e$.

The variables α_i^e and β_i^e are either equal to $k_{b,i}^2(\chi_i + 1)$ and $-k_{b,i}^2 \chi_i$ respectively, where $k_{b,i}$ is the background wavenumber and χ_i is the contrast value at a node i , as per the wave equation (2.30), or they are equal to $k_{b,i}^2$ and $-k_{b,i}^2$ according to (2.31).

The integrations above can be evaluated analytically with the aid of the following

formula [123]

$$\int_{\Omega^e} (\lambda_1^e)^l (\lambda_2^e)^m (\lambda_3^e)^n dv = 2A^e \frac{l! m! n!}{(l+m+n+2)!}, \quad (\text{A.11})$$

thus (A.7)-(A.10) become

$$\mathbf{S}^e = \frac{1}{4A^e} \begin{bmatrix} b_1^e b_1^e + c_1^e c_1^e & b_1^e b_2^e + c_1^e c_2^e & b_1^e b_3^e + c_1^e c_3^e \\ b_2^e b_1^e + c_2^e c_1^e & b_2^e b_2^e + c_2^e c_2^e & b_2^e b_3^e + c_2^e c_3^e \\ b_3^e b_1^e + c_3^e c_1^e & b_3^e b_2^e + c_3^e c_2^e & b_3^e b_3^e + c_3^e c_3^e \end{bmatrix}, \quad (\text{A.12})$$

$$\mathcal{T}_\alpha^e = \frac{A^e}{60} \begin{bmatrix} 6\alpha_1^e + 2(\alpha_2^e + \alpha_3^e) & 2(\alpha_1^e + \alpha_2^e) + \alpha_3^e & 2(\alpha_1^e + \alpha_3^e) + \alpha_2^e \\ 2(\alpha_1^e + \alpha_2^e) + \alpha_3^e & 6\alpha_2^e + 2(\alpha_1^e + \alpha_3^e) & 2(\alpha_2^e + \alpha_3^e) + \alpha_1^e \\ 2(\alpha_1^e + \alpha_3^e) + \alpha_2^e & 2(\alpha_2^e + \alpha_3^e) + \alpha_1^e & 6\alpha_3^e + 2(\alpha_1^e + \alpha_2^e) \end{bmatrix}, \quad (\text{A.13})$$

$$\mathcal{T}_\beta^e = \frac{A^e}{60} \begin{bmatrix} 6\beta_1^e + 2(\beta_2^e + \beta_3^e) & 2(\beta_1^e + \beta_2^e) + \beta_3^e & 2(\beta_1^e + \beta_3^e) + \beta_2^e \\ 2(\beta_1^e + \beta_2^e) + \beta_3^e & 6\beta_2^e + 2(\beta_1^e + \beta_3^e) & 2(\beta_2^e + \beta_3^e) + \beta_1^e \\ 2(\beta_1^e + \beta_3^e) + \beta_2^e & 2(\beta_2^e + \beta_3^e) + \beta_1^e & 6\beta_3^e + 2(\beta_1^e + \beta_2^e) \end{bmatrix}, \quad (\text{A.14})$$

$$\mathbf{S}^s = \frac{\gamma^s l^s}{6} \begin{bmatrix} 2 & 1 \\ 1 & 2 \end{bmatrix}. \quad (\text{A.15})$$

If α^e and β^e are defined for each triangle rather than on each node in the mesh, \mathcal{T}_α^e and \mathcal{T}_β^e simplify to

$$\mathcal{T}_\alpha^e = \frac{\alpha^e A^e}{12} \begin{bmatrix} 2 & 1 & 1 \\ 1 & 2 & 1 \\ 1 & 1 & 2 \end{bmatrix}, \quad (\text{A.16})$$

$$\mathcal{T}_\beta^e = \frac{\beta^e A^e}{12} \begin{bmatrix} 2 & 1 & 1 \\ 1 & 2 & 1 \\ 1 & 1 & 2 \end{bmatrix}. \quad (\text{A.17})$$

A.2 Vector Problems

After discretizing the problem into N_e domain elements and N_s boundary elements, the functional $F(\vec{u})$ can be written as

$$F(\vec{u}) = \sum_{e=1}^{N_e} F^e(\vec{u}^e) + \sum_{s=1}^{N_s} F^s(\vec{u}^s) \quad (\text{A.18})$$

where

$$\begin{aligned} F^e(\vec{u}^e) &= \frac{1}{2} \int_{\Omega^e} [(\nabla \times \vec{u}^e) \cdot (\nabla \times \vec{u}^e) - \alpha^e \vec{u}^e \cdot \vec{u}^e] dv - \int_{\Omega^e} \beta^e \vec{u}^e \cdot \vec{f}^e dv \\ F^s(\vec{u}^s) &= \int_{\Gamma_2^s} \left[\frac{\gamma^s}{2} (\hat{n} \times \vec{u}^s) \cdot (\hat{n} \times \vec{u}^s) + \vec{u}^s \cdot \vec{q}^s \right] ds. \end{aligned} \quad (\text{A.19})$$

Using the vector fields approximations in (3.46), (3.51) for 2D and (3.47), (3.52) for 3D, the above equations can be written as

$$\begin{aligned} F^e(\vec{u}^e) &= \frac{1}{2} (\underline{u}^e)^T [\underline{\mathbf{u}}^e - \underline{\mathbf{v}}_\alpha^e] (\underline{u}^e) - (\underline{u}^e)^T \underline{\mathbf{R}}_\beta^e \cdot \vec{f}^e \\ F^s(\vec{u}^s) &= \frac{1}{2} (\underline{u}^s)^T \underline{\mathbf{u}}^s (\underline{u}^s) + (\underline{u}^s)^T \underline{\mathbf{R}}^s \cdot \vec{q}^s. \end{aligned} \quad (\text{A.20})$$

where the spatial-vectors \vec{f}^e and \vec{q}^s are defined at the centroids of elements e and s respectively.

A.2.1 Two-Dimensional Case

For 2D vectorial problems, the vectors \underline{u}^e , \underline{u}^s in (A.20) are

$$\underline{u}^e = \begin{bmatrix} u_1^e \\ u_2^e \\ u_3^e \end{bmatrix}, \underline{u}^s = \begin{bmatrix} u_1^s \end{bmatrix}. \quad (\text{A.21})$$

The entries of each matrix in (A.20) are evaluated using the expansions (3.46), (3.51) and with the aid of the integral (A.11).

For a triangle e , the entry for the i^{th} row and j^{th} column of local matrices $\mathbf{U}^e \in \mathbb{R}^{3 \times 3}$ and $\mathbf{V}_\alpha^e \in \mathbb{C}^{3 \times 3}$ are

$$\begin{aligned} \mathcal{U}_{i,j}^e &= \frac{l_i^e l_j^e}{4 (A^e)^3} (b_{i_1}^e c_{i_2}^e - b_{i_2}^e c_{i_1}^e) (b_{j_1}^e c_{j_2}^e - b_{j_2}^e c_{j_1}^e) \\ \mathcal{V}_{\alpha i,j}^e &= \frac{\alpha^e l_i^e l_j^e}{48 A^e} (L_{i_1,j_1} f_{i_2,j_2}^e - L_{i_1,j_2} f_{i_2,j_1}^e - L_{i_2,j_1} f_{i_1,j_2}^e + L_{i_2,j_2} f_{i_1,j_1}^e) \end{aligned} \quad (\text{A.22})$$

where A^e is the area of triangle e , $\{l_i^e, l_j^e\}$ are the length of local triangle edges $\{i, j\}$, $\{i_1, i_2\}$ and $\{j_1, j_2\}$ are nodes forming these local edges as defined in Table 3.1, b_i^e and c_i^e are coefficients defined in Section 3.2.4, $f_{i,j}^e$ is evaluated as

$$f_{i,j}^e = b_i^e b_j^e + c_i^e c_j^e \quad (\text{A.23})$$

and $L_{i,j}$ is the $(i, j)^{\text{th}}$ entry of matrix $\mathbf{L} \in \mathbb{R}^{3 \times 3}$, given as

$$\mathbf{L} = \begin{bmatrix} 2 & 1 & 1 \\ 1 & 2 & 1 \\ 1 & 1 & 2 \end{bmatrix}. \quad (\text{A.24})$$

Next, the i^{th} entry of column vector $\vec{\mathcal{R}}_{\beta}^e \in \mathbb{C}^3$ is

$$\vec{\mathcal{R}}_{\beta i}^e = \frac{\beta^e l_i^e}{6} \left((b_{i_2}^e - b_{i_1}^e) \hat{x} + (c_{i_2}^e - c_{i_1}^e) \hat{y} \right) \quad (\text{A.25})$$

where i is the local edge index for an triangular element e .

Let an edge s , which belongs to triangle e , be a line segment at the boundary of the problem domain, then both \mathbf{u}^s and $\vec{\mathcal{R}}^s$ have single entries which they are calculated as

$$\begin{aligned} \mathbf{u}^s &= \frac{\gamma^s (l^s)^3}{12 (A^e)^2} \left((\hat{n}_x^s)^2 \left((c_{i_1}^e)^2 - c_{i_1}^e c_{i_2}^e + (c_{i_2}^e)^2 \right) - \right. \\ &\quad \left. \hat{n}_x^s \hat{n}_y^s \left(2b_{i_1}^e c_{i_1}^e - b_{i_1}^e c_{i_2}^e - b_{i_2}^e c_{i_1}^e + 2b_{i_2}^e c_{i_2}^e \right) + \right. \\ &\quad \left. (\hat{n}_y^s)^2 \left((b_{i_1}^e)^2 - b_{i_1}^e b_{i_2}^e + (b_{i_2}^e)^2 \right) \right) \\ \vec{\mathcal{R}}^s &= \frac{(l^s)^2}{4 A^e} \left((b_{i_2}^e - b_{i_1}^e) \hat{x} + (c_{i_2}^e - c_{i_1}^e) \hat{y} \right) \end{aligned} \quad (\text{A.26})$$

where $\{i_1, i_2\}$ are the local node indices of an edge s as given in Table 3.1, l^s is the length of the edge, \hat{n}_x^s and \hat{n}_y^s are the x - and y -components of an outward-normal unit vector \hat{n} to the segment s .

A.2.2 Three-Dimensional Case

For 3D vectorial problems, the vectors $\underline{u}^e, \underline{u}^s$ in (A.20) are

$$\underline{u}^e = \begin{bmatrix} u_1^e \\ u_2^e \\ \vdots \\ u_6^e \end{bmatrix}, \underline{u}^s = \begin{bmatrix} u_1^s \\ u_2^s \\ u_3^s \end{bmatrix}. \quad (\text{A.27})$$

The entries of each matrix in (A.20) are evaluated using the expansions (3.47), (3.52) and with the aid of the following formula [44]:

$$\int_{\Omega^e} (\lambda_1^e)^k (\lambda_2^e)^l (\lambda_3^e)^m (\lambda_4^e)^n dv = 6V^e \frac{k! l! m! n!}{(k+l+m+n+3)!} \quad (\text{A.28})$$

where $\lambda_{1,2,3,4}^e$ are the three-dimensional nodal linear basis functions (3.48) and V^e is the volume of tetrahedron element e .

For a tetrahedron e , the entries for the i^{th} row and j^{th} column of the local matrices $\mathbf{U}^e \in \mathbb{R}^{6 \times 6}$ and $\mathbf{V}_\alpha^e \in \mathbb{C}^{6 \times 6}$ are

$$\begin{aligned} \mathcal{U}_{i,j}^e &= \frac{4 l_i^e l_j^e}{1296 (V^e)^3} \left((b_{i_1}^e c_{i_2}^e - b_{i_2}^e c_{i_1}^e) (b_{j_1}^e c_{j_2}^e - b_{j_2}^e c_{j_1}^e) + \right. \\ &\quad (c_{i_1}^e d_{i_2}^e - c_{i_2}^e d_{i_1}^e) (c_{j_1}^e d_{j_2}^e - c_{j_2}^e d_{j_1}^e) + \\ &\quad \left. (d_{i_1}^e b_{i_2}^e - d_{i_2}^e b_{i_1}^e) (d_{j_1}^e b_{j_2}^e - d_{j_2}^e b_{j_1}^e) \right) \\ \mathcal{V}_{\alpha i,j}^e &= \frac{\alpha^e l_i^e l_j^e}{720 V^e} (L_{i_1,j_1} f_{i_2,j_2}^e - L_{i_1,j_2} f_{i_2,j_1}^e - L_{i_2,j_1} f_{i_1,j_2}^e + L_{i_2,j_2} f_{i_1,j_1}^e) \end{aligned} \quad (\text{A.29})$$

where V^e is the volume of tetrahedron e , $\{l_i^e, l_j^e\}$ are the length of edges $\{i, j\}$, $\{i_1, i_2\}$ and $\{j_1, j_2\}$ are nodes forming these local edges as defined in Table 3.2, b_i^e , c_i^e and d_i^e are coefficients defined in Section 3.3.4, $f_{i,j}^e$ is evaluated as

$$f_{i,j}^e = b_i^e b_j^e + c_i^e c_j^e + d_i^e d_j^e \quad (\text{A.30})$$

and $L_{i,j}$ is the (i,j) th entry of matrix $\mathbf{L} \in \mathbb{R}^{4 \times 4}$, given as

$$\mathbf{L} = \begin{bmatrix} 2 & 1 & 1 & 1 \\ 1 & 2 & 1 & 1 \\ 1 & 1 & 2 & 1 \\ 1 & 1 & 1 & 2 \end{bmatrix}. \quad (\text{A.31})$$

Next, the i th entry of column vector $\vec{\mathcal{R}}_{\beta}^e \in \mathbb{C}^6$ is

$$\vec{\mathcal{R}}_{\beta i}^e = \frac{\beta^e l_i^e}{24} ((b_{i_2}^e - b_{i_1}^e) \hat{x} + (c_{i_2}^e - c_{i_1}^e) \hat{y} + (d_{i_2}^e - d_{i_1}^e) \hat{z}) \quad (\text{A.32})$$

where i is the local edge index for a tetrahedral element e .

Let a triangular boundary facet s , which belongs to tetrahedron e , be transformed to an isoparametric element ζ^s (depicted in Figure 3.5), then the (i,j) th entry of local matrix $\mathbf{U}^s \in \mathbb{C}^{3 \times 3}$ is calculated by evaluating the following:

$$U_{i,j}^s = \int_0^1 \int_0^{1-\xi} 2 A^s \gamma^s (\hat{n}^s \times \vec{N}_i) \cdot (\hat{n}^s \times \vec{N}_j) d\eta d\xi \quad (\text{A.33})$$

where indices $\{i,j\}$ denote local triangle edges $\{s_i, s_j\}$ that map to local tetrahedron edges $\{e_i, e_j\}$, A^s is the area of surface triangle s , \hat{n}^s is the outward-normal unit vector at the centroid of triangle s and the vector-basis functions $\{\vec{N}_i, \vec{N}_j\}$ are a function of the isoparametric coordinates ξ and η . For a tetrahedron edge k defined by nodes $\{k_1, k_2\}$ and mapped to surface facet edge s_k

$$\hat{n}^s \times \vec{N}_k = \frac{l_k^e}{6 V^e} \begin{vmatrix} \hat{x} & \hat{y} & \hat{z} \\ \hat{n}_x^s & \hat{n}_y^s & \hat{n}_z^s \\ (\lambda_{k_1}^{\zeta^s} b_{k_2} - \lambda_{k_2}^{\zeta^s} b_{k_1}) & (\lambda_{k_1}^{\zeta^s} c_{k_2} - \lambda_{k_2}^{\zeta^s} c_{k_1}) & (\lambda_{k_1}^{\zeta^s} d_{k_2} - \lambda_{k_2}^{\zeta^s} d_{k_1}) \end{vmatrix}. \quad (\text{A.34})$$

If triangle s nodes $\{1, 2, 3\}$ maps to local tetrahedron e nodes $\{n_1, n_2, n_3\}$, the basis functions in (A.34) are given in isoparametric coordinates as

$$\lambda_{n_1}^{\zeta^s}(\xi, \eta) = \xi \quad , \quad \lambda_{n_2}^{\zeta^s}(\xi, \eta) = \eta. \quad (\text{A.35})$$

The third isoparametric coordinate is defined as

$$\lambda_{n_3}^{\zeta^s}(\xi, \eta) = 1 - \xi - \eta. \quad (\text{A.36})$$

Finally, the i^{th} entry of the column vector $\vec{\mathcal{R}}^s \in \mathbb{R}^3$ is

$$\vec{\mathcal{R}}_i^s = \frac{A^s l_i^s}{18 V^e} \left((b_{i_2}^e - b_{i_1}^e) \hat{x} + (c_{i_2}^e - c_{i_1}^e) \hat{y} + (d_{i_2}^e - d_{i_1}^e) \hat{z} \right) \quad (\text{A.37})$$

where index i corresponds to local triangle edge s_i that maps to local tetrahedron edge e_i , and $\{i_1, i_2\}$ are the local node indices of the edge e_i as given in Table 3.2.

B

Assembly of FEM Global Matrices

We consider first the 2D scalar case. Each node in the triangular mesh is associated with two indices: a local number to indicate its location in a given triangle and a global number to indicate its location relative to the entire mesh. After the assembly of the local matrices, the global numbering scheme is used to build the global FEM matrices.

Consider a local matrix \mathcal{K}^e

$$\mathcal{K}^e = \begin{bmatrix} \mathcal{K}_{1,1}^e & \mathcal{K}_{1,2}^e & \mathcal{K}_{1,3}^e \\ \mathcal{K}_{2,1}^e & \mathcal{K}_{2,2}^e & \mathcal{K}_{2,3}^e \\ \mathcal{K}_{3,1}^e & \mathcal{K}_{3,2}^e & \mathcal{K}_{3,3}^e \end{bmatrix}. \quad (\text{B.1})$$

For any triangle, as depicted in figure 3.2 (a), the local nodes $\{1, 2, 3\}$ are associated with global indices $\{i, j, k\}$; therefore local matrix \mathcal{K}^e can be rewritten as

$$\mathcal{K}^e = \begin{bmatrix} \mathcal{K}_{i,i}^e & \mathcal{K}_{i,j}^e & \mathcal{K}_{i,k}^e \\ \mathcal{K}_{j,i}^e & \mathcal{K}_{j,j}^e & \mathcal{K}_{j,k}^e \\ \mathcal{K}_{k,i}^e & \mathcal{K}_{k,j}^e & \mathcal{K}_{k,k}^e \end{bmatrix}. \quad (\text{B.2})$$

Here the global indices have replaced the local numbers in (B.1).

Next, consider a global matrix $\mathcal{K} \in \mathbb{C}^{N \times N}$. In the FEM matrix equation (3.26), this global matrix \mathcal{K} can be either

$$\mathcal{K} = \mathcal{S} - \mathcal{T}_\alpha \quad \text{or} \quad \mathcal{K} = \mathcal{T}_\beta. \quad (\text{B.3})$$

The global matrix \mathcal{K} is filled using the following scheme: the first local element $\mathcal{K}_{i,i}^e$ in \mathcal{K}^e is added to the i^{th} row and the i^{th} column of global matrix \mathcal{K} , the second local element $\mathcal{K}_{i,j}^e$ is added to the i^{th} row and the j^{th} column of global matrix \mathcal{K} , and so on. This is repeated for each triangular element.

For BVPs with Dirichlet boundary conditions, the values of u on the boundary are known; this results in changes to the structure of the global matrix \mathcal{K} . Given that node i is a boundary node, the j^{th} element of \mathcal{K} in row i is enforced to

$$\mathcal{K}_{i,j} = \begin{cases} 1 & \text{for } j = i \\ 0 & \text{for } j \neq i \end{cases}. \quad (\text{B.4})$$

Assuming that the global indices are assigned to the boundary nodes first and then to the free (interior) nodes, the global matrix \mathcal{K} splits into four sub-matrices as follows:

$$\mathcal{K} = \begin{bmatrix} \mathbf{I}_{\text{BB}} & \mathbf{0}_{\text{BF}} \\ \mathcal{K}_{\text{FB}} & \mathcal{K}_{\text{FF}} \end{bmatrix}, \quad (\text{B.5})$$

where subscripts B and F refer to the B boundary nodes and the F free (interior) nodes in the mesh, thus $N = B + F$. The dimensions of the sub-matrices in (B.5) are indicated by their subscripts; for example sub-matrix $\mathcal{K}_{\text{FB}} \in \mathbb{C}^{\text{F} \times \text{B}}$. Further, sub-matrix $\mathbf{I}_{\text{BB}} \in \mathbb{R}^{\text{B} \times \text{B}}$ is an identity matrix, and sub-matrix $\mathbf{0}_{\text{BF}} \in \mathbb{R}^{\text{B} \times \text{F}}$ is a zero matrix. The matrix \mathcal{K}_{FB} describes the interaction between boundary nodes and free

nodes.

For vectorial problems solved using FEM, where the unknowns are along the element edges, the assembly of the global matrices and the treatment of boundary edges are very similar to the node-based FEM. In 2D problems, the unknowns for any triangle are on the edges that are mapped from their local numbers $\{1, 2, 3\}$ to their global labels $\{i, j, k\}$. For 3D problems, the local edges of a tetrahedron $\{1, 2, 3, 4, 5, 6\}$ are associated with global indices $\{i, j, k, l, m, n\}$.

C

Required Gradients for FEM-CSI

In the first step of the FEM-CSI algorithm, the gradient of the cost functional, \vec{g}_t , with respect to the contrast source variables, \vec{w}_t , is required to calculate the updates. At a given point \vec{w}_t , \vec{g}_t is the gradient pointing in the direction in which the Gâteaux differential has the largest value [124]. The Gâteaux differential is evaluated first for the data-error function $\mathcal{F}^S(\vec{w}_t)$ and then for the domain-error equation $\mathcal{F}^D(\chi, \vec{w}_t)$.

C.1 Data-Error Equation Gradient

For a small variation in \vec{w}_t taken along the search direction \vec{h}_t , the Gâteaux differential of the data-error function $\mathcal{F}^S(\vec{w}_t)$ is given by

$$\begin{aligned}
 d_{\vec{h}_t} \mathcal{F}^S(\vec{w}_t) &= \lim_{\epsilon \rightarrow 0} \frac{\mathcal{F}^S(\vec{w}_t + \epsilon \vec{h}_t) - \mathcal{F}^S(\vec{w}_t)}{\epsilon} \\
 &= \lim_{\epsilon \rightarrow 0} \eta_S \frac{\left\| \vec{u}_t - \vec{\mathcal{M}}_S \vec{\mathcal{L}}[\vec{w}_t + \epsilon \vec{h}_t] \right\|_S^2 - \left\| \vec{\rho}_t \right\|_S^2}{\epsilon} \\
 &= \lim_{\epsilon \rightarrow 0} \eta_S \frac{\left\| \vec{\rho}_t - \epsilon \vec{\mathcal{M}}_S \vec{\mathcal{L}}[\vec{h}_t] \right\|_S^2 - \left\| \vec{\rho}_t \right\|_S^2}{\epsilon}
 \end{aligned} \tag{C.1}$$

where $\vec{\rho}_t$ is a function of \vec{w}_t , given as

$$\vec{\rho}_t = \vec{u}_t - \vec{\mathcal{M}}_S \vec{\mathcal{L}}[\vec{w}_t]. \tag{C.2}$$

Expanding the norm, we get

$$\begin{aligned}
d_{\vec{h}_t} \mathcal{F}^S(\vec{w}_t) &= \lim_{\epsilon \rightarrow 0} \eta_S \frac{\left\| \vec{\rho}_t \right\|_S^2 - 2\epsilon \operatorname{Re} \left\langle \vec{\mathcal{M}}_S \vec{\mathcal{L}}[\vec{h}_t], \vec{\rho}_t \right\rangle_S + \epsilon^2 \left\| \vec{\mathcal{M}}_S \vec{\mathcal{L}}[\vec{h}_t] \right\|_S^2 - \left\| \vec{\rho}_t \right\|_S^2}{\epsilon} \\
&= \lim_{\epsilon \rightarrow 0} \eta_S \frac{-2\epsilon \operatorname{Re} \left\langle \vec{\mathcal{M}}_S \vec{\mathcal{L}}[\vec{h}_t], \rho_t \right\rangle_S + \epsilon^2 \left\| \vec{\mathcal{M}}_S \vec{\mathcal{L}}[\vec{h}_t] \right\|_S^2}{\epsilon} \\
&= \operatorname{Re} \left\langle -2\eta_S \vec{\mathcal{M}}_S \vec{\mathcal{L}}[\vec{h}_t], \vec{\rho}_t \right\rangle_S.
\end{aligned} \tag{C.3}$$

Next, to obtain the direction \vec{h}_t that will maximize the differential, the direction \vec{h}_t can be isolated in the inner product using the adjoint operator $\vec{\mathcal{G}}_S$ which satisfies

$$\left\langle -2\eta_S \vec{\mathcal{M}}_S \vec{\mathcal{L}}[\vec{h}_t], \vec{\rho}_t \right\rangle_S = \left\langle \vec{h}_t, \vec{\mathcal{G}}_S[\vec{\rho}_t] \right\rangle_{\mathcal{D}}. \tag{C.4}$$

Thus $\vec{h}_t = \vec{\mathcal{G}}_S[\vec{\rho}_t]$ is the direction of maximum ascent which is what we are looking for.

C.1.1 Case 1: 2D TM

Recall that, for 2D TM inversion problems, the electric field is assumed to be z -polarized with no transverse components in the $x - y$ plane, hence

$$\begin{aligned}
\vec{\rho}_t &= \rho_{t,z} \hat{z} & \vec{h}_{t,z} &= h_{t,z} \hat{z} \\
\vec{\mathcal{M}}_S &= \mathcal{M}_{S,z} \hat{z} & \vec{\mathcal{L}} &= \mathcal{L}_z \hat{z}.
\end{aligned}$$

and the adjoint operator we are looking for is written as

$$\vec{\mathcal{G}}_S = \mathcal{G}_{S,zz} \hat{z} \hat{z}.$$

Using the inner product definitions given in (4.7) and (4.8), both sides of (C.4) are expanded as follows:

$$-2\eta_S \rho_{\underline{t},z}^H \mathcal{M}_{S,z} \mathcal{L}_z[h_{\underline{t},z}] = \rho_{\underline{t},z}^H (\mathcal{G}_{S,zz})^H \mathcal{T}_{\mathcal{D}} h_{\underline{t},z}. \quad (\text{C.5})$$

where the $\mathcal{T}_{\mathcal{D}}$ matrix comes from the fact that the right inner product is taken over \mathcal{D} . Thus, we can identify

$$\mathcal{G}_{S,zz} = -2\eta_S \mathcal{T}_{\mathcal{D}}^{-1} \mathcal{L}_z^H \mathcal{M}_{S,z}^H, \quad (\text{C.6})$$

and thus the Gâteaux differential can be written as

$$d_{\underline{h}_{\underline{t},z}} \mathcal{F}^S(\underline{w}_{\underline{t},z}) = \text{Re} \left\langle \underline{h}_{\underline{t},z}, -2\eta_S \mathcal{T}_{\mathcal{D}}^{-1} \mathcal{L}_z^H \mathcal{M}_{S,z}^H \rho_{\underline{t},z} \right\rangle_{\mathcal{D}}. \quad (\text{C.7})$$

To maximize the value of the differential, the search direction $\underline{h}_{\underline{t},z}$ is chosen as

$$\underline{h}_{\underline{t},z} = -2\eta_S \mathcal{T}_{\mathcal{D}}^{-1} \mathcal{L}_z^H \mathcal{M}_{S,z}^H \rho_{\underline{t},z}. \quad (\text{C.8})$$

This search direction $\underline{h}_{\underline{t},z}$ is the gradient of the data-error equation $\mathcal{F}^S(\underline{w}_{\underline{t},z})$ with respect to the contrast source variables $\underline{w}_{\underline{t},z}$ for 2D TM problems.

C.1.2 Case 2: 2D TE

Recall that, for 2D TE configurations, the electric field is assumed to be polarized in the $x - y$ plane with no longitudinal component in the z -direction, therefore in

(C.4)

$$\begin{aligned}\vec{\rho}_t &= \underline{\rho}_{t,x} \hat{x} + \underline{\rho}_{t,y} \hat{y} & \vec{h}_t &= \underline{h}_{t,x} \hat{x} + \underline{h}_{t,y} \hat{y} \\ \vec{\mathcal{M}}_S &= \mathcal{M}_{S,x} \hat{x} + \mathcal{M}_{S,y} \hat{y} & \vec{\mathcal{L}} &= \mathcal{L}_x \hat{x} + \mathcal{L}_y \hat{y}\end{aligned}$$

and the adjoint operator we are looking for can be written as

$$\bar{\mathcal{G}}_S = \mathcal{G}_{S,xx} \hat{x} \hat{x} + \mathcal{G}_{S,yx} \hat{y} \hat{x} + \mathcal{G}_{S,xy} \hat{x} \hat{y} + \mathcal{G}_{S,yy} \hat{y} \hat{y}.$$

Using the inner product definitions (4.9) and (4.9), both sides in (C.4) are expanded as follows:

$$\begin{aligned}& -2\eta_S \left((\underline{\rho}_{t,x}^H \mathcal{M}_{S,x} \mathcal{L}_x + \underline{\rho}_{t,y}^H \mathcal{M}_{S,y} \mathcal{L}_x) \underline{h}_{t,x} + (\underline{\rho}_{t,x}^H \mathcal{M}_{S,x} \mathcal{L}_y + \underline{\rho}_{t,y}^H \mathcal{M}_{S,y} \mathcal{L}_y) \underline{h}_{t,y} \right) \\ &= (\underline{\rho}_{t,x}^H \mathcal{G}_{S,xx}^H \mathcal{T}_{\mathcal{D}} + \underline{\rho}_{t,y}^H \mathcal{G}_{S,xy}^H \mathcal{T}_{\mathcal{D}}) \underline{h}_{t,x} + (\underline{\rho}_{t,x}^H \mathcal{G}_{S,yx}^H \mathcal{T}_{\mathcal{D}} + \underline{\rho}_{t,y}^H \mathcal{G}_{S,yy}^H \mathcal{T}_{\mathcal{D}}) \underline{h}_{t,y}. \quad (\text{C.9})\end{aligned}$$

Comparing both sides of (C.9), it can be easily deduced that

$$\begin{aligned}\mathcal{G}_{S,xx} &= -2\eta_S \mathcal{T}_{\mathcal{D}}^{-1} \mathcal{L}_x^H \mathcal{M}_{S,x}^H & \mathcal{G}_{S,xy} &= -2\eta_S \mathcal{T}_{\mathcal{D}}^{-1} \mathcal{L}_x^H \mathcal{M}_{S,y}^H \\ \mathcal{G}_{S,yx} &= -2\eta_S \mathcal{T}_{\mathcal{D}}^{-1} \mathcal{L}_y^H \mathcal{M}_{S,x}^H & \mathcal{G}_{S,yy} &= -2\eta_S \mathcal{T}_{\mathcal{D}}^{-1} \mathcal{L}_y^H \mathcal{M}_{S,y}^H,\end{aligned} \quad (\text{C.10})$$

and thus the Gâteaux differential for the 2D TE case can be written as

$$d_{\vec{h}_t}^{\vec{\rho}_t} \mathcal{F}^S(\vec{w}_t) = \text{Re} \left\langle \vec{h}_t, \bar{\mathcal{G}}_S[\vec{\rho}_t] \right\rangle_{\mathcal{D}} \quad (\text{C.11})$$

where the terms of the adjoint operator $\bar{\bar{\mathcal{G}}}_S$ are given in (C.10). Further, to maximize the value of the differential the search direction \vec{h}_t is chosen to be

$$\vec{h}_t = (\mathcal{G}_{S,xx}\underline{\rho}_{t,x} + \mathcal{G}_{S,xy}\underline{\rho}_{t,y})\hat{x} + (\mathcal{G}_{S,yx}\underline{\rho}_{t,x} + \mathcal{G}_{S,yy}\underline{\rho}_{t,y})\hat{y}. \quad (\text{C.12})$$

This search direction \vec{h}_t is the gradient of the data-error equation $\mathcal{F}^S(\underline{w}_t)$ with respect to the contrast source variables \underline{w}_t for 2D TE problems.

C.1.3 Case 3: 3D Full-Vectorial

For 3D full-vectorial problems, a similar procedure as outlined for 2D TE can be done to calculate the gradient of the data-error equation. This results in the search direction \vec{h}_t that will maximize the differential (C.1) to be evaluated as

$$\vec{h}_{t,n} = \bar{\bar{\mathcal{G}}}_S \cdot \vec{\rho}_t \quad (\text{C.13})$$

where

$$\vec{\rho}_t = \underline{\rho}_{t,x}\hat{x} + \underline{\rho}_{t,y}\hat{y} + \underline{\rho}_{t,z}\hat{z} \quad (\text{C.14})$$

and

$$\begin{aligned} \bar{\bar{\mathcal{G}}}_S = & \mathcal{G}_{S,xx}\hat{x}\hat{x} + \mathcal{G}_{S,yx}\hat{y}\hat{x} + \mathcal{G}_{S,zx}\hat{z}\hat{x} + \\ & \mathcal{G}_{S,xy}\hat{x}\hat{y} + \mathcal{G}_{S,yy}\hat{y}\hat{y} + \mathcal{G}_{S,zy}\hat{z}\hat{y} + \\ & \mathcal{G}_{S,xz}\hat{x}\hat{z} + \mathcal{G}_{S,yz}\hat{y}\hat{z} + \mathcal{G}_{S,zz}\hat{z}\hat{z}. \end{aligned} \quad (\text{C.15})$$

Here each term is given by

$$\mathcal{G}_{S,uv} = -2\eta_S \mathcal{T}_D^{-1} (\mathcal{L}_u^H \mathcal{M}_{S,v}^H) \quad (\text{C.16})$$

where subscripts u, v are selected to represent either x, y or z . The search direction \vec{h}_t is the gradient of the data-error equation $\mathcal{F}^S(\vec{w}_t)$ with respect to the contrast source variables \vec{w}_t for 3D full-vectorial problems.

C.2 Domain-Error Equation Gradient

Next the Gâteaux differential of the domain-error equation $\mathcal{F}^D(\underline{\chi}, \vec{w}_t)$ is evaluated, with the contrast, $\underline{\chi}$, held constant. For a small variation in \vec{w}_t taken along the search direction \vec{h}_t , the Gâteaux differential of $\mathcal{F}^D(\underline{\chi}, \vec{w}_t)$ is given by

$$\begin{aligned}
d_{h_t} \mathcal{F}^D(\underline{\chi}, \vec{w}_t) &= \lim_{\epsilon \rightarrow 0} \frac{\mathcal{F}^D(\underline{\chi}, \vec{w}_t + \epsilon \vec{h}_t) - \mathcal{F}^D(\underline{\chi}, \vec{w}_t)}{\epsilon} \\
&= \lim_{\epsilon \rightarrow 0} \eta_D \frac{\left\| \vec{r}_t - \epsilon (\vec{h}_t - \underline{\chi} \odot \vec{\mathcal{M}}_D \vec{\mathcal{L}}[\vec{h}_t]) \right\|_D^2 - \|\vec{r}_t\|_D^2}{\epsilon} \\
&= \lim_{\epsilon \rightarrow 0} \eta_D \frac{-2\epsilon \operatorname{Re} \left\langle \vec{h}_t - \underline{\chi} \odot \vec{\mathcal{M}}_D \vec{\mathcal{L}}[\vec{h}_t], \vec{r}_t \right\rangle_D + \epsilon^2 \left\| \vec{h}_t - \underline{\chi} \odot \vec{\mathcal{M}}_D \vec{\mathcal{L}}[\vec{h}_t] \right\|_D^2}{\epsilon} \\
&= \operatorname{Re} \left\langle -2\eta_D (\vec{h}_t - \underline{\chi} \odot \vec{\mathcal{M}}_D \vec{\mathcal{L}}[\vec{h}_t]), \vec{r}_t \right\rangle_D.
\end{aligned} \tag{C.17}$$

Here \vec{r}_t is taken to be the residual in the domain-error equation, which is a function of \vec{w}_t and is given by

$$\vec{r}_t = \underline{\chi} \odot \vec{E}_t^{\text{inc}} - \vec{w}_t + \underline{\chi} \odot \vec{\mathcal{M}}_D \vec{\mathcal{L}}[\vec{w}_t]. \tag{C.18}$$

To evaluate the direction \vec{h}_t that maximizes the differential, the differential is rewritten so as to isolate the direction \vec{h}_t using an adjoint operator $\vec{\mathcal{G}}_D$ which satisfies

$$\left\langle -2\eta_D (\vec{h}_t - \underline{\chi} \odot \vec{\mathcal{M}}_D \vec{\mathcal{L}}[\vec{h}_t]), \vec{r}_t \right\rangle_D = \left\langle \vec{h}_t, \vec{\mathcal{G}}_D[\vec{r}_t] \right\rangle_D. \tag{C.19}$$

C.2.1 Case 1: 2D TM

For 2D TM assumption, the different components of (C.19) are given as

$$\begin{aligned}\vec{r}_t &= r_{t,z} \hat{z} & \vec{h}_{t,z} &= h_{t,z} \hat{z} \\ \vec{\mathcal{M}}_{\mathcal{D}} &= \mathcal{M}_{\mathcal{D},z} \hat{z} & \vec{\mathcal{L}} &= \mathcal{L}_z \hat{z} & \vec{\mathcal{G}}_{\mathcal{D}} &= \mathcal{G}_{\mathcal{D},zz} \hat{z} \hat{z}.\end{aligned}$$

Utilizing (4.7), the expansion of the inner products results in

$$-2\eta_{\mathcal{D}} r_{t,z}^H \mathcal{T}_{\mathcal{D}} (\mathcal{I} - \mathcal{X} \mathcal{M}_{\mathcal{D},z} \mathcal{L}_z) h_{t,z} = r_{t,z}^H (\mathcal{G}_{\mathcal{D},zz})^H \mathcal{T}_{\mathcal{D}} h_{t,z} \quad (\text{C.20})$$

where \mathcal{I} is an identity matrix and $\mathcal{X} = \text{diag}(\underline{\chi})$ is a diagonal matrix. Solving for $\mathcal{G}_{\mathcal{D},zz}$ we obtain

$$\mathcal{G}_{\mathcal{D},zz} = -2\eta_{\mathcal{D}} \mathcal{T}_{\mathcal{D}}^{-1} (\mathcal{I} - \mathcal{L}_z^H \mathcal{M}_{\mathcal{D},z}^T \mathcal{X}^H) \mathcal{T}_{\mathcal{D}}. \quad (\text{C.21})$$

The Gâteaux differential of the domain-error equation $\mathcal{F}^{\mathcal{D}}(\underline{\chi}, \underline{w}_{t,z})$ becomes

$$d_{\underline{h}_{t,z}} \mathcal{F}^{\mathcal{D}}(\underline{\chi}, \underline{w}_{t,z}) = \text{Re} \langle \underline{h}_{t,z}, -2\eta_{\mathcal{D}} \mathcal{T}_{\mathcal{D}}^{-1} (\mathcal{I} - \mathcal{L}_z^H \mathcal{M}_{\mathcal{D},z}^T \mathcal{X}^H) \mathcal{T}_{\mathcal{D}} r_{t,z} \rangle_{\mathcal{D}}. \quad (\text{C.22})$$

Thus, to maximize the Gâteaux differential, the search direction $\underline{h}_{t,z}$ is chosen as

$$\underline{h}_{t,z} = -2\eta_{\mathcal{D}} \mathcal{T}_{\mathcal{D}}^{-1} (\mathcal{I} - \mathcal{L}_z^H \mathcal{M}_{\mathcal{D},z}^T \mathcal{X}^H) \mathcal{T}_{\mathcal{D}} r_{t,z}. \quad (\text{C.23})$$

This is the gradient of the domain-error equation $\mathcal{F}^{\mathcal{D}}(\underline{\chi}, \underline{w}_{t,z})$ with respect to the contrast source variables $\underline{w}_{t,z}$ for 2D TM problems.

C.2.2 Case 2: 2D TE

For 2D TE configurations, the different components in (C.19) are given as

$$\begin{aligned}\vec{r}_t &= r_{t,x}\hat{x} + r_{t,y}\hat{y} & \vec{h}_t &= h_{t,x}\hat{x} + h_{t,y}\hat{y} \\ \vec{\mathcal{M}}_{\mathcal{D}} &= \mathcal{M}_{\mathcal{D},x}\hat{x} + \mathcal{M}_{\mathcal{D},y}\hat{y} & \vec{\mathcal{L}} &= \mathcal{L}_x\hat{x} + \mathcal{L}_y\hat{y}\end{aligned}$$

$$\vec{\mathcal{G}}_{\mathcal{D}} = \mathcal{G}_{\mathcal{D},xx}\hat{x}\hat{x} + \mathcal{G}_{\mathcal{D},yx}\hat{y}\hat{x} + \mathcal{G}_{\mathcal{D},xy}\hat{x}\hat{y} + \mathcal{G}_{\mathcal{D},yy}\hat{y}\hat{y}.$$

The expansion of the inner products in (C.19) results in

$$\begin{aligned}& -2\eta_{\mathcal{D}}\left(r_{t,x}^H\mathcal{T}_{\mathcal{D}}(\mathcal{I} - \mathcal{X}\mathcal{M}_{\mathcal{D},x}\mathcal{L}_x) - r_{t,y}^H\mathcal{T}_{\mathcal{D}}\mathcal{X}\mathcal{M}_{\mathcal{D},y}\mathcal{L}_x\right)h_{t,x} \\ & -2\eta_{\mathcal{D}}\left(-r_{t,x}^H\mathcal{T}_{\mathcal{D}}\mathcal{X}\mathcal{M}_{\mathcal{D},x}\mathcal{L}_y + r_{t,y}^H\mathcal{T}_{\mathcal{D}}(\mathcal{I} - \mathcal{X}\mathcal{M}_{\mathcal{D},y}\mathcal{L}_y)\right)h_{t,y} \\ & = (r_{t,x}^H\mathcal{G}_{\mathcal{D},xx}^H\mathcal{T}_{\mathcal{D}} + r_{t,y}^H\mathcal{G}_{\mathcal{D},xy}^H\mathcal{T}_{\mathcal{D}})h_{t,x} + (r_{t,x}^H\mathcal{G}_{\mathcal{D},yx}^H\mathcal{T}_{\mathcal{D}} + r_{t,y}^H\mathcal{G}_{\mathcal{D},yy}^H\mathcal{T}_{\mathcal{D}})h_{t,y}. \quad (\text{C.24})\end{aligned}$$

The comparison of both sides in (C.24) leads to

$$\begin{aligned}\mathcal{G}_{\mathcal{D},xx} &= -2\eta_{\mathcal{D}}\mathcal{T}_{\mathcal{D}}^{-1}(\mathcal{I} - \mathcal{L}_x^H\mathcal{M}_{\mathcal{D},x}^H\mathcal{X}^H)\mathcal{T}_{\mathcal{D}} \\ \mathcal{G}_{\mathcal{D},xy} &= 2\eta_{\mathcal{D}}\mathcal{T}_{\mathcal{D}}^{-1}\mathcal{L}_x^H\mathcal{M}_{\mathcal{D},y}^H\mathcal{X}^H\mathcal{T}_{\mathcal{D}} \\ \mathcal{G}_{\mathcal{D},yx} &= 2\eta_{\mathcal{D}}\mathcal{T}_{\mathcal{D}}^{-1}\mathcal{L}_y^H\mathcal{M}_{\mathcal{D},x}^H\mathcal{X}^H\mathcal{T}_{\mathcal{D}} \\ \mathcal{G}_{\mathcal{D},yy} &= -2\eta_{\mathcal{D}}\mathcal{T}_{\mathcal{D}}^{-1}(\mathcal{I} - \mathcal{L}_y^H\mathcal{M}_{\mathcal{D},y}^H\mathcal{X}^H)\mathcal{T}_{\mathcal{D}}. \quad (\text{C.25})\end{aligned}$$

The Gâteaux differential for the 2D TE domain-error equation $\mathcal{F}^{\mathcal{D}}(\underline{\chi}, \underline{\vec{w}}_t)$ can be written as

$$d_{\vec{h}_t}\mathcal{F}^{\mathcal{D}}(\underline{\chi}, \underline{\vec{w}}_t) = \text{Re}\left\langle \vec{h}_t, \vec{\mathcal{G}}_{\mathcal{D}}[\vec{r}_t] \right\rangle_{\mathcal{D}}. \quad (\text{C.26})$$

where the terms of the adjoint operator $\bar{\mathcal{G}}_{\mathcal{D}}$ are given in (C.25). Subsequently, to maximize the Gâteaux differential the search direction \vec{h}_t is chosen as

$$\vec{h}_t = (\mathcal{G}_{\mathcal{D},xx}r_{t,x} + \mathcal{G}_{\mathcal{D},xy}r_{t,y})\hat{x} + (\mathcal{G}_{\mathcal{D},yx}r_{t,x} + \mathcal{G}_{\mathcal{D},yy}r_{t,y})\hat{y}. \quad (\text{C.27})$$

This search direction is the gradient of the domain-error equation $\mathcal{F}^{\mathcal{D}}(\underline{\chi}, \vec{w}_{t,z})$ with respect to the contrast source variables $\vec{w}_{t,z}$ for 2D TE cases.

C.2.3 Case 3: 3D Full-Vectorial

For 3D full-vectorial problems, a similar procedure as outlined for 2D TE can be performed to calculate the gradient of the domain-error equation. This results in the search direction \vec{h}_t that will maximize the differential (C.17) be evaluated as

$$\vec{h}_{t,n} = \bar{\mathcal{G}}_{\mathcal{D}} \cdot \vec{r}_t \quad (\text{C.28})$$

where

$$\vec{r}_t = r_{t,x}\hat{x} + r_{t,y}\hat{y} + r_{t,z}\hat{z} \quad (\text{C.29})$$

and

$$\begin{aligned} \bar{\mathcal{G}}_{\mathcal{D}} = & \mathcal{G}_{\mathcal{D},xx}\hat{x}\hat{x} + \mathcal{G}_{\mathcal{D},yx}\hat{y}\hat{x} + \mathcal{G}_{\mathcal{D},zx}\hat{z}\hat{x} + \\ & \mathcal{G}_{\mathcal{D},xy}\hat{x}\hat{y} + \mathcal{G}_{\mathcal{D},yy}\hat{y}\hat{y} + \mathcal{G}_{\mathcal{D},zy}\hat{z}\hat{y} + \\ & \mathcal{G}_{\mathcal{D},xz}\hat{x}\hat{z} + \mathcal{G}_{\mathcal{D},yz}\hat{y}\hat{z} + \mathcal{G}_{\mathcal{D},zz}\hat{z}\hat{z}. \end{aligned} \quad (\text{C.30})$$

Here each term is given by

$$\mathcal{G}_{\mathcal{D},uv} = \begin{cases} -2\eta_{\mathcal{D}}\mathcal{T}_{\mathcal{D}}^{-1}(\mathcal{I} - \mathcal{L}_u^H \mathcal{M}_{\mathcal{D},v}^H \mathcal{X}^H) \mathcal{T}_{\mathcal{D}} & \text{for } u = v \\ 2\eta_{\mathcal{D}}\mathcal{T}_{\mathcal{D}}^{-1} \mathcal{L}_u^H \mathcal{M}_{\mathcal{D},v}^H \mathcal{X}^H \mathcal{T}_{\mathcal{D}} & \text{for } u \neq v \end{cases} \quad (\text{C.31})$$

where subscripts u, v are selected to represent either x, y or z . The search direction \vec{h}_t is the gradient of the domain-error equation $\mathcal{F}^{\mathcal{D}}(\vec{w}_t)$ with respect to the contrast source variables \vec{w}_t for 3D full-vectorial problems.

C.3 Summary

In conclusion, regardless of the configuration, the gradient of the cost functional for contrast source variables $\vec{w}_{t,n-1}$ and contrast variables $\underline{\chi}_{n-1}$ at the n^{th} iteration can be written as

$$\vec{g}_{t,n} = \bar{\bar{\mathcal{G}}}_S \cdot \vec{\rho}_{t,n-1} + \bar{\bar{\mathcal{G}}}_D \cdot \vec{r}_{t,n-1} \quad (\text{C.32})$$

where the adjoint operators $\bar{\bar{\mathcal{G}}}_S$ and $\bar{\bar{\mathcal{G}}}_D$ are defined in (C.6) and (C.21) for the 2D TM case, in (C.10) and (C.25) for the 2D TE case, and in (C.15) and (C.30) for the 3D full-vectorial configuration.

D

The Contrast Variables Update - Analytic

In the second step of the FEM-CSI method, a new contrast $\underline{\chi}$ is chosen which minimizes the modified domain-error equation

$$\mathcal{F}_m^{\mathcal{D}}(\underline{\chi}) = \eta_{\mathcal{D}} \sum_t \left\| \vec{\mathcal{E}}_t \underline{\chi} - \vec{w}_t \right\|_{\mathcal{D}}^2 \quad (\text{D.1})$$

where $\vec{\mathcal{E}}_t \in \mathbb{C}^{I \times I}$ is the total field diagonal matrix with diagonal entries equal to the elements of vector $\vec{E}_t = \vec{E}_t^{\text{inc}} + \mathcal{M}_{\mathcal{D}} \vec{\mathcal{L}}[\vec{w}_t]$. In this step the contrast source \vec{w}_t is kept constant, as well as the normalization factor $\eta_{\mathcal{D}}$.

The minimizer of $\mathcal{F}_m^{\mathcal{D}}(\underline{\chi})$ is obtained by first evaluating the Gâteaux differential. For a small variation with respect to $\underline{\chi}$ along a search direction \underline{h} , the differential is calculated as

$$\begin{aligned} d_{\underline{h}} \mathcal{F}_m^{\mathcal{D}}(\underline{\chi}) &= \lim_{\epsilon \rightarrow 0} \frac{\eta_{\mathcal{D}}}{\epsilon} \left[\sum_t \left\| \vec{\mathcal{E}}_t(\underline{\chi} + \epsilon \underline{h}) - \vec{w}_t \right\|_{\mathcal{D}}^2 - \sum_t \left\| \vec{\mathcal{E}}_t \underline{\chi} - \vec{w}_t \right\|_{\mathcal{D}}^2 \right] \\ &= \lim_{\epsilon \rightarrow 0} \frac{\eta_{\mathcal{D}}}{\epsilon} \left[\sum_t \left\| \vec{\mathcal{E}}_t \underline{\chi} - \vec{w}_t + \epsilon \vec{\mathcal{E}}_t \underline{h} \right\|_{\mathcal{D}}^2 - \sum_t \left\| \vec{\mathcal{E}}_t \underline{\chi} - \vec{w}_t \right\|_{\mathcal{D}}^2 \right] \\ &= \lim_{\epsilon \rightarrow 0} \frac{\eta_{\mathcal{D}}}{\epsilon} \left[\sum_t \left\| \vec{r}_t + \epsilon \vec{\mathcal{E}}_t \underline{h} \right\|_{\mathcal{D}}^2 - \sum_t \left\| \vec{r}_t \right\|_{\mathcal{D}}^2 \right] \end{aligned} \quad (\text{D.2})$$

where \vec{r}_t , a function of $\underline{\chi}$, is defined as

$$\vec{r}_t = \vec{\mathcal{E}}_t \underline{\chi} - \vec{w}_t, \quad (\text{D.3})$$

Expanding the norms in (D.2)

$$\begin{aligned}
d_{\underline{h}}\mathcal{F}_m^{\mathcal{D}}(\underline{\chi}) &= \lim_{\epsilon \rightarrow 0} \frac{\eta_{\mathcal{D}}}{\epsilon} \left[\sum_t \|\vec{r}_t\|_{\mathcal{D}}^2 + 2\epsilon \sum_t \operatorname{Re} \langle \vec{r}_t, \vec{\mathcal{E}}_t \underline{h} \rangle_{\mathcal{D}} + \epsilon^2 \sum_t \left\| \vec{\mathcal{E}}_t \underline{h} \right\|_{\mathcal{D}}^2 - \sum_t \|\vec{r}_t\|_{\mathcal{D}}^2 \right] \\
&= 2\eta_{\mathcal{D}} \sum_t \operatorname{Re} \langle \vec{r}_t, \vec{\mathcal{E}}_t \underline{h} \rangle_{\mathcal{D}} \\
&= 2\eta_{\mathcal{D}} \sum_t \operatorname{Re}(\underline{h}^H \vec{\mathcal{E}}_t^H \cdot \mathcal{T}_{\mathcal{D}} \vec{r}_t).
\end{aligned} \tag{D.4}$$

Using the inner product definition (4.7), the differential can be written as

$$d_{\underline{h}}\mathcal{F}_m^{\mathcal{D}}(\underline{\chi}) = \operatorname{Re} \left\langle 2\eta_{\mathcal{D}} \sum_t \mathcal{T}_{\mathcal{D}}^{-1} \vec{\mathcal{E}}_t^H \cdot \mathcal{T}_{\mathcal{D}} \vec{r}_t, \underline{h} \right\rangle_{\mathcal{D}}. \tag{D.5}$$

The search direction that will maximize the Gâteaux differential is therefore

$$\underline{h} = 2\eta_{\mathcal{D}} \sum_t \mathcal{T}_{\mathcal{D}}^{-1} \vec{\mathcal{E}}_t^H \cdot \mathcal{T}_{\mathcal{D}} \vec{r}_t.$$

Thus, at the n^{th} iteration the gradient of the modified domain equation evaluated at $\underline{\chi} = \underline{\chi}_n$ is

$$\underline{g}_{\mathcal{D},n}^{\chi} = 2\eta_{\mathcal{D},n-1} \sum_t \mathcal{T}_{\mathcal{D}}^{-1} \vec{\mathcal{E}}_{t,n}^H \cdot \mathcal{T}_{\mathcal{D}} \vec{r}_{t,n}. \tag{D.6}$$

The $\underline{\chi}_n$ that minimizes $\mathcal{F}_m^{\mathcal{D}}(\underline{\chi}_n)$ is found by setting (D.6) to zero, then requiring the solution of

$$\left(\sum_t \vec{\mathcal{E}}_{t,n}^H \cdot \mathcal{T}_{\mathcal{D}} \vec{\mathcal{E}}_{t,n} \right) \underline{\chi}_n = \sum_t \vec{\mathcal{E}}_{t,n}^H \cdot \mathcal{T}_{\mathcal{D}} \vec{w}_{t,n}. \tag{D.7}$$

E

The Initial Guess for FEM-CSI

An initial guess to begin the FEM-CSI updating procedure is found by calculating the contrast sources which minimize $\mathcal{F}^S(\underline{\vec{w}}_t)$ in the steepest-descent direction, starting with a zero initial guess. Note that this is the standard starting technique when applying most variations of the conjugate-gradient technique. For a single transmitter, the data-error equation $\mathcal{F}_t^S(\underline{\vec{w}}_t)$ is

$$\mathcal{F}_t^S(\underline{\vec{w}}_t) = \left\| \underline{\vec{w}}_t - \vec{\mathcal{M}}_S \mathcal{L}[\underline{\vec{w}}_t] \right\|_S^2 \quad (\text{E.1})$$

As derived in Appendix C, at the n^{th} iteration, the gradient of $\mathcal{F}_t^S(\underline{\vec{w}}_t)$ with respect to the contrast source variable $\underline{\vec{w}}_t$ is given by

$$\underline{\vec{g}}_{S,t,n} = \bar{\vec{\mathcal{G}}}_S \cdot \underline{\vec{\rho}}_{t,n-1}, \quad (\text{E.2})$$

where $\underline{\vec{\rho}}_{t,n-1} = \underline{\vec{w}}_t - \vec{\mathcal{M}}_S \mathcal{L}[\underline{\vec{w}}_{t,n-1}]$.

The update equation for the first iteration of method of steepest descent is

$$\underline{\vec{w}}_{t,0} = \underline{\vec{w}}_{t,-1} - \beta_0 \bar{\vec{\mathcal{G}}}_S \cdot \underline{\vec{\rho}}_{t,-1}, \quad (\text{E.3})$$

where $\underline{\vec{w}}_{t,-1}$ is the initial guess for the method of steepest descent which will be set to zero, and β_0 is a real update coefficient selected to minimize $\mathcal{F}_t^S(\underline{\vec{w}}_{t,-1} - \beta_0 \bar{\vec{\mathcal{G}}}_S \cdot \underline{\vec{\rho}}_{t,-1})$.

Once β_0 is found, $\vec{w}_{t,0}$ becomes the initial guess for the FEM-CSI updating procedure. Thus, we have

$$\vec{w}_{t,0} = -\beta_0 \vec{\mathcal{G}}_S \cdot \vec{u}_t. \quad (\text{E.4})$$

To find β_0 , (E.4) is substituted into $\mathcal{F}_t^S(\vec{w}_t)$ giving

$$\begin{aligned} \mathcal{F}_t^S(\vec{w}_{t,0}) &= \left\| \vec{u}_t + \beta_0 \vec{\mathcal{M}}_S \vec{\mathcal{L}}[\vec{\mathcal{G}}_S \cdot \vec{u}_t] \right\|_S^2 \\ &= (\vec{u}_t + \beta_0 \vec{\mathcal{M}}_S \vec{\mathcal{L}}[\vec{\mathcal{G}}_S \cdot \vec{u}_t])^H (\vec{u}_t + \beta_0 \vec{\mathcal{M}}_S \vec{\mathcal{L}}[\vec{\mathcal{G}}_S \cdot \vec{u}_t]) \\ &= \|\vec{u}_t\|_S^2 + 2\beta_0 \text{Re} \left\langle \vec{\mathcal{M}}_S \vec{\mathcal{L}}[\vec{\mathcal{G}}_S \cdot \vec{u}_t], \vec{u}_t \right\rangle_S + \beta_0^2 \left\| \vec{\mathcal{M}}_S \vec{\mathcal{L}}[\vec{\mathcal{G}}_S \cdot \vec{u}_t] \right\|_S^2. \end{aligned}$$

Differentiating with respect to the real scalar variable β_0 gives

$$\frac{\partial \mathcal{F}_t^S}{\partial \beta_0} = 2 \text{Re} \left\langle \vec{\mathcal{M}}_S \vec{\mathcal{L}}[\vec{\mathcal{G}}_S \cdot \vec{u}_t], \vec{u}_t \right\rangle_S + 2\beta_0 \left\| \vec{\mathcal{M}}_S \vec{\mathcal{L}}[\vec{\mathcal{G}}_S \cdot \vec{u}_t] \right\|_S^2, \quad (\text{E.5})$$

which is set equal to zero to give the following formula for β_0 :

$$\beta_0 = -\frac{\text{Re} \left\langle \vec{\mathcal{M}}_S \vec{\mathcal{L}}[\vec{\mathcal{G}}_S \cdot \vec{u}_t], \vec{u}_t \right\rangle_S}{\left\| \vec{\mathcal{M}}_S \vec{\mathcal{L}}[\vec{\mathcal{G}}_S \cdot \vec{u}_t] \right\|_S^2}. \quad (\text{E.6})$$

Substituting (E.6) into (E.4), the initial guess for the FEM-CSI updating procedure becomes

$$\vec{w}_{t,0} = \frac{\text{Re} \left\langle \vec{\mathcal{M}}_S \vec{\mathcal{L}}[\vec{\mathcal{G}}_S \cdot \vec{u}_t], \vec{u}_t \right\rangle_S}{\left\| \vec{\mathcal{M}}_S \vec{\mathcal{L}}[\vec{\mathcal{G}}_S \cdot \vec{u}_t] \right\|_S^2} \vec{\mathcal{G}}_S \cdot \vec{u}_t. \quad (\text{E.7})$$

F

Required Gradients for MR-FEMCSI

F.1 Domain-Error Gradient with respect to χ

In the second step of the MR-FEMCSI algorithm, the gradient $\underline{g}_{\mathcal{D}}^{\chi}$ of the domain-error equation $\mathcal{F}^{\mathcal{D}}(\underline{\chi}, \underline{\vec{w}}_t)$ with respect to the contrast variable, $\underline{\chi}$, is required with the contrast $\underline{\vec{w}}_t$ held constant.

As detailed in Appendix D, the gradient of the domain-error equation at the n^{th} iteration for $\underline{\chi}_{n-1}$ is

$$\underline{g}_{\mathcal{D},n}^{\chi} = 2\eta_{\mathcal{D},n-1} \sum_t \mathcal{T}_{\mathcal{D}}^{-1} \vec{\mathcal{E}}_{t,n}^H \cdot \mathcal{T}_{\mathcal{D}} \vec{\mathcal{I}}_{t,n}. \quad (\text{F.1})$$

where

$$\begin{aligned} \vec{\mathcal{E}}_{t,n} &= \text{diag}(\underline{\vec{E}}_t^{\text{inc}} + \vec{\mathcal{M}}_{\mathcal{D}} \vec{\mathcal{L}}[\underline{\vec{w}}_{t,n}]) \\ \vec{\mathcal{I}}_{t,n} &= \vec{\mathcal{E}}_{t,n} \underline{\chi}_{n-1} - \underline{\vec{w}}_{t,n}. \end{aligned} \quad (\text{F.2})$$

In balanced MR-FEMCSI, the gradients of the domain-error equation, $\underline{g}_{\mathcal{D}}^{\chi R}$, and $\underline{g}_{\mathcal{D}}^{\chi I}$ with respect to the real and imaginary components of the contrast variable are evaluated separately. For two complex variables, ϕ and γ ,

$$\text{Re} \langle \phi, \gamma \rangle_{\mathcal{D}} = \langle \phi_{\text{R}}, \gamma_{\text{R}} \rangle_{\mathcal{D}} + \langle \phi_{\text{I}}, \gamma_{\text{I}} \rangle_{\mathcal{D}}, \quad (\text{F.3})$$

where the subscripts R and I indicate the real and imaginary parts of the variables, ϕ and γ . Thus, the result in (D.5) can be rewritten as

$$d_h \mathcal{F}^{\mathcal{D}}(\underline{\chi}, \underline{\vec{w}}_t) = \left\langle \text{Re} \left(2\eta_{\mathcal{D}} \sum_t \mathcal{T}_{\mathcal{D}}^{-1} \vec{\mathcal{E}}_t^H \cdot \mathcal{T}_{\mathcal{D}} \vec{l}_t \right), h_{\text{R}} \right\rangle_{\mathcal{D}} + \left\langle \text{Im} \left(2\eta_{\mathcal{D}} \sum_t \mathcal{T}_{\mathcal{D}}^{-1} \vec{\mathcal{E}}_t^H \cdot \mathcal{T}_{\mathcal{D}} \vec{l}_t \right), h_{\text{I}} \right\rangle_{\mathcal{D}}. \quad (\text{F.4})$$

The first term in (F.4) is maximized by setting the search direction

$$h_{\text{R}} = \text{Re} \left(2\eta_{\mathcal{D}} \sum_t \mathcal{T}_{\mathcal{D}}^{-1} \vec{\mathcal{E}}_t^H \cdot \mathcal{T}_{\mathcal{D}} \vec{l}_t \right), \quad (\text{F.5})$$

which is the gradient, $\underline{g}_{\mathcal{D}}^{\chi_{\text{R}}}$, of the domain-error equation $\mathcal{F}^{\mathcal{D}}(\underline{\chi}, \underline{\vec{w}}_t)$ with respect to $\underline{\chi}_{\text{R}}$, the real component of $\underline{\chi}$. Similarly, the second term in (F.6) is then maximized by setting

$$h_{\text{I}} = \text{Im} \left(2\eta_{\mathcal{D}} \sum_t \mathcal{T}_{\mathcal{D}}^{-1} \vec{\mathcal{E}}_t^H \cdot \mathcal{T}_{\mathcal{D}} \vec{l}_t \right) \quad (\text{F.6})$$

which is the gradient, $\underline{g}_{\mathcal{D}}^{\chi_{\text{I}}}$, of $\mathcal{F}^{\mathcal{D}}(\underline{\chi}, \underline{\vec{w}}_t)$ with respect to $\underline{\chi}_{\text{I}}$, the imaginary component of $\underline{\chi}$.

Thus, at the n^{th} iteration of the balanced MR-CSI algorithm, the gradients of the domain-error equation evaluated at $\underline{\chi} = \underline{\chi}_{n-1}$ are

$$\begin{aligned} \underline{g}_{\mathcal{D},n}^{\chi_{\text{R}}} &= \text{Re} \left(2\eta_{\mathcal{D},n-1} \sum_t \mathcal{T}_{\mathcal{D}}^{-1} \vec{\mathcal{E}}_{t,n}^H \cdot \mathcal{T}_{\mathcal{D}} \vec{l}_{t,n} \right) \\ \underline{g}_{\mathcal{D},n}^{\chi_{\text{I}}} &= \text{Im} \left(2\eta_{\mathcal{D},n-1} \sum_t \mathcal{T}_{\mathcal{D}}^{-1} \vec{\mathcal{E}}_{t,n}^H \cdot \mathcal{T}_{\mathcal{D}} \vec{l}_{t,n} \right). \end{aligned} \quad (\text{F.7})$$

F.2 MR term Gradient with respect to Contrast

The second step of MR-FEMCSI requires the gradients of the multiplicative regularization term $\mathcal{F}_n^{\text{MR}}(\underline{\chi})$ with respect to the contrast $\underline{\chi}$: $g_{\text{MR},n}^{\underline{\chi}}$.

Let $\mathcal{C}_n^{\text{MR}}(\chi)$ be the MR term in the continuous domain. At a given point χ , $g_{\text{MR}}^{\underline{\chi}}$ is the gradient pointing in the direction in which the Gâteaux differential of $\mathcal{C}_n^{\text{MR}}(\chi)$ with respect to χ is maximized. For a small variation in χ taken along the search direction h , the Gâteaux differential of the MR term is given by

$$\begin{aligned}
 d_h \mathcal{C}_n^{\text{MR}}(\chi) &= \lim_{\epsilon \rightarrow 0} \frac{\mathcal{C}_n^{\text{MR}}(\chi + \epsilon h) - \mathcal{C}_n^{\text{MR}}(\chi)}{\epsilon} \\
 &= \lim_{\epsilon \rightarrow 0} \frac{\|b_n \nabla(\chi + \epsilon h)\|_{\mathcal{D}}^2 - \|b_n \nabla \chi\|_{\mathcal{D}}^2}{\epsilon} \\
 &= \lim_{\epsilon \rightarrow 0} \frac{\|b_n \nabla \chi\|_{\mathcal{D}}^2 + 2\epsilon \text{Re} \langle b_n \nabla \chi, b_n \nabla h \rangle_{\mathcal{D}} + \epsilon^2 \|b_n \nabla h\|_{\mathcal{D}}^2 - \|b_n \nabla \chi\|_{\mathcal{D}}^2}{\epsilon} \\
 &= \text{Re} \langle 2 b_n \nabla \chi, b_n \nabla h \rangle_{\mathcal{D}}.
 \end{aligned} \tag{F.8}$$

Next, the direction h is isolated using the first Green's theorem as follows:

$$\begin{aligned}
 \langle b_n \nabla \chi, b_n \nabla h \rangle_{\mathcal{D}} &= \int_{\mathcal{D}} (b_n \nabla \chi) \cdot (b_n \nabla h)^* dv \\
 &= \int_{\mathcal{D}} 2 b_n^2 \nabla \chi \cdot (\nabla h)^* dv \\
 &= - \int_{\mathcal{D}} 2 h^* (\nabla \cdot b_n^2 \nabla \chi) dv + \oint_{\Gamma_{\mathcal{D}}} 2 b_n^2 h^* (\nabla \chi \cdot \hat{n}) ds \\
 &= - \int_{\mathcal{D}} 2 h^* (\nabla \cdot b_n^2 \nabla \chi) dv \\
 &= \langle -2 \nabla \cdot b_n^2 \nabla \chi, h \rangle_{\mathcal{D}}.
 \end{aligned} \tag{F.9}$$

The surface integral vanishes because of assuming $\chi(\vec{r} \in \Gamma_{\mathcal{D}}) = 0$, where $\Gamma_{\mathcal{D}}$ is the boundary of the imaging domain \mathcal{D} . Therefore, to maximize the Gâteaux differential

in (F.8) the search direction h is chosen as

$$h = -2 \nabla \cdot b_n^2 \nabla \chi. \quad (\text{F.10})$$

This direction is the gradient g_{MR}^{χ} of the MR term, $\mathcal{C}_n^{\text{MR}}(\chi)$, with respect to χ . When the problem is discretized in MR-FEMCSI, the gradient of $\mathcal{F}_n^{\text{MR}}(\underline{\chi})$ at the n^{th} iteration evaluated at $\underline{\chi} = \underline{\chi}_{n-1}$ is given as

$$\underline{g}_{\text{MR},n}^{\chi} = -2 \nabla \cdot \left(\underline{b}_n^2 \odot \nabla \underline{\chi}_{n-1} \right) \quad (\text{F.11})$$

where $\underline{b}^2 = \underline{b} \odot \underline{b}$. Here the gradient (∇) and the divergence ($\nabla \cdot$) in (F.11) represent matrix operators to perform spatial derivatives in the discretized imaging domain \mathcal{D} .

Utilizing a similar procedure in BMR-FEMCSI, the gradients $\underline{g}_{\text{BMR}}^{\chi_{\text{R}}}$, $\underline{g}_{\text{BMR}}^{\chi_{\text{I}}}$ of the BMR term with respect to $\underline{\chi}_{\text{R}}$ and $\underline{\chi}_{\text{I}}$, the real and the imaginary components of the contrast variable, can be derived. Thus, at the n^{th} iteration of the BMR-CSI algorithm, the gradients of the BMR term for contrast variable χ_{n-1} are

$$\begin{aligned} \underline{g}_{\text{MR},n}^{\chi_{\text{R}}} &= -2 \nabla \cdot \left(\underline{b}_n^2 \odot \nabla \underline{\chi}_{\text{R},n-1} \right) \\ \underline{g}_{\text{MR},n}^{\chi_{\text{I}}} &= -2 \nabla \cdot \left(\underline{Q}^2 \odot \underline{b}_n^2 \odot \nabla \underline{\chi}_{\text{I},n-1} \right). \end{aligned} \quad (\text{F.12})$$

G

Multiplicative Regularization Step-size

The MR update step-size α_n^x can be calculated analytically by first introducing $\vec{w}_{t,n}$ and $\underline{\chi}_n^{\text{CSI}} + \alpha^x \underline{d}_n^x$ in the cost functional (5.5). This results in a fourth-degree polynomial in α^x as follows

$$\mathcal{F}_n = (A + B \alpha^x + C \alpha^{x^2})(D + E \alpha^x + F \alpha^{x^2}), \quad (\text{G.1})$$

where

$$A = \mathcal{F}_n^{\text{MR}}(\underline{\chi}_n^{\text{CSI}}), \quad (\text{G.2})$$

$$B = 2 \operatorname{Re} \left\langle \underline{b}_n \odot \nabla \underline{\chi}_n^{\text{CSI}}, \underline{b}_n \odot \nabla \underline{d}_n^x \right\rangle_{\mathcal{D}}, \quad (\text{G.3})$$

$$C = \|\underline{b}_n \odot \nabla \underline{d}_n^x\|_{\mathcal{D}}^2, \quad (\text{G.4})$$

and

$$D = \mathcal{F}^{\text{CSI}}(\underline{\chi}_n^{\text{CSI}}, \vec{w}_{t,n}), \quad (\text{G.5})$$

$$E = 2\eta_{\mathcal{D},n-1} \sum_t \operatorname{Re} \left\langle \underline{d}_n^x \odot \vec{E}_{t,n}, \vec{r}_{t,n} \right\rangle_{\mathcal{D}}, \quad (\text{G.6})$$

$$F = \eta_{\mathcal{D},n-1} \sum_t \left\| \underline{d}_n^x \odot \vec{E}_{t,n} \right\|_{\mathcal{D}}^2. \quad (\text{G.7})$$

Here $\eta_{\mathcal{D},n-1}$ is the normalization factor of the domain-error equation $\mathcal{F}^{\mathcal{D}}(\underline{\chi}, \underline{\vec{w}}_t)$ at the n^{th} iteration [29].

Next the derivative of (G.1) with respect to α^x is set equal to zero to find the minimizers of the polynomial. This yields three values for α^x , one real and one complex-conjugate pair. The real α^x is the desired step-size α_n^x . This derivation of the step-size follows the procedure discussed in [80].

The derivation of the step-sizes α^{xR} and α^{xI} for BMR-FEMCSI can be obtained through a similar procedure.

H

Approximating Spatial Derivatives

Let \hat{w} denote a constant unit vector and $\psi(\vec{r})$ be a scalar function. Over a region Ω , the average of $\hat{w} \cdot \nabla\psi(\vec{r})$ is given by

$$\langle \hat{w} \cdot \nabla\psi(\vec{r}) \rangle_{\Omega} = \frac{1}{V} \int_{\Omega} \hat{w} \cdot \nabla\psi(\vec{r}) \, dv \quad (\text{H.1})$$

where V is the area (in 2D) or the volume (in 3D) of region Ω . Using differentiation vector identities, (H.1) is expanded to

$$\langle \hat{w} \cdot \nabla\psi(\vec{r}) \rangle_{\Omega} = \frac{1}{V} \int_{\Omega} \left[\nabla \cdot (\psi(\vec{r})\hat{w}) - \psi(\vec{r})(\nabla \cdot \hat{w}) \right] \, dv. \quad (\text{H.2})$$

Since \hat{w} is a constant vector, $\nabla \cdot \hat{w} = 0$. Therefore,

$$\langle \hat{w} \cdot \nabla\psi(\vec{r}) \rangle_{\Omega} = \frac{1}{V} \int_{\Omega} \nabla \cdot (\psi(\vec{r})\hat{w}) \, dv. \quad (\text{H.3})$$

Next using divergence theorem, the volume integral is transformed to a closed contour integration as follows:

$$\langle \hat{w} \cdot \nabla\psi(\vec{r}) \rangle_{\Omega} = \frac{1}{V} \oint_{\Gamma} \psi(\vec{r})\hat{w} \cdot \hat{n} \, ds \quad (\text{H.4})$$

where Γ is the boundary of region Ω , and \hat{n} is an outward unit normal vector to Γ .

I

Incident Field in Conductive Enclosures

For problems bounded by a conductive enclosure, the incident field inside the chamber has to be evaluated in order to either generate synthetic data using a forward solver or to utilize the CSI inversion algorithm .

For 2D TM scalar problems, the z -polarized scalar incident field $E_{t,z}^{\text{inc}}$, bounded by a conductive enclosure Γ (of any shape or size), is governed by the Helmholtz equation

$$\nabla^2 E_{t,z}^{\text{inc}}(\vec{r}) + k_b^2 E_{t,z}^{\text{inc}}(\vec{r}) = j\omega\mu_0 J_{t,z}(\vec{r}) \quad (\text{I.1})$$

where k_b is the background wavenumber and $J_{t,z}$ is a z -polarized current source. The incident field at the chamber boundary, Γ , should satisfy a homogeneous Dirichlet boundary condition, hence

$$E_{t,z}^{\text{inc}}(\vec{r} \in \Gamma) = 0. \quad (\text{I.2})$$

In the thesis, the electric source $J_{t,z}$ considered is a point source and is given as

$$J_{t,z}(\vec{r}) = \frac{-1}{j\omega\mu_0} \delta(\vec{r} - \vec{r}_t) \quad (\text{I.3})$$

where \vec{r}_t is the location of the point source within the problem domain Ω . Substituting (I.3) in (I.1), the wave equation can be rewritten as

$$\nabla^2 E_{t,z}^{\text{inc}}(\vec{r}) + k_b^2 E_{t,z}^{\text{inc}}(\vec{r}) = -\delta(\vec{r} - \vec{r}_t). \quad (\text{I.4})$$

As shown in [20], a solution for this equation that satisfies the homogeneous Dirichlet boundary condition (I.2) is given as

$$E_{t,z}^{\text{inc}}(\vec{r}) = E_{t,z}^{\text{inc,fs}} + p_t(\vec{r}). \quad (\text{I.5})$$

Here $E_{t,z}^{\text{inc,fs}}$ is the free-space field due to a point source and is calculated as

$$E_{t,z}^{\text{inc,fs}} = \frac{1}{j4} H_0^{(2)}(k_b |\vec{r} - \vec{r}_t|) \quad (\text{I.6})$$

where $H_0^{(2)}$ is the zeroth-order Hankel function of the second kind. The function $p_t(\vec{r})$ in (I.5) can be evaluated by solving the following BVP:

$$\begin{aligned} \nabla^2 p_t(\vec{r}) + k_b^2 p_t(\vec{r}) &= 0 & \vec{r} \in \Omega \\ p_t(\vec{r}) &= -E_{t,z}^{\text{inc,fs}} & \text{on } \Gamma. \end{aligned} \quad (\text{I.7})$$

The BVP can be solved using the finite-element method described for 2D TM problems in Section 3.2.

For 2D TE vectorial cases, a similar procedure can be used to solve for the incident field within a PEC chamber due to a magnetic point source.

J

Selected Publications

Herein is a list of selected papers published during the research.

J.1 Published Journal Papers

1. **Amer Zakaria** and Joe LoVetri, "Application of Multiplicative Regularization to the Finite-Element Contrast Source Inversion Method," *IEEE Transactions on Antennas and Propagation*, vol. 59, no. 9, pp. 3495-3498, 2011.
2. **Amer Zakaria**, Colin Gilmore and Joe LoVetri, "Finite-element Contrast Source Inversion Method of Microwave Imaging," *Inverse Problems*, 26 (2010) 115010.
3. Colin Gilmore, **Amer Zakaria**, Puyan Mojabi, Majid Ostadrahimi, Stephen Pistorius and Joe LoVetri, "The University of Manitoba Imaging Repository: A 2D Microwave Scattering Database for Testing Inversion and Calibration Algorithms," *IEEE Antennas and Propagation Magazine*, vol. 35, no. 5, pp. 126-133, October 2011.
4. Colin Gilmore, Puyan Mojabi, **Amer Zakaria**, Majid Ostadrahimi, Sima Noghianian, Lotfollah Shafai, Stephen Pistorius and Joe LoVetri, "A Wideband Microwave Tomography System with a Novel Frequency Selection Procedure," *IEEE Transactions on Biomedical Engineering*, vol. 57, no. 4, pp. 894-904, April 2010.

J.2 Submitted Journal Papers

1. **Amer Zakaria** and Joe LoVetri, "The Finite-Element Method Contrast Source Inversion Algorithm for 2D Transverse Electric Vectorial Problems," *IEEE Transactions on Antennas and Propagation*, revised and resubmitted in January 2012.

2. Colin Gilmore, **Amer Zakaria**, Stephen Pistorius and Joe LoVetri, "A Study of Matching Fluid Loss in Biomedical Microwave Tomography System," *IEEE Transactions on Biomedical Engineering*, revised and resubmitted in December 2011.
3. Colin Gilmore, **Amer Zakaria**, Stephen Pistorius and Joe LoVetri, "A Pilot Study of Human Forearm Imaging for a Microwave Tomography System," *IEEE Transactions on Medical Imaging*, to be resubmitted in 2012.

J.3 Referred Conference Papers

1. **Amer Zakaria** and Joe LoVetri, "Using Prior Information with FEM-CSI for Biomedical Microwave Imaging," *European Electromagnetics Conference 2012*, Toulouse, France, July 2-6, 2012.
2. **Amer Zakaria** and Joe LoVetri, "A Three-Dimensional Finite-Element Contrast Source Inversion Method for Microwave Imaging Applications," *Advanced Electromagnetics Symposium*, Paris, France, April 16-19, 2012
3. **Amer Zakaria**, Colin Gilmore, Stephen Pistorius and Joe LoVetri, "Balanced Multiplicative Regularization for the Contrast Source Inversion Method," *The 28th International Review of Progress in Applied Computational Electromagnetics Conference*, Columbus, Ohio, USA, April 10-14, 2012.
4. **Amer Zakaria** and Joe LoVetri, "Application of Finite-Element Contrast Source Inversion on TM and TE Experimental Data," *2011 IEEE International Symposium on Antennas and Propagation and USNC/URSI National Radio Science Meeting*, Spokane, Washington, USA, July 3-8, 2011.
5. **Amer Zakaria** and Joe LoVetri, "A Study of Adaptive Meshing in FEM-CSI for Microwave Tomography," *The 14th International Symposium Antenna and Electromagnetics and the American Electromagnetics Conference (ANTEM AMEREM 2010)*, Ottawa, Ontario, Canada, July 5-9, 2010.
6. Puyan Mojabi, Colin Gilmore, **Amer Zakaria** and Joe LoVetri, "Biomedical Microwave Inversion in Conducting Cylinders of Arbitrary Shapes," *13th International Symposium on Antenna Technology and Applied Electromagnetics (ANTEM) and the Canadian Radio Sciences Meeting (URSI/CNC)*, 2009. Banff, AB, Canada, February 15-18, 2009.

References

- [1] C. Sagan, “The burden of skepticism,” *Skeptical Enquirer*, vol. 12, p. 46, 1987.
- [2] P. M. Meaney, M. W. Fanning, T. Raynolds, C. J. Fox., Q. Fang, C. A. Kogel, S. P. Poplack, and K. D. Paulsen, “Initial clinical experience with microwave breast imaging in women with normal mammography,” *Academic Radiology*, March 2007.
- [3] A. Abubakar, P. M. van den Berg, and J. J. Mallorqui, “Imaging of biomedical data using a multiplicative regularized contrast source inversion method,” *Microwave Theory and Techniques, IEEE Transactions on*, vol. 50, no. 7, pp. 1761–1777, July 2002.
- [4] S. Y. Semenov and D. R. Corfield, “Microwave tomography for brain imaging: Feasibility assessment for stroke detection,” *International Journal of Antennas and Propagation*, vol. 2008, p. 8, 2008.
- [5] A. Abubakar and P. M. Van den Berg, “Non-linear three-dimensional inversion of cross-well electrical measurements,” *Geophysical Prospecting*, vol. 48, no. 1, pp. 109–134, Jan 2000.
- [6] A. Abubakar, T. M. Habashy, V. L. Druskin, L. Knizhnerman, and D. Alumbaugh, “2.5D forward and inverse modeling for interpreting low-frequency electromagnetic measurements,” *Geophysics*, vol. 73, no. 4, pp. F165–F177, 2008.
- [7] L.-P. Song, C. Yu, and Q. H. Liu, “Through-wall imaging (TWI) by radar: 2-D tomographic results and analyses,” *Geoscience and Remote Sensing, IEEE Transactions on*, vol. 43, no. 12, pp. 2793 – 2798, Dec 2005.
- [8] R. Zoughi, *Microwave Non-Destructive Testing and Evaluation*. Kluwer Academic Publishers, 2000.
- [9] D. Sheen, D. McMakin, and T. Hall, “Three-dimensional millimeter-wave imaging for concealed weapon detection,” *Microwave Theory and Techniques, IEEE Transactions on*, vol. 49, no. 9, pp. 1581 –1592, Sep. 2001.
- [10] Hadamard, *Lectures on Cauchy’s Problem in Linear Partial Differential Equations*. Yale University Press, 1923.

-
- [11] P. Rocca, M. Benedetti, M. Donelli, D. Franceschini, and A. Massa, "Evolutionary optimization as applied to inverse scattering problems," *Inverse Problems*, vol. 25, no. 12, p. 123003, 2009.
- [12] P. Mojabi and J. LoVetri, "Overview and classification of some regularization techniques for the Gauss-Newton inversion method applied to inverse scattering problems," *Antennas and Wireless Propagation Letters, IEEE*, vol. 8, pp. 645–648, 2009.
- [13] M. Donelli, G. Franceschini, A. Martini, and A. Massa, "An integrated multiscaling strategy based on a particle swarm algorithm for inverse scattering problems," *Geoscience and Remote Sensing, IEEE Transactions on*, vol. 44, no. 2, pp. 298 – 312, Feb 2006.
- [14] J. Sill and E. Fear, "Tissue sensing adaptive radar for breast cancer detection-experimental investigation of simple tumor models," *Microwave Theory and Techniques, IEEE Transactions on*, vol. 53, no. 11, pp. 3312–3319, 2005.
- [15] X. Li and S. Hagness, "A confocal microwave imaging algorithm for breast cancer detection," *Microwave and Wireless Components Letters, IEEE*, vol. 11, no. 3, pp. 130–132, 2001.
- [16] E. Bond, X. Li, S. Hagness, and B. Van Veen, "Microwave imaging via space-time beamforming for early detection of breast cancer," *Antennas and Propagation, IEEE Transactions on*, vol. 51, no. 8, pp. 1690–1705, 2003.
- [17] P. Kosmas and C. Rappaport, "Time reversal with the FDTD method for microwave breast cancer detection," *Microwave Theory and Techniques, IEEE Transactions on*, vol. 53, no. 7, pp. 2317–2323, 2005.
- [18] R. Amineh, M. Ravan, A. Khalatpour, and N. Nikolova, "Three-dimensional near-field microwave holography using reflected and transmitted signals," *Antennas and Propagation, IEEE Transactions on*, vol. 59, no. 12, pp. 4777–4789, dec. 2011.
- [19] M. Oristaglio and H. Blok, *Wavefield Imaging and Inversion in Electromagnetics and Acoustics*. Delft University, 1995.
- [20] C. Gilmore and J. LoVetri, "Enhancement of microwave tomography through the use of electrically conducting enclosures," *Inverse Problems*, vol. 24, no. 3, p. 035008, 2008. [Online]. Available: <http://stacks.iop.org/0266-5611/24/i=3/a=035008>
- [21] C. Kaye, C. Gilmore, P. Mojabi, D. Firsov, and J. LoVetri, "Development of a resonant chamber microwave tomography system," *Ultra-Wideband, Short*

- Pulse Electromagnetics 9*, ISBN 978-0-387-77844-0. Springer Science+ BusinessMedia, LLC, 2010, p. 481, vol. 1, p. 481, 2010.
- [22] C. Gilmore, P. Mojabi, A. Zakaria, M. Ostadrahimi, C. Kaye, S. Noghianian, L. Shafai, S. Pistorius, and J. LoVetri, "A wideband microwave tomography system with a novel frequency selection procedure," *Biomedical Engineering, IEEE Transactions on*, vol. 57, no. 4, pp. 894–904, April 2010.
- [23] P. Mojabi and J. LoVetri, "A novel microwave tomography system using a rotatable conductive enclosure," *Antennas and Propagation, IEEE Transactions on*, vol. 59, no. 5, pp. 1597–1605, May 2011.
- [24] M. Ostadrahimi, P. Mojabi, S. Noghianian, L. Shafai, S. Pistorius, and J. LoVetri, "A novel microwave tomography system based on the scattering probe technique," *Instrumentation and Measurement, IEEE Transactions on*, vol. PP, no. 99, pp. 1–12, 2011.
- [25] M. Ostadrahimi, P. Mojabi, C. Gilmore, A. Zakaria, S. Noghianian, S. Pistorius, and J. LoVetri, "Analysis of incident field modeling and incident/scattered field calibration techniques in microwave tomography," *Antennas and Wireless Propagation Letters, IEEE*, vol. 10, pp. 900–903, 2011.
- [26] C. Gilmore, A. Zakaria, S. Pistorius, and J. LoVetri, "A pilot study of human forearm imaging for a microwave tomography system," (*submitted to*) *Medical Imaging, IEEE Transactions on*, 2012.
- [27] C. Gilmore, P. Mojabi, and J. LoVetri, "Comparison of an enhanced distorted Born iterative method and the multiplicative-regularized contrast source inversion method," *Antennas and Propagation, IEEE Transactions on*, 2009.
- [28] P. Mojabi and J. LoVetri, "Microwave biomedical imaging using the multiplicative regularized Gauss–Newton inversion," *Antennas and Wireless Propagation Letters, IEEE*, vol. 8, pp. 645–648, 2009.
- [29] A. Zakaria, C. Gilmore, and J. LoVetri, "Finite-element contrast source inversion method for microwave imaging," *Inverse Problems*, vol. 26, no. 11, p. 115010, 2010. [Online]. Available: <http://stacks.iop.org/0266-5611/26/i=11/a=115010>
- [30] W. C. Chew and Y. M. Wang, "Reconstruction of two-dimensional permittivity distribution using the distorted Born iterative method," *Medical Imaging, IEEE Transactions on*, vol. 9, no. 2, pp. 218–225, 1990.
- [31] I. T. Rekanos, T. V. Yioultsis, and T. D. Tsiboukis, "Inverse scattering using the finite-element method and a nonlinear optimization technique," *Microwave*

- Theory and Techniques, IEEE Transactions on*, vol. 47, no. 3, pp. 336–344, Mar 1999.
- [32] A. Abubakar, W. Hu, P. van den Berg, and T. Habashy, “A finite-difference contrast source inversion method,” *Inverse Problems*, vol. 24, p. 065004 (17pp), 2008.
- [33] K. D. Paulsen, P. Meaney, M. Moskowitz, and J. S. Jr., “A dual mesh scheme for finite element based reconstruction algorithms,” *Medical Imaging, IEEE Transactions on*, vol. 14, no. 3, pp. 504–514, Sept 1995.
- [34] C. Gilmore, “Towards an improved microwave tomography system,” Ph.D. dissertation, University of Manitoba, 2010.
- [35] P. Mojabi and J. LoVetri, “Comparison of TE and TM inversions in the framework of the Gauss-Newton method,” *Antennas and Propagation, IEEE Transactions on*, vol. 58, no. 4, pp. 1336–1348, 2010.
- [36] B. Kooij and P. van den Berg, “Nonlinear inversion in TE scattering,” *Microwave Theory and Techniques, IEEE Transactions on*, vol. 46, no. 11, pp. 1704–1712, 1998.
- [37] G. Otto and W. Chew, “Inverse scattering of H_z waves using local shape-function imaging: A T-matrix formulation,” *International Journal of Imaging Systems and Technology*, vol. 5, no. 1, pp. 22–27, 1994.
- [38] J. Geffrin, P. Sabouroux, and C. Eyraud, “Free space experimental scattering database continuation: experimental set-up and measurement precision,” *Inverse Problems*, vol. 21, p. S117, 2005.
- [39] J. M. Geffrin and P. Sabouroux, “Continuing with the Fresnel database: experimental setup and improvements in 3D scattering measurements,” *Inverse Problems*, vol. 25, no. 2, p. 024001, 2009.
- [40] Q. Fang, P. M. Meaney, and K. D. Paulsen, “Viable three-dimensional medical microwave tomography: Theory and numerical experiments,” *Antennas and Propagation, IEEE Transactions on*, vol. 58, no. 2, pp. 449–458, 2010.
- [41] R. Feynman, *The Feynman Lectures on Physics: Volume 2*, ser. The Feynman Lectures on Physics. Boston: Addison-Wesley, 1963, vol. 2.
- [42] R. F. Harrington, *Time-Harmonic Electromagnetic Fields*. Wiley-IEEE Press, 1968.
- [43] M. Born and E. Wolf, *Principles of Optics*, 7th ed. Cambridge University Press, 2005.

-
- [44] J. Jin, *The Finite Element Method in Electromagnetics*. New York: John Wiley and Sons, 2002.
- [45] N. Bojarski, "The k -space formulation of the scattering problem in the time domain," *The Journal of the Acoustical Society of America*, vol. 72, p. 570, 1982.
- [46] T. Sarkar, E. Arvas, and S. Rao, "Application of FFT and the conjugate gradient method for the solution of electromagnetic radiation from electrically large and small conducting bodies," *Antennas and Propagation, IEEE Transactions on*, vol. 34, no. 5, pp. 635–640, 1986.
- [47] V. Rokhlin, "Rapid solution of integral equations of classical potential theory," *Journal of Computational Physics*, vol. 60, no. 2, pp. 187–207, 1985.
- [48] L. Greengard and V. Rokhlin, "A fast algorithm for particle simulations* 1," *Journal of Computational Physics*, vol. 73, no. 2, pp. 325–348, 1987.
- [49] C. Lu and W. Chew, "Fast algorithm for solving hybrid integral equations," in *Microwaves, Antennas and Propagation, IEE Proceedings H*, vol. 140, no. 6. IET, 1993, pp. 455–460.
- [50] P. Mojabi, "Investigation and development of algorithms and techniques for microwave tomography," Ph.D. dissertation, University of Manitoba, May 2010.
- [51] S. Caorsi, A. Massa, and M. Pastorino, "A computational technique based on a real-coded genetic algorithm for microwave imaging purposes," *Geoscience and Remote Sensing, IEEE Transactions on*, vol. 38, no. 4, pp. 1697–1708, 2000.
- [52] S. Barkeshli and R. Lautzenheiser, "An iterative method for inverse scattering problems based on an exact gradient search," *Radio science*, vol. 29, no. 4, pp. 1119–1130, 1994.
- [53] R. Kleinman and P. Berg, "A modified gradient method for two-dimensional problems in tomography* 1," *Journal of Computational and Applied Mathematics*, vol. 42, no. 1, pp. 17–35, 1992.
- [54] R. Kleinman, "Extended range modified gradient technique for profile inversion," DTIC Document, Tech. Rep., 1992.
- [55] P. M. van den Berg and R. E. Kleinman, "A contrast source inversion method," *Inverse Problems*, vol. 13, no. 6, p. 1607, 1997.
- [56] P. M. van den Berg, A. L. van Broekhoven, and A. Abubakar, "Extended contrast source inversion," *Inverse Problems*, vol. 15, no. 5, p. 1325, 1999.

- [57] O. C. Zienkiewicz and R. L. Taylor, *The Finite Element Method for Solid and Structural Mechanics*, 5th ed. Butterworth-Heinemann, 2005.
- [58] A. Taflove, S. Hagness *et al.*, *Computational Electrodynamics: the Finite-Difference Time-Domain Method*. Artech House Boston, 2005, vol. 2010.
- [59] P. Bonnet, X. Ferrieres, B. Michielsen, P. Klotz, and J. Roumiguères, *Finite-Volume Time Domain Method*. San Diego, CA: Academic Press, 1999.
- [60] I. Jeffrey, “Finite-volume simulations of Maxwell’s equations on unstructured grids,” Ph.D. dissertation, University of Manitoba, 2011.
- [61] W. Hoefler, “The transmission-line matrix method—theory and applications,” *Microwave Theory and Techniques, IEEE Transactions on*, vol. 33, no. 10, pp. 882–893, 1985.
- [62] R. W. Clough, “The finite element method in plane stress analysis,” in *2nd ASCE Conf. on Electronic Computation*, Pittsburgh, Pa., Sept 1960.
- [63] A. M. Winslow, *Magnetic field calculations in an irregular triangular mesh*, Lawrence Radiation Lab., Livermore, CA Std., 1965.
- [64] J. Volakis, A. Chatterjee, and L. Kempel, *Finite Element Method for Electromagnetics: Antennas, Microwave Circuits, and Scattering Applications*. Wiley-IEEE Press, 1998.
- [65] P. Solin, *Partial differential equations and the finite element method*. Wiley Online Library, 2006.
- [66] C. Geuzaine and J.-F. Remacle, “GMSH: A 3-D finite element mesh generator with built-in pre- and post-processing facilities,” *International Journal for Numerical Methods in Engineering*, vol. 79, p. 13091331, 2009.
- [67] A. Bayliss, M. Gunzburger, and E. Turkel, “Boundary conditions for numerical solution of elliptic equations in exterior regions,” *SIAM J. Appl. Math.*, vol. 42, pp. 430–451, April 1982.
- [68] J. Webb, “Edge elements and what they can do for you,” *Magnetics, IEEE Transactions on*, vol. 29, no. 2, pp. 1460–1465, 1993.
- [69] J. Lee, D. Sun, and Z. Cendes, “Full-wave analysis of dielectric waveguides using tangential vector finite elements,” *Microwave Theory and Techniques, IEEE Transactions on*, vol. 39, no. 8, pp. 1262–1271, 1991.
- [70] H. Whitney, “Geometric integration theory,” *Bull. Amer. Math. Soc.* 64 (1958), 38-41. DOI: 10.1090/S0002-9904-1958-10143-3 PII: S, vol. 2, no. 9904, pp. 10 143–3, 1958.

- [71] J. Nédélec, “Mixed finite elements in \mathbb{R}^3 ,” *Numerische Mathematik*, vol. 35, no. 3, pp. 315–341, 1980.
- [72] Z. Csendes and P. Silvester, “Numerical solution of dielectric loaded waveguides: I-finite-element analysis,” *Microwave Theory and Techniques, IEEE Transactions on*, vol. 18, no. 12, pp. 1124–1131, 1970.
- [73] M. Hano, “Finite-element analysis of dielectric-loaded waveguides,” *Microwave Theory and Techniques, IEEE Transactions on*, vol. 32, no. 10, pp. 1275–1279, 1984.
- [74] G. Mur and A. de Hoop, “A finite-element method for computing three-dimensional electromagnetic fields in inhomogeneous media,” *Magnetics, IEEE Transactions on*, vol. 21, no. 6, pp. 2188–2191, 1985.
- [75] A. Kameari, “Three dimensional eddy current calculation using edge elements for magnetic vector potential,” *Applied Electromagnetics in Materials*, pp. 225–236, 1989.
- [76] D. Davidson, *Computational Electromagnetics for RF and Microwave Engineering*. Cambridge Univ Pr, 2010.
- [77] P. C. Sabatier, “Past and future of inverse problems,” *Journal of Mathematical Physics*, vol. 41, p. 4082, 2000.
- [78] C. Gilmore, A. Abubakar, W. Hu, T. Habashy, and P. van den Berg, “Microwave biomedical data inversion using the finite-difference contrast source inversion method,” *Antennas and Propagation, IEEE Transactions on*, vol. 57, no. 5, pp. 1528–1538, May 2009.
- [79] P. Mojabi and J. LoVetri, “Eigenfunction contrast source inversion for circular metallic enclosures,” *Inverse Problems*, vol. 26, no. 2, p. 025010, 2010.
- [80] P. M. van den Berg, A. Abubakar, and J. Fokkema, “Multiplicative regularization for contrast profile inversion,” *Radio Science*, vol. 38, no. 2, pp. 23 (1–10), 2003.
- [81] A. Abubakar, P. M. van den Berg, and S. Y. Semenov, “Two- and three-dimensional algorithms for microwave imaging and inverse scattering,” *Journal of Electromagnetic Waves and Applications*, vol. 17, no. 2, pp. 209–231, 2003.
- [82] P. M. Meaney, N. K. Yagnamurthy, and K. D. Paulsen, “Pre-scaled two-parameter Gauss-Newton image reconstruction to reduce property recovery imbalance,” *Physics in Medicine and Biology*, vol. 47, no. 7, p. 1101, 2002. [Online]. Available: <http://stacks.iop.org/0031-9155/47/i=7/a=308>

- [83] A. Zakaria and J. LoVetri, "Application of multiplicative regularization to the finite-element contrast source inversion method," *Antennas and Propagation, IEEE Transactions on*, vol. 59, no. 9, pp. 3495–3498, Sept 2011.
- [84] A. Abubakar, P. Van Den Berg, T. Habashy, and H. Braunisch, "A multiplicative regularization approach for deblurring problems," *Image Processing, IEEE Transactions on*, vol. 13, no. 11, pp. 1524–1532, 2004.
- [85] K. van Dongen and W. Wright, "A full vectorial contrast source inversion scheme for three-dimensional acoustic imaging of both compressibility and density profiles," *The Journal of the Acoustical Society of America*, vol. 121, p. 1538, 2007.
- [86] L. Rudin, S. Osher, and E. Fatemi, "Nonlinear total variation based noise removal algorithms," *Physica D: Nonlinear Phenomena*, vol. 60, no. 1-4, pp. 259–268, 1992.
- [87] P. Mojabi and J. LoVetri, "A Prescaled Multiplicative Regularized Gauss-Newton Inversion," *Antennas and Propagation, IEEE Transactions on*, vol. 59, no. 8, pp. 2954–2963, Aug 2011.
- [88] P. M. van den Berg and A. Abubakar, "Contrast source inversion method: State of art," *Progress in Electromagnetic Research*, vol. 34, pp. 189–218, 2001.
- [89] J. Wesley, *Letters of John Wesley*, J. Telford, Ed. London: Epworth Press, 1931.
- [90] C. Gilmore, P. Mojabi, A. Zakaria, S. Pistorius, and J. LoVetri, "On super-resolution with an experimental microwave tomography system," *Antennas and Wireless Propagation Letters, IEEE*, vol. 9, pp. 393–396, 2010.
- [91] C. Gilmore, A. Zakaria, S. Pistorius, and J. LoVetri, "A study of matching fluids loss in a biomedical microwave tomography system," (*revised and resubmitted*) *Biomedical Engineering, IEEE Transactions on*, 2012.
- [92] A. Broquetas, J. Romeu, J. Rius, A. Elias-Fuste, A. Cardama, and L. Jofre, "Cylindrical geometry: A further step in active microwave tomography," *Microwave Theory and Techniques, IEEE Transactions on*, vol. 39, no. 5, pp. 836–844, 1991.
- [93] T. Davis and I. Duff, "An unsymmetric-pattern multifrontal method for sparse lu factorization," *SIAM Journal on Matrix Analysis and Applications*, vol. 18, no. 1, pp. 140–158, 1997.

- [94] T. Davis, "A column pre-ordering strategy for the unsymmetric-pattern multifrontal method," *ACM Transactions on Mathematical Software (TOMS)*, vol. 30, no. 2, pp. 165–195, 2004.
- [95] O. Schenk and K. Gärtner, *Parallel sparse direct and multi-recursive iterative linear solvers (PARDISO) user guide version 4.0.0*, 2009.
- [96] Y. Saad and M. Schultz, "GMRES: A generalized minimal residual algorithm for solving nonsymmetric linear systems," *Journal of Science and Statistical Computing, SIAM*, vol. 7, no. 3, pp. 856–869, 1986.
- [97] A. Wirgin, "The inverse crime," *Arxiv preprint math-ph/0401050*, 2004.
- [98] A. Abubakar, P. M. van den Berg, and S. Y. Semenov, "A robust iterative method for Born inversion," *Geoscience and Remote Sensing, IEEE Transactions on*, vol. 42, no. 2, pp. 342–354, Feb 2004.
- [99] P. Meaney, E. Demidenko, N. Yagnamurthy, D. Li, M. Fanning, and K. Paulsen, "A two-stage microwave image reconstruction procedure for improved internal feature extraction," *Medical Physics*, vol. 28, p. 2358, 2001.
- [100] P. Mojabi, C. Gilmore, A. Zakaria, and J. LoVetri, "Biomedical microwave inversion in conducting cylinders of arbitrary shapes," in *Antenna Technology and Applied Electromagnetics and the Canadian Radio Science Meeting, 2009. ANTEM/URSI 2009. 13th International Symposium on*, Feb 2009, pp. 1–4.
- [101] C. Gabriel, S. Gabriel, and E. Corthout, "The dielectric properties of biological tissues: III. Parametric models for the dielectric spectrum of tissues," *Physics in Medicine and Biology*, vol. 41, no. 11, pp. 2271–2294, Nov 2000.
- [102] E. Zastrow, S. Davis, M. Lazebnik, F. Kelcz, B. Van Veen, and S. Hagness, "Development of anatomically realistic numerical breast phantoms with accurate dielectric properties for modeling microwave interactions with the human breast," *Biomedical Engineering, IEEE Transactions on*, vol. 55, no. 12, pp. 2792–2800, Dec 2008.
- [103] M. Lazebnik and *et. al.*, "A large-scale study of the ultrawideband microwave dielectric properties of normal, benign, and malignant breast tissues obtained from cancer surgeries," *Physics in Medicine and Biology*, vol. 52, pp. 6093–6115, 2007.
- [104] S. Semenov, R. Svenson, A. Bulyshev, A. Souvorov, A. Nazarov, Y. Sizov, V. Posukh, A. Pavlovsky, P. Repin, and G. Tatsis, "Spatial resolution of microwave tomography for detection of myocardial ischemia and infarction—experimental study on two-dimensional models," *Microwave Theory and Techniques, IEEE Transactions on*, vol. 48, no. 4, pp. 538–544, 2000.

- [105] J. De Zaeytjyd, A. Franchois, C. Eyraud, and J.-M. Geffrin, “Full-wave three-dimensional microwave imaging with a regularized Gauss–Newton method—theory and experiment,” *Antennas and Propagation, IEEE Transactions on*, vol. 55, no. 11, pp. 3279–3292, 2007.
- [106] Y. Saad, *Iterative Methods for Sparse Linear Systems*. Society for Industrial Mathematics, 2003.
- [107] M. Ostadrahimi, S. Noghianian, L. Shafai, A. Zakaria, C. Kaye, and J. LoVetri, “Investigating a double layer Vivaldi antenna design for fixed array field measurement,” *International Journal of Ultra Wideband Communications and Systems*, vol. 1, no. 4, pp. 282–290, 2010.
- [108] W. S. Bigelow and E. G. Farr, “Impulse propagation measurements of the dielectric properties of several polymer resins,” *Measurement Notes, Note 55*, pp. 1–52, 1999.
- [109] R. Halter, T. Zhou, P. Meaney, A. Hartov, R. Barth, K. Rosenkranz, W. Wells, C. Kogel, A. Borsic, E. Rizzo *et al.*, “The correlation of *in vivo* and *ex vivo* tissue dielectric properties to validate electromagnetic breast imaging: initial clinical experience,” *Physiological Measurement*, vol. 30, p. S121, 2009.
- [110] J. Mallorqui, N. Joachimowicz, A. Broquetas, and J. C. Boloiney, “Quantitative images of large biological bodies in microwave tomography by using numerical and real data,” *Electronics Letters*, vol. 32, no. 23, pp. 2138–2140, Nov 1996.
- [111] A. Abubakar, P. M. van den Berg, and T. M. Habashy, “Application of the multiplicative regularized contrast source inversion method on TM- and TE-polarized experimental fresnel data,” *Inverse Problems*, vol. 21, pp. S5–S13, 2005.
- [112] R. Bloemenkamp, A. Abubakar, and P. Berg, “Inversion of experimental multi-frequency data using the contrast source inversion method,” *Inverse Problems*, vol. 17, p. 1611, 2001.
- [113] A. Litman and L. Crocco, “Testing inversion algorithms against experimental data: 3D targets,” *Inverse Problems*, vol. 25, no. 2, p. 020201, 2009. [Online]. Available: <http://stacks.iop.org/0266-5611/25/i=2/a=020201>
- [114] M. Li, A. Abubakar, and P. van den Berg, “Application of the multiplicative regularized contrast source inversion method on 3D experimental fresnel data,” *Inverse Problems*, vol. 25, p. 024006, 2009.
- [115] C. Yu, M. Yuan, and Q. H. Liu, “Reconstruction of 3D objects from multi-frequency experimental data with a fast DBIM-BCGS method,”

- Inverse Problems*, vol. 25, no. 2, p. 024007, 2009. [Online]. Available: <http://stacks.iop.org/0266-5611/25/i=2/a=024007>
- [116] J. D. Zaeytjyd and A. Franchois, “Three-dimensional quantitative microwave imaging from measured data with multiplicative smoothing and value picking regularization,” *Inverse Problems*, vol. 25, no. 2, p. 024004, 2009. [Online]. Available: <http://stacks.iop.org/0266-5611/25/i=2/a=024004>
- [117] W. Chew and J. Lin, “A frequency-hopping approach for microwave imaging of large inhomogeneous bodies,” *Microwave and Guided Wave Letters, IEEE*, vol. 5, no. 12, pp. 439–441, 1995.
- [118] A. Zakaria and J. LoVetri, “A study of adaptive meshing in FEM-CSI for microwave tomography,” in *Antenna Technology and Applied Electromagnetics & the American Electromagnetics Conference (ANTEM-AMEREM), 2010 14th International Symposium on*. IEEE, 2010, pp. 1–4.
- [119] J. Hesthaven and T. Warburton, *Nodal discontinuous Galerkin methods: algorithms, analysis, and applications*. Springer Verlag, 2008, vol. 54.
- [120] A. Abubakar and P. Berg, “The contrast source inversion method for location and shape reconstructions,” *Inverse Problems*, vol. 18, p. 495, 2002.
- [121] P. Mojabi, J. LoVetri, and L. Shafai, “A multiplicative regularized gauss-newton inversion for shape and location reconstruction,” *Antennas and Propagation, IEEE Transactions on*, vol. PP, no. 99, p. 1, 2011.
- [122] E. Maor, *To Infinity and Beyond*. Boston: Birkhauser, 1987.
- [123] P. P. Silvester and R. L. Ferrari, *Finite Element for Electrical Engineers*, 3rd ed. Cambridge University Press, 1996.
- [124] L. Kantorovich and G. Akilov, “Functional analysis. 1982.”

